Material Extrusion based Additive Manufacturing of Semicrystalline Polymers: Correlating Rheology with Print Properties

Arit Das

Dissertation submitted to the Faculty of the
Virginia Polytechnic Institute and State University
in partial fulfillment of the requirements for the degree of

Doctor of Philosophy
in
Chemical Engineering

Michael J. Bortner, Chair
Christopher B. Williams
Donald G. Baird
Stephen M. Martin
Steven H. McKnight

August 2, 2022
Blacksburg, Virginia

Keywords: additive manufacturing, material extrusion, polymer diffusion, rheology, interlayer adhesion
Copyright 2022, Arit Das

Material Extrusion based Additive Manufacturing of Semicrystalline Polymers: Correlating Rheology with Print Properties

Arit Das

(ABSTRACT)

Filament-based material extrusion (MatEx) additive manufacturing has garnered huge interest in both academic and industrial communities. Moreover, there is an increasing need to expand the material catalog for MatEx to produce end use parts for a wide variety of functional applications. Current approaches towards MatEx of semicrystalline thermoplastics are in their nascent stage with fiber reinforcements being one of the most common techniques. MatEx of commodity semicrystalline thermoplastics has been investigated but most of the current methods are extremely material and machine specific.

The goal of this dissertation is to enable MatEx of semicrystalline polymers with mechanical properties approaching that of injection molded parts. Tailored molecular architectures of blends that can control the crystallization kinetics from the melt state are investigated. By modifying the crystallization time window, the time during which chain diffusion can occur across the deposited layers is prolonged, which allows for a stronger bond between layers. Such differences in the crystallization process impact the z-axis adhesion and residual stress state, which directly affect mechanical properties and warpage in the printed parts. The impact of blend composition on polymer chain diffusion, crystallization profiles, and print properties resulting from the repeated non-uniform thermal history in filament based MatEx is studied. The melt flow behaviour is characterized using rheology and its effect on the interlayer adhesion of printed parts and print precision is explored. The extent of polymer chain re-entanglement post deposition on the printer bed is quantitatively determined using interrupted shear rheology protocols. Tensile bars are printed and mechanically characterized to analyze the tensile performance of the printed parts. Correlating the rheological findings with the mechanical performance of the printed parts provides valuable insights into the complex interlayer welding process during MatEx and is critical to improving existing machine designs and feedstocks in order to achieve printed parts with properties approaching their injection molded counterparts. The results will be essential in identifying optimal processing conditions to maximize material specific printed part performance as well as highlight the associated limitations to enable MatEx of next generation materials.

Material Extrusion based Additive Manufacturing of Semicrystalline Polymers: Correlating Rheology with Print Properties

Arit Das

(GENERAL AUDIENCE ABSTRACT)

Compared to traditional subtractive manufacturing techniques, additive manufacturing (AM) has the potential to transform modern manufacturing capabilities due to its unique advantages including design flexibility, mass customization, energy efficiency, and economic viability. The filament-based material extrusion (MatEx), also referred to as fused filament fabrication (FFF), employing thermoplastic polymers (and composites) has emerged as one of the most common AM modality for industrial adoption due to its operational simplicity. However, the widespread application of MatEx has been limited due to the lack of compatible materials, anisotropic mechanical properties, and lack of quality assurance. Most of the research on FFF has been performed on amorphous polymers with almost negligible levels of crystalline content such as polylactic acid (PLA) and acrylonitrile-butadiene-styrene (ABS). Semicrystalline polymers are an attractive choice for FFF feedstocks compared to the amorphous ones due to their improved thermal resistance, toughness, and deformability. However, processing semicrystalline polymers using FFF is challenging due to the volumetric shrinkage encountered during crystallization from the melt state. This results in the buildup of significant levels of residual stresses at temperatures lower than the crystallization temperature of the polymer resulting in warpage of the printed parts.

The research presented in this dissertation aims to address the aforementioned challenges by characterizing semicrystalline polymer feedstocks under conditions representative of the multiphysics encountered during a typical FFF process. Several strategies to limit shrinkage and warpage are discussed that involve tuning the thermal profile and crystallization kinetics during printing. The former is achieved by addition of thermally conductive carbon fiber reinforcements while the latter is realized by blending amorphous resins or low crystallinity polymers to the semicrystalline polymer matrix. The fibers results in a more homogenous temperature distribution during printing while the incorporation of the resins modify the rate of crystallization; both of which play a pivotal role in reducing the residual stress build-up and hence minimizing the warpage during printing. The printability of the materials is investigated based on the shear- and temperature dependent viscous response of

the polymers. The printed parts with fiber reinforcements exhibit high levels of mechanical anisotropy compared to the blends with the resins, likely due to differences in polymer chain mobility at the interface. The tensile properties of the printed polymer blends are slightly inferior to those obtained using traditional manufacturing techniques; however, properties close to 90-95% of injection molded properties are recovered through a simple post-processing thermal annealing step. The obtained results will assist in optimizing the processing parameters and feedstock formulation in order to consistently produce printed parts with minimal defects and tailored mechanical properties for functional applications.

Dedication

To my parents, Sonali and Dhruba Ranjan Das.

Acknowledgments

The journey to a Ph.D. is a long and arduous one. The presence of affectionate friends and family along with supportive mentors go a long way in easing the process. This dissertation would have never materialized without the support and encouragement from numerous brilliant and caring individuals.

I would like to sincerely thank my dissertation advisor, Dr. Michael J. Bortner, for his guidance, teachings, support, and feedback over the course of the last five years. I have always turned to you when in doubt and time and again you have addressed my concerns. I really appreciate your patience with me as I worked on my writing and presentation skills. You constantly provided me with opportunities that were best suited for my career aspirations and always had my back when the going got tough. Aside from being an excellent research advisor and mentor, I really enjoyed the course you taught on *Applied Rheology*. Thank you for everything, Dr. Bortner!

I was extremely fortunate to have exceptional academicians who served on my Ph.D. advisory committee. Their inputs have greatly enhanced my knowledge base and provided valuable perspective to what it takes to succeed in an academic career. Dr. Baird, thank you for your course on *Transport Phenomena II* and for allowing me to use the ARES G2 rheometer for my research. Dr. Martin, I appreciate your mentorship and patience while I was writing my first paper and proposal. Thank you for granting me access to the hot stage polarized microscope and goniometer in your lab. Dr. McKnight, thank you for all your feedback and suggestions that guided me to carve out the research direction after my preliminary examination. Dr. Williams, thank you for being an excellent mentor and a great role model. One of my biggest regrets during my time at Virginia Tech (VT) is that I never got to take a course with you as the instructor. I appreciate you taking the time from your busy schedule to meet me whenever I needed help; working with you and collaborating with the DREAMS lab has truly been an enriching experience.

The research performed in this dissertation would not have been possible without the help and support of my colleagues in the Polymer Composite and Materials Laboratory (PCML). Dr. Joseph, I cannot thank you enough for all the fruitful discussions when I was starting out. Jake, Eric, Cailean, Kathleen, and David thank you so much for making me feel welcome in

the group and for all the initial trainings and assistance. Subsequently, at different points of my graduate studies Brad, Tyler, Jack Reynolds, Martin, Al, Justin, Yimin, Jack Bryant, Larry, and Daniel joined the group. All of them were instrumental in helping me with my research; I will really miss working with such a wonderful group of researchers that made my time here so much more enjoyable. I hope that our paths cross again in the near future. I am thankful to all the awesome undergraduate researchers that I had the opportunity to mentor at PCML. Alex, Emma, Nish, Jim, Jocelyn, Aliya, Samantha, and Jouke, thank you for all your efforts and contributions.

I am thankful to Department of Chemical Engineering and the Macromolecules Innovation Institute (MII) at VT. The support system provided by Diane, Andrea, Stacey, Tina, Skyler, Brad, Jennifer Clark, Kim, Jennifer Galford, and Reilly are one of the major reasons why graduate students like me could focus only on performing research while they expertly took care of all the associated activities (from material procurement to conference travels to poster printing). I would like to acknowledge MII for providing the collaborative infrastructure at VT focused across the spectrum of polymer science and engineering. For a major portion of my time in graduate school, I was funded by the Adhesives Manufacturers Association Adhesive and Sealant Science scholarship through MII. Moreover, I am indebted to the Thermoset Resin Formulators Association (TRFA), American Institute of Chemical Engineers (AIChE), American Chemical Society (ACS) Industrial & Engineering Chemistry (I&EC) Division, VT Graduate Student Assembly (GSA), and Adhesion Society for providing funding to attend and present my research at different conferences. Funding and material donation from various industrial sponsors including Braskem, NanoSonic, Arakawa Chemicals, ExxonMobil, Boston Scientific, Henkel, Hexcel, Boeing, and Google are gratefully acknowledged.

I was a part of the International Research Experience for Students (IRES) program through the VT College of Engineering that allowed me to spend two wonderful summers at the University of Nottingham (UoN). I would like to express my gratitude to Dr. Jack Lesko and Dr. Nicole Sanderlin for providing me with this opportunity as well as to all the personnel working behind the scenes both at VT and UoN to make the IRES experience thoroughly enjoyable. I would also like to thank Dr. Davide De Focatiis for agreeing to host me in his lab during my time at Nottingham as well as for all his inputs and advice on the project that I was working on. Gabriel, Matt, and Vinnie, thank you for helping me as I started at the "P. Lab" at UoN; I had a great time sharing the lab with you guys.

Over the last five years, I have been fortunate enough to work with a number of distinguished

researchers and scientists. I really enjoyed and learned a lot though the collaboration with Dr. Dillard (who also co-taught probably my favorite graduate course, *Polymer Viscoelasticity*). Dr. Moore (the other instructor of the *Polymer Viscoelasticity* course) and Dr. Long, thank you for all the mentorship and career advice. The collaborations with Dr. McIlroy and Dr. Peterson have helped shape my research outlook and provided me with a different perspective about approaching research.

Since a lot of my research is interdisciplinary in nature, I must acknowledge the contributions of the excellent graduate students I had the good fortune of working with. Cam, Callie, Yifeng, & Jack Bryant (DREAMS lab), Tianran (Dr. Baird's lab), Glenn & Michelle (Moore Research Group), Dennis (Dr. Stark's lab), Tianyi (Dr. Esker's lab), and James (Dr. Long's lab), I have learnt so much from you all and thank you for letting me be a small part of your wonderful research.

My family has been a constant source of encouragement and support throughout my life. My parents, Sonali and Dhruba Ranjan Das, hammered home the importance of education and academic excellence ever since I was a little boy. The person I am today has been shaped by their teachings. This dissertation has its roots firmly planted in the efforts my mother put during my childhood making sure I studied diligently. My father taught me to be a patient and tenacious individual; traits that have helped me immensely during my days here at VT. I know my parents have suffered and grieved a lot over the last five years since their only son was 8000 miles away from them. I am really sorry for that, but I am trying my best every day to reduce that distance.

The time I spent in school is one of the most cherished memories of my life. Although I am thankful to all of my teachers, I want to mention the effect my Physics and Chemistry teacher, Gupta Ma'am, had on me in deciding to pursuing a career in science and engineering. Reconnecting with my school friends: Binayak, Debmahul, Rohan, Rounak, and Soumyadip, was probably one of the best things that could have happened to me. Now, for better or worse, I can't imagine a week without our "ridiculous, hilarious" and honestly, slightly childish group calls. You guys are all very special to me and I am sure you will continue to make me proud in the upcoming days.

Ashmita, thanks for the wonderful friendship; I thoroughly enjoyed our interactions. You are one of the most compassionate individuals I have ever met. You are well on your way to becoming a brilliant polymer scientist (never doubt yourself) and I wish you all the best for your future. Hope you find all the happiness in life!

My undergraduate days at Jadavpur University (JU) not only introduced me to research but also to a number of exceptional people. I especially want to thank CB Sir, RC Ma'am, SS Ma'am, and SB Sir for the courses they taught as well as for the research mentorship they provided. I have to mention a couple of the JU friends who are very close to me. Arka, there are very few people like you and I can't wait to see what you achieve in the coming days. Sankhadeep, I probably should not say much about you knowing the cynic you are, but you have always been a great friend, honest critic (sometimes unnecessarily harsh), and a safe place to gossip and ramble on about my problems. Hopefully, we will be able to meet up in person soon!

I had the chance to meet a number of wonderful people at Blacksburg. Abhijit Da and Shreya Di, thank you for all the *addas* and lunch/dinners at your place but most of all for providing the *Arit kaka* status to me. Niharika will always hold a special place in my heart, and I wish her all the happiness and success. Srijan Da and Swarnali Di, it was a pleasure getting to know you guys and hopefully we will have more frequent meetups in the future. Padhi, you are one of the humblest human beings I ever met and thanks for the memories on the cricket field. Anindya thanks for putting up with my fish dishes and for the wonderful late-night music performances. Debasmita thanks for all the delicious food you prepared for us over the last couple of years. You might find it hard to believe but I will miss our banters. Anish, one of the most endearing people at Blacksburg, thanks for all the entertaining anecdotes and also for finding humor in my poor jokes. I never expected that we will become such good friends :p

Finally, I come to the friends with whom I have spent the most time in Blacksburg. I have tried to emulate all of you in one way, shape, or form in an effort to become a better individual. The only person I knew in Blacksburg before joining VT was Mayuk Da (who I now refer to as Santa). Santa, thank you for everything from guiding me in my initial days here to introducing me to *Pahaartowlir Loop* to helping with literally anything and everything. I am really lucky and proud to have a brother like you. Shuchismita Di, thanks for those unplanned three course dinners and well-planned trips. I will really miss those awesome desserts (I will not miss the herbal tea). Pal, thanks for the discussions ranging from research to cricket to work-life balance. Lekha, thanks for being the link between the Millennials and Gen-Z and for the *Dhania Chicken*. I hope the walls of your house gets covered up soon with all the well-deserved accolades.

GB, thanks for providing an example of what is possible to achieve in graduate school. I also

really appreciate your efforts in helping me to maintain a healthy sleeping schedule. Esha Di, thanks for all the cakes and melodious singing in our parties. I appreciate you not killing me when I cracked one of my signature jokes. Ranit Da, thanks for all the advice, pranks, culinary journeys, and mindless conversations. There is no shame in admitting that I tried to copy a lot of your traits; mostly because, I was able to relate to you the most. Thanks also for not losing your patience with me when I kept messing up my driver's license test. Gupta Da, there is a lot to thank you for so please pardon me if I miss anything. Firstly, thanks for laying the foundations of VT Bengali Students' Association during your initial days as a graduate student that has since grown from strength to strength providing us with the opportunity to recreate the magic of Kolkata and Bengal at VT. I will definitely miss the delicious food you made and also picked up for us when you were driving down from Maryland. Thanks for taking care of me, especially in the weeks leading up to my defense (Yes, Poorna Di you did too!). Thanks for all the great advice about every facet of life (I have constantly tapped into your seemingly endless reservoir of knowledge and will continue to do so) and the insightful discussions (ranging from what is the best XI India should play in the cricketing field to why the formatting in this document is looking off). Hopefully, we get the chance to open the innings one more time.

Poorna Di and Sreeya Di (I will not take any chances to incite needless arguments by mentioning one of you before the other), both of you are the elder sisters I never had. Thank you for the amazing time we shared together; I will miss watching your arguments silently. Poorna Di thank you for the *pnathar mangsher jhol* and *bori diye macher jhol*; two things that always put a smile to my face no matter what I was going through. Sreeya Di thank you for being a great support system, for hosting the most happening parties, and especially, for *that* conversation on a cold December night in Kolkata. I really appreciate it that you guys scolded me whenever I did something wrong, and I know I can always turn to you if I am confused about anything or need honest advice. One other thing specific to Poorna Di, I think after having me as a roommate for the past two years, I am sure you are properly equipped to handle the potential challenges you might encounter if you decide to welcome a "roommate" in the near future.

Although I mention "friends" three paragraphs back, it is safe to say that I am leaving Blacksburg with an extended family and a treasure trove of memories that are enough to last a lifetime.

Contents

List of Figures xx

List of Tables xxxviii

1 Introduction 1

1.1 Motivation . . . 2

1.2 Research Hypotheses . . . 3

1.3 Research Objectives . . . 3

2 Material extrusion-based additive manufacturing of polyolefins 5

2.1 Introduction . . . 6

2.2 Roadmap . . . 8

2.3 Additive Manufacturing of Polyolefins . . . 10

2.4 Material Extrusion (MatEx): Process Considerations . . . 11

2.5 MatEx of Polyethylene (PE) . . . 14

2.5.1 Printing with PE . . . 14

2.5.2 MatEx of PE blends with other polymers . . . 23

2.5.3 MatEx of filler reinforced PE composites . . . 25

2.6 MatEx of Polypropylene (PP) . . . 30

2.6.1 Printing with PP . . . 30

2.6.2 MatEx of PP blends with other polymers . . . 36

2.6.3 MatEx of Filler-reinforced PP composites . . . 40

2.7 MatEx of Polyolefins: Future Directions . . . 45

2.7.1 Print temperature . . . 46
2.7.2 Print speed . . . 47
2.7.3 Layer thickness . . . 47
2.7.4 Print orientation . . . 48
2.7.5 Accessory heating . . . 48
2.7.6 Toolpath design: Neat vs. filled systems . . . 49
2.7.7 Comprehensive material characterization . . . 49
2.8 Conclusions . . . 50

3 Importance of polymer rheology on material extrusion additive manufacturing: Correlating process physics to print properties 52

3.1 Introduction . . . 53
3.2 Material Extrusion: Filament and pellet-fed modes . . . 55
3.3 Why Rheology? . . . 57
3.4 Importance of polymer rheology in material extrusion based AM . . . 62
3.5 Dynamics inside the print nozzle . . . 62
3.5.1 Effect of printing parameters on shear rates . . . 62
3.5.2 Failure modes inside the nozzle . . . 66
3.5.3 Pressure build-up and filament buckling . . . 66
3.5.4 Fluid flow analysis inside the heated nozzle . . . 69
3.6 Dynamics in the stand-off region between nozzle and print bed . . . 78
3.6.1 Die swell: Origin and implications in MatEx . . . 78
3.6.2 Flow instabilities: Origin and implications in MatEx . . . 82
3.6.3 Rheological measurements relevant to die swell . . . 84
3.6.4 Experimental and simulation studies for the standoff region . . . 85

3.6.5 Importance of heat transfer effects . . . 87
3.6.6 Importance of extensional viscosity in MatEx . . . 88
3.6.7 Extensional rheological characterizations: Missing links for MatEx . . . 91
3.7 Dynamics of post-deposition on the print bed . . . 92
3.7.1 Interlayer chain diffusion and bond formation . . . 92
3.7.2 Sintering models and printed part properties . . . 95
3.7.3 Effect of print parameters on printed part properties . . . 96
3.7.4 Mechanical integrity of the deposited extrudate . . . 99
3.7.5 Quantifying the extent of chain interdiffusion . . . 100
3.7.6 Routes to promote interlayer welding in printed parts . . . 101
3.8 Discussion and future outlook . . . 104
3.8.1 Print nozzle . . . 104
3.8.2 Stand-off region . . . 104
3.8.3 Printer bed . . . 105
3.8.4 Big Area Additive Manufacturing (BAAM) . . . 105
3.8.5 Combining experimental and modeling approaches . . . 109
3.8.6 Incorporating semicrystalline polymers . . . 110
3.8.7 Rheological implications of incorporating fillers . . . 111
3.9 Conclusions . . . 115

4 Advances in modeling transport phenomena in material-extrusion additive manufacturing: Coupling momentum, heat, and mass transfer 116

4.1 Introduction . . . 117
4.2 Momentum transport: Flow and geometry . . . 125
4.3 Heat transfer . . . 128

4.4 Anisotropy and inter-diffusion . . . 131
4.5 Polymer crystallization . . . 133
4.6 Discussion and future directions . . . 136

5 Rheological investigation of nylon-carbon fiber composites fabricated using material extrusion based additive manufacturing 139

5.1 Introduction . . . 141
5.2 Materials and methods . . . 143
5.2.1 Filament materials . . . 143
5.2.2 Taguchi approach for determining printing parameters and design of experiments . . . 143
5.2.3 Thermogravimetric analysis . . . 144
5.2.4 Dynamic scanning calorimetry . . . 145
5.2.5 Rheology . . . 146
5.2.6 Tensile testing . . . 146
5.2.7 Scanning electron microscopy (SEM) . . . 146
5.3 Results and Discussion . . . 147
5.3.1 Thermal characterization . . . 147
5.3.2 Melting, crystallization, and crystallinity of PA6 and CF-PA6 . . . 148
5.3.3 Rheological characterization . . . 151
5.3.4 Tensile properties of printed parts: Effect of print parameters . . . 157
5.3.5 SEM analysis . . . 164
5.4 Conclusions . . . 164

6 Material extrusion-based additive manufacturing with blends of polypropylene and hydrocarbon resins 167

6.1 Introduction . . . 168
6.2 Materials and methods . . . 171
6.2.1 Materials . . . 171
6.2.2 Preparation of Blends of PP and Hydrocarbon Resins . . . 172
6.2.3 Thermogravimetric Analysis (TGA) . . . 172
6.2.4 Differential Scanning Calorimetry (DSC) . . . 172
6.2.5 Hot Stage Polarized Light Microscopy (HS-PLM) . . . 173
6.2.6 Rheology of PP/Hydrocarbon Resin Blends . . . 173
6.2.7 Scanning Electron Microscopy (SEM) of Blends . . . 174
6.2.8 Filament Generation and MEAM . . . 174
6.2.9 Tensile Testing of Printed Parts . . . 174
6.3 Results and Discussion . . . 175
6.3.1 Melting, crystallization and crystallinity of the blends . . . 175
6.3.2 Hot stage polarized light microscopy of PP/hydrocarbon resin blends 177
6.3.3 Rheology of the prepared PP/FH and PP/PH blends . . . 179
6.3.4 Printed part bed adhesion and warpage . . . 180
6.3.5 Mechanical properties of printed parts . . . 181
6.3.6 Effect of annealing on mechanical properties of printed PP/hydrocarbon resin parts . . . 184
6.3.7 Effect of Print Orientation on Mechanical Properties of PP/Hydrocarbon Resin Blends . . . 187
6.3.8 SEM Imaging of the PP/Hydrocarbon Resin Blends . . . 188
6.4 Conclusions . . . 190

7 3D printing of semicrystalline polymer blends: Effect of melt flow rate 191

7.1 Introduction . . . 192
7.2 Materials and methods . . . 194
7.2.1 Materials . . . 194
7.2.2 Blend preparation . . . 194
7.2.3 Thermal analysis . . . 194
7.2.4 Rheology . . . 195
7.2.5 MatEx of PP blends . . . 196
7.2.6 Tensile testing . . . 196
7.2.7 Geometric accuracy and warpage . . . 197
7.3 Results and discussion . . . 197
7.3.1 Melting and crystallization . . . 197
7.3.2 Shear and oscillatory rheology . . . 199
7.3.3 Interrupted shear rheology . . . 200
7.3.4 Printing performance . . . 202
7.4 Conclusions . . . 205

8 Customized blends of polypropylene for extrusion based additive manufacturing 206

8.1 Introduction . . . 207
8.2 Materials and Methods . . . 209
8.2.1 Materials . . . 209
8.2.2 Preparation of PP/LCPP Blends . . . 210
8.2.3 Differential Scanning Calorimetry (DSC) of PP/LCPP Blends . . . 210
8.2.4 Rheology of PP/LCPP Blends . . . 211
8.2.5 3D Printing of PP/LCPP Blends . . . 211

8.2.6 Tensile Testing of Printed Parts . . . 211
8.2.7 Dynamic Mechanical Analysis (DMA) of Printed Parts . . . 212
8.3 Results and Discussions . . . 212
8.3.1 Melting and Crystallization Behavior of the Blends . . . 212
8.3.2 Rheological Characterizations of the Blends . . . 215
8.3.3 Printing Performance and Mechanical Properties of the Blends . . . 219
8.3.4 Viscoelastic Properties of the Printed Parts . . . 223
8.4 Conclusions . . . 225

9 Conclusions and Scientific Contributions 226
9.1 Conclusions . . . 226
9.2 Scientific Contributions . . . 228

10 Future work 229
10.1 Effect of fiber reinforcements . . . 229
10.2 Effect of crystallinity on interlayer strength . . . 232
10.3 Other semicrystalline feedstocks for MatEx . . . 234
10.3.1 Improving filler matrix adhesion . . . 234
10.3.2 Tailoring blend composition . . . 234
10.3.3 Enhancing miscibility in blends . . . 234

11 Publications 236
11.1 Journal publications . . . 236
11.2 Technical report . . . 238
11.3 Manuscripts under review/in revision . . . 238
11.4 Manuscripts in preparation . . . 238

11.5 Refereed conference proceedings 238

Bibliography **240**

Appendices **305**

Appendix A Recent advances in material development and process monitoring in polymer additive manufacturing **306**

A.1 Introduction 307

A.2 Material Development in Polymer AM 308

A.3 Process Monitoring in Polymer AM 311

A.4 Future Directions 313

Appendix B Rheological investigation of nylon-carbon fiber composites fabricated using material extrusion based additive manufacturing **315**

B.1 Thermal stability of PA6 and CF-PA6 315

B.2 Melting and crystallization of PA6 and Onyx 316

B.3 Complex viscosity of PA6 and CF-PA6 316

B.4 Viscoelastic properties of PA6 and CF-PA6 317

B.5 ANOVA tests for print parameter optimization 318

Appendix C Material extrusion-based additive manufacturing with blends of polypropylene and hydrocarbon resins **319**

C.1 Composition of PP/hydrocarbon resin blends 319

C.2 Thermal stability of PP/hydrocarbon resin blends 319

C.3 Melting and crystallization profiles of PP/FH blends 322

C.4 Cooling scans of pure hydrocarbon resins from non-isothermal DSC experiments 323

C.5 DSC melting endotherms of PP and blends zoomed in the region of 160-180°C 324

C.6 Melting and crystallization temperature and enthalpy of PP/hydrocarbon resin blends 325
C.7 Degree of crystallinity of PP/hydrocarbon resin blends 326
C.8 Isothermal crystallization and print bed temperature 326
C.9 Effect of cooling rate on crystallization behavior of the blends 328
C.10 Size of spherulites formed during isothermal crystallization of PP/hydrocarbon resin blends 330
C.11 Mechanical properties of PP/FH blends printed at ±45° raster angle 330
C.12 Mechanical properties of annealed PP/FH blends printed at ±45° raster angle 332
C.13 Mechanical properties of PP/hydrocarbon resin 80/20 blends printed at 90° raster angle 333

List of Figures

2.1 Current (2017) and projected (2027) evolution of revenues from different polymer-based AM processing techniques from use in professional environments (data adapted from [Publishing, 2018] 9

2.2 Schematic illustration of the filament-based material extrusion process for semicrystalline polymers. A pinch roller mechanism feeds the polymer filament into the heated section of the nozzle (nozzle temperature: T_N) at a continuous rate (U_0). Upon deposition of the melt on the print bed (at constant speed of U_N), the velocity gradients in the flow result in polymer deformation. The flow of the polymer melt and subsequent deposition on the print bed constitutes Region I in the figure. The cooling of the deposited extrudate on the print bed occurs in Region II where the deformations in the polymer relax since velocity gradients are absent in this region. As the polymer melt cools, the temperature drops below the melting temperature that initiates nucleation and growth of spherulites. Crystallization of the polymer is amplified if residual stretch is present during the initiation of nucleation in this region (image reprinted from [McIlroy and Graham, 2018] with permission from Elsevier). 12

2.3 (a) The effect of nozzle diameter and raster pattern on the tensile modulus, maximum tensile strength, and elongation at break of HDPE samples printed using FFF and compared with the injection molded properties (image reprinted from [Schirmeister et al., 2019] with permission from Elsevier); (b) Digital images of 3D printed rectangular bars. (i) Bar of HDPE printed without using a brim, (ii) 10 mm high HDPE bar printed with a brim, (iii) 10 mm high functionalized HDPE bar printed with a brim, (iv) 10 mm high functionalized HDPE bar prior to detaching from the brim. The functionalized HDPE bars printed with brims exhibit minimal warpage (image reprinted from [Gudadhe et al., 2019] with permission from American Chemical Society); (c) Impact testing results as a function of print temperature (260, 280, 300°C) for the FFF printed samples of PC/ABS, LDPE shell-PC/ABS, and HDPE shell-PC/ABS. The left image corresponds to prints printed in the XZ orientation while the right image corresponds to prints printed in XY orientation (image reprinted from [Peng et al., 2019a] with permission from American Chemical Society) 23

2.4 Illustration of the cross-sectional view of (a) polymer chains, and the inter and intra-layer bonds; (b) the presence of reinforcement affecting the interlayer bonds (reduced extent of interlayer bonding due to presence of reinforcement) 29

2.5 (a) A typical warped PP print during FFF, (b) schematic of the origin of warpage during FFF of polypropylene, (c) correlation between the warpage encountered during printing polypropylene and the stereochemistry of the polymer (image reprinted with permission from [Peng et al., 2019a] with permission from Springer Nature) 31

2.6 Schematic of the recommended processing considerations (nozzle temperature, bed temperature) during melt-based AM of polyolefins based on maximizing the polymer chain diffusion between the layers post-deposition on the print bed. 32

2.7 Effect of layer thickness on the molecular diffusion and void formation across the layer interfaces. Parts printed with lower layer thicknesses tend to have a higher degree of crystallinity since they are associated with longer print times. As a result, the parts are exposed to the heated print bed for a longer time period which induces an annealing effect and parts with increased crystalline content are obtained. 34

2.8 (a) Schematic description of the in-situ 3D printing equipment where a sample part is printed through a static printing nozzle on a moveable print bed that can be heated; (b) schematic description of the in-situ X-ray scattering experiments that were performed by placing the aforementioned 3D printed in the path of an X-ray beamline. The scattering intensities during SAXS and WAXS are measured through a photoncounting and a charge-coupled device (CCD) detector, respectively; (c) (d) digital images highlighting the details of the entire experimental setup; (e) variation in the degree of crystallinity across the cross-section of printed layer of isotactic PP; (f-g)Variation in the degree of crystallinity, temperature, and long-spacing of the printed part of isotactic PP post deposition on the heated print bed. The different symbols correspond to the measurements performed at different positions in the top layer of a printed sample: 0.10 cm (black hollow circles), 0.90 cm (red squares), 1.40 cm (green triangles), and 1.90 cm (yellow triangles) from the wall of the printed polymer sample. (images reprinted from [Nogales et al., 2019] with permission from American Chemical Society) 35

2.9 (a) Small angle X-ray scattering profiles of isotactic polypropylene as a function of location (from the filament interface to the filament core); (b) azimuthal scan indicating the presence of kebab peak at the different radial locations from the filament interface to the core; (c) azimuthal scan indicating the presence of shish peak at the different radial locations from the filament interface to the core; (d) the integrated 1D plots of the scattering intensity as a function of the scattering vector from the 2D SAXS profiles; (e) schematic of the structural changes at the interfacial region of two filaments, highlighting the aligned shish structures (green), the interdiffusion of the kebab structures (blue), and the reptation of the amorphous tie chains (yellow) (image reprinted from [Shmueli et al., 2019b] with permission from American Chemical Society) 37

2.10 Schematic diagram of FFF of PP/PS blends, along with the corresponding SAXS profiles, at three different stages (a) solid filament being fed into the printer nozzle where the shear forces are negligible, and the sample consists of elliptical PS phase and PP spherulites; (b) the extrusion of the filament through a heated nozzle induces a shearing effect where the PS phase undergoes significant deformation and results in formation of microfibers; (c) deposition of the extrudate on the printer bed where a combination of microfibers and shish-kebab morphology is observed. The mechanical performance of the printed parts is dictated by the effects of the crystal structure orientation and PS microfibers (image reprinted from [Jiang et al., 2019] with permission from Elsevier) (d) Schematic description of isotactic PP chains transcrystallizing on top of the oriented GNP lattice. The shear experienced by the PP filament is enough to exfoliate the GNPs. The force required to extrude the composite filament through the nozzle reduces since the viscosity of the material decreases with increasing shear rates. In neat PP, the shear forces resulted in the formation of shish-kebab structure during extrusion through the nozzle (image reprinted from [Shmueli et al., 2020] with permission from Elsevier) . 41

2.11 Effect of the nozzle temperature on the interlayer morphology of a printed part of polypropylene at constant bed (85°C) and ambient (25°C) temperature. Three different nozzle temperatures are highlighted, namely, (a) 180°C; (b) 210°C; and (c) 230°C (image reprinted from [Hertle et al., 2016] with permission from John Wiley & Sons Ltd.) 46

3.1 (a) Schematic of the overall FFF process. 1) filament spool, 2) thermoplastic materials. 3) heated barrel consisting of 4) pinch rollers, 5) liquefier, 6) nozzle, 7) layer-by-layer deposited materials, and 8) movable build plate (image reprinted from [Spoerk et al., 2020] under the Creative Commons Attribution License, CC BY 4.0 Copyright 2019 Spoerk et al. Journal of Applied Polymer Science published by Wiley Periodicals, Inc.); (b) Overview of the rheological measurements needed to be performed as well as the relevant datasets to be analyzed in order to describe the behavior of the polymer melt during different stages of the MatEx process. 56

3.2 (a) Representative plot of the viscosity (or complex viscosity) as a function of shear rate (or frequency) for MatEx based processing. The different rheological techniques typically used to obtain such data are highlighted in the figure. The overlap between the steady and SAOS measurements from a rotational rheometer can usually be described by Cox-Merz's rule for pure polymers; (b) Numerical simulation and analytical results illustrating the inlet velocity field, shear rate distribution, and viscosity inside the liquefier for a 0.5mm nozzle (image reprinted from [Bakrani Balani et al., 2019] with permission from Elsevier); and (c) Overlay of small amplitude oscillatory shear (hollow shapes) and steady torsional shear (filled shapes) rheometry of Ultem 1010 at 345°C (circles), 360°C (triangles), and 375°C (squares). The blue and green boxes highlight the viscosity values associated with the extrusion through the print nozzle and the bond consolidation process upon deposition on the print bed, respectively (image reprinted with permission from [Gilmer et al., 2019] Copyright 2019 American Chemical Society). 65

3.3 (a) Depictions of the common failure modes inside the FFF nozzle. From left to right: inconsistent filament diameter, annular backflow, and filament buckling; (b) A typical buckling analysis performed on low density polyethylene (LDPE), ABS, and sodium sulfonated polyethylene glycol (NaSPEG) based on Equation 3.8. The shear rates within the vertical dotted lines represent the rates experienced during a typical printing process employing a 0.3mm nozzle. The horizontal dotted line separates the data points corresponding to which the polymer feedstock experiences buckling; and (c) Visual representation of annular backflow (left) and filament buckling (right) observed during extrusion of NaSPEG and LDPE, respectively, through the print nozzle (all the images are reprinted from [Gilmer et al., 2018] with permission from Elsevier). 69

3.4 Variation in the (a) pressure drop and (b) shear rate inside a typical 3D printer nozzle (images reprinted from [Phan et al., 2020] with permission from Elsevier); (c) Simulated velocity profile of the polymer melt during initial extrusion (image reprinted from [Heller et al., 2019] with permission from Elsevier); (d) Simulated velocity profile of the polymer melt when the extrudate attained the final shape (image reprinted from [Heller et al., 2019] with permission from Elsevier); and (e) The variation in the thermal profiles at three different Péclet numbers. The different vertical lines indicate locations that had been normalized with the distance required to reach T_g (image reprinted from [Pigeonneau et al., 2020] with permission from Elsevier). . . . 77

3.5 (a) Illustration of die swell in a typical FFF process post-extrusion through the nozzle. The polymer chains in the filament feed may have some residual alignment depending upon the filament production process; (b), visualization & (c) estimation of die swelling observed in different PLA samples printed at 180°C under different extrusion speeds (image reprinted from [Tang et al., 2020] with permission from John Wiley & Sons Ltd.); and (d) The effect of nozzle inlet velocity and associated shear rate on the shape of the polymer extrudate obtained by printing at 195°C using a 0.5mm nozzle along with numerical simulation of the extrudate geometry (image reprinted from [Bakrani Balani et al., 2019] with permission from Elsevier). 79

3.6 (a) A typical wall shear stress versus shear rate plot highlighting the flow behavior during extrusion of linear polyethylene along with the regions of related flow instabilities (image reprinted with permission from [Jabbari et al., 2018] under the terms of the Creative Commons CC-BY 4.0 license); (b) The filament feeding force and die swell ratio at different print temperatures and feeding velocity for PLA and ABS printed using 0.4mm nozzle. The dashed lines in the figure are indicative of the flow instabilities encountered during extrusion through the nozzle (image reprinted from [Serdeczny et al., 2020b] with permission from Elsevier); and (c) Visual representation of extrudates exiting the print nozzle exhibiting stable extrusion, melt fracture instability, and sharkskin instability (image reprinted from [Serdeczny et al., 2020b] with permission from Elsevier). 83

3.7 (a) Representative extensional rheology data for PLA at 170°C obtained using both the Sentmanat extensional rheology fixture (TA Instruments SER) and Cogswell analysis of entrance pressure method. The solid line represents the Phan-Thien-Tanner model fits to the experimental data while the dashed line represents a Tr of 3 (image reprinted from [Phan et al., 2020] with permission from Elsevier); (b) Evolution of extensional viscosity as a function of time at different extension rates for PLA at 170°C measured using the extensional fixture in a rheometer. The solid lines represent the Phan-Thien-Tanner model fits to the experimental data (image reprinted from [Phan et al., 2020] with permission from Elsevier); (c) Effect of polymer molecular weight on the steady-state Trouton ratio and extensional relaxation time (image reprinted from [Khandavalli and Rothstein, 2014] Copyright 2014 The Society of Rheology); and (d) The steady extensional viscosity of a concentrated polystyrene solution (6.0 wt.%, $M_w = 10.2 \times 10^6$ g/mol) with $Z \sim 26$ entanglements per molecule and the associated prediction of the Doi-Edwards-Marrucci-Grizutti (DEMG) model and the Mead-Larson-Doi (MLD) model without contour length fluctuations relaxation mechanisms. In order to calculate Z, the values of M_w and M_e can be obtained using gel-permeation chromatography and linear rheology, respectively (image reprinted from [McKinley and Sridhar, 2002] with permission from Annual Reviews). 90

3.8 Overall depiction of the interfacial polymer diffusion that takes place post-deposition on a print bed during MatEx. (a-c) illustrates the reptation mechanism for molecular diffusion and randomization behavior across the interface during healing for a single polymer chain (χ is the average distance of the segments from the interface between the two adjacent chains) (image reprinted with permission from [Bousmina et al., 1998] Copyright 1998 American Chemical Society); and (d) highlights the details of entire polymer chain networks across the interface during healing (image reprinted with permission from [Grewell and Benatar, 2007] Copyright 2007, Carl Hanser Verlag, Munich) . 94

3.9 (a) Effect of temperature on the number averaged relaxation timescales of three different polymer filaments (image reprinted from [Coogan and Kazmer, 2020] with permission from Elsevier); (b) steady shear rate sweeps performed using a rotational rheometer on the three materials at 190°C (image reprinted from [Coogan and Kazmer, 2020] with permission from Elsevier); (c) The polymer interdiffusion distance (χ) normalized to the radius of gyration of the polymer size, as a function of time. The X-axis is scaled by the time taken to reach T_g such that at $t/t_g = 1, T = T_g$. Details of the model can be found in [McIlroy and Olmsted, 2017b] (image reprinted from [Das et al., 2021c] with permission from Springer Nature); and (d) The dependence of complete re-entanglement time of PEI on the temperature of the print, obtained using interrupted shear measurements performed on a cone and plate rheometer (image reprinted from [Gilmer et al., 2019] Copyright 2019 American Chemical Society). 98

3.10 Variation in the complex viscosity of (a) neat, (b) 25 wt% CF reinforced PPSU, and (c) 35 wt% CF reinforced PPSU as a function of angular frequency; variation in the (d) storage and (e) loss modulus for neat and CF reinforced PPSU as a function of angular frequency obtained at three different processing temperatures using a linear viscoelastic strain of 1%; The rheology tests were performed in a 25mm parallel plate fixture with a gap height in the range of 1.5-1.8mm and in nitrogen environment to limit any thermally triggered side reactions and/or degradation of the polymers (all the images are reprinted from [Ajinjeru et al., 2018b] with permission from Elsevier); and (f) a typical SEM image of the interlayer bond obtained during BAAM scale printing of 20 wt% glass fiber reinforced ABS using a Cincinnati BAAM-100 system (image reprinted from [Schnittker et al., 2019] with permission from Elsevier). . . . 107

3.11 (a) Effect of print temperature (200, 250, and 300°C) and entanglement number on the interfacial weld strength of a polycarbonate part printed at constant speed (10 mm s^{-1}). The solid lines represent Equation 3.26 (image reprinted from [McIlroy and Graham, 2018] with permission from Elsevier); (b) Time required to achieve 10% of the maximum crystallinity in PCL printed parts as a function of the corrected nozzle wall shear rates under varying print temperatures (90, 110, and 140°C) (image reprinted from [Northcutt et al., 2018] with permission from Elsevier); (c) The van Gurp-Palmen plots illustrating the variation of phase angle with complex modulus of neat PPS. The data presented in the figure were obtained by performing isothermal frequency sweeps at different temperatures (image reprinted from [Liu et al., 2018b] with permission from Elsevier); and (d) Variation in viscosity (η) and elastic modulus (G') of PP/CNF composites as a function of shear rate and frequency, respectively, obtained from steady shear flow and SAOS tests. The sample nomenclature in the figure represents PP (main component)-X% (weight percent of CNFs in the blends)-MA (maleic anhydride modified PP) (image reprinted from [Wang et al., 2018a] with permission from John Wiley & Sons). 113

4.1 Schematic of the MatEx based 3D printing process. The solid polymer filament is fed into the heated section (at a temperature of T_N) at a constant rate (U_0) using the pinch roller mechanism. The polymer melt is deposited on the build plate (print bed) at a constant extrusion speed (U_N) which is usually kept equal to the print bed speed (U_L). The flow profile inside the nozzle is highlighted by the dotted lines. Region 1 highlights the melt flow region in the nozzle and subsequent deposition on the print bed while Region II represents the rapid cooling of the polymer extrudate and relaxation of the polymer chains. For a crystalline material, the crystallization process is initiated in Region II (image reprinted from [McIlroy and Graham, 2018] with permission from Elsevier). 119

4.2 Overview of the process-structure-property relationships in material extrusion (MatEx) based additive manufacturing (AM). Green boxes indicate the critical physical phenomena associated with the process and the modeling approaches toward these phenomena are reviewed in this paper. 121

4.3 (a) Phase map of the pressure across the printer nozzle as a function of print velocity showing the risks associated that can lead to print failure (image reprinted from [Agassant et al., 2019] with permission from Elsevier); (b) Cross-sectional shapes of the extruded filaments from CFD simulations and as observed experimentally using optical microscopy using PLA (image reprinted from [Serdeczny et al., 2018a] with permission from Elsevier); (c) SEM image of a cross-section of a single layer of print using polyether imide (PEI) (image reprinted with permission from [Gilmer et al., 2019] Copyright 2019 American Chemical Society); (d) Experimental 3D printed lattices and simulations of the lattice models as generated by the VOLCO model as a function of layer thickness. The filament spreading as a function of layer thickness was accurately captured by the VOLCO model (image reprinted from [Gleadall et al., 2018] under the terms of the Creative Commons CC-BY license). 127

4.4 (a) Infrared thermographs obtained at three different times for rastering of a single road of print where the nozzle moves from left to right (image reprinted from [Ravoori et al., 2019a] with permission from Elsevier); (b) FE simulations of the thermal profile inside a typical MatEx nozzle (image reprinted from [Wang et al., 2019b] with permission from Elsevier); (c) the thermal profile at a cross-section of the filament (image reprinted from [Gilmer et al., 2019] Copyright 2019 American Chemical Society); (d) simulated thermal profile of an entire printed part (image reprinted from [[Brenken et al., 2019] with permission from Elsevier). 130

4.5 (a) Residual alignment in a single deposited road of PLA printed at 120 mm/s and 190°C, as predicted by the numerical model described in [McIlroy and Olmsted, 2017b]; (b) Prediction of the thermal profiles of the deposited layers using FE simulations; the different layers spend varying time periods above T_g which determines the extent of their mobility (image reprinted from [D'Amico and Peterson, 2018] with permission from Elsevier); (c) The polymer diffusion distance, χ, scaled by the polymer size, R_g (radius of gyration), as a function of time. Time scaled by the time taken to reach the glass transition temperature, so that at $t/t_g = 1, T = T_g$. The effects of polymer alignment in the flow give rise to anisotropic diffusion, which hinders diffusion between filaments, i.e., in the transverse z-direction. See [McIlroy and Olmsted, 2017b] for details of the model; (d) Reduction in tensile properties of printed ABS and polyether-ether-ketone (PEEK) samples compared to injection molded parts (image reprinted from [Wu et al., 2015] under the Creative Commons Attribution License). 132

4.6 (a) Effect of changes in percent crystallinity of printed part on the tensile strength of polyphenylene sulfide (data adapted from [Fitzharris et al., 2018] with permission from Elsevier); (b) Flow-induced crystallization plot (image reprinted from [McIlroy and Graham, 2018] with permission from Elsevier); (c) Optical microscopy of annealed PLA printed cross-sections. Darker regions in the weld correspond to smaller sized spherulites due to flow-enhanced crystallization. The scale bar is 200 μm. (image reprinted with permission from [McIlroy et al., 2019] Copyright 2019 American Chemical Society); (d) Improvement in tensile and flexural properties post-annealing for 3D printed PLA and PLA/cellulose nanofiber (CNF) composites (data adapted from [Dong et al., 2019a] with permission from Elsevier). 135

5.1 TGA profiles for the as received PA6 and CF-PA6 filaments as well as CF-PA6 print performed under nitrogen atmosphere with a heating rate of 10°C min^{-1}. 148

5.2 (a) DSC melting endotherms from the second heat of the nonisothermal experiments for PA6 and CF-PA6 (Onyx); (b) DSC cooling exotherms from the nonisothermal experiments for PA6 and CF-PA6 (Onyx); (c) Degree of crystallinity as measured using Equation 1 for PA6 and CF-PA6 (Onyx filament and print). The enthalpy of melting was calculated from the second heat of the nonisothermal experiments. 150

5.3 Complex viscosity as a function of angular frequency as obtained using SAOS rheometry at different temperatures for (a) PA6 and (b) CF-PA6. The solid lines indicate the data fits to the Carreau model (Equation 5.2). 153

5.4 Overlay of the steady torsional shear (filled symbols) and small amplitude oscillatory shear (open symbols) rheometry of PA6 and CF-PA6 at the respective printing temperatures of 275°C and 280°C. 154

5.5 Mechanical spectra for storage modulus (closed symbols) and loss modulus (open symbols) as a function of angular frequency for (a) PA6 and (b) CF-PA6 samples at different temperatures. 156

5.6 Representative stress-strain plots of the different CF-PA6 printed parts used in this study. The numbers in the inset of the figure refers to the sample numbers as listed in Table 5.2 with different layer thickness, raster angle, and infill pattern. The printing temperature, printing speed, and infill density was kept constant at 280°C, 40 mm s−1, and 37% respectively 158

5.7 Signal to noise ratios for (a) maximum tensile strength, (b) elongation at break, and (c) tensile modulus of printed parts of CF-PA6 as a function of layer thickness, raster angle, and infill pattern. 162

5.8 Scanning electron micrographs of the fracture surface of CF-PA6 prints after tensile testing (a) fiber pullout from the polymer matrix but no evidence of matrix cracking of layer delamination; (b) clean surface of the carbon fibers suggesting poor interfacial adhesion with the polymer matrix; and (c) dark patches in the polymer matrix due to localized deformations near the fibers. 165

6.1 (a) DSC melting endotherms from the second heat of non-isothermal experiments for the different compositions of PP/PH blends (b) DSC cooling exotherms from the non-isothermal experiments for the different compositions of PP/PH blends. Data for PP/FH blends are provided in Figure C.3 176

6.2 Hot stage polarized optical micrographs taken at comparable times for (a) pure PP, (b) 80/20 blends of PP/PH, and (c) 80/20 blends of PP/FH resins obtained after cooling from the melt and held isothermal at 120°C 178

6.3 Shear thinning behavior of PP and 80/20 blends with FH and PH resins at 180°C performed under steady shear in a TA ARG2 rheometer. The vertical line indicates the onset of shearing thinning behavior, which is observed at a shear rate of $0.7s^{-1}$ for all the systems. 179

6.4 Printed parts of pure PP, 90/10 PP/PH, and 80/20 PP/PH blends. The pure PP parts shows significant warpage which reduces progressively as resin content is increased in the blends. 180

6.5 Warpage in printed parts of PP/FH and PP/PH blends as a function of increasing resin concentration. 181

6.6 (a) Stress-strain curves for the PP/PH printed parts (45° raster angle) in compositional ratios up to 20 wt% resin; (b) effect of increasing PH resin content on the maximum tensile stress; (c) effect of increasing PH resin content on the elongation at break; and (d) effect of increasing PH resin content on the Young's modulus of the printed parts of PP/PH blends. 182

6.7 Comparison of the (a) maximum tensile stress; (b) elongation at break; and (c) Young's modulus of the as printed and annealed PP/PH parts (45° raster angle) with respect to inection molded PP. 184

6.8 (a) ±45° and 0° raster angle print orientation used for printing dogbones in this study; (b) effect of print orientation on the tensile modulus of PP/FH blends; and (c) effect of print orientation on the tensile modulus of PP/PH blends. 188

6.9 SEM micrographs of the cross-section after cryo-fracturing of (a) pure PP, (b) 80/20 blend of PP/FH, and (c) 80/20 blend of PP/PH. 189

7.1 DSC melting and crystallization profiles of PP blends with different MFRs . 198

7.2 Variation in the melting and crystallization temperatures of the blends as a function of blend composition 198

7.3 Overlay of steady shear (η) and complex (η^*) viscosities normalized by a factor (A) for the PP/hydrocarbon resin blends. 200

7.4 Representative plot of the shear stress profile obtained during interrupted shear rheology and effect of blend composition on the degree of recovery. . . 201

7.5 Warpage in the printed parts of PP/hydrocarbon resin blends as a function of the blend composition and grade of PP used. 202

7.6 (a) Maximum tensile stress and (b) Young's modulus of PP/hydrocarbon resin blends as a function of the blend composition and grade of PP used . . 203

7.7 Correlating the degree of recovery measured using interrupted shear rheology to the maximum tensile strength of the printed parts 204

7.8 Effect of thermal annealing on the tensile properties of PP/hydrocarbon resin blends 205

8.1 (a) Melting endotherms from the second heating cycle of the heat-cool-heat DSC tests for the different blends of PP and LCPP; and (b) crystallization exotherms from the cooling cycle of the heat-cool-heat DSC tests for the different blends of PP and LCPP. 213

8.2 (a) Complex viscosity of the different PP/LCPP blends as a function of angular frequency; the solid lines are representative of the non-linear curve fits to the Carreau Yasuda model; (b) storage modulus (G'); (c) loss modulus (G"); (d) tan δ associated with the different blends of PP and LCPP as a function of angular frequency; (e) Cole-Cole plot highlighting the variation of η" vs. η'; and (f) Han plot describing the variation of storage modulus vs. loss modulus. All the experiments were performed at 200°C with a linear viscoelastic strain of 1% using a 25mm parallel plate geometry. 219

8.3 (a) Representative stress-strain plots obtained from tensile testing of the printed PP/LCPP (0° raster angle) as a function of blend composition; (b) effect of blend composition on the maximum tensile stress of the printed parts; (c) effect of blend composition on the maximum tensile stress of the printed parts; (d) effect of blend composition on the maximum tensile stress of the printed parts; and (e) variation in the degree of anisotropy, as defined in Equation 8.7, in the printed parts as a function of blend composition. 222

8.4 (a) Representative plot of storage and loss modulus as a function of frequency performed at 25°C and 120°C for the 5wt% PP/LCPP blend; and (b) variation in storage modulus corresponding to a frequency of 1Hz as a function of LCPP content in the blends at 25°C and 120°C. All the measurements were performed under a linear viscoelastic strain of 0.1%. 224

10.1 Schematic of the (a) parallel and (b) perpendicular printed DMA bars having a length L, width w, and thickness T. The height of each road is given by z and the bars have a total of n_x and n_y roads in the parallel and perpendicular directions, respectively. The red regions indicate the weld between the roads (pure nylon) while the blue regions indicate the CF/nylon roads (image reprinted from Pu et al. [Pu et al., 2021] with permission from Elsevier. . . . 230

10.2 Comparison of the degree of crystallinity, as measured by DSC, of the single road width wall PP printed at different print temperatures (180°C, 200°C, and 220°C) and a constant print speed of 10 mm/s with the values predicted from a conventional quiescent and flow induced crystallization model. 232

10.3 Effect of print temperature and print speed on the storage modulii (E') of the SRWW PP prints. The image on the left represents the E' values corresponding to the parallel testing configuration while the image on the right highlights the values for the perpendicular testing configuration. 233

10.4 Representative hot-stage polarized optical micrographs of isotactic polypropylene during cooling from the melt. Three different isothermal crystallization temperatures (130°C, 135°C, and 140°C) were studied and micrographs were captured at regular time intervals. 235

A.1 Cross-polarized optical microscopy of cross sections of printed parts after annealing at 140°C for 1 hour (Scale bar 200 μm). The size of the semicrystalline domains increases after the annealing process. The temperatures on the left indicate the print temperature. (image reprinted with permission from [McIlroy et al., 2019] Copyright 2019 American Chemical Society) 308

A.2 Effect of post-printing annealing on the (a) maximum tensile stress, (b) elongation at break, and (c) Young's modulus of printed blends of polypropylene/partially hydrogenated resin (PP/PH). The numbers in the X-axis of the plots indicate the composition of PP and PH. (image reprinted with permission from [Das et al., 2020b] Copyright 2020 American Chemical Society) 310

A.3 Complex thermal history during MatEx printing of polycarbonate filaments at 325°C as a function of different print speeds. The timescales highlighted are the times the extruded filament stays above the glass transition temperature. (image reprinted from [Peng et al., 2018] with permission from Elsevier) . . . 312

A.4 (a) Illustration of the cure-through correction algorithm implemented by changing the slicing procedure; (b) 3DBenchy and (c) hollow egg printed using the corrected and uncorrected slicing procedure (scale bar 5mm); (d) schematic of the printer apparatus with the important non-dimensionalized parameters, such as, z-position (ζ), dosage (Ω_n), and light intensity (Φ_n) (image reprinted from [Pritchard et al., 2019] with permission from John Wiley and Sons) . . 313

B.1 Frequency dependence of storage modulus of (a) PA6 and (b) CF-PA6 at different temperatures. The dashed lines represent the fits to the power law equation $G' = a_1\omega^{a_2}$ 317

C.1 TGA profiles for the fully hydrogenated (FH) and partially hydrogenated (PH) resins used in this study for blend preparation. 320

C.2 TGA profiles for the prepared blends of (a) PP/FH and (b) PP/PH. 321

C.3 (a) DSC melting endotherms from the second heat of non-isothermal experiments for the different compositions of PP/FH blends (b) DSC cooling exotherms from the non-isothermal experiments for the different compositions of PP/FH blends. 322

C.4 Cooling scan from the non-isothermal DSC experiments for the pure FH and PH resins. 323

C.5 DSC melting endotherm of pure PP, 80/20 blends of PP/FH and PP/PH zoomed in the region of 160°C-180°C. 324

C.6 Variation in percent crystallinity of the PP/FH and PP/PH blends as a function of the content of hydrocarbon resin present in the blends. 326

C.7 Isothermal crystallization profiles for (a) PP; (b) PP/FH; and (c) PP/PH blends carried out at different crystallization temperature in the range of 120°C to 130°C. 327

C.8 Crystallization profiles during cooling from the melt for (a) PP/FH blend cooled at 10°C/min; (b) PP/PH blend cooled at 10°C/min; (c) PP/FH blend cooled at 50°C/min and (d) PP/PH blend cooled at 50°C/min. 329

C.9 Effect of crystallization temperature and resin type on the size of the spherulites formed during cooling from the melt and held isothermal at different crystallization temperatures (120° C and 130° C) for pure PP and its blends with hydrocarbon resins. 330

C.10 (a) Stress-strain curves for the PP/FH printed parts (±45° raster angle) in compositional ratios up to 20 wt% resin; (b) effect of increasing FH resin content on the maximum tensile stress; (c) effect of increasing FH resin content on the elongation at break; and (d) effect of increasing FH resin content on the Young's modulus of the printed parts of PP/FH blends. 331

C.11 Comparison of the (a) maximum tensile stress; (b) elongation at break; and (c) Young's modulus of the as printed and annealed PP/FH parts (±45° raster angle) with respect to injection molded PP. 332

C.12 Tensile strength and tensile modulus of pure PP and 80/20 blends of PP/FH and PP/PH printed under the same conditions as used in this study at 90° raster pattern. This raster pattern allows to directly measure the strength of interlayer bonding by testing the printed layer adhesion. 333

List of Tables

2.1 Common physical properties of polyethylene and polypropylene 10

2.2 Mechanical properties of pure polyolefins and their composites along with the relevant print conditions when printed using MatEx. 15

3.1 Correlating processing parameters in MatEx with the impact they have on printed part properties along with the necessary rheological characterizations needed to understand the effect of material and processing conditions on final part properties. 58

3.2 Brief summary of the recent research on the fluid flow analysis inside the heated nozzle of a typical desktop MatEx 3D printer. The polymer material experimentally studied to verify model predictions, the dimensionality of the model, the software employed, and the key findings from each study is highlighted 70

4.1 Summary of the modeling approaches in material extrusion based additive manufacturing along with the polymer materials that were used to validate the models. The checkmarks indicate the fundamental models that were analyzed in the corresponding studies. The terms within parenthesis in the Material column indicate the scale (road/part) of the simulation performed. It is worth mentioning that the term "road" has been used to denote both the extrudate exiting the nozzle and the material that is deposited on the printer bed. . . . 122

5.1 Printing parameters employed in this study and their levels 144

5.2 Printing conditions employed for printing the carbon-fiber reinforced polyamide 6 (CF-PA6) filament 144

5.3 Tensile properties of printed specimens of the CF-PA6 material as a function of the processing parameters employed in this study. 159

5.4 Comparison of mechanical properties available in the literature for carbon fiber reinforced nylon composite (Onyx) with other filler reinforced polymer composites manufactured using FFF. 160

5.5 Optimum factor levels for maximum tensile strength, elongation at break, and tensile modulus of the CF-PA6 printed parts 161

6.1 Tensile properties of printed parts (±45° raster angle) of pure PP and blends with hydrocarbon resins. 183

6.2 Comparison of mechanical properties of PP/hydrocarbon resin blends obtained in this study with values reported in literature for PP based composites processed using MEAM. 186

8.1 Peak melting temperature, enthalpy of melting from the second heating cycle as well as the peak crystallization temperature and enthalpy of crystallization from the cooling cycle of the heat-cool-heat DSC tests for the different blends of PP and LCPP. The degree of crystallinity was calculated based on the enthalpy of melting from the second heating cycle as highlighted in Equation 8.1 214

8.2 The parameters of the Carreau-Yasuda model obtained by fitting the complex viscosity versus angular frequency data from the small amplitude oscillatory shear rheology experiments along with the corresponding coefficient of determination (R^2) values. The values of the critical shear stress (τ^*) was calculated using Equation 8.3 217

8.3 Tensile properties of the PP/LCPP blends parts printed at 0° and 90° raster angle. All the parts were printed with a nozzle temperature of 200°C, bed temperature of 100°C, infill of 75%, layer thickness of 0.1mm, and print speed of 20mm/s. 221

8.4 Tensile properties of the printed specimens of PP/LCPP blends in comparison to those reported in literature for 3D printed polypropylene based blends and composites. 223

B.1 Degradation temperatures for PA6 filament, CF-PA6 filament, and CF-PA6 print along with the residue left after the samples have been heated to 600°C under nitrogen environment (reported values are an average of three runs) . 315

B.2 Peak melting temperatures (from the second heating scan) and peak crystallization temperatures (from the cooling scan) as well as enthalpy of melting (from the second heating scan) and crystallization (from the cooling scan) of PA6 and CF-PA6 samples obtained using the nonisothermal DSC experiments. 316

B.3 Parameters for the Carreau model fitted to the complex viscosity vs. angular frequency data obtained at different temperatures for PA6 and CF-PA6 . . . 316

B.4 Power law parameters fitted to the storage modulus vs. angular frequency data obtained at different temperatures for PA6 and CF-PA6 317

B.5 Analysis of Variance for maximum tensile strength of printed CF-PA6 parts 318

B.6 Analysis of Variance for elongation at break of printed CF-PA6 parts 318

B.7 Analysis of Variance for tensile modulus of printed CF-PA6 parts 318

C.1 Different blend compositions of PP and resins along with the mixing temperature used in this study. 319

C.2 Degradation temperature for pure PP and its blends with the FH and PH resins. 321

C.3 Peak melting temperatures (from the 2^{nd} heating scan) and peak crystallization temperatures (from the cooling scan) as well as enthalpy of melting (from the 2^{nd} heating scan) and crystallization (from the cooling scan) of the prepared PP/FH and PP/PH blends obtained using the non-isothermal DSC experiments. 325

C.4 Effect of cooling rate on the time required to reach the crystallization peak for PP, PP/PH, and PP/FH blends while maintaining isothermal crystallization conditions. 328

List of Abbreviations

ΔH_c	Enthalpy of crystallization
ΔH_m	Enthalpy of melting
$\dot{\gamma}$	Shear rate
$\dot{\gamma}_{app}$	Apparent shear rate
η	Shear viscosity
η^*	Complex viscosity
λ	Characteristic relaxation time
ω	Angular frequency
τ_R	Rouse time
$\tau_m(\dot{\gamma}, \infty)$	Stress overshoot after infinite relaxation time
$\tau_m(\dot{\gamma}, t_r)$	Stress overshoot after relaxation time t_r
τ_{rep}	Reptation time
τ_{ss}	Steady state shear stress
G"	Loss modulus
G'	Storage modulus
T_c	Peak crystallization temperature
T_m	Peak melting temperature
$tan\delta$	Loss tangent
ABS	Acrylonitrile butadiene styrene
AM	Additive manufacturing

CAM Computer aided manufacturing

CF Carbon fiber

CNC Cellulose nanocrystal

CNF Cellulose nanofibril

CNT Carbon nanotube

CNT Computer aided design

De Deborah number

DIW Direct ink writing

DOE Design of experiments

FFF Fused filament fabrication

HDPE High density polyethylene

LDPE Low density polyethylene

LLDPE Linear low-density polyethylene

MatEx Material extrusion

PBF Powder bed fusion

PE Polyethylene

PLA Polylactic acid

PP Polypropylene

SL Stereolithography

Tr Trouton ratio

UHMWPE Ultra high molecular weight polyethylene

Attribution & Dissertation Format

The chapters contained in this dissertation are published manuscripts (Chapters 3, 4, 5, 6, and Appendix A) and manuscripts currently under review (Chapters 2 and 8). Research presented in Chapter 7 includes work that is under preparation for a journal submission. Each chapter contains separate sections dedicated to background, experimental methods, relevant discussions, and conclusions. The chapters are presented in their manuscript format with permission from the respective journals (wherever applicable).

The research presented in this dissertation has been performed with the help of multiple colleagues across different laboratories at Virginia Tech and University of Lincoln, UK; a true testament to the interdisciplinary nature of the investigation. The respective contributions from different colleagues have been briefly described in this section.

Chapter 2 is a portion of a manuscript currently under review for publication in the **Polymer Reviews** journal. The sections presented in this dissertation are the ones where A. Das was the sole contributor. The sections not included in the dissertation describe additive manufacturing of polyolefins through the powder bed fusion modality and were written by J.S. Bryant, a Ph.D candidate in the Macromolecular Science and Engineering program.

Chapter 3 has been published as an *invited review article* in the **ACS Applied Polymer Materials** journal. E.L. Gilmer and S. Biria were a Ph.D candidate and a postdoctoral researcher, respectively, in the Department of Chemical Engineering. Specifically, E.L Gilmer wrote the subsections 3.5.2 and 3.5.3 while S. Biria was responsible for the subsections 3.6.4, 3.6.5, and 3.6.6. Additionally, E.L. Gilmer and A. Das shared the responsibilities for the subsections 3.5.1, 3.5.4, 3.7.2, and 3.7.5. S. Biria and A. Das co-wrote the section 3.2 and subsections 3.6.1 and 3.6.2. A. Das was the sole contributor for the other sections of the paper including assembling all the figures and tables.

Chapter 4 has been published in the **Progress in Additive Manufacturing** journal. A. Das and C. McIlroy are co-first authors and contributed equally to the publication. The introduction section (4.1) was written by both the authors. Specifically, C. McIlroy was the lead contributor for Sections 4.4 and 4.6 while A. Das had the leading role in writing Sections 4.2, 4.3, and 4.5. All the sections were reviewed, refined, and edited by both A. Das and C.

McIlroy.

Chapter 5 has been published in the *Additive Manufacturing of Polymer Composites* special issue of the **Polymer Composites** journal. M. Etemadi contributed to the publication by performing the printing and associated design of experiments analysis (subsection 5.2.2). M. Etemadi and A. Das co-wrote Section 5.1 and subsection 5.3.4.

Chapter 6 has been published in the **ACS Applied Polymer Materials** journal. A.E.C. Marnot was an undergraduate researcher in the Department of Chemical Engineering and contributed to the publication by preparing the blends and performing the preliminary differential scanning calorimetry characterizations.

Chapter 7 is currently under preparation for submission to a journal for publication. E.M. Dartevelle was an undergraduate researcher in the Department of Chemical Engineering and was responsible for blend preparation, crystallization experiments, and printing the blends.

Chapter 8 is a manuscript currently under review for publication in *The Role of Additives in Rheology and Processing* special issue of the **Journal of Vinyl & Additive Technology**. N. Shanmugham was an undergraduate researcher in the Department of Chemical Engineering and contributed to the manuscript by assisting in filament preparation and performing the initial printing experiments.

Chapter 1

Introduction

Additive manufacturing (AM) is a technique of fabricating three-dimensional parts from a variety of materials including metals, polymers, and composites using computer aided design (CAD) files. The advantages of AM over traditional processing techniques include high design fidelity, rapid prototyping, and low production costs, as highlighted in Appendix A. Depending on the feedstock and machinery employed, AM can be classified into different categories [Gao et al., 2015]; out of which polymer-based material extrusion (MatEx) has emerged to be one of the most commonly employed technique due to its operational flexibility and low energy demands. In a typical MatEx process, the polymer feedstock (in the form of filaments or pellets) is extruded through a heated nozzle and subsequently deposited on a printer bed (generally, heated) [Turner et al., 2014]. Next, the nozzle and/or the printer bed moves according to the design file and the process is repeated to build the entire part in a layer-by-layer manner.

Semicrystalline thermoplastics are the material of choice for a variety of consumer and commodity applications. Traditionally processed using melt forming techniques such as injection molding, the AM of such polymers is usually carried out through melt-based MatEx [Das et al., 2020a]. Thermoplastic parts processed using MatEx have been deployed for a multifunctional applications including medical implants, robotics, and environmental remediation [Choi et al., 2015, Gao et al., 2016, Compton and Lewis, 2014, Kennedy et al., 2022, McQueen et al., 2022]. Although, MatEx is adept at creating such complex parts its the industrial implementation is somewhat restricted due to the moderate accuracy and relatively long build times. Moreover, concerns regarding the consistency and repeatability in the part properties manufactured by MatEx since the evolution of properties during processing is yet to be completely understood [Forster, 2015].

The MatEx-based AM paradigm is poised to be of great benefit to the current production market subject to widespread adoption. Reduction in production costs, reduced lead times, and ease of processing are a few areas where MatEx can improve the traditional manufactur-

ing technologies. However, to realize this potential the challenges and limitations associated with the process must be addressed.

1.1 Motivation

Filament-based MatEx is currently limited by the production of parts with inconsistent qualities with respect to mechanical properties, dimensional stability, and surface finish. Although there is a substantial amount of current literature that investigates the effect of process variables on the print part properties through various experimental measurements [Lubombo and Huneault, 2018, Mahmood et al., 2017, García Plaza et al., 2019, Young et al., 2019, Tsouknidas et al., 2016, Zandi et al., 2020] such approaches typically focus on empirical data fits rather than a fundamental understanding and model analysis of the key process physics. Therefore, empirical validation is most commonly used to identify the important printing parameters [de Ciurana et al., 2013, Anitha et al., 2001, Tymrak et al., 2014]. In recent years, improving and expanding the material selection library for AM has garnered significant interest. MatEx was originally developed as a prototyping tool and is now progressively challenged each day to produce end use parts for a wide variety of applications [Huang et al., 2015, Compton and Lewis, 2014]. Semicrystalline polymers exhibit improved thermal stability, toughness, and deformability compared to their amorphous counterparts [Rubenstein and Colby, 2003]; and hence, are an attractive class of materials for MatEx.

In MatEx based AM, intra-/inter-layer self-adhesion is one of the primary limitations that hinders the widespread application of AM because of poor mechanical properties of the manufactured parts. The interface between two deposited layers is a source of mechanical defect in a printed part. This problem exists primarily in the z-axis, or the direction perpendicular to the build plate, as parts tested in the direction parallel to the printing direction have much higher strength and modulus than those tested in the direction perpendicular to the printing direction [Górski et al., 2015]. Therefore, the application of AM is still restricted to the development and testing of prototypes rather than widespread use in real-world applications [Kruth et al., 1998]. The goal of the AM work is to enable production of thermoplastics without compromising mechanical robustness and dimensional stability, with a focus on the competing effects of crystallization (in semicrystalline polymers), polymer inter-diffusion, and stress buildup. However, processing semicrystalline polymers in MatEx is challenging

due to crystallization and thermal expansion induced shrinkage and part warpage [Carneiro et al., 2015, Knoop et al., 2015, Watanabe et al., 2016].

1.2 Research Hypotheses

The primary goal of the current work is to establish the intricate interplay among the processing parameters, polymer material properties, and fundamental process physics to enable MatEx of semicrystalline thermoplastics (filled systems and blends). The following hypotheses inspire the current research:

- Fiber reinforced polymers can aid in printing parts with reduced warpage by providing load bearing pathways but hinder polymer chain diffusion across the layers due to their stiffness and therefore are associated with high levels of mechanical anisotropy.
- The addition of low molecular weight amorphous hydrocarbon resins to semicrystalline polymers will retard the crystallization process and broaden the time window for residual stress relaxation, resulting in printed parts with greater geometric accuracy and dimensional stability.
- The molecular weight, molecular weight distribution, and related molecular architecture of semicrystalline polymer blends can have a significant effect on the printing performance by altering the extent of interlayer chain diffusion which in turn dictates the mechanical properties of the parts.

1.3 Research Objectives

The focus of this dissertation is to develop a fundamental understanding of MatEx based processing of semicrystalline polymers through a detailed study of the underlying process physics and associated material properties that is critical to guide feedstock modifications. It is expected that the current research will enhance the capabilities of the MatEx process through physics-guided process parameter optimization, machining modifications, and generation of feedstocks with tailored molecular architecture; thereby broadening the catalog of compatible materials with MatEx.

The specific research objectives are listed below:

- Highlight the importance of MatEx process parameter selection on the printed part properties of commercially available semicrystalline polymer feedstocks and elucidate the existing limitations. The purpose of this study is to explore the process-structure-property relationships through detailed crystallization and rheological characterizations.
- Investigate and develop an approach for MatEx based AM of semicrystalline thermoplastic polymer blends with minimum warpage while retaining close-to injection molding grade properties. This will include studying the complex interplay between the thermal and crystallization behavior of the polymer system as well as characterizing the mechanical properties of the printed parts.
- Analyze the effect of molecular weights and molecular weight distributions on polymer chain diffusion, crystallization profiles, and corresponding printed part properties resulting from the repeated non-uniform thermal history in filament based MatEx of polyolefin blends. The outcome of this objective is to identify the optimal processing conditions to maximize material specific printed part performance as well as highlight the limitations in processing conditions and indicate necessary modifications to enable MatEx of next generation materials and parts.

These three objectives will contribute to the knowledge base by providing a generalized framework for printing semicrystalline thermoplastics using MatEx. Current research on AM of semicrystalline thermoplastics generally focusses on "trial and error" approaches (depending on the polymer in question) to predict behavior and identify optimal printing conditions. Therefore, new techniques are required that can be applied to successfully print parts irrespective of the variations in material properties. The research will elucidate the complexities between processing variables and part performance, as well as be of industrial relevance as it can potentially save significant time and money and reduce waste in the polymer manufacturing and processing sectors.

Chapter 2

Material extrusion-based additive manufacturing of polyolefins

Arit Das[1,2], Jackson S. Bryant[1,2,3], Christopher B. Williams[2,3], and Michael J. Bortner[1,2]

[1]Department of Chemical Engineering, Virginia Polytechnic and State University, Blacksburg, VA 24061, USA

[2]Macromolecules Innovation Institute, Virginia Polytechnic and State University, Blacksburg, VA, 24061, USA

[3]Department of Mechanical Engineering, Virginia Tech, Virginia Polytechnic and State University, VA 24061, USA

This chapter is currently under review for publication as a portion of a broader manuscript in the **Polymer Reviews** journal.

Abstract

Polyolefin-based thermoplastics such as polyethylene (PE) and polypropylene (PP) constitute a major fraction of the polymers employed in commodity applications due to their ease of processability, recyclability, durability, and economic viability. Additive manufacturing (AM) of polyolefins offers both a viable path towards functional prototyping of design concepts and direct manufacturing of end-use parts. However, melt-based AM of semicrystalline polymers including polyolefins has been severely limited due to the problems associated with shrinkage, warpage, void formation, and interlayer adhesion. The focus of this review article is to evaluate the latest state of the art for processing polyolefin thermoplastics by powder bed fusion (PBF) and material extrusion (MatEx) AM modalities. Recent progress in processing neat, filled, and blends of polyolefins using PBF and MatEx are discussed to highlight the importance of the rheological and morphological characteristics of the polymer melt on the performance of the printed parts. The authors emphasize the known challenges to

AM of polyolefins and recommend strategies to address the limitations through a better understanding of the associated process-structure-property relationships. A holistic approach spanning synthetic modifications for feedstock development, improved AM system design, and physics guided process parameter selection is required to broadly adopt melt-based AM of polyolefins.

Keywords: additive manufacturing; polyolefins; interlayer bonding; crystallization; warpage

2.1 Introduction

Additive manufacturing (AM), also referred to as 3D printing, is a processing technique in which complex 3D part geometries are fabricated in a layerwise fashion [Gao et al., 2015]. AM has proven to be a valuable tool for prototyping design concepts and a viable path for end use product manufacturing due to its lack of need for additional tooling. Although there are different embodiments to AM based on the associated process physics and material requirements, the digitally controlled layer-by-layer assembly to fabricate part is identical across the modalities [Gebhardt, 2011]. AM offers a paradigm of geometric flexibility (thereby allowing parts with complex features) and optimized mechanical properties in a manufactured part compared to existing manufacturing processes such as injection molding. However, the widespread application of AM in the current market is still limited due to inherent challenges associated with it. One of the major problems, recent progress notwithstanding, associated with the extensive realization of AM of polymer feedstocks through melt forming techniques such as PBF and MatEx is the limited material catalogue that is compatible with these processing techniques [Penumakala et al., 2020]. To establish AM as a viable alternative for traditional manufacturing techniques, both commodity and high-performance polymers must be processible.

Polymeric parts manufactured using AM has been a topic of much research in recent years since they have applications in aerospace, automotive, and healthcare industries [Goh et al., 2019, Ngo et al., 2018]. Specifically, semicrystalline thermoplastic polymers have been heavily researched in AM for their consumer and commodity based applications [Das et al., 2020a]. Thermoplastics have been traditionally processed using melt-forming methods and hence similar modes of AM, namely, material extrusion (MatEx) and powder bed fusion (PBF) are employed for printing them. PBF and MatEx have inherent advantages over other polymer-

based AM techniques due to their customizability and economic viability [Chatham et al., 2019a, Ambrosi and Pumera, 2016]. Although, there are evidences of AM of semicrystalline thermoplastics using vat photopolymerization [Deng et al., 2012]; it is associated with the requirement of photocrosslinking molecules that need to be synthesized through complex synthetic routes.

Polyolefins are a class of commodity polymers that are inexpensive, recyclable, and can be easily processed through traditional techniques [Gopanna et al., 2019]. There has been a rapid increase in the application of polyolefin-based components and parts in various industries across the globe. For example, in the automotive industry, parts made of such polymers are not only lightweight, thereby improving fuel efficiency, but also have the added benefits of safety and comfort [Chirayil et al., 2016]. In spite of possessing a variety of attractive properties suited for versatile applications, research on the suitability of polyolefins in melt-based AM is still in its nascent stage. There has been a long-standing industrial interest to process polyolefins such as polyethylene and polypropylene using AM as they are the most used polymers in consumer products. 3D printing of such materials allows manufacturers to functionally evaluate their design before injection molding. Although, printing polyolefins at production scale is also of interest it has been limited by the anomalous behavior of the polymers as compared to 3D printable materials such as polylactic acid (PLA) and acrylonitrile butadiene styrene (ABS). The semicrystalline nature of the polyolefins that induces significant amounts of volumetric shrinkage and residual stress build-up during cooling from the melt makes it extremely challenging to process using MatEx [Spoerk et al., 2020]. The print characteristics associated with the techniques are generally dictated by thermal and rheological behavior of the concerned polymer melts. Understanding the complex interplay among melt-flow behavior, thermal history, crystallization behavior, and viscoelasticity of the polymer is of critical importance in controlling the printability and property evolution in a printed polyolefin part [Das et al., 2021b].

In this paper, we review the major advancements in AM of polyolefins using PBF and MatEx. The specific aim of the work is to summarize the state-of the-art in polyolefin printing by (1) highlighting the current approaches to print these polymers (neat, fiber & filler reinforced, and polymer blends); (2) analysing the influence of PBF and MatEx processing on the part properties; (3) exploring the limitations of the current printing approaches; (4) identifying existing research trends and gaps in the governing process physics for polyolefins; and (5) provide recommendations that can potentially assist in successfully printing dimensionally

accurate parts without compromising their properties. It is expected that an improved interpretation of the multiphysics associated with the relevant processing techniques will aid in successfully printing polyolefin functional parts and assist in realizing the future potential of polyolefin-based feedstocks for application in PBF and MatEx.

2.2 Roadmap

There has been an abundance of published literature over the course of the last decade that address different process and material specific aspects associated with AM; this rapid rise in interest has coincided with the increasing adoption of AM technologies for a plethora of applications. Recent articles have reviewed in detail the development of polymer-based feedstocks to expand the AM material library [Wu et al., 2020a, Tan et al., 2020, Palanikumar et al., 2020, Valino et al., 2019, Parandoush and Lin, 2017]. Comprehensive reviews on all the different AM modalities along with detailed discussions about the material requirements, processing conditions, and subsequent printed part applications, have also been reported [Bourell et al., 2017, Ligon et al., 2017]. A limitation of these extensive review articles is that they neither focus on any particular modality of the AM family nor on a distinct class of materials and hence are rather generalized in terms of their discussion. In contrast, there are also a number of review articles available that limit their discussion to a particular class of polymers processed using specific AM methods [Penumakala et al., 2020, Das et al., 2020a, Chatham et al., 2019a, Ferreira et al., 2019, Sheoran and Kumar, 2020, Chaunier et al., 2018, Mervine et al., 2020, Mohan et al., 2020] or investigate the potential of polymer-based AM for producing parts for a specific applications [Szymczyk-Ziółkowska et al., 2020, Prasad and Smyth, 2016, Klippstein et al., 2018, Zhakeyev et al., 2019, González-Henríquez et al., 2019, Camposeo et al., 2019].

Figure 2.1 highlights the current and projected revenues from the different AM techniques, and it is evident from the data that the MatEx has one of the largest market share. Therefore, in the current scope of the manuscript we have limited our discussion to the approaches and challenges with processing of semicrystalline polyolefins, such as polyethylene (PE) and polypropylene (PP), through MatEx, while elucidating the associated structure-process-property relationships. There are a few material specific reviews in MatEx for example, with acrylonitrile butadiene styrene (ABS) [Peterson, 2019], polypropylene [Spoerk et al., 2020], reinforced polymer composites [Fallon et al., 2019] being the chief focus. A recent review ar-

ticle has investigated the process-structure-property relations in a wide range of polymers for MatEx [Goh et al., 2019]; but to the best of our knowledge there is no work in current literature that focuses on PBF and MatEx based processing of polyolefins. Further substantiating the need for a review focused on polyolefins is the fact that recent articles provide limited information about the multiphysics associated with polyolefin processing using MatEx.

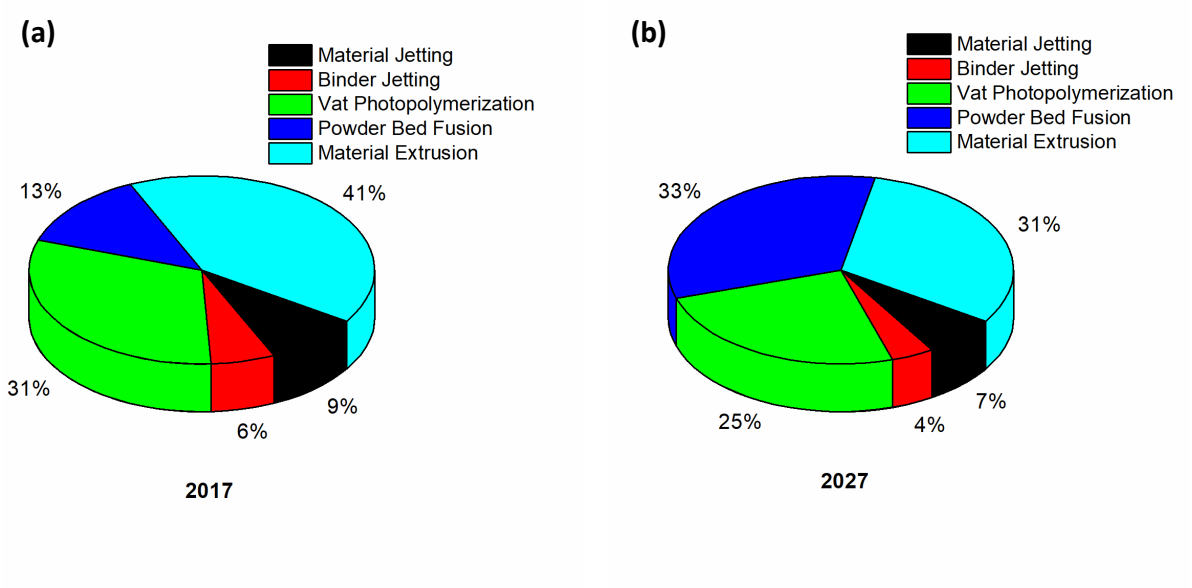


Figure 2.1: Current (2017) and projected (2027) evolution of revenues from different polymer-based AM processing techniques from use in professional environments (data adapted from [Publishing, 2018]

The discussion presented in this paper has been divided to a three major sections, beginning with an overview of polyolefins in AM and a brief summary of the MatEx process. This is followed by a detailed synthesis of research regarding the printing of such materials through the aforementioned technique. The main emphasis is in capturing the recent findings related to successful printing of each polymer and how altering the processing parameters (and related process physics) and/or material composition can affect the quality of the polyolefinic parts printed by MatEx. We provide recommendations for additional research based on the current state-of-the-art that aim to move away from the traditional "trial-and-error" printing methodology, thereby paving the way for a consolidated physics-based material-specific approach for consistent and future materials discovery efforts.

2.3 Additive Manufacturing of Polyolefins

Polyolefins belong to the class of thermoplastic polymers that are obtained through catalytic polymerization of olefinic compounds sourced from natural gas, crude oil, etc. In this paper, we limit our discussion to two of the most common polyolefins, namely, polyethylene (PE) and polypropylene (PP). Both of the polymers are attractive choices for a wide variety of industrial applications due to their physical and/or chemical properties, low cost, bio-inertness, and easy availability. Table 2.1 lists the common physical properties of PE and PP.

Table 2.1: Common physical properties of polyethylene and polypropylene

Polymer	**Melting temperature (°C)**	**Glass transition temperature (°C)**	**Density (g cm^{-3})**	**Coefficient of thermal expansion (m/m°C)**	**Crystallinity**	**Properties**
PE	105-135	-110	0.88-0.96	11-20 $\times$ 10^{-5}	<35% (LDPE) to >75% (HDPE)	Low temperature resistance, electrical insulator, low moisture absorption, solvent resistance, biocompatible
PP	130-170	-15	0.85-0.95	6-17 $\times$ 10^{-5}	∼0 (atatic) to ∼70% (isotactic)	Decent impact and flexural strength, chemical resistance, electrical insulator, fatigue resistant, efficient barrier

PE is the most used thermoplastic in the world and is most commonly available in three different forms depending on the extent of chain branching: low density PE (LDPE), high

density PE (HDPE), and ultrahigh molecular weight PE (UHMWPE). HDPE is associated with a high amount of crystallinity due to its ordered stereo-regular structure compared to LDPE, which is more amorphous due to the presence of chain branching and other defects. HDPE has received industrial attention for a broad range of applications due to its chemical resistance, biocompatibility, impact properties, and optical properties [Peacock, 2000]. PP is also generally semicrystalline; the extent of the crystallinity is controlled by the stereo-chemistry and processing conditions [Karian, 2003]. The crystalline content increases from atactic to syndiotactic to isotactic PP. Because of its excellent mechanical, thermal, and physical properties, PP has emerged to be the most important polyolefin in the automobile industry with an average utilization of 70 kg per vehicle manufactured [Sadiku et al., 2017]. As a result, AM of polyolefin thermoplastics as an economic, sustainable, and economic manufacturing technique has garnered substantial research interest both from the academic and industrial research sectors.

2.4 Material Extrusion (MatEx): Process Considerations

Material extrusion (MatEx) refers to an AM technique where a three-dimensional object is fabricated via selective extrusion of a polymer material through a nozzle in a layer-wise manner. Depending on the nature of the feedstock used, MatEx can be subdivided into two main categories, namely, melt-based polymer MatEx which includes both filament-based (or fused filament fabrication, FFF) as well as pellet-fed MatEx and paste extrusion (direct ink writing, DIW). The MatEx process involves feeding a solid polymer filament or polymer pellets (via a conveyor system) through a heated nozzle where the material transitions into the fluidic state. In FFF, the end of the filament remains in the molten state, while the portion above the heated nozzle remains in the solid state. The solid portion of the filament then acts as a piston, that forces the subsequent portion of the filament into the heated nozzle and thereby continues the extrusion process by supplying fresh polymer material into the nozzle. The extrusion nozzle then moves by a controlled gantry system and deposits the polymer extrudate in a pattern as directed by a computer aided manufacturing (CAM) model. Following the deposition of a layer (generally, layer thickness is less than 0.5 mm in FFF), the nozzle generally moves in x-y plane and the print bed moves along the z-axis to continue the deposition process. This sequence is repeated until the entire 3D object from

the CAM model is fabricated. Figure 2.2 provides a schematic representation of a typical filament based MatEx process along with the major components.

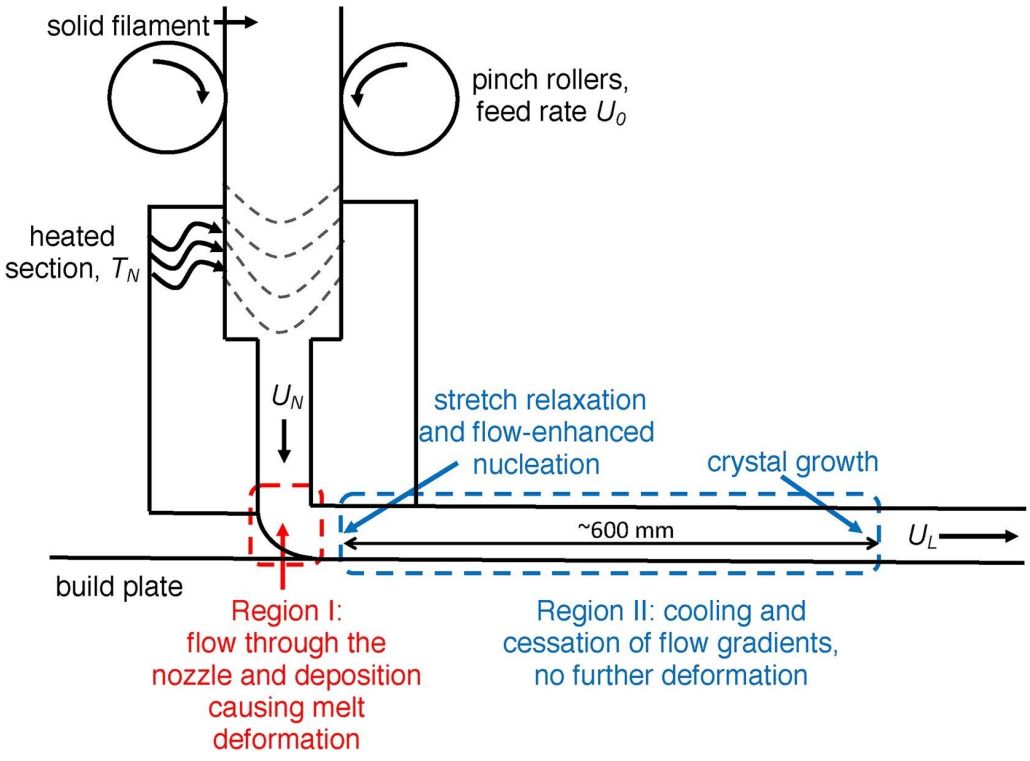


Figure 2.2: Schematic illustration of the filament-based material extrusion process for semicrystalline polymers. A pinch roller mechanism feeds the polymer filament into the heated section of the nozzle (nozzle temperature: T_N) at a continuous rate (U_0). Upon deposition of the melt on the print bed (at constant speed of U_N), the velocity gradients in the flow result in polymer deformation. The flow of the polymer melt and subsequent deposition on the print bed constitutes Region I in the figure. The cooling of the deposited extrudate on the print bed occurs in Region II where the deformations in the polymer relax since velocity gradients are absent in this region. As the polymer melt cools, the temperature drops below the melting temperature that initiates nucleation and growth of spherulites. Crystallization of the polymer is amplified if residual stretch is present during the initiation of nucleation in this region (image reprinted from [McIlroy and Graham, 2018] with permission from Elsevier).

Currently, the widespread application of MatEx is limited and is relegated to small-scale manufacturing of accessory, non-critical bearing parts such as jigs, fixtures, ducts, and wire

harnesses [Huang et al., 2015]. A major drawback for MatEx processed parts is that their mechanical performance is invariably inferior when compared to parts processed using conventional techniques such as injection molding [Gao et al., 2021]. Material selection in MatEx is limited due to challenges such as filament buckling, annular backflow, warpage, and limited knowledge regarding the effect of process physics on the polymer melt behavior [Gilmer et al., 2018]. Although there is a strong interest in processing polyolefins through MatEx, the semicrystalline nature of these polymers and the associated shrinkage during solidification further aggravates the issues associated with the reduction in interlayer weld strength, warping, and residual stress build-up in the printed parts. The interaction among crystallization, polymer melt flow, and deposition through the heated nozzle can lead to poor interlayer wetting, which results in void formation and parts with poor mechanical properties.

In a typical MatEx process, the polymer melt experiences shear rates on the order of 100-1000 s^{-1}, in contrast to that experienced by the polymer melt during PBF, that influences the extent of chain orientation and stretch and can drastically accelerate the crystallization kinetics for semicrystalline polymers such as PE and PP [Liu et al., 2018a, McIlroy and Graham, 2018, Bakrani Balani et al., 2019]. As a result of the rapid crystallization, the viscosity in the melt increases significantly, during solidification, which limits interfacial polymer chain diffusion and leads to printed parts with only a fraction of the polymer's bulk properties [Srinivas et al., 2018]. Increased amount of crystallinity in a printed part can strengthen interlayer bonding as the crystallites act as interfacial physical crosslinks; however, the brittleness of printed part increases with the amount of crystalline content. The implications of crystallinity evolution and its control during MatEx through careful process parameter selection is of particular importance when processing polymers like PE and PP.

In order to classify any polymer feedstock as "printable" for MatEx, it must satisfy a number of criteria including (i) successful extrusion through the nozzle (pressure driven), (ii) the extrudate must have a well-defined shape that is retained until deposition on the print bed, (iii) the deposited filament must be resilient enough to support the weight of subsequent layers while maintaining its shape during interlayer welding, and (iv) minimal warpage or shape distortion during solidification [Duty et al., 2018]. The requirements for polymer "printability" for semicrystalline polymers using MatEx have also been investigated with an emphasis on the importance of shape retention during polymer extrudate deposition [Zawaski et al., 2019, Chatham et al., 2019b]. However, most current research on polyolefin

MatEx focusses on investigating the impact of processing conditions on printed part performance. Only a handful of works highlight the importance of material- and machine-specific modifications that enable consistent, successful printing of polyolefins. In the subsequent sections, we scrutinize the published research on processing of PE and PP using MatEx, analyse the importance of material and machine modifications required for consistent printing, and offer recommendations to overcome the limitations associated with the current printing approaches.

2.5 MatEx of Polyethylene (PE)

2.5.1 Printing with PE

Polyethylene-based polymers can have a variety of different molecular architecture and as such, the majority of commercial PE polymers are classified into four different categories, namely, low density polyethylene (LDPE), linear low-density polyethylene (LLDPE), high density polyethylene (HDPE), and ultra-high molecular weight polyethylene (UHMWPE). Although PE dominates the global market for consumer products, it is still in the nascent stage for MatEx based processing. As summarized in Table 2.2, there is limited research that evaluate the suitability of PE as a potential material feedstock for the FFF modality of AM. The main reason behind this is the volume change during crystallization which induces residual stresses that lead to layer warpage [Watanabe et al., 2016]. Moreover, most of the existing research do not correlate the crystallization behavior of PE polymers with their printability and print part performance. LDPE has significantly lower crystallinity and elastic modulus than HDPE as well as slightly lower thermal conductivity (0.25-0.32 W $m^{-1}K^{-1}$ vs. 0.35-0.39 W $m^{-1}K^{-1}$) [Chaudhry et al., 2020] which reduces warpage in LDPE printed parts. The decreased modulus, however, can lead to filament buckling during MatEx even when printing at very slow speeds [Hart et al., 2018b]. Optimisation of the printing conditions has been shown to produce LDPE parts with similar modulus to the feedstock, but the tensile strength decreased due to voids introduced during printing [Hart et al., 2018b].

Table 2.2: Mechanical properties of pure polyolefins and their composites along with the relevant print conditions when printed using MatEx.

Polymer	**Mechanical properties of printed parts**	**Print conditions**	**Reference**
HDPE	Tensile strength: 25.8 ± 1.6 MPa; Tensile modulus: 1020 ± 50 MPa; Elongation at break: 90 ± 50%	Nozzle temperature of 220°C; bed temperature of 60°C; 25mm/s speed; 90° raster; 100% infill; 0.2mm layer thickness (first layer 0.35mm thick)	[Schirmeister et al., 2019]
PE	Tensile modulus: 670 ± 110 MPa; Elongation at break: 10.11 ± 0.53%	No information was provided	[Tarrés et al., 2018]
PE + 20% pulp	Tensile modulus: 1510 ± 120 MPa; Elongation at break: 5.51 ± 0.33%	No information was provided	[Tarrés et al., 2018]
HDPE	Young's modulus: 5.1 GPa; Ultimate tensile stress: 159 MPa; Toughness: 20.1 kJ m^{-2}	Nozzle diameter of 0.4mm; nozzle temperature 230°C; bed temperature of 70°C; 20mm/s speed; 0.2mm layer thickness; 100% infill; 105% extrusion ratio	[Tan and Low, 2018]
10 vol% metal filled HDPE	Young's modulus: 7.6 GPa; Ultimate tensile stress: 180 MPa; Toughness: 12.5 kJ m^{-2}	Nozzle diameter of 0.4mm; nozzle temperature 230°C; bed temperature of 70°C; 20mm/s speed; 0.2mm layer thickness; 100% infill; 105% extrusion ratio	[Tan and Low, 2018]
LLDPE	Tensile strength: 10.05 ± 0.39 MPa; Flexural strength: 13.33 ± 0.31 MPa; Flexural modulus: 340.67 ± 11.06 MPa	Nozzle diameter of 0.4mm; nozzle temperature 140°C; bed temperature of 100°C; 0.25mm layer thickness; 100% infill; post-printing annealing at 115°C	[Mohan and Bhattacharyya, 2020]

Table 2.2 – continued from previous page

Polymer	Mechanical properties of printed parts	Print conditions	Reference
LLDPE + 6% GNP + 2% polypyrrole	Tensile strength: 11.23 ± 0.15 MPa; Flexural strength: 14.80 ± 0.36 MPa; Flexural modulus: 410 ± 11.27 MPa	Nozzle diameter of 0.4mm; nozzle temperature 140°C; bed temperature of 100°C; 0.25mm layer thickness; 100% infill; post-printing annealing at 115°C	[Mohan and Bhattacharyya, 2020]
UHMWPE + 17% HDPE-g-SMA + 12% PP	Tensile strength: 30.1 ± 1.3 MPa; Yield strength: 25.8 ± 0.4 MPa; Tensile modulus: 1145 ± 41 MPa; Elongation at break: 356 ± 42%	Nozzle diameter of 0.4mm; nozzle temperature of 170°C; bed temperature of 100°C; 20mm/s speed; 100% infill	[Dontsov et al., 2020]
Milled LLDPE + 30% GNP	Tensile strength: 14.1 MPa; Tensile modulus: 616.0 MPa	Nozzle diameter of 0.6mm; nozzle temperature of 170°C; bed temperature of 90-100°C; 1000mm/min speed; 0.35mm layer thickness; 100% infill	[Jing et al., 2020]
16% HDPE wax + 74% HDPE + 10% UHMWPE	Tensile strength: 82.0 ± 10.0 MPa; Elastic modulus: 2.00 ± 0.18 GPa; Elongation at break: 5.4 ± 0.9%; Impact strength: 18.5 ± 0.9 kJ m^{-2}	Nozzle diameter of 0.8mm; nozzle temperature of 210°C, bed temperature of 60°C, 150mm/s speed; 0.2mm layer height, 0.7mm line width, 100% infill, 0° raster; material flow of 100−107%	[Schirmeister et al., 2021a]
PP	Tensile strength: 27.5 ± 4.3 MPa; Tensile modulus: 1200 ± 100 MPa	Nozzle temperature of 165°C; bed at room temperature; 60mm/s speed (first layer 8mm/s); 0.2mm layer thickness; 0° raster; 100% infill	[Carneiro et al., 2015]

Table 2.2 – continued from previous page

Polymer	Mechanical properties of printed parts	Print conditions	Reference
PP + 30% glass fiber	Tensile strength: 40.2 ± 2.5 MPa; Tensile modulus: 1320 ± 80 MPa	Nozzle temperature of 185°C; bed at room temperature; 8mm/s speed; 0.2mm layer thickness; ±45° raster; 100% infill	[Carneiro et al., 2015]
50% PP + 50% PC	Tensile strength: 27.93 MPa; Elongation at break: 3.98 mm/mm	Nozzle temperature of 215°C; bed temperature of 90°C; 2000mm/min speed; 0.1mm layer height; 0° raster	[Zhou et al., 2017b]
Compatibilized blends of PP/PC	Tensile strength: 33.82 MPa; Elongation at break: 1.83 mm/mm	Nozzle temperature of 215°C; bed temperature of 90°C; 2000mm/min speed; 0.1mm layer height; 0° raster	[Zhou et al., 2017b]
PP	Tensile strength: 16.5 MPa; Tensile modulus: 230 MPa	Nozzle temperature of 230°C; bed temperature of 25°C; 0.1mm layer height	[Milosevic et al., 2017]
PP + 20wt% Harakeke	Tensile strength: 24.0 MPa; Tensile modulus: 325 MPa	Nozzle temperature of 230°C; bed temperature of 25°C; 0.1mm layer height	[Milosevic et al., 2017]
Recycled PP	Tensile strength: 20.1 ± 2 MPa; Ultimate strain: 0.2 ± 0.02%	Nozzle temperature of 260°C; bed temperature of 100°C; 50mm/s speed; 0.2mm layer height; ±45° raster	[Zander et al., 2019a]
Recycled PP/PET SEBS-MA	Tensile strength: 24.2 ± 1 MPa; Ultimate strain: 0.04 ± 0.0006%	Nozzle temperature of 260°C; bed temperature of 100°C; 50mm/s speed; 0.2mm layer height; ±45° raster	[Zander et al., 2019a]

Table 2.2 – continued from previous page

Polymer	Mechanical properties of printed parts	Print conditions	Reference
Recycled PP/PS	Tensile strength: 23.0 ± 1 MPa; Ultimate strain: 0.1 ± 0.05%	Nozzle temperature of 260°C; bed temperature of 100°C; 50mm/s speed; 0.2mm layer height; ±45° raster	[Zander et al., 2019a]
PP	Tensile strength: 20.9 ± 0.8 MPa; Ultimate strain: 1631.2 ± 21.0%; Tensile modulus: 830 ± 10 MPa	Nozzle temperature of 230°C; bed temperature of 70°C; chamber temperature of 55°C; 0.25mm layer thickness; 56.6mm/s speed (first layer printed at half speed)	[Spoerk et al., 2018b]
PP + 20wt% carbon fiber	Tensile strength: 57.1 ± 0.6 MPa; Ultimate strain: 2.9 ± 0.2%; Tensile modulus: 5.7 ± 0.47 GPa	Nozzle temperature of 230°C; bed temperature of 70°C; chamber temperature of 55°C; 0.25mm layer thickness; 56.6mm/s speed (first layer printed at half speed)	[Spoerk et al., 2018b]
PP + 0.3wt% MWCNT	Tensile strength: 29.4 ± 0.60 MPa; Ultimate strain: 4.71 ± 0.14%	Nozzle temperature of 175°C; bed temperature of 25°C; 0.2mm layer height; 0° raster; 30mm/s speed	[Stanciu et al., 2019]
PP	Tensile strength: 29 ± 1 MPa; Ultimate strain: 14.5 ± 0.3%; Tensile modulus: 750 ± 63 MPa	Nozzle temperature of 220°C; bed temperature of 100°C; 100% infill; ±45° raster; 50mm/s speed	[Zander et al., 2019b]
PP + 30 wt% nylon	Tensile strength: 25.7 ± 0.5 MPa; Flexural modulus: 720 ± 100 MPa	Nozzle temperature of 250°C; bed temperature of 110°C; 0.1mm layer height; 30mm/s speed	[Peng et al., 2019a]

Table 2.2 – continued from previous page

Polymer	Mechanical properties of printed parts	Print conditions	Reference
PP	Tensile strength: 41.5 ± 5.5 MPa; Ultimate strain: 405 ± 73%; Tensile modulus: 1073 ± 203 MPa	Nozzle temperature of 250°C; bed temperature of 120°C; 0.25mm layer height; 15mm/s speed; 0° raster	[Jin et al., 2018]
PP	Tensile strength: 16.4 ± 0.7 MPa; Tensile modulus: 2.7 ± 0.2 GPa; Flexural strength: 27.5 ± 0.8 MPa; Flexural modulus: 1.8 ± 0.1 GPa	Nozzle temperature of 250°C; bed temperature of 130°C; 0.1mm layer height; 45mm/s speed	[Wang et al., 2018c]
PP	Maximum load at break: 724 N; Elongation at break: 7.8% (Reported values from shear test specimens)	Nozzle temperature of 230°C; bed temperature of 85°C; 36mm/s print speed; Cooling system temperature of 25°C	[Hertle et al., 2016]
PP + 7.5% PLA + 0.75% graphene	Tensile strength: 30.5 MPa; Elongation at break: 10%; Tensile modulus: 450 MPa	Nozzle diameter of 0.4mm; Nozzle temperature of 200°C; bed temperature of 110°C; 20mm/s speed; 0.2mm layer height; 30% infill	[Aumnate et al., 2020]
PP + PET microfibrillar composite	Tensile strength: 39.0 ± 6.0 MPa; Tensile modulus: 2.7 ± 0.3 GPa	Nozzle temperature of 210°C; bed temperature of 140°C; 5mm/s speed; 0.2mm layer thickness; 100% infill; 0° raster	[Huang and Schlarb, 2021]
PP	Interlayer adhesion strength normalized by contact length : 21 ± 2 kN/m	Nozzle temperature of 180°C; bed temperature of 110°C; 0.27mm layer thickness	[Charlon et al., 2021]

Table 2.2 – continued from previous page

Polymer	Mechanical properties of printed parts	Print conditions	Reference
PP reinforced with short glass fibers	Tensile strength: 57.4 ± 5.1 MPa; Elongation at break: 0.025 ± 0.011 mm/mm; Tensile modulus: 5280 ± 345 MPa	Nozzle diameter of 0.6mm; Nozzle temperature of 260°C; bed temperature of 95°C; chamber temperature of 35°C; 50mm/s speed; 0.1mm layer thickness; 100% infill; 90° raster	[Shulga et al., 2020]
PP + precision cut carbon fibers	Yield strength: 37.5 ± 0.7 MPa; Elastic modulus: 4655 ± 214 MPa; Elongation at break: 1.4 ± 0.1%; Impact strength: 7.16 ± 0.36 kJ m^{-2}	Nozzle diameter of 0.8mm; Nozzle temperature of 210°C; bed temperature of 55°C; chamber temperature of 50°C; 45mm/s speed (first layer at 18mm/s); 100% infill; 0.25mm layer thickness; 0° raster; 0.95 flow ratio; bed made of thermoforming PP sheet	[Savandaiah et al., 2021]
PP + milled carbon fibers	Yield strength: 20.1 ± 0.6 MPa; Elastic modulus: 2644 ± 199 MPa; Elongation at break: 5.5 ± 1.2%; Impact strength: 10.03 ± 0.34 kJ m^{-2}	Nozzle diameter of 0.8mm; Nozzle temperature of 210°C; bed temperature of 55°C; chamber temperature of 50°C; 45mm/s speed (first layer at 18mm/s); 100% infill; 0.25mm layer thickness; 0° raster; 0.95 flow ratio; bed made of thermoforming PP sheet	[Savandaiah et al., 2021]
PP	Tensile strength: 31.6 ± 0.6 MPa; Tensile modulus: 0.47 ± 0.01 GPa; Flexural strength: 29.3 ± 3.1 MPa; Flexural modulus: 0.59 ± 0.05 GPa	Nozzle temperature of 230°C; bed temperature of 80°C; 30mm/s speed; 0.2mm layer thickness; 100% infill; 45° raster	[Vidakis et al., 2021]

Table 2.2 – continued from previous page

Polymer	Mechanical properties of printed parts	Print conditions	Reference
PP + alkali treated bamboo fiber	Tensile strength: 21.8 MPa; Elongation at break: 14.20%	Nozzle temperature of 180-200°C; bed temperature of 40-60°C; 40-60mm/s speed	[Long et al., 2019]
PP + silane treated bamboo fiber	Tensile strength: 28.1 MPa; Elongation at break: 11.80%	Nozzle temperature of 180-200°C; bed temperature of 40-60°C; 40-60mm/s speed	[Long et al., 2019]
PP	Tensile strength: 26.9 ± 2.0 MPa; Tensile modulus: 872 ± 36 MPa	Nozzle temperature of 180°C; bed temperature of 120°C; 1000mm/min speed; 100% infill; 0° raster	[Das et al., 2020b]
PP + 20% hydrocarbon resin	Tensile strength: 32.4 ± 2.1 MPa; Tensile modulus: 938 ± 29.9 MPa	Nozzle temperature of 180°C; bed temperature of 120°C; 1000mm/min speed; 100% infill; 0° raster	[Das et al., 2020b]

The use of recycled feedstocks for FFF is critical in establishing a circular economy. However, recycled HDPE is a challenging material in this context due to problems associated with interlayer adhesion and warpage from the print bed [Chong et al., 2017]. Chong et al. [Chong et al., 2017] suggested heating the print bed and applying PE tape to the bed to address these issues but made no attempt to print parts for mechanical characterization. Hamod studied the viability of using recycled HDPE as a filament feedstock for MatEx and reported that the recycled polymer had a lower viscosity than the virgin polymer, which was likely due to chain scission triggered by the multiple thermal processing history [Hamod, 2014]. Even with this loss in molecular weight, mechanical properties of the recycled filaments were found to be better than that of virgin HDPE. Unfortunately, the study did not shed any light on the printed properties obtained using the recycled filaments [Hamod, 2014].

Pan et al. [Pan et al., 2018] characterized recycled HDPE/PP filaments reinforced with metallic powders for MatEx but did not print these filaments. Similar work with hydroxyapatite reinforced UHMWPE showed a reduction in crystallinity with increasing filler content

which should have reduced part warpage [Ansari and Ibrahim, 2017]. Again, Ansari and Ibrahim60 only studied the extrudability of the material in MatEx but did not conduct any printing. Recent work with UHMWPE composites looked at reducing UHMWPE's viscosity to enable processing via MatEx [Panin et al., 2019]. Blending with HDPE has been found to be a potential technique to improve the processability of UHMWPE but there is limited information about the printability of such blends using MatEx [Ramli et al., 2016]. The authors address the flow issues in UHMWPE but do not investigate the composite's crystallization and print properties. Researchers are also investigating blends of HDPE with phase change materials and cork powders for applications in MatEx but this research is currently only preliminary [Freeman et al., 2019, Brites et al., 2019]. Another such viability study for LDPE and HDPE was performed by Stanciu et al. [Stanciu et al., 2018] The melt flow characteristics of the polymers were characterized at shear rates relevant to MatEx using capillary rheology and filaments with acceptable dimensional tolerance were obtained. However, as stated for the previous works, the authors did not print any actual parts using the filaments and only hypothesized on the importance of extrusion parameters on the printing process [Stanciu et al., 2018].

The first successful print of functional parts with PE was reported by Filgueira et al. [Filgueira et al., 2018]. They blended bio-based PE with chemically modified thermomechanical pulp fibers to improve interfacial adhesion. Parts made using this composite material did not warp during print. Moreover, they printed on a bed at ambient temperature without applying adhesive to the print bed surface. In a subsequent work, they described the mechanical properties of the printed composites using micromechanical models [Tarrés et al., 2018]. The model predicted optimum blend compositions for tensile properties and validated those predictions experimentally. However, the tensile properties were significantly lower than those obtained for injection molded HDPE.

Schirmeister et al. [Schirmeister et al., 2019] performed a systematic study to optimize the processing parameters for MatEx of HDPE filaments. They employed poly(styrene-block-ethene-co-butene-block-styrene) elastomer (SEBS) as the print bed to improve adhesion to HDPE, while aiding easy detachment of the printed part post-printing. Further, to limit void formation and limit shrinkage during crystallization of HDPE the authors employed a gradient in the extrusion rate from 100-107%. The tensile strength and modulus of the warpage-free printed parts approached IM properties (Figure 2.3a). Schirmeister et al. [Schirmeister et al., 2019] suggests with such modifications increased chain diffusion and entanglements

across the layer interface are obtained, which led to the improved isotropic mechanical properties that had minimal dependence on nozzle temperature and diameter.

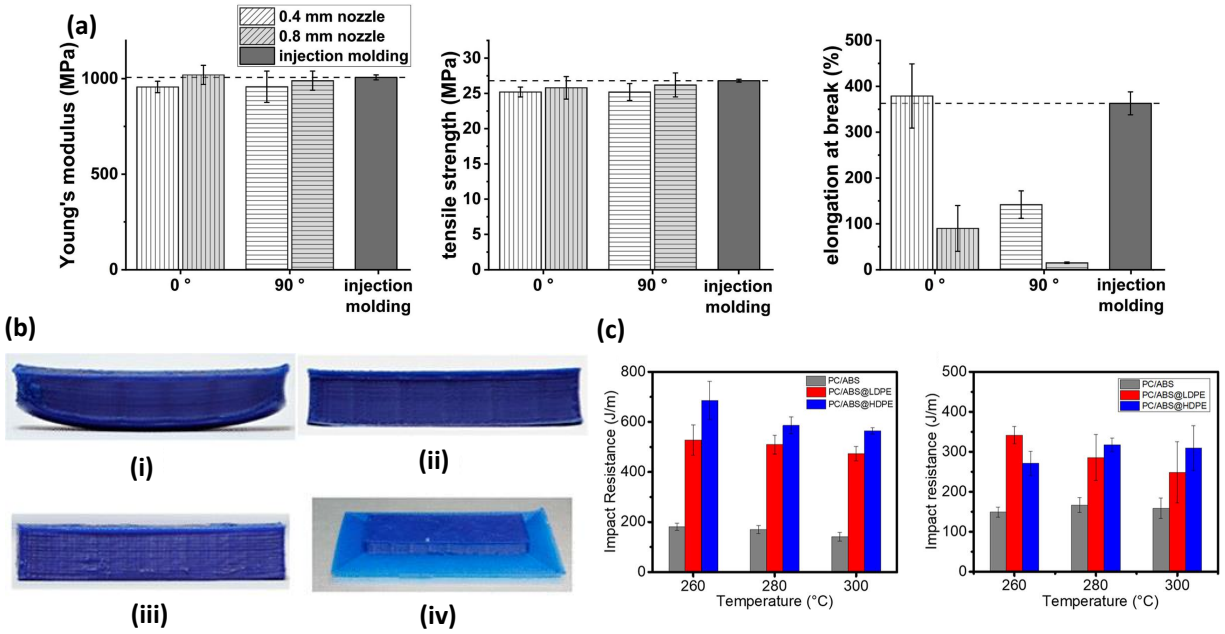


Figure 2.3: (a) The effect of nozzle diameter and raster pattern on the tensile modulus, maximum tensile strength, and elongation at break of HDPE samples printed using FFF and compared with the injection molded properties (image reprinted from [Schirmeister et al., 2019] with permission from Elsevier); (b) Digital images of 3D printed rectangular bars. (i) Bar of HDPE printed without using a brim, (ii) 10 mm high HDPE bar printed with a brim, (iii) 10 mm high functionalized HDPE bar printed with a brim, (iv) 10 mm high functionalized HDPE bar prior to detaching from the brim. The functionalized HDPE bars printed with brims exhibit minimal warpage (image reprinted from [Gudadhe et al., 2019] with permission from American Chemical Society); (c) Impact testing results as a function of print temperature (260, 280, 300°C) for the FFF printed samples of PC/ABS, LDPE shell-PC/ABS, and HDPE shell-PC/ABS. The left image corresponds to prints printed in the XZ orientation while the right image corresponds to prints printed in XY orientation (image reprinted from [Peng et al., 2019a] with permission from American Chemical Society)

2.5.2 MatEx of PE blends with other polymers

The potential for binary blends of recycled ABS and recycled HDPE was determined by Decker and Yee [Decker and Yee, 2017]. When processed using MatEx, the blends had issues with inconsistent extrusion of the melt from the print nozzle. The ease of part removal from

the print bed increased upon incorporation of HDPE compared to ABS, but the printed parts had poor geometric accuracy and reduced tensile properties. The miscibility of ABS and HDPE was one of the major issues behind such poor mechanical performance and the use of compatibilizers might help in addressing this problem [Decker and Yee, 2017].

Gudadhe et al. [Gudadhe et al., 2019] investigated the feasibility of MatEx using HDPE derived from plastic waste streams and explored the origin of residual stresses associated with the printing process using finite element simulations. The researchers blended dimethyl dibenzylidene sorbitol and linear LDPE with the HDPE to limit the effects of warpage during printing. Moreover, a brim was printed around the actual part to promote adhesion to the print bed (Figure 2.3b) by reducing the debonding stresses. This study highlights how modifying the material as well as the printing process can accommodate printing of semicrystalline polymers like HDPE.

Harris et al. [Harris et al., 2020] used a maleic anhydride grafted PE for the compatibilizing ABS and HDPE blends for MatEx processing. The blends exhibited intermolecular interactions as confirmed by reduction in the enthalpy of melting compared to the neat polymer [Harris et al., 2020].Using a design of experiments (DOE), the authors optimized the print temperature, bed temperature, and thermal annealing conditions to achieve the maximum mechanical properties. Thermal annealing post-printing caused heterogeneous crystallization to occur in the blends and was found to play a significant role in improving the thermal and mechanical properties of the printed parts by improving chain diffusion across deposited layers [Harris et al., 2020].

Peng et al. [Peng et al., 2019a] incorporated LDPE and HDPE into polycarbonate (PC)/ABS blends to make core-shell filaments for MatEx. The impact properties of the core-shell prints increased (Figure 2.3c) compared to those of PC/ABS blend, while the addition of LDPE slowed down the crystallization process and thereby provided a larger window for residual stress dissipation during FFF. The stiffer PC/ABS core minimized the warping tendency that is invariably associated with the volumetric shrinkage during the crystallization of PE leading to parts with greater geometric accuracy [Peng et al., 2019a].

Ternary blends of ABS with UHMWPE and styrene ethylene butadiene styrene (SEBS) have been printed using MatEx and the printed parts demonstrated a reduced amount of mechanical anisotropy (i.e., reduced effect of build orientation on mechanical properties) compared to pure ABS [Torrado et al., 2015]. Improved interlayer bonding in the ternary blends was

a result of the lower complex viscosity of the material above T_g and increased wetted interfacial contact area. However, the tensile strength of ABS printed parts were superior to the ternary blends because the additives in the blends most likely led to plasticization [Torrado et al., 2015]. A PE-based ionomer (Surlyn 9520) was printed using MatEx and the shape memory behavior of the printed part was characterized [Zhao et al., 2017]. The shape memory characteristics including the fixity and recovery during the first cycle were similar for the printed and compression molded (CM) samples but the former outperformed the latter in the subsequent cycles.

Dontsov et al. employed Taguchi statistical analysis to determine the optimal printing parameters for a UHMWPE composite consisting of maleic anhydride grafted HDPE (HDPE-g-SMA as a compatibilizer) and PP (as a plasticizer) [Dontsov et al., 2020]. MatEx processing resulted in a homogenous composite materials with good dispersion of PP in base polymer matrix. Although, the printed parts had more voids in their structures compared to CM parts, their densities were comparable. Similar work with a different blend composition has also been reported where the tribomechanical performance of printed parts were found to be superior than melt-pressed samples [Panin et al., 2020]. The homogeneity in the molecular architecture and increased crystallinity in the printed parts were held responsible for the observed trends in mechanical properties.

Amza et al. performed a systematic study on incorporating UHMWPE fibers into a polylactic acid (PLA) matrix in an effort to improve the fracture toughness of the printed parts [Amza et al., 2019]. The fiber orientations and print temperatures were found to be the major factors controlling the success of the embedding process. The authors reported a 23% increase in tensile strength for 3D printed composite parts with only 0.75 wt% of UHMWPE fibers [Amza et al., 2019]. Maximizing the mechanical properties and better insights into the thermal behavior of the embedded fibers in PLA during printing are the main research directions for such composite materials.

2.5.3 MatEx of filler reinforced PE composites

Fillers have been commonly employed to slow down the crystallization rate of pure PE to reduce residual stresses induced by crystallization in the printed part. Tan and Low prepared HDPE filaments filled with different metal fillers and characterized the electrical performance of the MatEx printed parts [Tan and Low, 2018]. The metal fillers acted as a

viscosity modifier, which contributed to a better particle distribution in the HDPE matrix. The authors acknowledged that further tuning of print conditions is necessary to reduce porosity in the printed parts and improve the interlayer adhesion between the deposited layers [Tan and Low, 2018]. The feasibility of using copper-filled PE for MatEx printing was studied by Nabipour et al. through process modifications (print speed, print temperature, bed material) to eliminate flow inconsistencies through the print nozzle, warpage, and poor adhesion to the print bed [Nabipour et al., 2020]. The composite printed parts exhibited higher flexural strength and modulus compared to neat PE prints, while the electrical conductivity of the composite prints increased by two orders of magnitude. However, increased copper concentrations led to printed parts with increased voids that can lead to inferior tensile performance [Nabipour et al., 2020]. In another feasibility study, Singh et al. studied zirconium oxide reinforced HDPE prepared using twin-screw extrusion for applications in 3D printing, without actually printing any parts [Singh et al., 2019b]. Waste filaments of HDPE and LDPE have been blended with iron powder to aid the melt-reprocessing of the polymers. The composite filament was found to be a promising feedstock for MatEx based on the mechanical and morphological characterizations [Kumar et al., 2019].

Activated carbon (AC), derived from coconut fiber waste, has been investigated as a filler for preparing recycled HDPE filaments for MatEx [Chong et al., 2020]. The degree of crystallinity of the composite decreased with the addition of AC. Due to the poor compatibility between AC and HDPE, PP was added to the blends to improve miscibility. The authors speculated that the increase in elongation at break of the composite filaments was due to the strong interactions between the methyl group of PP and AC [Bagheri and Julkapli, 2016]. However, no parts were printed using the prepared filaments and further work is required to answer how the process physics during printing would affect the printed part properties.

Preliminary studies on the recyclability of injection molded multi-walled carbon nanotube (MWCNT) reinforced LDPE displayed that remanufacturing using MatEx was a viable option, since the mechanical and electrical properties after recycling were minimally affected compared to the virgin composites [Stan et al., 2019b]. In a following work, Stan et al. also incorporated MWCNTs in HDPE matrix and investigated the effect of blend composition on the "printability" of the composite material using MatEx [Stan et al., 2019a]. The authors reported the importance of shear thinning characteristics of the blends on the printed part properties and found that, at 5 wt% MWCNT content, nozzle clogging caused issues during printing. However, at compositions of 0.1 and 1wt%, the composite filaments can be printed

consistently and parts with dimensional accuracy as well as decent mechanical and electrical properties can be obtained[Stan et al., 2019a]. Daver et al. incorporated CNTs with linear LDPE and functionalized rubber particles and evaluated the printability of the resultant nanocomposite filaments using MatEx [Daver et al., 2016]. The addition of a compatibilizer improved the electrical conductivity of the 3D printed composites; although mechanical properties were lower than the CM parts. A strong percolating network of CNTs formed at higher rubber loadings, which can be exploited to manufacture the next-generation of electronic devices with tunable conductivities using MatEx [Daver et al., 2016].

In a similar approach, linear LDPE composites were prepared containing graphene nanoplatelets (GnPs) and polypyrrole [Mohan and Bhattacharyya, 2020]. The mechanical and electrical performance of the 3D printed parts were found to be better than the printed parts of neat linear LDPE; but the properties were still inferior to CM counterparts. Moreover, the researchers only investigated a narrow processing window and future work should be directed at optimizing the print conditions to minimize the defects generated in the printed parts [Mohan and Bhattacharyya, 2020]. Jing et al. examined the MatEx processing of linear LDPE/GnP nanocomposites for applications in electronic devices [Jing et al., 2020]. Due to the long-range alignment of the GnPs in the polymer matrix, imparted by the shearing along the print direction during MatEx, the printed parts exhibited superior thermal conductivity values compared to neat linear LDPE.

Olesik et al. developed a model to predict the printing speed for LDPE reinforced powdered waste glass composites based on a buckling analysis [Olesik et al., 2019]. They were able to successfully print composites parts that exhibited higher tensile modulus and wear resistance than neat LDPE, which makes this material a suitable choice for frictional applications. Composite filaments of HDPE, dibutyl phthalate (compatibilizer), and hollow glass microspheres (HGS), with 30-50 vol% of HGS, have been prepared through twin-screw extrusion for application in MatEx [Parsons et al., 2019]. The filaments had low permittivity and dielectric constants over a range of radio and microwave frequencies. Representative samples were printed using the filaments to characterize the dielectric properties, which justified their application in electromagnetic devices [Parsons et al., 2019]. MatEx printed syntactic foams of HDPE and GMBs were also analysed with respect to their compressive strengths [Singh et al., 2019a]. An interesting finding was the formation of a three-phase morphology in the printed foams comprised of the base HDPE, GMBs, and air voids; the last of which contributed to the foams being less dense than CM samples. However, the same voids led to

inferior compressive modulus and yield strength for the 3D printed parts compared to the CM samples [Singh et al., 2019a]. In a follow-up work, the flexural performance of the 3D printed GMB/HDPE sandwich composite was characterized and improved bonding at the interface was achieved through carefully tuning print parameters [Bharath et al., 2020b]. The printed structures exhibited a similar three-phase morphology which provided a pathway for load dissipation.

Doddamani studied the potential for fly ash cenosphere reinforced HDPE composites as a feedstock for MatEx [Doddamani, 2020]. X-ray diffraction revealed higher crystalline content in printed parts compared to the composite filaments and preliminary dynamic mechanical analysis (DMA) highlighted the potential for such environmentally benign filaments in MatEx [Doddamani, 2020]. Subsequent work from the same group evaluated highly filled (up to 60 volume%) HDPE/GMB filaments as a feedstock for MatEx to print lightweight composite foams [Bharath et al., 2020a]. The incorporation of GMBs reduced the coefficient of thermal expansion (CTE) of HDPE at the expense of increased melt flow resistance. This led to a reduction in the thermally induced stress build-up in the printed parts and subsequently parts with reduced warpage were obtained. The printed foams exhibited excellent tensile and flexural properties with modulus almost two times higher than conventionally molded samples [Bharath et al., 2020a].

Jeyachandran et al. employed bioactive glass in a HDPE matrix by melt-mixing to arrest warpage during printing and fabricate parts for biomedical implants [Jeyachandran et al., 2020]. The prepared filaments were able to successfully withstand the forces during extrusion from the print nozzle and resulted in printed parts with mechanical properties almost similar or even superior to injection molded samples. The excellent mechanical performance of the composite printed part was attributed to the uniform distribution and dispersion of the glass filler in HDPE [Jeyachandran et al., 2020].

Another interesting filler material to eliminate warpage during MatEx of HDPE is nanoclay [Beesetty et al., 2020]. The addition of the stiff filler increases the restriction to molecular motion in the blends (and reduces the melt flow index of the composites compared to neat HDPE), as highlighted in Figure 2.4, while the crystalline content and crystallization temperature increased. Incorporation of the fibers within the polymer hinders interlayer diffusion and as a result the interlayer weld strength decreases. The printed tensile and flexural properties of the composites were found to be higher than that of neat HDPE prints, although the composites failed from brittle fracture [Beesetty et al., 2020]. The improvement

in the mechanical properties is attributed to the efficient load-transfer pathway caused by the increased surface area of the nanoclay.

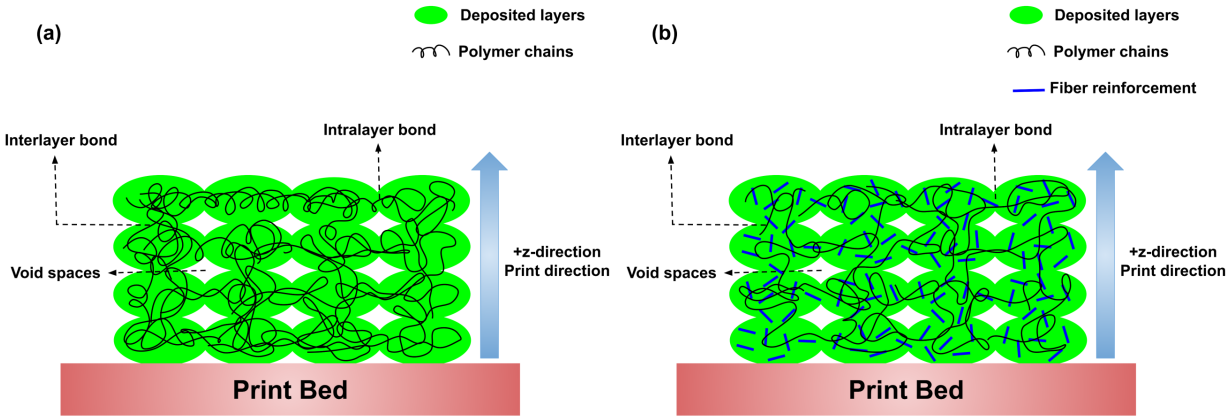


Figure 2.4: Illustration of the cross-sectional view of (a) polymer chains, and the inter and intra-layer bonds; (b) the presence of reinforcement affecting the interlayer bonds (reduced extent of interlayer bonding due to presence of reinforcement)

Gregor-Svetec et al. incorporated cardboard dust (up to 75 wt%) to HDPE polymer and prepared 3D printable filaments [Gregor-Svetec et al., 2020]. Increased filler content resulted in filaments with increased porosity and surface roughness. The crystalline content decreased in the blends with the addition of cardboard dust compared to neat HDPE and the prepared filaments were found to be brittle making it difficult to process in a MatEx printer. Although the authors present a novel way to use an industrial residue in filament preparation, questions about the quality of the printed parts still persists and needs to be investigated in greater detail [Gregor-Svetec et al., 2020].

As evident from the above discussion, there is a great deal of published research on the experimental approach of printing PE-based materials using MatEx. However, physics-based modeling of the printing process is still in its emerging stage. This is likely due to the computational complexities associated with modeling the coupled effects of flow behavior,

thermal history, and viscoelastic properties [McIlroy and Graham, 2018, Das et al., 2021c]. Although, recent progress is being made on modeling such polymers [McIlroy and Graham, 2018, Costanzo et al., 2020, Yuan et al., 2020], to the best of our knowledge there is only one published article that deals with simulations related to MatEx of HDPE [Dayam et al., 2020]. By simulating the flow and thermal profile in the nozzle during MatEx of HDPE, Dayam et al. reported the impact of flow velocity on the pressure required to extrude the polymer melt through the nozzle [Dayam et al., 2020]. Such studies will provide more insights into the process-property relationships during printing and help guide intelligent process parameter selection.

2.6 MatEx of Polypropylene (PP)

2.6.1 Printing with PP

Similar to MatEx of PE, there are relatively few works that deal with MatEx of pure PP due to shrinkage and warpage during printing. The warpage issue in PP is highlighted in Figure 2.5a. As is the case with HDPE, the warpage in the printed parts arises due to the semicrystalline nature of PP. During a typical MatEx process, the temperature of the deposited layers drops below the crystallization temperature (T_c) of the polymer within 2-3s , that results in restricted chain mobility and a high level of volumetric shrinkage to occur, which is further exacerbated by the regular arrangement of polymer chains in isotactic PP (Figure 2.5b). A potential avenue to counter this effect is by impeding the ordered arrangement of the polymer chains and reduce the crystallizability of the polymer (Figure 2.5c).

The crystallization behavior of isotactic PP under cooling rates representative of those experienced in MatEx (100°C s^{-1}) [Seppala and Migler, 2016] has been studied using flash dynamic scanning calorimetry (DSC) [Schawe, 2017]. At cooling rates greater than 90 K s^{-1} a less stable mesomorphic phase appears and the content of the more stable crystalline phase diminishes. At even higher cooling rates (>500 K s^{-1}), crystallization is arrested and the material quenches to an amorphous state, likely due to not enough time for the chains to relax and rearrange into a crystalline form. These results suggest heating accessories must be incorporated during MatEx of PP to slow down the cooling process and allow for the development of crystallinity in the printed sample. Figure 2.6 present a schematic of the

process considerations for maximizing the printed part performance of polyolefins such as PE and PP based on the polymer chain mobility and thermal characteristics such as T_g, crystallization and melting temperatures.

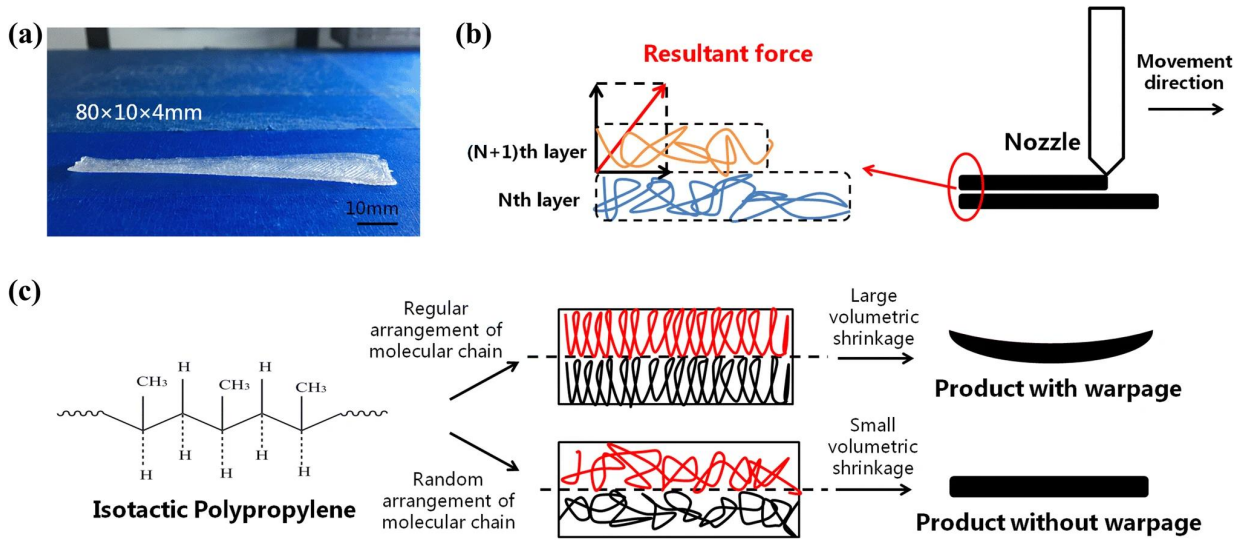


Figure 2.5: (a) A typical warped PP print during FFF, (b) schematic of the origin of warpage during FFF of polypropylene, (c) correlation between the warpage encountered during printing polypropylene and the stereochemistry of the polymer (image reprinted with permission from [Peng et al., 2019a] with permission from Springer Nature)

Table 2.2 summarizes the mechanical properties of PP and their composites manufactured using MatEx along with the relevant print parameters. One of the earliest reports on MatEx of PP was reported in the early 2000s by Kalita et al. who developed a PP/ceramic composite [Kalita et al., 2003]. The material was modified with plasticizers and wax (processing aides) and printed into a porous scaffold for biomedical applications. Using a similar approach, Katschnig et al. recently printed and characterized PP parts for cranial bone replacements [Katschnig et al., 2017]. Their study reported a processing window within which the implants were printed consistently and had more mechanical stability than the control bone samples. Volpato et al. developed a piston-driven extrusion head that was able to prepare filaments from PP pellets, which laid the groundwork for big area AM of PP [Volpato et al., 2015]. However, their work focussed more on the quality of the filament produced using the tech-

nique and did not attempt to use the filament prepared for MatEx purposes. The authors suggested to integrate this approach with AM by minimizing the material degradation and issues associated with flow irregularities in the filaments. Carneiro et al. [Carneiro et al., 2015] was the first to investigate the effects of print parameters (layer thickness, infill, build orientation) on part properties for PP processed via MatEx. However, depending upon the parameters chosen, the mechanical properties suffered by approximately 20-30% compared to compression molded samples. Parts printed with higher layer thicknesses likely resulted in increased coalescence and hence improved mechanical properties. The use of glass fiber improved the mechanical properties of the printed parts while exhibiting minimal warpage.

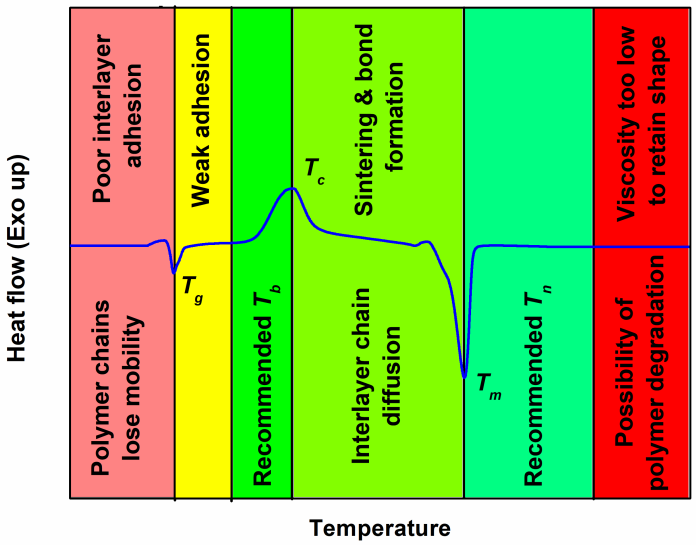


Figure 2.6: Schematic of the recommended processing considerations (nozzle temperature, bed temperature) during melt-based AM of polyolefins based on maximizing the polymer chain diffusion between the layers post-deposition on the print bed.

Jin et al. [Jin et al., 2018] proposed a novel technique to injection mould PP filament rods for MatEx and use the molded rods as a feedstock material for the printer. They studied two different PP grades and found that part warpage increased with increasing crystallinity. They also printed blends of PP and a PP/PE random copolymer to reduce warpage. However, blending significantly decreased the mechanical properties of the parts. In order to counteract the propensity of warpage and low melt strength of PP, Spoerk et al. [Spoerk et al., 2018a]

investigated improving the adhesion of extruded PP to the printer bed by employing a print bed of UHMWPE. Thus, ensuring bed adhesion, they used a PP based random copolymer blended with amorphous polyolefin modifier and perlite filler to address the issues related to interlayer welding and warpage. In addition to the print settings the authors found that increased surface roughness of the printer bed improved wetting and contact area, which improved bed adhesion [Spoerk et al., 2018a].

Jagenteufel et al. [Jagenteufel et al., 2017] performed rheological measurements on high melt strength PP and developed a master curve to describe the time-temperature relationships for applications in MatEx but no attempt was made to evaluate the printed part properties. Bachhar et al. [Bachhar et al., 2020] used a simplified approach to print PP by adding a brim that adheres to the print bed and helps minimize warpage during printing. The experimentally observed warpage measurements closely agreed with FEM simulations of the stresses generated at the interface of the print part and the print bed. Preliminary studies on optimizing the print parameters for MatEx of recycled PP has been performed using Taguchi and ANOVA statistical analyses but these approaches lack the inherent understanding of the process physics and how that translates to print properties [Atsani and Mastrisiswadi, 2020].

The bond formation of PP during MatEx was investigated by performing shear tests on printed parts fabricated using different processing parameters where the print temperature and the temperature of the nth layer were the main factors in controlling the welding strength between the nth and (n+1)th layer [Hertle et al., 2016]. The fracture mechanism associated with pure PP printed thin specimens fabricated using MatEx along with the impact of printing parameters has been recently studied [Lorenzo-Bañuelos et al., 2020]. The results obtained highlighted the importance of raster orientation during printing to produce that are mechanically robust in load bearing applications.

Further work on neat PP revealed that high nozzle temperature, slow print speed, and small layer height improved interfacial chain diffusion, which resulted in parts with properties that were close to injection molded PP [Wang et al., 2018c]. The effect of layer height and print temperature on the impact strength of cellular PP components has been investigated [Wang and Gardner, 2017]. Layer height was found to control the print density, as illustrated in Figure 2.7, by reducing the void fraction in the prints with lower layer heights. On the other hand, the impact strength of the printed part decreased with increases in print temperature due to the formation of a smaller fraction of β-crystals at higher print temperatures [Wang and Gardner, 2017].

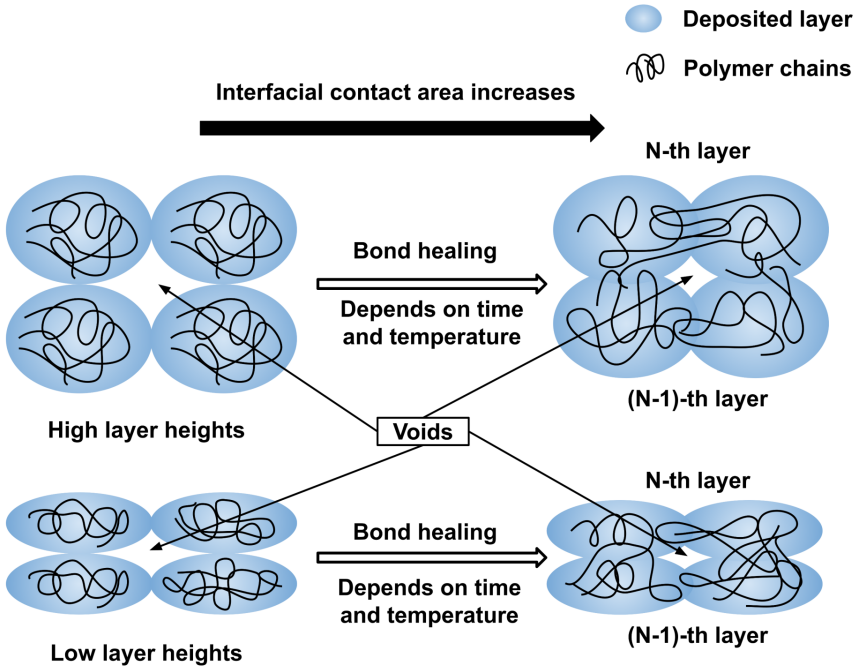


Figure 2.7: Effect of layer thickness on the molecular diffusion and void formation across the layer interfaces. Parts printed with lower layer thicknesses tend to have a higher degree of crystallinity since they are associated with longer print times. As a result, the parts are exposed to the heated print bed for a longer time period which induces an annealing effect and parts with increased crystalline content are obtained.

In the same research, the degree of crystallinity of prints from a commercial PP filament was evaluated as a function of nozzle temperature, print speed, and layer thickness [Wang and Gardner, 2017, Wang et al., 2018c]. The printed samples exhibited peaks corresponding to the β- and β'-crystals ($\sim$45-150°C) in addition to the characteristic α-crystal melting peak ($\sim$165°C) of PP. Wide angle X-ray scattering was employed to characterize the crystalline morphology in the prints; the samples printed at 200°C were found to have increased β-crystal content compared to those printed at 250°C which had more α-crystal content [Wang and Gardner, 2017, Wang et al., 2018c]. The impact strength of the prints improved with increasing β-crystal content, but the tensile properties were found to decrease.

Investigating the crystalline microstructure development in pure PP during the printing process has gained significant interest over the last couple of years. Nogales et al. characterized the morphology and bond formation process during PP printing in an X-ray synchrotron beamline (Figures 2.8a-d) [Nogales et al., 2019]. The authors reported the crystallization

mechanism to be similar to quiescent crystallization and the ability of the chains to inter-diffuse prior to crystallization promoted the formation of strong interlayer welds (Figures 2.8e-g)[Nogales et al., 2019].

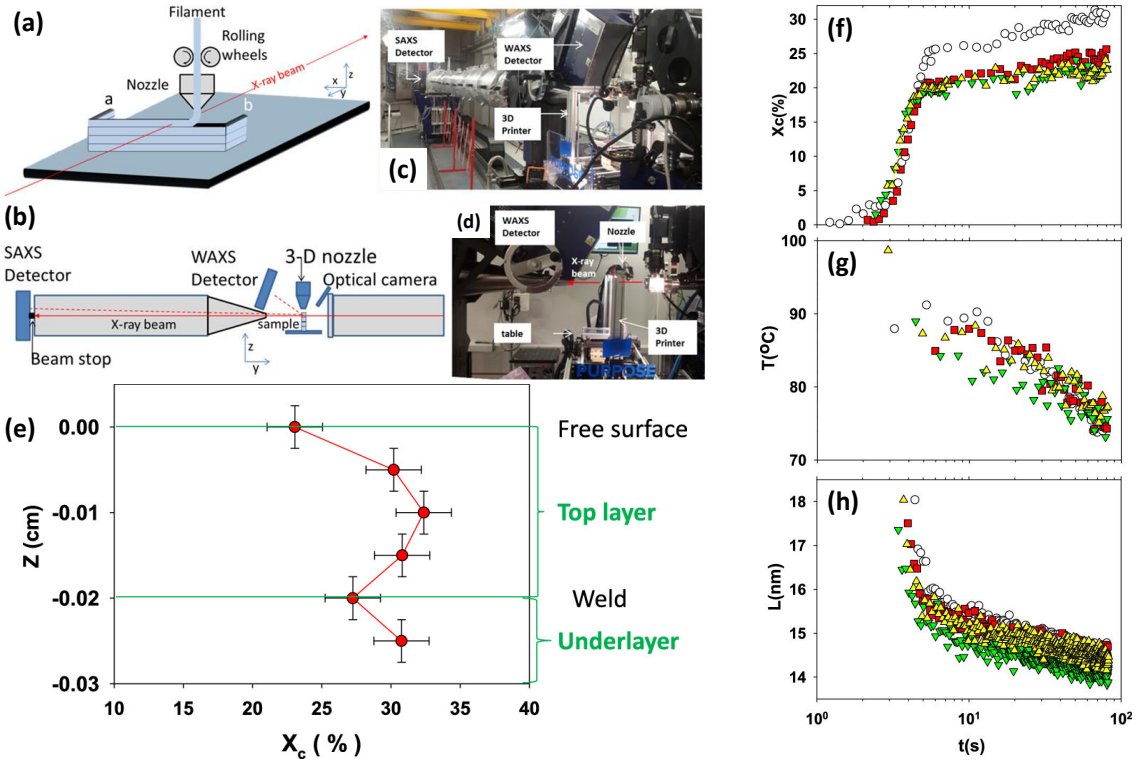


Figure 2.8: (a) Schematic description of the in-situ 3D printing equipment where a sample part is printed through a static printing nozzle on a moveable print bed that can be heated; (b) schematic description of the in-situ X-ray scattering experiments that were performed by placing the aforementioned 3D printed in the path of an X-ray beamline. The scattering intensities during SAXS and WAXS are measured through a photoncounting and a charge-coupled device (CCD) detector, respectively; (c) (d) digital images highlighting the details of the entire experimental setup; (e) variation in the degree of crystallinity across the cross-section of printed layer of isotactic PP; (f-g)Variation in the degree of crystallinity, temperature, and long-spacing of the printed part of isotactic PP post deposition on the heated print bed. The different symbols correspond to the measurements performed at different positions in the top layer of a printed sample: 0.10 cm (black hollow circles), 0.90 cm (red squares), 1.40 cm (green triangles), and 1.90 cm (yellow triangles) from the wall of the printed polymer sample. (images reprinted from [Nogales et al., 2019] with permission from American Chemical Society)

Shmueli et al. [Shmueli et al., 2019a] studied the morphology evolution in weakly semicrystalline PLA by performing in-situ X-ray scattering experiments coupled with infrared imaging during printing and subsequently extended the technique to track the spatio-temporal evolution of the crystalline structure during MatEx of isotactic PP [Shmueli et al., 2019b]. The chains that experienced high shear at the nozzle oriented themselves into shish-kebab morphology post-extrusion through the nozzle, as represented in Figure 2.9 [Shmueli et al., 2019b]. The shish-kebab crystalline domains were found to be strongest towards the filament core but gradually weakened at the interface between filaments, that promoted chain diffusion across the interface [Shmueli et al., 2019b]. The studies from Shmueli et al. and Nogales et al. demonstrate how deposition of a new layer causes partial melting and polymer chain relaxation of the layer beneath it which ensures sufficient interlayer bonding through interfacial chain diffusion [Nogales et al., 2019, Shmueli et al., 2019b]. More recently, Petersmann et al. investigated the effect of print temperature and print speed on the morphology and interlayer weld dynamics of a PP copolymer during MatEx [Petersmann et al., 2020]. It was demonstrated that by tuning the aforementioned parameters, the morphology, chain orientation, type of crystals formed, and crystalline content can be controlled in the printed parts. Printing at the highest temperature (250°C) with the lowest speed (2.25 mm/s) resulted in a uniform morphology with strong interlayer bond formation as evidenced by the results from trouser-tear tests [Petersmann et al., 2020].

2.6.2 MatEx of PP blends with other polymers

Blends of other polymers with PP have also been reported to control the crystallization profile and morphology thereby improving its printability compared to neat PP. For blends of PP and PC processed using MatEx, a fibrillar morphology was reported, which is presumably caused due to the molecular chains orienting themselves under the shearing and stretching forces imparted on the polymer melt by the nozzle on the deposited material [Zhou et al., 2017b]. The development of such in-situ fibrils during printing resulted in improved mechanical properties of the printed parts.

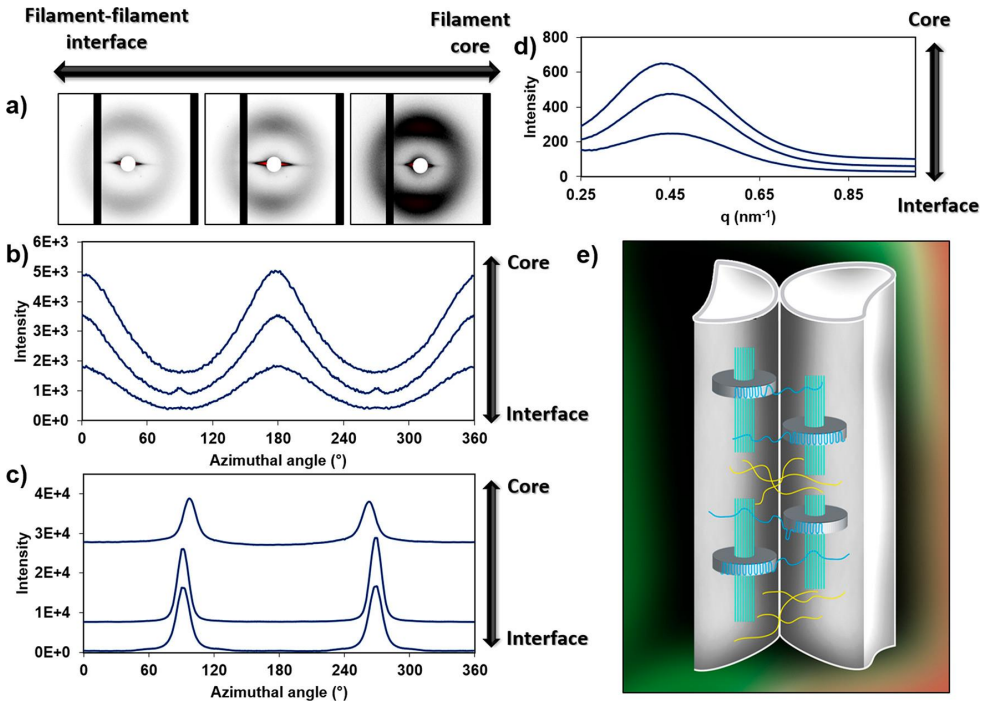


Figure 2.9: (a) Small angle X-ray scattering profiles of isotactic polypropylene as a function of location (from the filament interface to the filament core); (b) azimuthal scan indicating the presence of kebab peak at the different radial locations from the filament interface to the core; (c) azimuthal scan indicating the presence of shish peak at the different radial locations from the filament interface to the core; (d) the integrated 1D plots of the scattering intensity as a function of the scattering vector from the 2D SAXS profiles; (e) schematic of the structural changes at the interfacial region of two filaments, highlighting the aligned shish structures (green), the interdiffusion of the kebab structures (blue), and the reptation of the amorphous tie chains (yellow) (image reprinted from [Shmueli et al., 2019b] with permission from American Chemical Society)

Harris et al. used a maleic anhydride grafted PE as a compatibilizer ABS/PP blends for MatEx processing [Harris et al., 2019]. Using a design of experiment approach, the authors optimized the print temperature (185°C, 195°C, 205°C), bed temperature (25°C, 50°C, 75°C), and post-printing thermal ageing intervals (0, 3, and 6 days) to achieve maximum tensile properties. The tensile strength of the blend was superior to neat ABS and resistant to prolonged thermal exposure. The improved thermo-mechanical performance of the printed blends was attributed to chemical compatibility between the components and localized physical interlocking of the fibers [Harris et al., 2019]. Fly-ash based geopolymer blends containing PP were manufactured using MatEx and the interlayer bond strength and flexu-

ral properties were characterized. The former decreased by 20% whereas the latter increased by 17% upon the incorporation of PP in the geopolymer [Nematollahi et al., 2018].

Blends of PP with polyethylene terephthalate (PET) were investigated as a feedstock material for FFF [Chatham et al., 2019b]. The degree of crystallinity of the printed parts was found to be higher than that of the filament, attributed to the time the polymer chains were above the glass transition temperature of PET and melting temperature of PP. Addition of a compatibilizer enhanced the nucleation process during crystallization through phase separation and prints with higher crystalline content were obtained compared to the neat polymers [Chatham et al., 2019b]. Zander et al. explored the suitability of recycled PP blends with polyethylene terephthalate (PET) and polystyrene (PS) compounded in the presence and absence of a SEBS modifier. Compatibilization using SEBS resulted in improved interlayer bonding during the printing process and the approach provided a solution to reduce and reuse plastic waste as a raw material for 3D printing. However, molecular weight reduction during repeated thermal cycling can lead to poor mechanical properties [Zander et al., 2019a, Chatham et al., 2021].

Banerjee et al. investigated the effect of PP/SEBS blend composition on the printability characteristics using a commercial off the shelf printer [Banerjee et al., 2019]. The interface between the PP and SEBS phases was a point of weakness and resulted in poor mechanical properties in the printed parts compared to injection molded parts. In order to improve the mechanical performance of the 3D printed parts, carbon black was used as a reinforcement and the corresponding printed parts approached 80% of the injection molded properties [Banerjee et al., 2019].

Nylon-6/PP composite filaments have been prepared for FFF employing maleic anhydride-grafted poly(ethylene-octene) (POE-g-MAH) as a compatibilizer [Peng et al., 2019b]. The printed parts from the composite filaments exhibited excellent dimensional accuracy (the amorphous compatibilizer reduced warpage during printing) and mechanical properties (attributed to the presence of nylon-6) while also demonstrating shape memory characteristics. The authors optimized print conditions to maximize the shape memory effects in the printed parts. The study also highlights the potential of such polyolefin-based polymer blends to produce smart, self-deployable structures in an efficient and cost-effective manner [Peng et al., 2019b]. Although further work must be performed to address the trade-off between mechanical performance and shape memory behavior of the printed parts, the research establishes 4D printing of PP blends as a material of choice for manufacturing parts that can be tailored

to fit the application needs.

Beloshenko et al. employed a PP/copolyamide blend for manufacturing filters using MatEx [Beloshenko et al., 2019]. The blend demonstrated decent adhesion to the print bed during deposition as well as excellent interlayer adhesion. The printed filters exhibited very low degrees of warpage and filtered out almost 100% of the particles in the range of 0.3-1 μm [Beloshenko et al., 2019].

Successful printing of PP-based polymers can also be achieved through a combination of process modification and material formulation. Addition of low molecular weight amorphous hydrocarbon resins delays the onset of crystallization of the matrix polymer [Das et al., 2020b]. As a result, the blends retain their molecular mobility for a longer time which is critical in the interlayer bond formation. The strength of the interlayer welds improved due to enhanced interfacial polymer chain diffusion. Post-printing the parts were annealed for 24 hours at 120°C, which resulted in lamellar thickening of the existing spherulites and more than 90% of the properties measured for neat, injection-molded PP parts were achieved. Fitzharris et al. (using semicrystalline polyphenylene sulfide) [Fitzharris et al., 2018] and Hart et al. (using amorphous ABS) [Hart et al., 2018a] also identified post-printing heat treatments to significantly increase the mechanical properties of a printed material.

Jin et al. prepared 3D printable blends using a PP/ethylene random copolymer and amorphous PP to reduce the warpage during printing while maintaining excellent interlayer bonding through careful tuning of the crystallinity, stiffness, and weld strength in the printed parts [Jin et al., 2020]. The authors demonstrated the suitability of the prepared filaments by 3D printing geometrically intricate structures using MatEx. Similar efforts have been made to synthesize novel PP copolymers that exhibit excellent printing performance with negligible warp deformations, but there still remains scope for research in evaluating the printed part properties using these formulations [Spiegel and Paulik, 2020]. Synthetic modifications of the PP backbone through co-polymerization with butene and hexene have been studied to create filament feedstocks for FFF [Spiegel and Paulik, 2020]. The copolymerization process reduced the overall degree of crystallinity (at higher monomer loadings) and resulted in lower amounts of volumetric shrinkage that was essential in successful processing through FFF.

Leng et al. developed a print bed with an array of conical holes to promote part-print bed adhesion and account for the high shrinkage associated with blends of HDPE and PP during MatEx [Leng et al., 2020]. Under the influence of the nozzle-induced shear during extrusion

(controlled through variations in printing speed) and polymer stretch during deposition on the bed, the printed part showed (along the print direction) shish-kebab structure in the PP phase while the HDPE phase formed a epitaxy crystalline structure. The formation of the shish-kebab morphology in the PP was in accordance with previous findings from Shmueli et al. [Shmueli et al., 2019b]. Controlling the morphology in the printed parts as well as the amount of β-crystals in the PP phase were critically important to tailor impact properties of the printed composites [Leng et al., 2020]. Using a similar modified print bed, Jiang et al. successfully printed blends of PP and polystyrene (PS) [Jiang et al., 2019]. As highlighted for the HDPE/PP blends by Leng et al. [Leng et al., 2020], the crystalline morphology evolution was characterized for the PP/PS blends. The PS phase was deformed significantly upon exposure to shear at the nozzle, but the PP phase exhibited the same shish-kebab morphology (Figures 2.10a-c). The extent of fiber orientation and homogeneity increased the printing speed and resulted in printed parts with superior mechanical properties than their compression molded counterparts [Jiang et al., 2019].

Dong et al. studied two different PP grades with different melt flow characteristics and crystallization behavior for MatEx [Dong et al., 2019b]. In an effort to address the warpage issues, the authors investigated the role of different fillers such as wood powder, calcium carbonate nanoparticles and even a PC polymer. The immiscibility in the PP/PC blend made it difficult to process while the other fillers led to undesired agglomeration in the PP matrix. However, blending PP with $CaCO_3$ and a petroleum resin was found to improve the printing performance [Dong et al., 2019b].

2.6.3 MatEx of Filler-reinforced PP composites

An advantage of the MatEx process over PBF is that it can incorporate high levels of filler/fiber reinforcements [Fallon et al., 2019] in a thermoplastic polymer matrix. Optimized reinforced composites can be designed to minimize the effects of nozzle clogging through process simulations and shear forces imparted by the nozzle during extrusion can align the fibers during extrusion [Lewicki et al., 2017]. Incorporating stiff fibers into a printed part impedes contraction of the deposited polymer chains and therefore limits the amount of warpage as long as the fibers are aligned in the direction of the print [Spoerk et al., 2020]. Moreover, thermally conductive fillers such as carbon fiber can increase the overall thermal conductivity of its blends with PP. The increased thermal conductivity helps generate a more

uniform thermal profile inside the part during MatEx reducing the cooling rate experienced by the polymer melt and thus increasing the time window for polymer chain diffusion and entanglements. Therefore, the internal stresses during printing can relax to a greater extent, which allows for dimensionally accurate prints compared to pure PP.

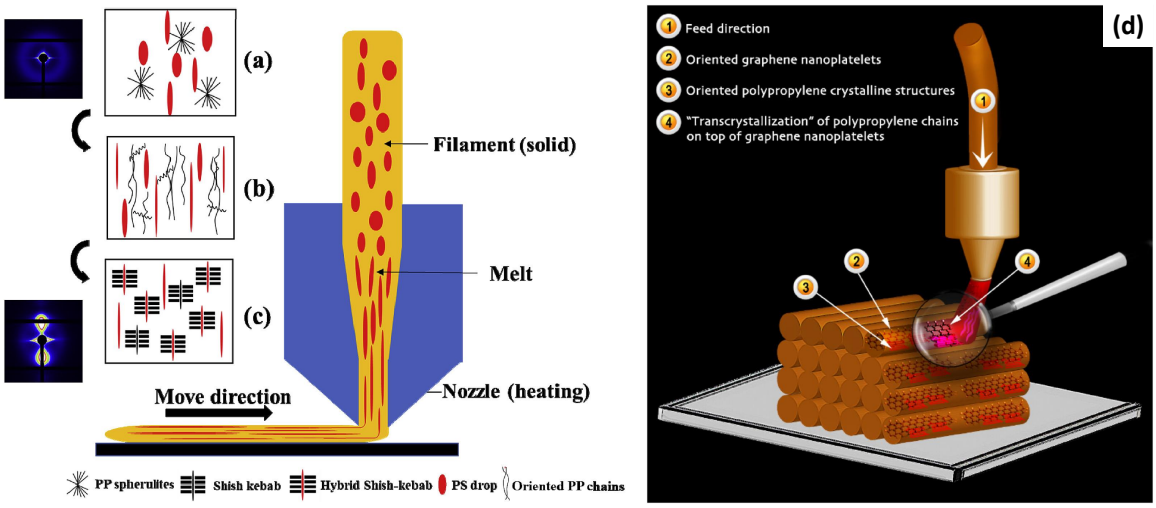


Figure 2.10: Schematic diagram of FFF of PP/PS blends, along with the corresponding SAXS profiles, at three different stages (a) solid filament being fed into the printer nozzle where the shear forces are negligible, and the sample consists of elliptical PS phase and PP spherulites; (b) the extrusion of the filament through a heated nozzle induces a shearing effect where the PS phase undergoes significant deformation and results in formation of microfibers; (c) deposition of the extrudate on the printer bed where a combination of microfibers and shish-kebab morphology is observed. The mechanical performance of the printed parts is dictated by the effects of the crystal structure orientation and PS microfibers (image reprinted from [Jiang et al., 2019] with permission from Elsevier) (d) Schematic description of isotactic PP chains transcrystallizing on top of the oriented GNP lattice. The shear experienced by the PP filament is enough to exfoliate the GNPs. The force required to extrude the composite filament through the nozzle reduces since the viscosity of the material decreases with increasing shear rates. In neat PP, the shear forces resulted in the formation of shish-kebab structure during extrusion through the nozzle (image reprinted from [Shmueli et al., 2020] with permission from Elsevier)

Natural fibers have been employed to produce printed parts with dimensional stability and control shrinkage during printing. Stoof and Pickering investigated the addition of harakeke, hemp fibers, and recycled gypsum to recycled PP [Stoof and Pickering, 2018]. Tensile

strength and modulus of recycled and fiber reinforced PP were found to decrease compared to pure PP upon printing but incorporation of fibers greatly reduced shrinkage by dissipating residual stresses [Stoof and Pickering, 2018, Pickering and Stoof, 2017]. However, the printed parts were porous, which reduced mechanical performance [Milosevic et al., 2017]. Natural fiber reinforced PP presents an interesting case; the fibers allow for better shape retention post-extrusion by improving the rigidity in the melt-state. Further, the strong orientation effects of the fibers addresses the warpage associated with printing PP. But the drawback in using such fiber-reinforced PP for AM, other than the mechanical anisotropy in the printed parts as hihglghted in Figure 2.4, is the requirement of expensive and often toxic coupling agents to promote sufficient adhesion between the polar fibers and the non-polar polyolefin material [Mazzanti et al., 2019].

Long et al. studied the influence of different surface modifications of bamboo fiber filler on the mechanical properties of 3D printed PP/PLA blends [Long et al., 2019]. To improve the compatibility between the polymer matrix and the bamboo fiber, maleated PP was used as a compatibilizer. The chemical treatments of the filler led to formation of surface irregularities and cracks on the fiber surface that resulted in diffusion of the polymer into the filler through capillary action. Finally, the composite filaments were processed using MatEx and parts with negligible warpage were obtained. However, the tensile strength of the prints approached only 65-75% of injection molded properties [Long et al., 2019]. But the approach presents an interesting route to fabricate environmentally friendly and recyclable filaments for MatEx in an economic manner.

Cellulose has been used as a reinforcing agent for recycled PP to improve printed part strength [Zander et al., 2019b]. Cellulose fillers are stiffer than PP matrix, which improved the tensile modulus of the printed parts, but they warped during printing. The feasibility of PP/microcrystalline cellulose (MCC) composites in MatEx was studied by Kaynak et al. [Kaynak et al., 2018]. They concluded that surface modification of cellulose was necessary to reduce fiber agglomeration and retain mechanical properties. The addition of surface modified MCC modified to n-octyltriethoxysilane treated PP resulted in a significant increase in the modulus compared to pure PP. Further, the surface roughness of the printed parts was greatly reduced in the composites [Kaynak et al., 2018].

The effect of spray dried cellulose nanofibrils (CNFs) loading on the non-isothermal crystallization kinetics of its blends with PP was studied [Wang et al., 2018b]. At 10 wt% CNF loading the crystallization rate was found to be slower than pure PP; a direct consequence

of this observation is a longer time window for residual stresses to relax during printing. Retardation of the crystallization rate coupled with reduced CTE values made 10 wt% CNF/PP composite a viable candidate for MatEx [Wang et al., 2018b]. These initial findings were then used to prepare PP/CNF filaments for 3D printing and the rheological properties of the filaments were characterized [Wang et al., 2018a]. Using parallel-plate rheometry, the shear dependent behavior of the blends were probed to translate to the MatEx process. The results indicate enhanced interaction between the filler and the PP matrix along with increased stiffness due to the presence of CNFs in the blends [Wang et al., 2018a].

Based on these two previous works, Wang et al. [Wang et al., 2019a] 3D printed parts using spray dried CNF filled PP blends . Crystallization profiles of the blends suggested the CNFs acted as nucleating agents and those corresponding to the printed samples indicated the presence of three different crystals (β, β', and α). The presence of the β crystals improved the heat deflection temperature (HDT) for the printed samples compared to IM specimens while the presence of voids was held responsible for the higher HDT of the PP/CNF prints compared to PP prints as it arrested the chain mobility of the polymer in the amorphous domains [Wang et al., 2019a]. Sanders et al. characterized the printing and mechanical performance of the CNF reinforced PP samples [Sanders et al., 2020]. Although the CNFs were successful in alleviating residual stresses during printing, which led to dimensionally stable prints, mechanical properties of the printed blends were found to be 30% inferior to pure PP due to void formation and limited interlayer diffusion in the prints [Sanders et al., 2020]. It is worth mentioning that a maleic anhydride PP coupling agent was employed for all the PP/CNFs blends in order to have improved filler-matrix adhesion.

Similar to the studies on metal filled PE compounds, Shahmirzadi et al. [Shahmirzadi et al., 2016] examined the structural and rheological properties of copper filled PP blends for applications in MatEx; but the authors did not print using the prepared feedstocks and only commented on its potential. Kwok et al. [Kwok et al., 2017] investigated conductive PP/carbon black composite for applications in electrical circuits. The printed parts exhibited excellent electrical performance with low resistivity and was also able to withstand different weathering stress tests. However, the adhesion strength of PP based composites was a cause of concern for wider applications.

Following on the work with neat PP [Shmueli et al., 2019b], Shmueli et al. [Shmueli et al., 2020] investigated the microstructure and thermal profile during MatEx of PP/-graphene nanocomposites using a similar in-situ X-ray scattering setup .These composites

shear thinned to a greater extent, which helped facilitate the printing process. Strong orientation effects were reported with trans-crystallization of the PP chains occurring on top of the graphene fillers (Figure 2.10d). The filled samples crystallized much faster than neat PP and the degree of crystallinity was approximately twice of that of PP [Shmueli et al., 2020].

Spoerk et al. [Spoerk et al., 2017, Spoerk et al., 2019b] also studied the shrinkage behavior of PP random copolymers in the presence of fillers of varying size distributions and densities. The inclusion of glass spheres and expanded spherical perlite reduced warpage without significantly affecting mechanical properties. The low aspect ratio fillers distributed uniformly in the matrix and reduced the overall crystallinity. The addition of 30 vol% expanded perlite fillers resulted in a 34% reduction in shrinkage [Spoerk et al., 2017]. The addition of the fillers at higher loadings improves the dimensional accuracy of the printed parts; however, further research must be performed to optimize the ternary blend compositions with amorphous polyolefins in order to achieve parts that have decent mechanical performance as well as dimensional stability.

Subsequent work from the same group aimed at MatEx of PP/short carbon fiber (CF) composites and investigated the effect of fiber orientation on the mechanical and thermal properties of printed parts [Spoerk et al., 2018b]. The composite prepared using PP, processing stabilizer, PP-grafted maleic anhydride compatibilizer, and short CFs displayed homogenous dispersion of the fillers at low loadings and excellent adhesion at the fiber-matrix interface and was easily printed using a commercially available printer. Uniform dispersion of short CFs in PP increased flexural properties compared to neat PP; although incorporation of the CFs increased mechanical anisotropy in the printed parts [Spoerk et al., 2018b]. Spoerk et al. [Spoerk et al., 2019a] developed a PP based heterophasic copolymer functionalized with maleic anhydride and blended it with a coated mineral filler to prepare filaments for 3D printing. Similar to their previous work [Spoerk et al., 2018b], a processing stabilizer was also employed. The printed composite in absence of the heat stabilizer displayed improved interfacial polymer chain diffusion and had an uniform distribution of the mineral filler in the PP matrix [Spoerk et al., 2019a].

Stanciu et al. [Stanciu et al., 2019] tackled warpage by printing carbon nanotube (CNT) reinforced PP. The CNTs improved the heat retention in a part during the print resulting in a more uniform thermal profile (compared to neat PP). This resulted in lower residual stress development and improved interlayer adhesion in the composite parts which resulted in tensile strengths comparable to IM PP. However, nozzle clogging at higher loadings due

to CNT aggregation limited further investigation.

PP reinforced with short glass fiber in the presence of a maleic anhydride polyolefin compatibilizer (POE-g-MA) was also evaluated as a filament feedstock for MatEx [Sodeifian et al., 2019]. The printed samples exhibited increased mechanical strength and interlayer adhesion compared to the compression molded samples. However, the incorporation of an elastomeric modifier counteracted the stiffness imparted by the short glass fibers and hence POE-g-MA was deemed to be a non-ideal coupling agent for the PP based composites studied [Sodeifian et al., 2019]. Veer et al. also employed short glass fiber to investigate the MatEx printed tensile properties of recycled PP feedstocks and found that the properties could approach 85% of virgin unfilled PP [Veer et al., 2017]. Other filler materials used for preparing PP blends for MatEx include kaolinite [Chaka et al., 2017] and organoclay [Aumnate et al., 2019]. For example, Aumnate et al. [Aumnate et al., 2019] probed the thermal, rheological, morphological, and mechanical properties of PP/organoclay composites manufactured using MatEx. The crystallization of the composites was delayed with the addition of the filler and the authors found an optimal loading level for obtaining adequate mechanical properties. However, further research must be performed to better understand the interactions between the filler and PP matrix to design tailored blends that can be printed using MatEx for specific applications.

2.7 MatEx of Polyolefins: Future Directions

MatEx of polyolefins is especially challenging due to their rapid crystallization behavior and subsequent volume contraction, which can cause significant warpage in printed parts. As elucidated in the preceding sections, MatEx can manufacture parts from polyolefins-based compounds with properties comparable to traditionally manufactured parts of the same polymers, as long as certain inherent challenges are addressed through tailored material selection, employing a heated bed and printing inside a heated print environment, and cautious selection of processing parameters.

2.7.1 Print temperature

Specifically, for MatEx, higher nozzle temperature is usually associated with increased interfacial polymer chain mobility and enhanced diffusion by expanding the time window the chains stay above the crystallization temperature (T_c). Such behavior directly translates to improved weld formation across the deposited layers due to an increase in the extent of polymer coalescence and interfacial entanglements. As highlighted in Figure 2.11, the welding between two layers improved with increasing the print temperature form 180°C to 230°C. A microcrystalline morphology of the layers is a strong function of the extrusion temperature. The extent of void formation is also an important aspect during the printing process, as the morphology of the final part is dictated by the interfacial heat transfer through the voids [Hertle et al., 2016].

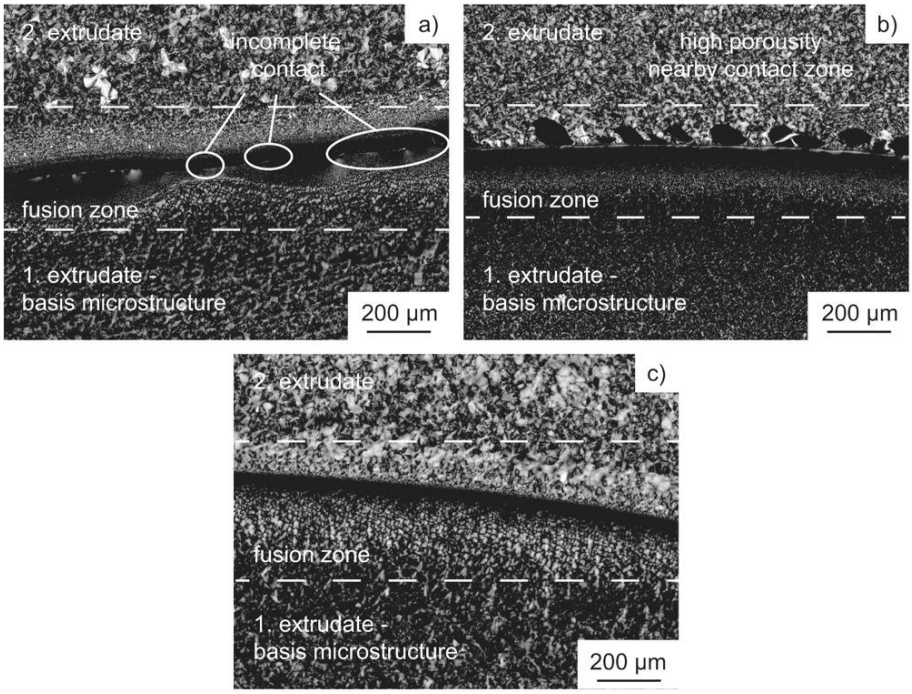


Figure 2.11: Effect of the nozzle temperature on the interlayer morphology of a printed part of polypropylene at constant bed (85°C) and ambient (25°C) temperature. Three different nozzle temperatures are highlighted, namely, (a) 180°C; (b) 210°C; and (c) 230°C (image reprinted from [Hertle et al., 2016] with permission from John Wiley & Sons Ltd.)

2.7.2 Print speed

The extent of polymer diffusion across the layer interface is strongly dependent on time-temperature relationships. Careful tuning of extrusion speed during MatEx can maximize the time spent above T_c to facilitate interfacial diffusion by controlling the thermal history of the deposited layers. Radiative and conductive heat transfer from a new deposited layer can be used to reheat both the preceding and the adjoining layers, which can increase the temperature of the concerned layers above T_c for a few seconds to promote better diffusion and hence improved weld formation. Slower print speeds or increased layer times (time elapsed between the deposition of successive layers) is beneficial for improving the bond quality. Radiative effects from the FFF print nozzle are significant under such conditions results in localized heating of the deposited polymer melt.

The selection of print speed becomes even more critical for semicrystalline polymers like polyolefins since it controls the phenomenon of flow-induced crystallization [McIlroy and Graham, 2018]. The ratio of the polymer relaxation timescale and the timescale of the printing process (referred to as the Deborah number, De) must be close to unity to limit the orientation effects during crystallization which occur post-deposition from the nozzle [Das et al., 2020b]. Therefore, controlling the print speed to ensure sufficient relaxation of the polymer chains is of significant importance, especially for polyolefins.

2.7.3 Layer thickness

Generally, reduction in layer thickness during printing of polyolefins results in reduced part warpage and improved dimensional stability. Printed parts with lower layer thickness also results in better interlayer bonding between the deposited layers [Abbott et al., 2018]. Since lower layer thickness results in printed parts with increased number of layers, the extent of reheating of the previously deposited layers increases which leads to better interlayer adhesion. The issue of poor adhesion between the printer bed and the deposited layers is further aggravated when printing parts containing sharp turns and edges, which is most likely due to the variations in contractile stress distributions. As evident from the discussion above, each printing parameter plays a vital role in dictating the printed part properties and each parameter is intimately related to the others. As such, future studies should aim at investigating their coupled effects rather than analysing their individual effects on

the printing process. Moreover, many aspects of the printing process, which include initial wetting, interlayer weld dynamics, and interfacial solidification have yet to be completely characterized and merit further investigation.

2.7.4 Print orientation

The effect of print orientation on the mechanical properties depends on the kind of bond (intralayer vs. interlayer) that is being tested. The area of contact (and the area across which polymer chains can migrate) for any pair of overlapping filaments is higher for the intralayer boundary compared to the interlayer boundary. Hence, for the same amount of time for interdiffusion it is expected that the intralayer boundary will be more mechanically robust compared to its interlayer counterpart. Furthermore, radiative heat transfer from the print nozzle facilitates intralayer bonding between adjacent layers to a greater extent than interlayer bonding between two successive deposited layers. Therefore, due to increased mobility of the polymer chains, the degree of interdiffusion across the intralayer boundaries is higher.

2.7.5 Accessory heating

Several research studies have investigated approaches to reduce the amount of heat dissipation from a printed layer and increase the time over which the polymer chains retain mobility. Laser assisted heating [Han et al., 2019, Striemann et al., 2020, Sabyrov et al., 2020] of a deposited layer is a common technique to improve the amount of interlayer diffusion above T_g which resulted in significant improvement in weld strength206 and interlayer bond toughness [Deshpande et al., 2019], albeit this technique is sometimes associated with increased surface roughness of a printed part [Sabyrov et al., 2020]. A recent work has also investigated the improvement in interlayer bonding through a time-intensive cold plasma treatment of the interface between deposited layers as an alternative to laser heating [Shih et al., 2019]. Finally, ultrasonic vibrations during printing have been employed to provide external energy and increase the interfacial diffusion rate [Tofangchi et al., 2019, Jiang et al., 2020b]. The improvement in interlayer bonding is lower than the aforementioned approaches; however, since this method only requires an ultrasonic source attached to the nozzle, it is much easier to implement compared to the costly laser or plasma-based techniques. Unfortunately,

most of the validations of the proposed techniques have been performed using amorphous polymers and the viability of extending them to semicrystalline polyolefins still remains a subject of future research.

2.7.6 Toolpath design: Neat vs. filled systems

The toolpath design can also be adjusted to increase the bond strength in 3D printed parts. Typically, printed parts are invariably associated with void formation between the deposited layers (as highlighted in Figure 2.7). Romeijn et al. [Romeijn et al., 2020] printed ABS employing a staggered pattern such that a layer is deposited on the interface of the two layers immediately beneath it in order to reduce the void formation. The proposed pattern resulted in increased surface contact in the interfacial region between the layers and significantly improved the maximum in-plane shear stress. This method appears to be material-agnostic and can easily be extended to improve part strength of printed polyolefins. Reinforcing the polymer with fillers can increase the mechanical robustness of the printed parts but issues such as extent of filler-matrix adhesion, uniformity of filler distribution can hinder the final part properties. Deviation from optimum levels of these variables can lead increased void formation and result in a part that exhibit poor mechanical properties. Utilization of suitable binding agents to improve the filler-matrix interaction can result in parts with reduced void content and enhanced mechanical performance.

2.7.7 Comprehensive material characterization

Another fundamental aspect for polyolefin-based 3D printing that has remained largely overlooked in current literature is the comprehensive rheological analysis of the materials and subsequent physics-based process parameter selection. The shear thinning nature of polyolefins [Wolff et al., 2009] can be exploited to design print nozzles that can minimize annular backflow and filament buckling. Control and monitoring rheological properties such as zero-shear viscosities (η_0) and storage modulus (G') of the polymer melt is of significant importance upon deposition on the print bed in order to ensure proper mechanical and shape integrity of the deposited layers. The importance of shear and/or elongational viscosities and extrudate swell (upon exit from the print nozzle) of the polymers under processing parameters relevant to the printing process must also be investigated.

A major limitation in MatEx of polyolefins is that researchers have been rarely successful when printing neat PE and PP. Most of the work on MatEx of polyolefins either involve blends with a different polymer or study the effect of incorporating additive(s) on the printing process. Also, the commercially available "printable" grade materials invariably contain nucleating agents and processing aides. Slower rates of crystallization can reduce printed part warpage by reducing the development of residual stresses during crystallization. Therefore, developing a framework that can address material and/or machine specific limitations without considerably affecting printed part properties is of utmost importance.

Currently, there is an interest in the production of polyolefin-based commodity polymers through MatEx that are environmentally benign and can be readily biodegraded [Choe et al., 2022]. Future research should be directed towards establishing a reliable method to recycle post-consumer plastics; a path that is fraught with difficulties as reviewed by Vogt et al. [Vogt et al., 2021]. Although the addition of fillers enhances the mechanical performance of the polyolefin printed parts, they are challenging to recycle and can cause issues associated with processing the composites over multiple cycles.

Finally, to optimize MatEx of polyolefins it is necessary to develop a physics-based understanding of each polymer's processing and then employ this understanding to determine appropriate print conditions for each polymer. The focus of most studies in current literature is to investigate the effect of print parameters on print properties (process-structure-property relationships). However, the fundamental polyolefin properties and modifications that can enable successful processing in AM (structure-process-processing relationships) must be investigated.

2.8 Conclusions

In this manuscript, we review the recent progress made in the field of MatEx-based AM processing of polyolefin thermoplastics. In spite of significant advances over the last decade in AM of polyolefins, most of the manufactured parts are largely relegated to prototyping applications. The semicrystalline nature and fast crystallization rates of the polyolefins present a challenge during printing in MatEx because of the shrinkage and residual stress. Commercial feedstocks are invariably chemically modified to assist in processing and ensure reliable printed parts. Neat PE and PP tend to exhibit poor dimensional stability due to

the warpage associated with the crystallization of the polymers during the printing process. Researchers have investigated various strategies to counteract the warping problem, namely synthetic modifications (using polymer blends or co-polymers), employing specific print bed material that promote adhesion, reducing the thermal gradients (through environmental heating) encountered during printing, and incorporating fillers (with different geometries) and/or stiff fibers in order to arrest the shrinkage by ensuring a more uniform thermal profile during AM. However, most of the current studies are limited to empirical studies to evaluate printability and performance of the fabricated parts. We anticipate that developing physics-guided models for this specific class of thermoplastics will enable suitable process parameter selection as a function of the inherent polymer properties and machine design. The extent of interlayer chain diffusion is critical in dictating the printed part performance and strategies to enhance it has been discussed. Finally, characterizing the melt flow behavior of the polymers as they crystallize during the printing process will shed valuable information on the coalescence and interlayer welding dynamics that is crucial in achieving parts with properties compared to that obtained using traditional manufacturing techniques.

Chapter 3

Importance of polymer rheology on material extrusion additive manufacturing: Correlating process physics to print properties

Arit Das[1,2], Eric L. Gilmer[1,2], Saeid Biria[1], and Michael J. Bortner[1,2]

[1]Department of Chemical Engineering, Virginia Polytechnic and State University, Blacksburg, VA 24061, USA

[2]Macromolecules Innovation Institute, Virginia Polytechnic and State University, Blacksburg, VA, 24061, USA

This chapter was originally published in the **ACS Applied Polymer Materials** journal.

ACS Appl. Polym. Mater. 2021, 3, 3, 1218–1249. https://doi.org/10.1021/acsapm.0c01228

Abstract

Recent advances in the field of additive manufacturing (AM) or 3D printing, have garnered serious interest for its potential to substitute time-consuming and costly subtractive and formative manufacturing techniques. Material extrusion (MatEx), employing filament and pellet-based feedstocks, is an AM technique for fabricating three-dimensional objects dictated by a computer-aided design (CAD) file in a layer-by-layer manner. Being inherently a "melt-and-form" technique, the physics of MatEx is strongly dependent on the melt flow behavior of the polymers and hence on their rheology. The focus of this review article is to analyze the current progress in rheological characterizations of filament and pellet-based polymeric feedstocks for application in MatEx. The importance of shear and temperature-dependent viscosities in relation to consistent extrusion through the print nozzle and in the

standoff region between nozzle and bed will be highlighted. The importance of shear and/or extensional viscosities and extent of die swell (upon exit from the nozzle) experienced by the polymers under processing parameters relevant to MatEx will be investigated. Postextrusion from the nozzle, the rheological characteristics of the viscous polymer melt as it cools once deposited on the print bed governs the degree of interlayer welding, that impacts the mechanical performance of the printed parts. Controlling and monitoring rheological properties such as zero-shear viscosities and shear moduli of the melt is of significant importance in this region in order to ensure proper mechanical robustness and shape integrity of the deposited layers. Both experimental and theoretical approaches based on polymer chain reptation mechanisms will be reviewed in detail and suggestions to address the existing limitations associated with the process will be provided. Fundamental understanding of the correlation between the classical theories and current understanding based on recent experimentation and analysis is expected to assist the design and development of the next generation of polymer feedstocks and machine designs for MatEx-based AM.

Keywords: 3D printing; material extrusion; polymer rheology; die swell; interlayer adhesion; polymer diffusion

3.1 Introduction

Additive manufacturing (AM), also referred to as 3D printing, is a relatively recent material processing technique that has the potential to revolutionize the manufacturing market with a rapid prototyping paradigm [Ligon et al., 2017]. There are different AM technologies that can process a wide range of materials including metals [Herzog et al., 2016], ceramics [Deckers et al., 2014], polymers [González-Henríquez et al., 2019], and composites [Parandoush and Lin, 2017]. Despite the relatively recent growth of AM, functional parts produced using this technique have found different industrial applications in the aerospace [Das et al., 2020a], automotive [Leal et al., 2017], and biomedical sectors [Stansbury and Idacavage, 2016] while also being prevalent for producing tools and fixtures for non-load bearing applications [Wu et al., 2020a].

AM offers multiple advantages over conventional manufacturing techniques. The layer-by-layer assembly in AM allows for the manufacturing of complex designs and geometrically intricate parts. Parts with internal voids can easily be manufactured using AM and hence

it has found applications in the production of cellular structures, architectural components, and personal ornaments [Rosen, 2007, Lim et al., 2012, Thompson et al., 2016]. With greater geometric design freedom, the printed parts can be tailored to obtain optimized mechanical properties such as strength and flexibility while reducing the amount of material required and waste produced. Manufacturing parts with similar properties using traditional processing approaches generally involves producing individual portions that are combined together in a post-processing step which makes the processing time labor intensive. Further, AM is an efficient and cost-effective manufacturing method as it overcomes the cost of designing and manufacturing molds for individual parts that is invariably associated with traditional manufacturing techniques such as injection molding.

AM can greatly reduce the production turnaround times since any part design can be directly printed from a computer aided design (CAD) model. Therefore, customized parts can be printed on-site, and on-demand depending on the specific application requirements and deployed immediately. AM can offer multiple benefits to the current production market subject to its extensive implementation. But there are certain inherent challenges associated with AM that limits its widespread application. These include a very limited polymer-based material catalog compatible with AM, high levels of mechanical anisotropy, and poor mechanical properties compared to molded counterparts due to insufficient adhesion between the deposited layers.

Currently there are seven different modes of AM techniques available in the market, namely, material extrusion, material jetting, binder jetting, vat polymerization, powder bed fusion, directed energy deposition, and sheet lamination [Gao et al., 2015]. However, certain AM modalities are either very expensive due to specific machine/equipment requirements (such as, directed energy deposition, material and binder jetting, powder bed fusion) or are limited by their availability (such as, sheet lamination). Polymers are generally processed in AM using powder bed fusion (PBF), vat polymerization, and material extrusion. Vat polymerization often involves the use of toxic chemicals and is unable to process highly filled polymers due to their interference with the curing process; most parts printed using this technique requires a post-processing step. PBF mode of AM is limited by two major factors, namely, the cost of the printers and the production of powder feedstocks with properties required for the process. Hence, material extrusion is a viable route for AM of polymers and is rapidly becoming one of the most prevalent techniques for AM processing. Material extrusion has several advantages compared to PBF and vat polymerization including using

widely available, relatively cheap polymeric feedstocks, low energy demands, easy maintenance, operational flexibility as well as the ability to process highly filled polymeric systems [Gomez-Gras et al., 2018, Ambrosi and Pumera, 2016].

3.2 Material Extrusion: Filament and pellet-fed modes

Material extrusion (MatEx), employing filament and pellet-based feedstocks, is a form of the AM process for rapid prototyping of thermoplastic polymers and it offers many advantages including on-demand tailoring of final part properties, streamlining of traditional methods, and mass customization [McIlroy et al., 2019]. MatEx-based AM includes several techniques such as fused filament fabrication (FFF) and 3D Dispensing including 3D Micro-Extrusion, 3D Plotting, and 3D Fiber Deposition. The FFF process, also known as Fused Deposition Modeling (FDM) when discussed in the context of using a Stratasys printer, is a commonly used and well-established, commercialized method of manufacturing 3D polymer parts by melting a solid thermoplastic filament and depositing successive layers that fuse to a continuous profile. This process involves the extrusion of thermoplastic materials in the form of filaments or solid pellets through a nozzle. During this process, the solid polymer filament is continuously fed into a temperature and pressure-controlled heated deposition unit, generally using two pinch rollers [Peng et al., 2018]. The filament is extruded through the nozzle by heating in the liquefier at a temperature where the thermoplastic filaments transition into their molten state. Upon exiting the nozzle, the extruded filament travels from nozzle tip to bed and dispenses on a movable build platform where the material undergoes solidification to fabricate the final product [Spoerk et al., 2020, Turner et al., 2014]. The deposition process of the filament through the nozzle on the build plate during FFF is shown in Figure 3.1(a). (adapted from Spoerk et al. [Spoerk et al., 2020]). where adjacent filaments merge with each other to build the eventual part in layerwise fashion.

In contrast, pellet-fed MatEx was developed to reduce the processing time and related thermal decomposition that might be associated with filament preparation and subsequent extrusion [Zhou et al., 2018]. The advantage of using pelletized feed is that it does not require any pre-processing steps (such as material compounding and filament preparation) and has led to the development of the paradigm of big area additive manufacturing (BAAM) [Duty et al., 2017]. This technique is particularly useful for AM of thermally unstable polymers and can also be modified to extrude multiple materials; resulting in printed parts with composi-

tional gradients. While a great deal of exploratory research has been performed in BAAM, it is imperative to further study the associated rheology to better understand polymer-based BAAM, which will be significantly different from that encountered in a FFF scale due to the higher thermal gradients, cooling rates, and deposition scales.

Several papers have reported the quality of the bonding of the final part can be impacted by thermal and mechanical effects [Kotlinski, 2014, Osborn et al., 2015, Sheth et al., 2017] including thermal conductivity lower than the thermal conductivity of filament material, lower strength, modulus, toughness, and strong anisotropy due to incomplete merging and significant thermal contact resistance between layers in the build plane or the build direction [Prajapati et al., 2019]. Therefore, it is important to understand the dependence of the final part on heat transfer and mechanical behavior to optimize and improve these properties and build desired parts. This can be achieved through a holistic analysis of the rheological properties of the entangled viscoelastic polymer melts and taking into account the complex multiphysics associated with MatEx. Such an analysis will allow researchers to bridge the gap between printing parameters and final part performance.

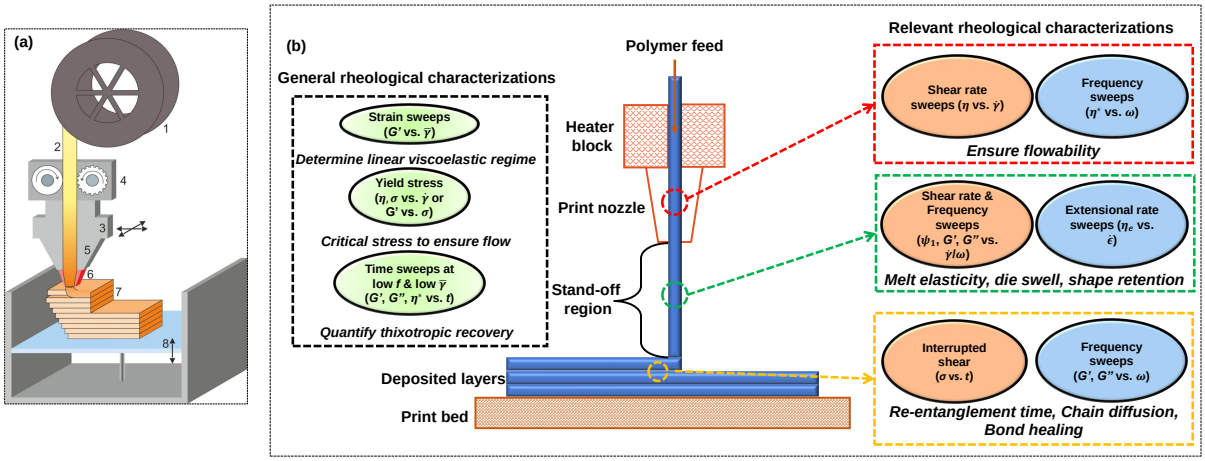


Figure 3.1: (a) Schematic of the overall FFF process. 1) filament spool, 2) thermoplastic materials. 3) heated barrel consisting of 4) pinch rollers, 5) liquefier, 6) nozzle, 7) layer-by-layer deposited materials, and 8) movable build plate (image reprinted from [Spoerk et al., 2020] under the Creative Commons Attribution License, CC BY 4.0 Copyright 2019 Spoerk et al. Journal of Applied Polymer Science published by Wiley Periodicals, Inc.); (b) Overview of the rheological measurements needed to be performed as well as the relevant datasets to be analyzed in order to describe the behavior of the polymer melt during different stages of the MatEx process.

In this review paper, we highlight the contemporary progress in rheological characterization of polymeric feedstocks for application in filament and pellet-fed MatEx based AM processes. The manuscript will focus on the application of rheological measurements in understanding the critical physics and implications on all aspects of the process beginning with nozzle flow, through the standoff region, and finally with deposition on the print bed. Collectively, this manuscript provides advanced rheological insights into AM by bridging the gap among the multiphysics associated with the process, the processing variables, and resulting print properties. We discuss the rationale behind studying the rheology of the polymers in the next section followed by detailed analysis of the rheological implications during the MatEx process. Finally, we highlight existing research gaps and provide future recommendations to address the relevant challenges that will lead to the design and development of the next generation of polymer feedstocks and machine capabilities that are compatible with MatEx based AM.

3.3 Why Rheology?

All polymers that are used in AM invariably exhibit viscoelastic behaviors, i.e., they are either shear-thinning or shear thickening or yield stress fluids. The successful realization of a MatEx process in terms of polymer printability and quality control of the printed part is heavily influenced by the rheology of the concerned polymeric material. However, a subtle trade-off is often required since material properties that aid printability (for example, reduced viscosity of the polymer melt during extrusion through the nozzle [Gilmer et al., 2018, Costakis et al., 2016, Ajinjeru et al., 2017]) are frequently in direct conflict with the properties necessary for a printed part with adequate mechanical integrity and robustness [Zaldivar et al., 2018]. Current approaches in MatEx of polymers are largely based on a time, cost and material-intensive "trial and error" methodology with printed parts often lacking the requisite mechanical properties and dimensional precision [Gilmer et al., 2019]. Further, most of the contemporary rheological approaches reported in literature focus on a single aspect of the printing process (e.g., extrusion through the nozzle or welding between deposited layers on the print bed). Table 3.1 relates the type of responses associated with the printing process (along with the important processing parameters employed during MatEx) to the relevant rheological properties and their implications at each stage of the process.

Table 3.1: Correlating processing parameters in MatEx with the impact they have on printed part properties along with the necessary rheological characterizations needed to understand the effect of material and processing conditions on final part properties.

Type of responses	**Material or process dependent**	**Controlling parameters**	**Rheological measurements**	**Comments**
Viscoelastic behavior	Dependent on material properties	Strain amplitude, process temperature	Strain sweeps (determining the linear viscoelastic regime)	performed at constant frequency and temperature
Time-temperature behavior	Dependent on material properties	Frequency, temperature	Frequency sweeps (measure of the relaxation timescales)	performed at constant strain at multiple temperatures
Flow in the nozzle	Dependent on the extrusion process (nozzle design and operation)	Print temperature, shear rate (print speed)	Shear rate sweeps & SAOS (shear-thinning behavior)	generally performed using parallel plate geometry
Extrudability	Dependent on the extrusion process (nozzle design and operation)	Temperature, shear rate, and shear stress	Shear stress sweeps (yield stress)	need to watch out for edge fracture during measurements
Extrudate shape	Dependent on the extrusion process (nozzle design and operation)	Extrudate temperature, normal stress, and normal stress coefficient	Extensional viscosity (elastic vs. viscous response) Frequency sweeps (relative magnitudes of G' & G")	performed using extensional fixtures or Cogswell method; affects dimensional accuracy of prints

Table 3.1 – continued from previous page

Type of responses	**Material or process dependent**	**Controlling parameters**	**Rheological measurements**	**Comments**
Shape recovery post-extrusion	Dependent on the entire printing process (includes dynamics in the nozzle, stand-off region, and print bed)	Extrudate temperature, time (feed speed and print speed)	Time sweeps (thixotropic recovery) Three-interval thixotropy tests (3ITT)	performed at low strain and low frequency
Stability of deposited layers	Dependent on the entire printing process (includes dynamics inside the nozzle, stand-off region, and print bed)	Extrudate temperature, time above T_g	Isothermal frequency and shear sweeps (crossover between G' and G")	G' $<$ G" ensures chain mobility; G' $>$ G" and high η_0 values ensure stability
Interlayer weld formation and chain diffusion	Dependent on the entire printing process (includes dynamics inside the nozzle, stand-off region, and print bed)	Localized temperature (depends on bed & environment temp.), time above T_g	Interrupted shear measurements (re-entanglement times)	quantify the print properties with respect to the bulk properties

Table 3.1 – continued from previous page

Type of responses	**Material or process dependent**	**Controlling parameters**	**Rheological measurements**	**Comments**
Interlayer adhesion	Dependent on the entire printing process (includes dynamics inside the nozzle, stand-off region, and print bed)	Time window for welding & polymer's characteristic timescales	TTS and stress relaxation	time required for the modulus to drop below the Dahlquist's criteria
Bond healing in printed parts	Dependent on the entire printing process (includes dynamics in the nozzle, stand-off region, and print bed)	Localized temperature & polymer relaxation times	Temperature ramp (viscosities at different temperatures)	guideline for post-processing parameters

The current polymer catalog for MatEx is almost completely dominated by either amorphous polymers like acrylonitrile butadiene styrene (ABS) or polymers with a very low degree of crystallinity like polylactic acid (PLA). Semicrystalline polymers such as polypropylene (PP) or polyether ether ketone (PEEK) undergo rapid crystallization from the melt and the crystallites, though acting as physical crosslinks, hinder the interfacial chain diffusion across the deposited layers resulting in parts with poor interlayer adhesion [Das et al., 2020b, Ding et al., 2019]. The large degrees of volumetric contraction experienced by such polymers during crystallization lead to entrapment of high levels of residual stresses within the printed

part that lead to warpage and shrinkage. However, the changes in volume and subsequent stress development are not associated with the rheology of the polymer melt. During extrusion through the nozzle, the viscosity of the polymers reduces drastically such that shape retention in the stand-off region and on the print bed is significantly affected; while during solidification on the print bed the viscosity increases considerably compared to amorphous polymers. These fluctuations in the melt viscosity during MatEx is the additional rheological effect that needs to be accounted for semicrystalline polymers.

Irrespective of being amorphous or semicrystalline, the question of "What makes a polymer printable?" has long been a concern of researchers. The field of traditional manufacturing possesses an extensive material catalog, but MatEx is severely limited because of a lack of answers to this question. Duty et al. [Duty et al., 2018] recently stated that a material is printable if it meets four criteria: i) must be able to be extruded out of a nozzle, ii) extruded material must hold its shape, iii) extruded material must be able to bridge a gap of a specific length, and iv) the extruded material must remain geometrically stable as the material cools to room temperature. Zawaski, et al. [Zawaski et al., 2019] and Chatham et al. [Chatham et al., 2019b] suggested similar requirements for "printability," although these researchers focused on deposition of the material, i.e. maintaining geometric accuracy, ability to produce small features, and gap bridging, with the assumption that any printable material will also be extrudable. All the aforementioned criteria are directly controlled by the polymers' rheological properties and therefore tailoring the polymer feedstocks through physical and/or chemical modifications to ensure appropriate rheological performance is essential for successfully producing desired part geometry and performance in any extrusion based 3D printing process. Further, optimization of the printing parameters and developing a better understanding of the processing-property relationships can only be achieved through a comprehensive study of the thermo-rheological characteristics of the feedstocks employed in MatEx. The main objective behind such studies is to establish a relationship between the inherent material properties and 3D printability; such thorough investigations are not only limited to MatEx but can easily be extended to other polymer based AM techniques such as PBF.

3.4 Importance of polymer rheology in material extrusion based AM

As mentioned previously, the scope of the current manuscript focuses on filament and pellet-fed modalities of MatEx. For such a printing process, careful control and monitoring of rheological properties are of paramount importance in order to ensure easy extrusion of the melt through the nozzle. Subsequently, the shape and integrity of the extrudate in the stand-off region between the nozzle exit and print bed as well as the solidification/welding of the deposited extrudate through interlayer polymer chain diffusion are both strongly correlated with the rheological characteristics associated with specified processing parameters. Figure 3.1(b) provides a brief overview of the key rheological measurements that are necessary for characterizing the behavior of the polymer melt during MatEx. It is worth mentioning that the measurements highlighted in Fig. 3.1(b) are by no means comprehensive and specific details regarding each stage of MatEx will be discussed in the following sections. The aim of the subsequent analysis presented in the paper is to highlight the importance of rheological properties of the polymer melt during the different stages of a typical MatEx process.

3.5 Dynamics inside the print nozzle

3.5.1 Effect of printing parameters on shear rates

Designing new polymer formulations is often complicated due to the limited information about the temperature- and shear-dependent viscosities. Generally, such characterizations are performed using time and cost intensive experiments where most of polymer chain dynamics during processing are not captured. A commonly used empirical screening technique is to compare the viscosity of the formulation with that of a printable material. This results in huge amounts of material wastage and often leads to discarding formulations that could have been printable by tuning the process parameters.

As evident from the above discussion, a primary consideration that must be accounted for in MatEx is the flow behavior of the polymer, specifically the viscosity, and how it changes based on the parameters of the process. Since viscosity (η) is a function of shear rate as well as temperature, it can be represented by Equation 3.1 [Karis et al., 1996, Bird et al.,

1987, Dealy and Plazek, 2009]

$$\eta\left(T_{\text{ref}}, \dot{\gamma}\right) = \frac{1}{a_T(T)}\eta\left(\dot{\gamma}a_T, T\right) \tag{3.1}$$

where, $a_T(T)$ is a temperature dependent horizontal shift factor that can be calculated using Equations 3.2 or 3.3, $\dot{\gamma}$ is the applied shear rate, T is the temperature of interest (in Kelvin) and T_{ref} is the reference temperature (in Kelvin) at which the shift factor is equal to unity. The dependence of viscosity on temperature can be expressed in terms of the shift factor (a_T) as follows:

$$a_T(T) = \exp\left[\frac{E_a}{R}\left(\frac{1}{T} - \frac{1}{T_{ref}}\right)\right] \tag{3.2}$$

$$a_T(T) = \exp\left[\frac{-c_1\left(T - T_{ref}\right)}{c_2 + \left(T - T_{ref}\right)}\right] \tag{3.3}$$

where, E_a is the activation energy for flow, R is the universal gas constant, while c_1 and c_2 are empirical constants. Equation 3.2, based on classical Arrhenius relationship, is valid at temperature ranges that are at least 100 K higher than T_g and works well for shifting viscosity data for linear polymers [Dealy and Plazek, 2009]. For temperatures in proximity to T_g, the Williams-Landel-Ferry (WLF) equation (Equation 3.3), based on Doolittle's relative free volume approach, is used to describe the shift factor [Ferry, 1980].

Therefore, as is evident from Equations 3.1-3.3, any time when T is not equal to the reference temperature, the temperature dependence becomes potentially important. This issue is not a concern in the nozzle when the system is operating at a quasi-steady state, where the heat supplied by the cartridge heater is sufficient to maintain a nearly isothermal temperature of the molten pool. However, with any change in the polymer flow, primarily due to lack of controlled filament feed rate, the conditions will change since inherently the MatEx process is associated with repeated non-uniform thermal history [Ferraris et al., 2019, Luo, 2020, D'Amico and Peterson, 2018, D'Amico and Peterson, 2020]. Moreover, due to the low thermal conductivities of the polymer, significant thermal gradients can be developed both in the axial and radial directions [Peng et al., 2019a]. An increase in the filament velocity will prevent the pool from attaining the isothermal behavior and will cause the local temperature of the polymer to decrease which, in turn, will cause the local viscosity to increase. This

could cause a buckling failure in the system due to a sudden increase of the pressure required to extrude the molten polymer or a backflow failure due to a change in the shear thinning behavior. Increased shear thinning behavior of the polymers assists in MatEx based printing by reducing the pressure required to extrude the material [Gilmer et al., 2018]. Consistent values of storage modulus (G'), loss modulus (G"), and complex viscosity ($\eta*$) within the MatEx processing window are desirable for ensuring a uniform rheological response, that is advantageous for controlling the melt flow behavior during printing [O'Mahony et al., 2020].

Measurement of the viscosity of polymeric materials is often performed on a capillary rheometer [Reynolds et al., 2018, Lewandowski et al., 2016, Peres et al., 2016, Bortner et al., 2004]. This instrument is particularly useful to examine materials for extrusion-based AM because it closely mimics the FFF system, i.e., a solid piston extrudes a molten pool of polymer through a narrow opening. Furthermore, this instrument can reliably measure the apparent viscosity of polymers at similar shear rates to those observed in FFF printing, $\dot{\gamma}$ greater than 100 s^{-1} and with significantly higher strain than can typically be accurately captured by torsional rheometry. If shear rates less than 100 s^{-1} are required, rotational steady and dynamic shear rheometry (small amplitude oscillatory shear, SAOS) may be performed with parallel plate or cone-and-plate geometries and related to the viscosity measured in the capillary rheometer through the Cox-Merz rule [Cox and Merz, 1958, Cox and Merz, 1959], assuming the appropriate corrections (Weissenberg-Rabinowitsch and Bagley) have been applied to the capillary rheometry measurements [Filip et al., 2020]. Figure 3.2(a) provides an overview of the viscosity (and/or complex viscosity) dependence on shear-rate (and/or frequency) over a range that is usually probed for MatEx along with the kind of rheometry employed to obtain the data. The shear rate profile inside the nozzle and the extrudate during MatEx of PLA has been simulated and highlighted in Figure 3.2(b). A maximum shear rate of 1600 s^{-1} was observed at the nozzle wall and the viscosity decreased by an order of magnitude from the center of the liquefier to the wall due to the shear-thinning nature of PLA [Bakrani Balani et al., 2019]. Excellent agreement between the numerical predictions and analytical studies was reported.

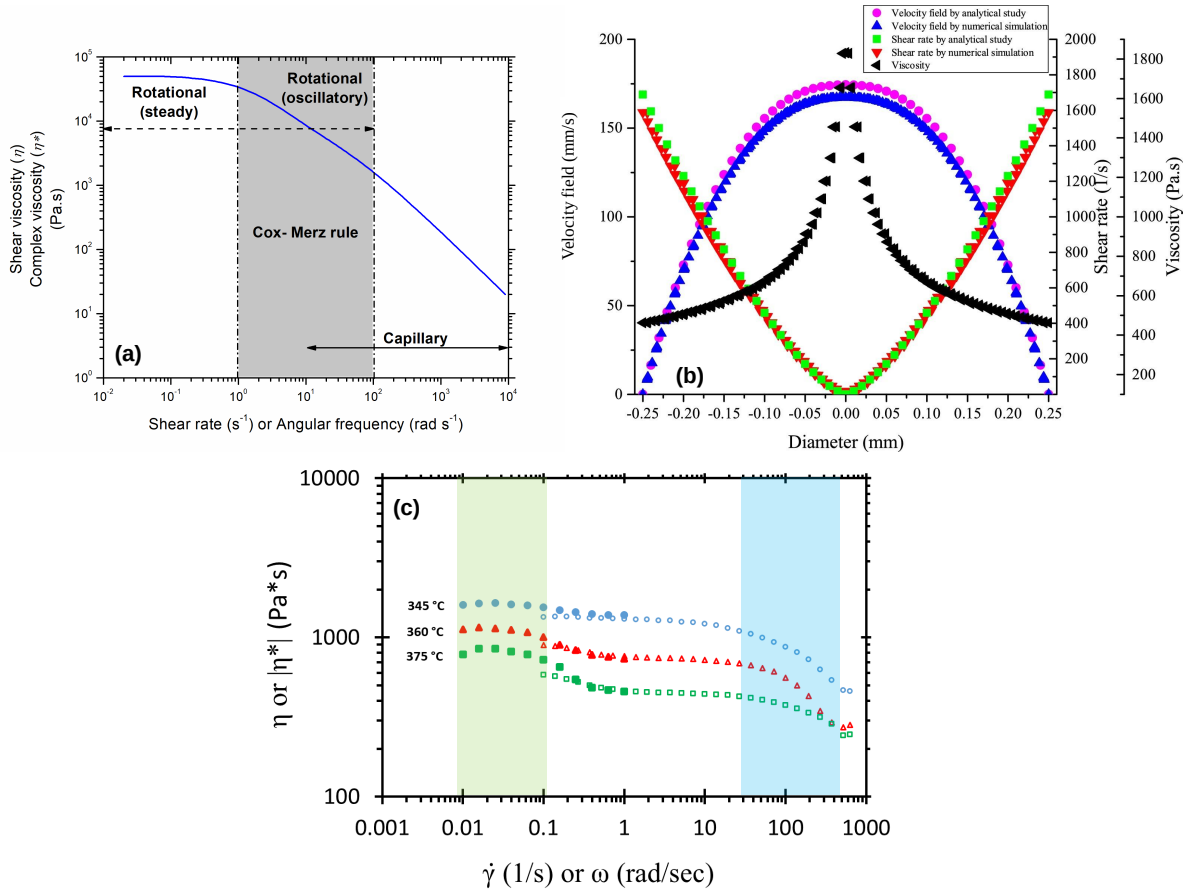


Figure 3.2: (a) Representative plot of the viscosity (or complex viscosity) as a function of shear rate (or frequency) for MatEx based processing. The different rheological techniques typically used to obtain such data are highlighted in the figure. The overlap between the steady and SAOS measurements from a rotational rheometer can usually be described by Cox-Merz's rule for pure polymers; (b) Numerical simulation and analytical results illustrating the inlet velocity field, shear rate distribution, and viscosity inside the liquefier for a 0.5mm nozzle (image reprinted from [Bakrani Balani et al., 2019] with permission from Elsevier); and (c) Overlay of small amplitude oscillatory shear (hollow shapes) and steady torsional shear (filled shapes) rheometry of Ultem 1010 at 345°C (circles), 360°C (triangles), and 375°C (squares). The blue and green boxes highlight the viscosity values associated with the extrusion through the print nozzle and the bond consolidation process upon deposition on the print bed, respectively (image reprinted with permission from [Gilmer et al., 2019] Copyright 2019 American Chemical Society).

Figure 3.2(c) illustrates the overlay of the data obtained from SAOS and steady flow experiments using a rotational rheometer for polyether imide (Ultem 1010) at different temperatures. Cicala et al. [Cicala et al., 2018] performed both rotational and capillary measurements on two different PLA (green and black) to characterize their shear-thinning behavior at the printing temperatures. The results from the SAOS tests in the low frequency range, revealed that green PLA had minimal elastic effects while the black samples had a more solid-like response, most likely due to the presence of additives. Similar overlay of steady flow and SAOS measurements were performed on pure and drug-loaded polycaprolactone (PCL) samples; Cox-Merz rule did not hold for the samples with high filler content since the molecular architecture of the polymer was compromised but MatEx of up to 50 wt% filler loaded PCL was successful while the high viscosity due to the addition of 70 wt% filler rendered it unprintable [Aho et al., 2019].

3.5.2 Failure modes inside the nozzle

Valkanaers, et al. identified three common potential failure modes that occur inside the FFF nozzle/liquefier: inconsistent filament diameter, filament buckling, and annular backflow, Figure 3.3(a) [Valkenaers et al., 2013, Gilmer et al., 2018]. Most computational models assume that a filament's diameter is consistent at all points, and this is substantiated through process control. In general, most commercially developed filaments possess a deviation less than $\pm$ 0.1 mm, much less than what is required to cause failure inside the nozzle. Because this is controlled through the production process, it has not been studied or modeled. Filament buckling and annular backflow, on the other hand, both depend on material properties and process parameters, suggesting further study of these phenomena is vitally important to increasing the understanding of the FFF process. A discussion of the current research exploring these phenomena and the viscosity that drives them both is presented below.

3.5.3 Pressure build-up and filament buckling

Filament buckling becomes an issue when the filament is not thick enough or stiff enough to withstand the forces required to expel the molten polymer through the nozzle [Turner and Gold, 2015]. The pressure experienced by the polymer inside the nozzle is approximately 30 MPa which is comparable to that experienced during traditional polymer processing

techniques such as blow molding and injection molding [Mackay, 2018]. The pressure built-up is a strongly dependent on the viscosity as well as the shear rate associated with the printing process. This dependence highlights the importance of measuring and analyzing the rheological properties under MatEx relevant conditions in order to successfully tackle issues caused due to filament buckling. However, it is worth mentioning that while pressure build-up and subsequent buckling presents a significant problem in filament-fed extrusion systems, the use of pellet-fed systems alleviates this issue entirely.

A method was developed to predict the potential for a polymer to buckle by calculating the critical buckling stress with Euler's analysis for pin ended boundary condition and comparing this to the pressure required to extrude the molten material, Equations 3.4 and 3.5, respectively [Beer and Johnston, 1992, Venkataraman et al., 2000].

$$\sigma_{cr} = \frac{\pi^2 E}{4\left(L/R_f\right)^2} \tag{3.4}$$

$$\Delta P = \frac{8\eta_a Q l}{\pi r^4} \tag{3.5}$$

In the above equations, σ_{cr} is the critical buckling stress, E is the elastic modulus, L is the length of the column from the top of the liquefier to the rollers, R_f is the radius of the filament, ΔP is the pressure difference measured in a capillary rheometer, η_a is the apparent viscosity, Q is the volumetric flow rate, l is the length of the capillary, and r is the radius of the capillary.

The pressure required to extrude the material, which is a function of the viscosity, should not exceed the critical buckling stress. Because it is difficult to measure the pressure in-situ, Venkataraman, et al. [Venkataraman et al., 2000] developed a method to relate the pressure measured in a capillary rheometer to the pressure inside the FFF nozzle. A material that requires a higher pressure to extrude in the capillary rheometer should exhibit similar behavior in the heated nozzle, for a fixed nozzle and liquefier geometry and volumetric flow rate. Since the systems are not perfectly identical, i.e. the capillary and nozzle possess different L/D values, and the liquefier and barrel are not the same diameter, the pressures and viscosities will not be equal at equivalent volumetric flow rates. To account for this, a scaling factor, k, was identified to relate the pressure measured in the capillary rheometer, ΔP, to that which the material would experience in the FFF nozzle, ΔP', shown in Equation

3.6 [Venkataraman et al., 2000].

$$\Delta P = k\Delta P' \tag{3.6}$$

The filament should buckle when the extrusion pressure exceeds the critical buckling stress, Equation 3.7, leading to the final relationship, shown in Equation 3.8.

$$\Delta P' > \sigma_{cr} \quad \text{or} \quad \Delta P/k > \sigma_{cr} \tag{3.7}$$

$$\frac{E}{\eta_a} < \frac{8Q\left(\frac{L}{R_f}\right)^2}{\pi^3 r^4 k} \tag{3.8}$$

In this equation, k is a scaling factor that allows the pressure measured in the capillary rheometer to apply in the FFF liquefier. Figure 3.3(b) illustrates the variation in the ratio of elastic modulus to apparent viscosity as a function of shear rate for three different polymers. The authors predicted that LDPE and NaSPEG filaments will buckle and backflow; a claim that was experimentally validated as highlighted in Figure 3.3(c). Recent studies performed by Coogan and Kazmer and Anderegg, et al. have shown that it is possible to measure the pressure inside the FFF nozzle with modified designs, although the two studies do not completely agree with each other regarding the potential accuracy of utilizing this method to calculate the viscosity of the material during printing [Coogan and Kazmer, 2019, Anderegg et al., 2019].

Venkataraman et al. [Venkataraman et al., 2000] tested multiple materials in a 508 μm nozzle and discovered that the critical value for most polymers lies in the E/η_a range of 3 x 10^5 to 5 x 10^5 s^{-1}. The materials they tested that exceeded this range printed without buckling, while materials that fell short of this range buckled during the extrusion process. This work was performed without changing nozzle geometry, nozzle temperature, or other system parameters, but proved that the buckling potential of the materials could be predicted with a mathematical model with minimal measurements performed outside the printer.

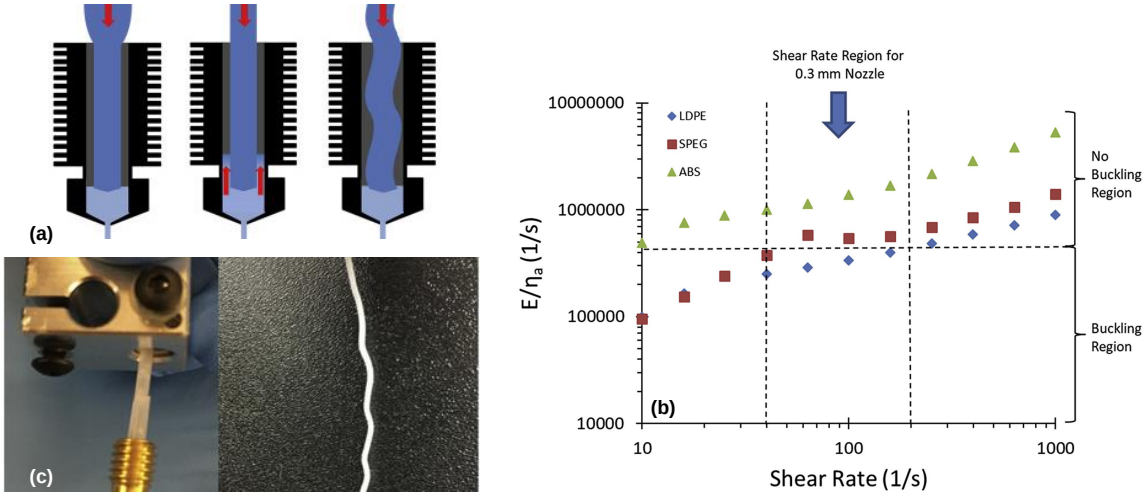


Figure 3.3: (a) Depictions of the common failure modes inside the FFF nozzle. From left to right: inconsistent filament diameter, annular backflow, and filament buckling; (b) A typical buckling analysis performed on low density polyethylene (LDPE), ABS, and sodium sulfonated polyethylene glycol (NaSPEG) based on Equation 3.8. The shear rates within the vertical dotted lines represent the rates experienced during a typical printing process employing a 0.3mm nozzle. The horizontal dotted line separates the data points corresponding to which the polymer feedstock experiences buckling; and (c) Visual representation of annular backflow (left) and filament buckling (right) observed during extrusion of NaSPEG and LDPE, respectively, through the print nozzle (all the images are reprinted from [Gilmer et al., 2018] with permission from Elsevier).

3.5.4 Fluid flow analysis inside the heated nozzle

Most work examining the fluid flow inside the nozzle has assumed that the filament diameter is equal to the nozzle diameter and immediately transitions from solid filament to molten polymer, removing the possibility of flow in the annular region between the filament and nozzle wall. This allowed researchers to model the thermal, velocity, and pressure profiles based on purely fluid flow inside the nozzle, similar to the flow within a cylindrical pipe [Mostafa et al., 2009, Ramanath et al., 2007]. Table 3.2 provides a summary of the recent research trends in modeling the polymer melt flow inside the heated nozzle prior to extrusion. Ramanath et al. [Ramanath et al., 2008] showed a slow transition to an isothermal state, which would greatly affect the viscosity and, by extension, the fluid flow. Nikzad et al.

[Mostafa et al., 2009] showed a system that reached the isothermal state very quickly, most likely due to different material properties such as heat capacity. However, these two groups focused primarily on the nozzle exit (i.e., not the nozzle entrance) and did not consider backflow to be a possibility.

Table 3.2: Brief summary of the recent research on the fluid flow analysis inside the heated nozzle of a typical desktop MatEx 3D printer. The polymer material experimentally studied to verify model predictions, the dimensionality of the model, the software employed, and the key findings from each study is highlighted

Study	**Material**	**Modeling granularity and software**	**Focus of the study**	**Additional comments**
[Phan et al., 2020]	PLA	2D FVM and FEM in Ansys Fluent and Ansys Polyflow, respectively	Melting behavior in FFF was simulated and validated experimentally	Model predicts complete melting of the polymer before reaching the printer nozzle
[Pigeonneau et al., 2020]	Polycarbonate & ABS	2D FEM in Rheolef C++ library	Numerical flow modeling of a polymer inside the liquefier	Model fails to account for polymer viscoelasticity
[Serdeczny et al., 2020a]	ABS	2D Volume of fluid (VOF) in FLOW-3D	CFD simulation of the polymer flow in the hot-end of a FFF printer	Extrusion becomes unstable at filament feeding rates higher than a critical limit
[Agassant et al., 2019]	ABS	3D FEM in CIMLIB-CFD	Simulation of the melting and spreading behavior of a polymer melt	Model is only valid for Newtonian fluids under isothermal conditions

Table 3.2 – continued from previous page

Study	Material	Modeling granularity and software	Focus of the study	Additional comments
[Bakrani Balani et al., 2019]	PLA	2D FEM with twophase flow in COMSOL	Numerical and analytical solutions of the velocity field, shear rate, and viscosity inside the nozzle	Extrudate morphology is strongly dependent on the shear rate inside the nozzle
[Heller et al., 2019]	ABS/CF composite	2D FEM in MATLAB	Computational study on the effect of nozzle design on the fiber alignment	Model is limited to Newtonian fluids under isothermal conditions
[Comminal et al., 2018a]	PLA	3D VOF in OpenFOAM	Model describes extrudate swell in pseudoplastic fluids	Model predicts shear thinning reduces die swell
[Phan et al., 2018]	PLA	Analytical	Quantify the flow and heat transfer effects during printing	Fouling of the nozzle appreciably limits the heat transfer
[Serdeczny et al., 2018a]	PLA	3D FEM in ANSYS Fluent	Shape of extrudate postextrusion from the nozzle is studied	Model valid for constant viscosity fluids under isothermal conditions

Table 3.2 – continued from previous page

Study	Material	Modeling granularity and software	Focus of the study	Additional comments
[Osswald et al., 2018]	ABS	Analytical	Melting behavior inside the nozzle is analytically described and experimentally validated	Nozzle design and temperature controls the polymer melting rate
[Gilmer et al., 2018]	ABS, LDPE, NaSPEG	1-D analytical in MATLAB	Rheological analysis of annular backflow of melt	Screening technique to identify extrusion failure
[Mackay et al., 2017]	PLA & ABS	Analytical	Describes the extrusion of polymer through a printing nozzle	Importance of the thermal and rheological properties is highlighted
[Heller et al., 2016a]	ABS/CF composite	3D FEM in COMSOL	Computational study on the effect of flow field on the orientation of the fibers	Die swell controls the fiber orientation in the printed parts
[Mostafa et al., 2009]	ABS/Fe composite	3D FEM in ANSYS	Numerical study on the melt flow behavior through a 90° bend inside the print nozzle	Material properties can significantly affect the behavior inside the nozzle
[Ramanath et al., 2008]	PCL	3D FEM in ANSYS	Computational study on the melt flow behavior of the polymer inside the nozzle	Polymer completely liquifies within 35% of the channel length

When considering the fluid flow inside the heated nozzle, one of the most vital parameters is the pressure exerted on the molten polymer to extrude it. Because the nozzle walls are stationary, this pressure provides the driving force for extrusion in a Hagen-Poiseuille style flow. Michaeli modeled this flow for die geometries, and Bellini et al. adopted the equations, Equations 3.9 to 3.12, to describe the flow for a polymer in a nozzle with a conventional cylindrical shape with a converging zone between the liquefier and nozzle tip [Hopmann and Michaeli, 2016, Bellini et al., 2004]. These equations take into account the non-isothermal behavior inside the liquefier by introducing an Arrhenius style relationship incorporating activation energy to flow (E_a).

$$\Delta P_1 = 2L_1 \left(\frac{v}{\phi}\right)^{\frac{1}{m}} \left(\frac{m+3}{(D_1/2)^{m+1}}\right) e^{\left[\frac{E_a}{R}(1/T - 1/T_{\text{ref}})\right]} \tag{3.9}$$

$$\Delta P_2 = \left(\frac{2m}{3\tan(\beta/2)}\right) \left(\frac{1}{D_2^{\frac{3}{m}}} - \frac{1}{D_1^{\frac{3}{m}}}\right) \left(\left(\frac{D_1}{2}\right)^2 (m+3) * 2^{m+3}\right)^{\frac{1}{m}} e^{\left[\frac{E_a}{R}(1/T - 1/T_{ref})\right]} \tag{3.10}$$

$$\Delta P_3 = 2L_2 \left(\frac{v}{\phi}\right)^{\frac{1}{m}} \frac{(m+3)\,(D_1/2)^2}{(D_2/2)^{m+3}} e^{\left[\frac{E_a}{R}(1/T - 1/T_{ref})\right]} \tag{3.11}$$

$$\Delta P = \Delta P_1 + \Delta P_2 + \Delta P_3 \tag{3.12}$$

where, ΔP is the calculated pressure gradient, ΔP_i is the calculated pressure gradient for section i ($i = 1$ represents the liquefier section; $i = 2$ represents the converging section of the nozzle; and $i = 3$ represents the nozzle-tip section), D_1 is the liquefier diameter, L_1 is the length of the liquefier, D_2 is the nozzle tip diameter and L_2 is the length of the nozzle tip, v is the solid filament feed rate, m and ϕ are material constants related to the viscosity, β is the convergence angle of the narrowing section of the nozzle, E_a is activation energy to flow, T is the temperature and T_{ref} is the reference temperature at which the activation energy was measured. Ramanath compared these calculations to values produced through ANSYS finite element simulation modeling [Ramanath et al., 2007]. The results were found to be comparable which suggests the calculations accurately predict the pressure drop produced during the AM process.

Some researchers have developed models, particularly finite element models to describe a material's thermal, velocity, and pressure profiles inside the FFF nozzle. Ramanath et al. [Ramanath et al., 2008] modeled PCL in an FFF nozzle with a very long liquefier. This allowed the polymer plenty of time to reach an isothermal state, which, in turn, provided the polymer the opportunity to achieve a consistent velocity and pressure until the nozzle diameter changed. Ramanath et al. studied this system to gain a better understanding of the melt flow behavior of the polymer, which aids in developing a better final print.

Ramanath's model predicted the PCL required about 42 mm inside the nozzle to reach an isothermal state. This is approximately 35% of the length of the liquefier they were using in the study. They also suggest that common AM polymers such as ABS would require even longer times to reach the isothermal state. This highlights the importance of material properties and nozzle design in the application of AM. The researchers further calculated the maximum pressure of the system to be 1.64 x 10^6 N/m^2 at the entrance of the liquefier. At the same time, the group performed the pressure calculations developed by Michaeli and Bellini [Hopmann and Michaeli, 2016, Bellini et al., 2004] and compared them to their modeling results based on finite element method (FEM). They saw similar trends between the Bellini calculations and the ANSYS FEM results, although the magnitude was slightly different, which they attributed to the FEM methodology, including causes such as the number and placement of nodes as well as the shape of the elements.

Nikzad et al. [Mostafa et al., 2009] performed a similar FEM analysis on the same style of liquefier with the goal of accelerating the identification of novel materials by modeling their behavior inside the liquefier. This group used an ABS-iron composite system as their subject and used similar boundary conditions as Ramanath [Ramanath et al., 2008] except that the entrance and liquefier temperatures were 60°C and 270°C, respectively. The researchers demonstrated a rapid, nearly immediate, transition to isothermal behavior. This further demonstrates the effect that different materials and different material properties may have on the behavior inside the liquefier. Nikzad et al. also showed that along with the temperature, the velocity and pressure both reach a steady value almost immediately at the entrance of the liquefier for the material in their study, and it only changes upon contraction of the liquefier at the nozzle exit.

Considering a more conventional nozzle design, Osswald et al. [Osswald et al., 2018] suggested a significantly smaller melt pool than Ramanath and Nikzad. This group still assumed a nearly instantaneous transition from solid to molten material and perfect contact between

the filament and the liquefier wall, but they developed a model for melting with pressure flow removal. Their results, which they validated empirically, indicated that the melting rate would be significantly influenced by the liquefier temperature, the temperature of the filament as it enters the liquefier, and the angle of the tip of the nozzle. Subsequent work from the same group built upon the previous modeling framework by accounting for the shear thinning behavior of the polymer melt [Colón Quintana et al., 2020]. The model predictions were found to be quite accurate when compared to experimental printing results obtained under different printing conditions [Colón Quintana et al., 2020].

Gilmer, et al. examined the fluid flow behavior of the molten polymer at the transition region from solid filament to liquid pool [Gilmer et al., 2018]. This analysis focused on the steady state velocity profiles of the molten polymer as it enters the annular region, potentially resulting in annular backflow. This group identified the primary parameters influencing backflow are the shear thinning behavior of the polymer and the filament diameter. The researchers also introduced a dimensionless flow identification number (FIN), as highlighted in Equation 3.13, based on the pressure drop per unit length across the nozzle ($\Delta P/L$), apparent viscosity (η_a), filament feed rate (v_f), nozzle diameter at the liquefier entrance (D_b), and filament diameter (D_f). The FIN analysis allows the rapid determination of backflow potential in novel materials.

$$FIN = \frac{\Delta P/L}{\eta_a v_f}\left(D_b^2 - D_f^2\right) \tag{3.13}$$

Recently, Serdeczny et al. [Serdeczny et al., 2020a] demonstrated the effectiveness of modeling the behavior of the material inside the nozzle using computational fluid dynamics (CFD) simulations. This group simulated the localized temperature inside the nozzle to better understand the fluid flow behavior of the molten polymer. Through this approach, Serdeczny et al. identified a backflow region, although they suggest that it should never cause failure. This groups results also corroborate data presented by Phan, et al. who had previously demonstrated that the temperature of the material exiting the nozzle does not always match the temperature of the nozzle, which is a common assumption in the modeling of the extrudate [Phan et al., 2020, Phan et al., 2018]. Figures 3.4(a) and Figures 3.4(b) highlights the pressure drop and shear rate profiles during a typical MatEx based process. Previous works have reported that the polymer melt experiences apparent shear rates inside the nozzle that are the range of 100-1000 s^{-1} while the pressure drop is in the range of 20-35 MPa [Phan et al., 2018, Mackay et al., 2017]. The simulation results obtained using the CFD approach

by Phan et al. [Phan et al., 2020] exhibited qualitative agreement with the experimental findings. Moreover, the spatial distribution of pressure (and hence shear stress) and the shear rates underscores the importance of capillary length when designing new nozzle geometries for MatEx.

Serdeczny et al. [Serdeczny et al., 2021] extended this analysis to study the influence of the inclusion of short fibers on the polymer flow. The group identified that, although the fibers significantly increase the viscosity of the material and pressure required to extrude it from the nozzle, they also increase the thermal conductivity. The increase in thermal conductivity can cause the material to liquefy to a greater degree, potentially lowering the viscosity a substantial amount. Models similar to these, especially coupled with sophisticated experimental measurements, can be further utilized to estimate the limits of filament feed rates based on the flow behavior of the material and nozzle geometry as well as understand the influence of the process parameters on the temperature of the material as it is deposited [Luo et al., 2020, Prajapati et al., 2018, Go et al., 2017, Serdeczny et al., 2020b, Serdeczny et al., 2019a].

Heller et al. [Heller et al., 2019] developed a computational approach to study the impact of two-dimensional planar flow field in presence of non-isothermal effects on the properties of a viscoelastic polymer extrudate during as well as after extrusion from the nozzle. The simulation results of the velocity profiles during extrusion in MatEx are presented in Figures Figures 3.4(c) and Figures 3.4(d). Employing a free surface minimization technique developed in this study, the shape of the extrudate was simulated. Nozzle height and geometry was found to influence the shape of the extrudate significantly. It is worth mentioning that although the predictions from this model are for the stand-off region, the main model was based on the polymer melt behavior inside the nozzle.

Mackay et al. [Mackay et al., 2017] examined the pressure drop inside the nozzle. Using this pressure, the group identified the maximum feed rate and minimum temperature that can be used during the FFF process. By examining three different materials, they were able to observe that their predictions can be made to follow a master curve by utilizing dimensionless numbers to describe the system [Mackay et al., 2017].

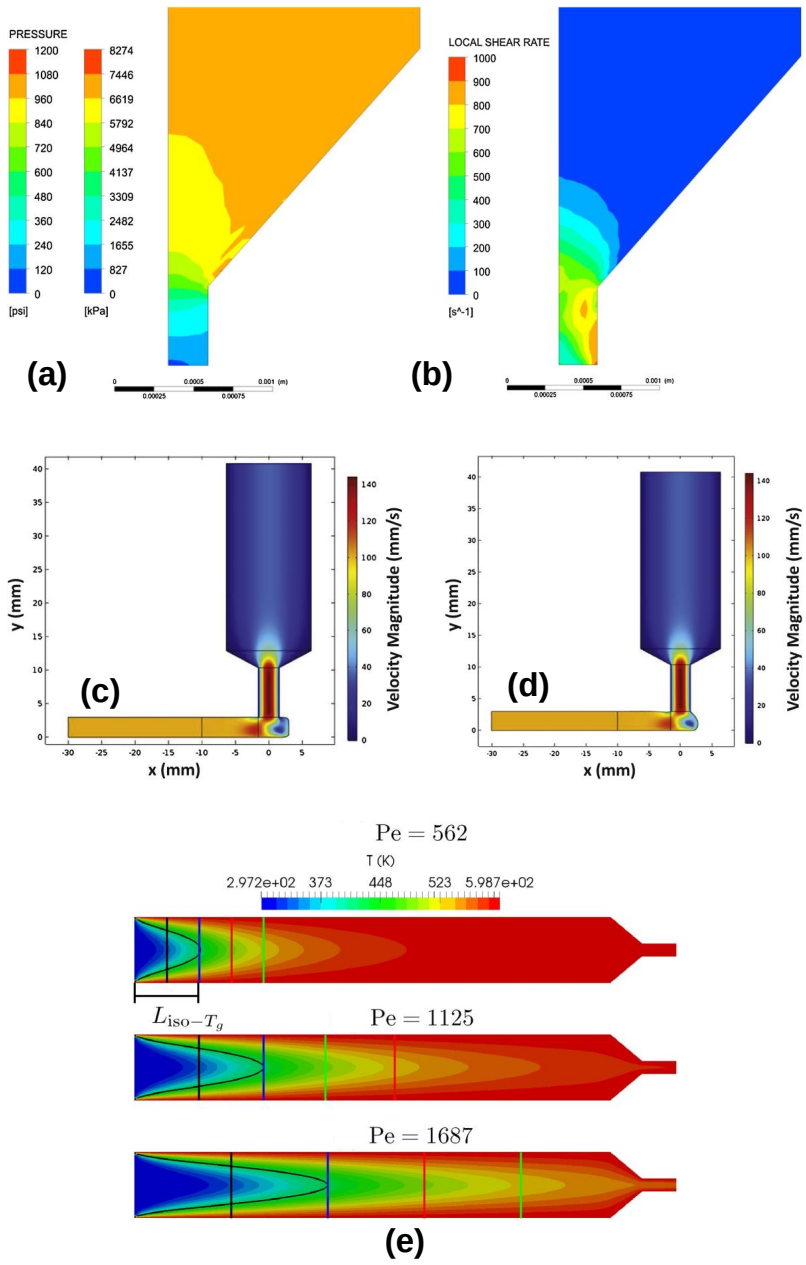


Figure 3.4: Variation in the (a) pressure drop and (b) shear rate inside a typical 3D printer nozzle (images reprinted from [Phan et al., 2020] with permission from Elsevier); (c) Simulated velocity profile of the polymer melt during initial extrusion (image reprinted from [Heller et al., 2019] with permission from Elsevier); (d) Simulated velocity profile of the polymer melt when the extrudate attained the final shape (image reprinted from [Heller et al., 2019] with permission from Elsevier); and (e) The variation in the thermal profiles at three different Péclet numbers. The different vertical lines indicate locations that had been normalized with the distance required to reach T_g (image reprinted from [Pigeonneau et al., 2020] with permission from Elsevier).

Pigeonneau et al. [Pigeonneau et al., 2020] studied the temperature fields inside the liquefier as a function of the velocity by examining the system with different Péclet (Pe) numbers (Equation 3.14), as highlighted in Figure 3.4(e). This study showed that the distance inside the nozzle required to attain an equilibrium temperature increases with increasing polymer velocity. In fact, the center of the flow may be below T_g at certain feed rates, and the amount of this low temperature material increases with increasing velocities [Pigeonneau et al., 2020].

$$Pe = \frac{\text{advective transport rate}}{\text{diffusive transport rate}} = \frac{UL}{\alpha} = \frac{\rho C_P U L_{\text{char}}}{k_{\text{cond}}} \tag{3.14}$$

In the above equation, U is the fluid velocity, L_{char} is the characteristic length scale, α is the thermal diffusivity, ρ is the density, C_p is the specific heat capacity, and k_{cond} is the thermal conductivity.

3.6 Dynamics in the stand-off region between nozzle and print bed

3.6.1 Die swell: Origin and implications in MatEx

Polymer processing techniques, such as melt extrusion during 3D printing, invariably results in significant levels of residual stress build-up due to the exposure of the polymer chain network to shear and compression forces. Under the influence of the shear forces, normal stresses are developed along the print direction as well as perpendicular to it due to the viscoelastic chain network in the melt [Polychronopoulos and Vlachopoulos, 2018]. The residual stresses can only relax when the polymer chains can re-orient and return to their original state once extruded through the nozzle. In order to maintain the shape of the extrudate, the polymer chains must recover from the significant deformation and orientation effects experienced during extrusion through the nozzle. This is attained through a time-dependent stress relaxation phenomenon known as die swelling, as illustrated schematically in Figure 3.5(a) in relation to MatEx.

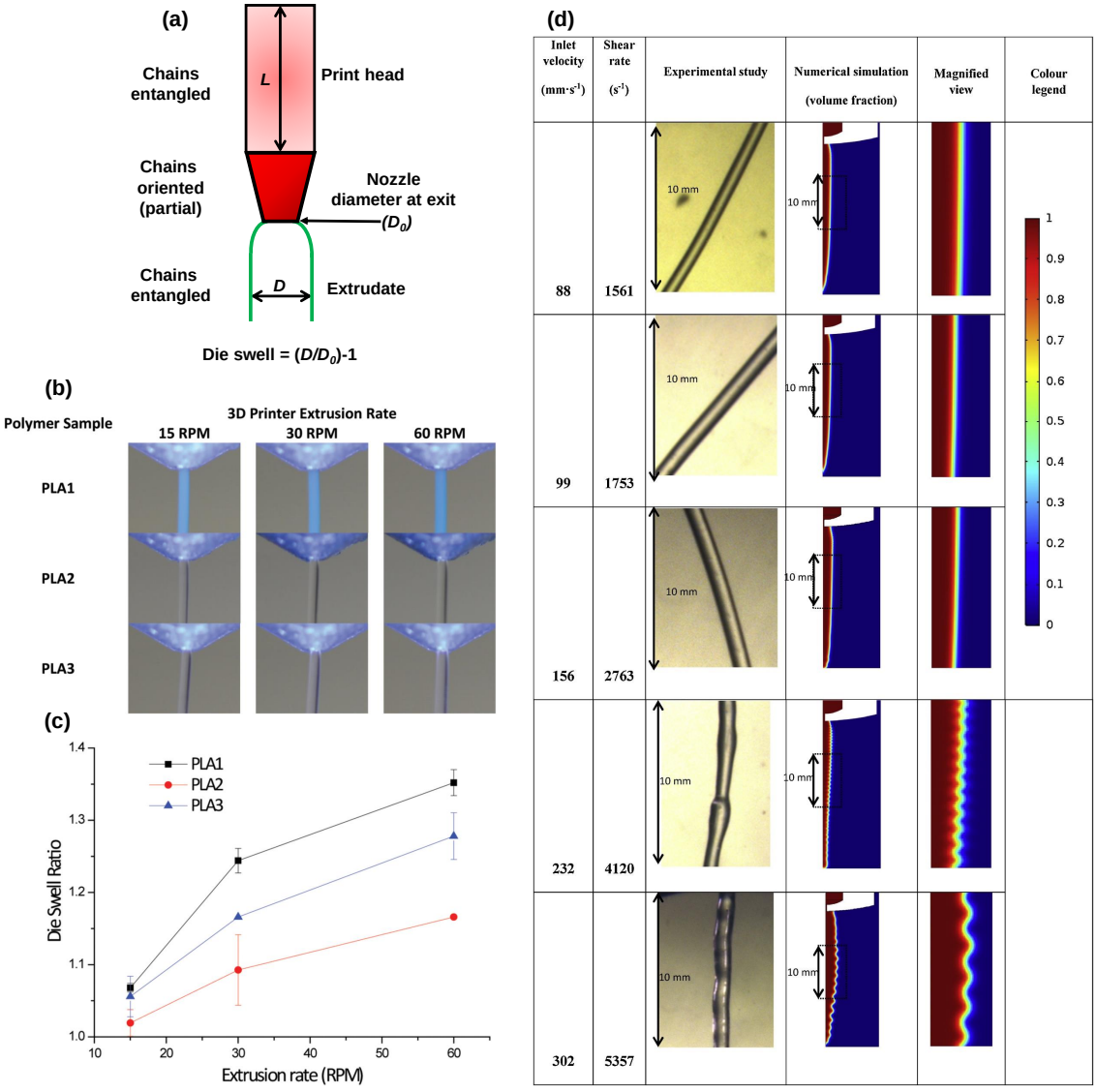


Figure 3.5: (a) Illustration of die swell in a typical FFF process post-extrusion through the nozzle. The polymer chains in the filament feed may have some residual alignment depending upon the filament production process; (b), visualization & (c) estimation of die swelling observed in different PLA samples printed at 180°C under different extrusion speeds (image reprinted from [Tang et al., 2020] with permission from John Wiley & Sons Ltd.); and (d) The effect of nozzle inlet velocity and associated shear rate on the shape of the polymer extrudate obtained by printing at 195°C using a 0.5mm nozzle along with numerical simulation of the extrudate geometry (image reprinted from [Bakrani Balani et al., 2019] with permission from Elsevier).

Die swell is also an important measure of the elasticity and is related to elastic strain energy stored in the polymer melt while being sheared within the nozzle (in case of MatEx). Upon exiting the nozzle, the elastic energy associated with the polymer chains attempts to restore them to their original configuration (prior to extrusion) resulting in swelling [Richardson, 1970]. It can influence final part properties by controlling the degree of residual stresses entrapped within injection molded components or the geometry of extruded parts [Münstedt et al., 2011]. Recent FEM simulations suggest that the reason behind increased die swell at the nozzle exit is the relaxation of the elastic stresses originating from the viscoelastic nature of the polymer melt [Wang and Smith, 2017]. Comminal et al. [Comminal et al., 2017] developed a two-dimensional model that investigated the flow characteristics of the polymer melt post-extrusion through the nozzle and prior to deposition on the print bed. Due to the simplistic boundary conditions implemented in this preliminary work, the thickness of the extrudate was found to rely on the print bed velocity. Further modeling studies must be performed to better understand the rheological implications on the extrudate dimensions while accounting for the non-isothermal nature of the MatEx process.

Several researchers have investigated the causes and effects of die swell in the MatEx process. During die-swelling, the molten polymer leaves the nozzle and entrapped stresses relax resulting in radial expansion of the extruded polymer [Turner and Gold, 2015]. Process modifications, especially novel nozzle designs, with smaller nozzle diameters (D_0) and longer print heads (resulting in higher L/D_0 ratios and increased residence time of the polymer inside the nozzle) can increase the time window for stress relaxation [Nikzad et al., 2011]. FEM simulations have highlighted the effect of die swell on the fiber orientation state that becomes more pronounced in the shear-dominated flow through the nozzle; however, alignment decreases during the expansion caused due to the die swell [Heller et al., 2015]. The high shear rates (100-1000 s^{-1}, depending on the printer) associated with the printing process can lead to high levels of deformation and polymer chain disentanglement resulting in increased die swell [McIlroy and Olmsted, 2017b, McIlroy and Olmsted, 2017a]. Moreover, increased print speed leads to higher pressure drops across the nozzle causing die-swell that results in the formation of deformed edges in printed parts [Papazetis and Vosniakos, 2019]. Figures 3.5(b) and 3.5(c) highlight both the qualitative and quantitative dependence of die swell on the print speed during MatEx of three different grades of PLA. At higher speeds, the polymer chains are subjected to increased magnitude of forces that lead to higher wall shear stresses and hence results in an increase in die swell [Tang et al., 2020]. The difference in the amount of die swell for the three PLA samples was attributed to their respective molecular

architecture where synergistic effects of both molecular weight (MW) and molecular weight distribution (MWD) are important. The increased MW ensures higher degree of chain entanglements (ν) that lead to elasticity-dominant effects in the polymer melt resulting in higher die swell [Sirisinha, 1997]. With respect to MWD, broader distributions yield greater die swell since the higher MW branch exhibits elastic effects while the increased viscous response of the lower MW tail impedes the recovery of the chain network [Tang et al., 2020, Sirisinha, 1997].

In terms of the print temperature, die swell decreases as the temperature increases since the polymer chains have enhanced molecular mobility that aid stress relaxation due to higher free volume around the chains. A recent study on FEM simulations of the die-swell characteristics of ABS during FFF reported that at increased nozzle temperature and lower material flow rates (lower print speeds) resulted in reduced die-swell of the extrudate due to the reasons discussed above [Shadvar et al., 2019]. The theoretical analysis underpredicted the extent of die swell by approximately 20%. The authors attribute this discrepancy in their study to the simplistic nature of their FEM framework and failure to account for the thermal fluctuations occurring during the printing process. It is expected that careful monitoring of the printing parameters and exploiting the simulation predictions (that take into account more realistic conditions) will assist in limiting the effects of die-swell thereby ensuring the quality and dimensional accuracy of the final printed part.

Figure 3.5(d) provides a comparison between the experimental and numerical results obtained by analyzing the extrudate shape at different inlet velocities and shear rates. The extrudate was found to be uniform and homogenous at shear rates up to $4000s^{-1}$ but increasing shear rates led to an unstable flow causing defects to appear on the extrudate [Bakrani Balani et al., 2019]. The two-phase flow numerical simulation closely matched the experimentally observed results by accurately predicting the wavy contours of the extrudates caused due to the high extensional stresses associated with increased inlet velocity and shear rates.

Finally, the die swell value also relies on the material feeding rate. At a high flow rate, the value increases, and the diameter of the extrudate begins to oscillate [Serdeczny et al., 2020b]. As mentioned earlier, the speed of material feeding through the die is a processing parameter that affects the disentanglement and degree of material deformation during extrusion and it should be controlled to avoid buckling and drawing to keep the width of the printed layer approximately equal to the nozzle diameter. It has been shown that this parameter has

a direct correlation to shear rate and an inverse correlation with residence time [McIlroy and Olmsted, 2017a]. Furthermore, the geometrical quality of the printed parts can be influenced by the force that needs to be applied to feed the filament through the nozzle. At higher feeding rates, this force which can be caused by viscoelastic phenomena of the molten polymer or by the fluctuations in the length of the melt zone inside the liquefier begins to oscillate and leads to pressure fluctuations. The fluctuations in pressure can result in an oscillating extrusion rate that negatively affects the geometrical quality of finished parts and leads to degradation84.

3.6.2 Flow instabilities: Origin and implications in MatEx

Figure 3.6(a) illustrates a typical flow curve and the associated instabilities encountered during extrusion of linear polyethylene. Although, most of initial analysis was performed with extrusion dies, the approach and results can be easily extended to extrusion based MatEx where the print nozzle inherently acts as a die. At low shear rates, the extrudates exhibit uniform surface features and are stable. With the increase in shear rate, sharkskin instability appears leading to the formation of extrudates with pores and cracks. At even higher shear rates, the polymer melt undergoes a stick-slip instability that is easily identifiable due to the inconsistent surface features in the extrudate and pressure oscillations in the nozzle. Finally, at very high shear rates, the polymer melt can experience gross melt fracture instability that is characterized by extrudate shape distortion. In terms of the printing process, all of these instabilities can be present depending on the relative magnitude of the elastic and viscous forces associated with the polymer melt. A simple way to characterize the effect is by calculating the Weissenberg number (Equation 3.15 that relates the polymer relaxation time (λ) to the deformation time during flow inside the nozzle.

$$Wi = \frac{\lambda U_{avg}}{R_N} \tag{3.15}$$

where, U_{avg} is the average velocity of the polymer melt in the nozzle and RN is the nozzle radius, respectively. The value of λ can be determined from steady flow shear rate sweeps at the relevant print temperatures.

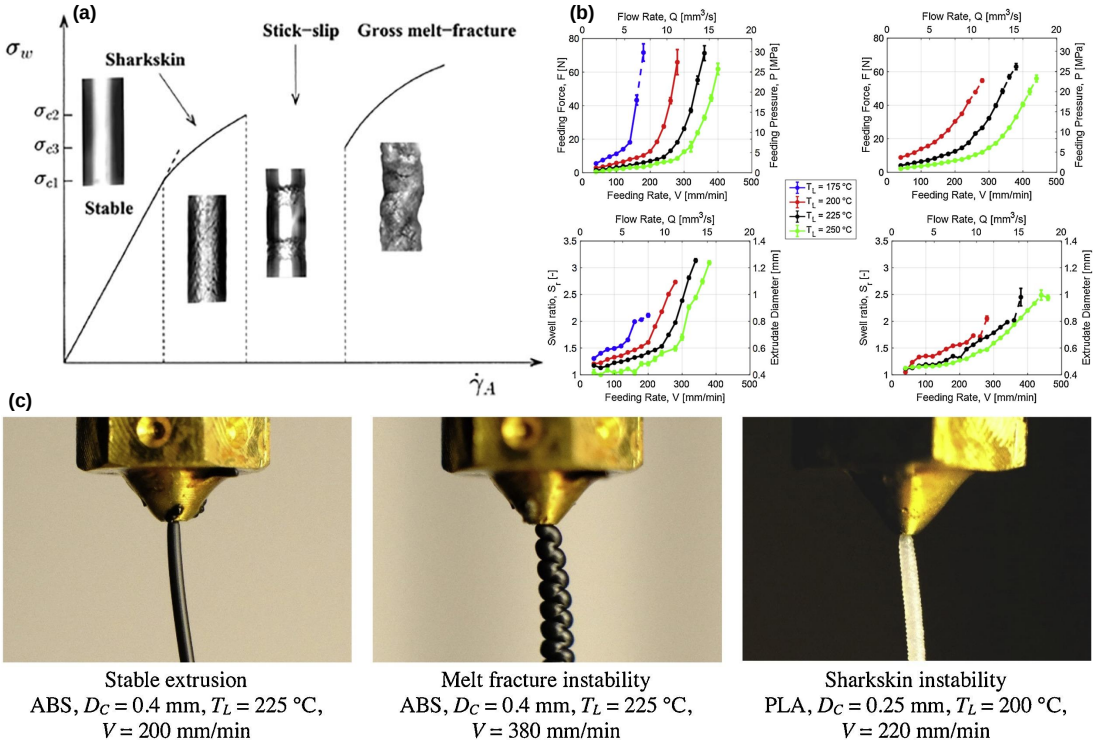


Figure 3.6: (a) A typical wall shear stress versus shear rate plot highlighting the flow behavior during extrusion of linear polyethylene along with the regions of related flow instabilities (image reprinted with permission from [Jabbari et al., 2018] under the terms of the Creative Commons CC-BY 4.0 license); (b) The filament feeding force and die swell ratio at different print temperatures and feeding velocity for PLA and ABS printed using 0.4mm nozzle. The dashed lines in the figure are indicative of the flow instabilities encountered during extrusion through the nozzle (image reprinted from [Serdeczny et al., 2020b] with permission from Elsevier); and (c) Visual representation of extrudates exiting the print nozzle exhibiting stable extrusion, melt fracture instability, and sharkskin instability (image reprinted from [Serdeczny et al., 2020b] with permission from Elsevier).

Serdeczny et al. studied the effects of filament feeding rate and nozzle temperature on the force required to feed a filament into the nozzle and the subsequent die swell characteristics as highlighted in Figure 3.6(b). The feeding force and die swell exhibited the similar trends, increasing with feeding rate (moderately at first and then rapidly) and decreasing with print temperature. The die swell behavior was consistent with the increased elastic effects imparted by the nozzle walls at lower print temperatures [Comminal et al., 2018a]. Moreover, the authors found at certain printing conditions, the flow instabilities including shark skin and melt fracture (Figure 3.6c) occurred due to the temperature and flow controlled viscoelastic

properties and wall slip effects experienced by the polymer melt while exiting the nozzle [Serdeczny et al., 2020b]. These deviations are caused since the extrudate retains the memory of the early deformation at the entrance region of the liquefier [Jeong and Leonov, 2003]. Heller et al. [Heller et al., 2016a]found that orienting stiff fibers along the extrudate increased the extensional flow in the convergence region of the nozzle and could significantly reduce the die swell during printing.

3.6.3 Rheological measurements relevant to die swell

Creep recovery and relaxation stress are two rheological tests that can be employed to analyze die swell behavior by gaining insights into related viscoelastic properties. It is worth mentioning that these characterizations can be performed on a rheometer, rather than the more traditional method of associating such tests with solid state properties. During a creep recovery test, the sample is loaded with constant stress σ_0 and its strain is measured. After some time, the sample is unloaded and the recoverable strain γ_r of the sample is observed as a function of recovery time t_r [Münstedt and Schwarzl, 2014]. Using creep recovery, the recoverable compliance J_r is determined to predict extrudate swelling. After unloading the sample, the ratio between γ_r as a function of t_r and applied stress σ_0 gives the recoverable compliance, as highlighted in Equation 3.16, which is positively correlated to extrudate swelling [Elbadawi, 2018].

$$J_r\left(\sigma_0, t_0, t_r\right) = \frac{\gamma_r\left(\sigma_0, t_0, t_r\right)}{\sigma_0} \tag{3.16}$$

The stress relaxation test is the counterpart of the creep test, which can be used to investigate the effects of this characteristic on the extrudate expansion. In this test, an instantaneous strain or deformation is enforced on a material that had previously been stress-free and the stress decay is recorded at the fixed strain [Elbadawi, 2018]. At the capillary exit, the extent of stress relaxation relies on the length to diameter ratio (L/D_0), i.e., on the recovery time of the polymer within the capillary. On leaving the capillary, the stress is released, and recovery takes place. The die swelling is almost instantaneous, which implies that the polymer relaxes very fast to an equilibrium state [Guillet and Seriai, 1991]. Therefore, the relaxation modulus at the capillary exit is determined from Equation 3.17. The relaxation

modulus (G_t) is determined to obtain the damping function which is proven to be most important in numerical predictions of swell [Konaganti et al., 2016].

$$G_t = \frac{\sigma_t}{\gamma} \tag{3.17}$$

The degree of stress relaxation can be quantified by relaxation time, with longer relaxation time resulting in a lower rate of stress relaxation and larger elastic response/more extrudate swell [Sirisinha, 1997]. The variations in the relaxation timescales due the extremely non-isothermal nature of MatEx process will be discussed in more detail in the following section. Deborah number (De), defined as relaxation time per observation time for the deformation process, is a descriptive factor that is helpful for analyzing die swell in capillary flow. In relation to the printing process, De can be defined as the ratio of the longest relaxation timescale of the polymer (determined from the onset of shear-thinning) to the time required to print a single layer (determined by the print speed) [Das et al., 2020b]. When De is greater than 1, the polymer does not have enough time to develop and relax during the process. Further, studies on the effect of processing time and die swell have shown that die swell increases with the apparent shear rate at constant De and it decreases with De to an equilibrium value depending on apparent shear rate [Thanh, 1974].

3.6.4 Experimental and simulation studies for the standoff region

After leaving the nozzle, extruded material is deposited in the form of strands or beads on the bed to create the manufactured part layer by layer. Since the shape and geometric characteristics of the extrudate in the stand-off region of MatEx are controlled by the melt flow behavior of the polymer, the geometric accuracy of the final printed part is also dependent on the temperature dependent complex flow fields arising during extrusion from the nozzle [Comminal et al., 2018a, Hebda et al., 2019]. Several experimental studies and numerical simulations have been investigated to predict the influence of processing conditions to control the shape of strands which predicts the mechanical properties, the porosity, and geometric accuracy of parts. It was found that both the strand-to-strand distance and the layer thickness impact the morphology and shapes of the strands. For instance, decreasing the layer thickness flattens the strands and the neighboring strands have larger intra-layer bonds and are more compact, as the values of the strand-to-strand distances were smaller than the width of the strands [Serdeczny et al., 2019b]. It has been quantified that decreasing the dis-

tance between the printing head and the substrate and reducing the velocity ratio, changes the cross-section of the strand from being almost circular to an elongated rectangular shape with rounded edges [Comminal et al., 2018a]. The dependency of the deposited strand's shape on different geometries of the extrusion nozzle has been simulated for an isothermal incompressible Newtonian fluid flow. The numerical results showed that the extrusion with the cylindrical nozzle plus a side plate enhanced the compactness of the strand cross-section by retaining the side flow, while it increased moderately the printing force. In contrast, the nozzle with square configuration did not improve the compactness and increased the printing force on the substrate [Comminal et al., 2018b].

In another numerical study, the effect of shear-thinning on the deposited strand and the force exerted on the substrate by printing force for Newtonian fluid flow has been quantified. The results showed no significant change in the shape of the strand. Moreover, the introduction of shear-thinning changes the magnitude of the printing force, but not its linear trend for printing speed [Serdeczny et al., 2018b]. The authors validated experimentally CFD simulations of the strand morphology for different printing conditions including velocity ratio (ratio of printing head velocity to average velocity inside the nozzle, V/U) and normalized gap height (ratio of gap height to nozzle diameter, g/D) has shown that when g/D or V/U is decreased, the cross-section of the strand deforms its shape from an almost circular to a flat cuboid with rounded edges. The presence of the nozzle does not influence the extruded material for the large value of these printing conditions (i.e. $g/D = 1.2$ and $V/U = 1$) [Serdeczny et al., 2018a]. The importance of considering the non-Newtonian nature of the polymer melt in predicting the strand shape post-extrusion has been numerically demonstrated by Behdani et al. [Behdani et al., 2020] Their results suggest that the conditions of small gap heights, the cross-sectional area of the extrudate is affected by its viscosity. Moreover, experimentally observed changes in strand shape and surface roughness due to heating from the nozzle were found to be in close agreement with the model predictions [Behdani et al., 2020]. Such modeling approaches provide excellent rationale for modifying the viscosities of polymer feedstocks such that the extrudate can exhibit adequate shape retention while minimizing roughness that can lead to undesirable surface finish on the printed parts.

3.6.5 Importance of heat transfer effects

As highlighted in the preceding sections, monitoring the thermal profile during printing is of importance due to the non-isothermal nature of the MatEx process. Correlating the interactions between momentum and thermal transport for a non-Newtonian polymer melt is not trivial, especially since it affects the relaxation spectra of the associated polymer [Incropera et al., 2013, Denn, 2008]. Die swell can increase by almost 5% due to fluctuations in the temperature between the polymer and the nozzle during printing [Polychronopoulos and Vlachopoulos, 2018, Aho et al., 2015]. Multiple studies have been reported for understanding the heat transfer in the standoff region between the nozzle exit and the print bed. The heat transfer in this region in the form of thermal radiation and/or conduction plays an important role to determine the temperature of material reaching the bed. The filament must not significantly cool down in the standoff region so that the filament is dispensed on the bed at a temperature close to the temperature near the nozzle tip [Prajapati et al., 2018]. The transient heat transfer during filament deposition and cooling has been studied, resulting in the prediction of bond quality between all adjacent filament segments of the final structure [Costa et al., 2017]. Numerical simulation of the deposition process confirmed the effect of operating parameters such as heat transfer and filament temperature on the finished product [Xia et al., 2018]. The experimental and theoretical model of filament temperature distribution using infrared thermography in the short standoff gap has been investigated, showing the effect of heat transfer on improving polymer AM processes by ensuring good filament-to-filament bonding [Ravoori et al., 2019a]. Finally, it must be recognized that radiative heat transfer effects and latent heat of crystallization (in case of semicrystalline polymers) can play a significant part in controlling the flow behavior of the polymer melt during extrusion. The radiative effects can usually be neglected for desktop based MatEx printing and as such previous modeling efforts describing thermal profiles associated with the process often tended to neglect these effects [Costa et al., 2017, Zhang et al., 2017a, D'Amico and Peterson, 2018, Coogan and Kazmer, 2017b]. However, recent work have highlighted the importance of radiation in BAAM scale printing [D'Amico and Peterson, 2020, Owens et al., 2022] and future work must account for its effects to better describe the corresponding processing-property relationships.

3.6.6 Importance of extensional viscosity in MatEx

Extensional viscosity (also referred to as elongational viscosity) which is defined as the resistance of the fluid to extensional deformation, is another rheological property that affects polymer melts at the die exit. Extensional viscosity (η_e) in FFF originates from the extensional flows during the motion of the polymer melt in the tapering section of the nozzle as well as during the deposition of the melt exiting the nozzle on the printer bed [McIlroy and Olmsted, 2017b, Phan et al., 2020]. Due to the complex extensional flow fields present, it is important to characterize the related rheological properties in order to understand its effect on the printed part properties. Depending upon the extensional rates of interest, an extensional viscosity fixture (for low rates) can be coupled with a traditional rheometer setup (or employing specialized instrumentation such as the Capillary Breakup Extensional Rheometer [McKinley and Tripathi, 2000]) while higher rates can be probed using the entrance pressure method (Cogswell analysis) [Mackay and Astarita, 1997]. Equations 3.18−3.20 relate the average extensional stress (σ_e) and extension rate ($\dot{\epsilon}_e$) to the pressure drop across the liquefier entrance (ΔP_{ent}), power-law index (n), apparent shear rate ($\dot{\gamma}_{app}$), and shear viscosity (η).

$$\sigma_e = 0.375(n+1)\Delta P_{ent} \tag{3.18}$$

$$\dot{\epsilon}_e = \frac{4\eta\dot{\gamma}_{app}^2}{3(n+1)\Delta P_{ent}} \tag{3.19}$$

$$\eta_e = \frac{9}{32\eta}\left\{\frac{(n+1)\Delta P_{ent}}{\dot{\gamma}_{app}}\right\}^2 \tag{3.20}$$

Trouton ratio (Tr) (extensional to shear viscosity ratio) can be used to quantify the additional extensional resistance of the polymer melt relative to shear. As evident from the aforementioned analysis, the calculation of Tr is non-trivial due to the complexities associated with measuring η_e but it is extremely important for quality control purposes. Figure 3.7(a) highlights extensional viscosity measurements performed on PLA using both the methods (extensional viscosity fixture and entrance pressure) outlined above. For all generalized Newtonian fluids, Tr=3 is observed but the values of η_e for PLA were found to be higher than three times the values of η ($Tr = 3$); indicative of the elastic effects dominating over the viscous nature of the polymer melt65. The assumption of purely uniaxial extension can

also lead to deviation from a Tr of 3. An easier route to quantitatively measure η_e is by estimating the melt strength of the polymer by determining the force required to break the extrudate exiting the nozzle [Polychronopoulos and Vlachopoulos, 2018]. The shortcoming of this technique is that the measurement is affected by the non-isothermal nature of the process (cooling behavior and varying rates) and extent of deformation induced in the extrudate. In order to better capture the behavior of the polymer melt under the shear and extensional flow fields inside the nozzle, detailed viscoelastic models such as the Phan-Thien-Tanner (PTT) model can be employed although it is computationally intensive.

An important aspect with respect to FFF is the time period during which the polymer melt experiences the extensional flow fields. An important parameter used to characterize such flow fields is the Hencky strain that refers to the logarithm of the final length to the initial length of the polymer filament during extension deformation. As highlighted in Figure 3.7(b), the 2-mode (one viscoelastic mode and one purely viscous mode) PTT model employed by Phan et al. [Phan et al., 2020] cannot accurately predict the extensional viscosity (up to a Hencky strain of 4). The model predictions deviated from experimental values during startup due to the large contribution of the purely viscous mode at early times [Phan et al., 2020]. But the steady state extensional viscosity values are captured accurately using the model. Depending on the print speed, the polymer melt might experience extensional flow fields for small time-scales that might not be enough to generate a fully developed flow profile inside the nozzle. Therefore, experimental characterization is important to characterize the transient start-up behavior while viscoelastic model predictions can serve as a good approximation of the steady-state extensional rheological behavior of the polymer melt; especially when experimental characterizations become challenging.

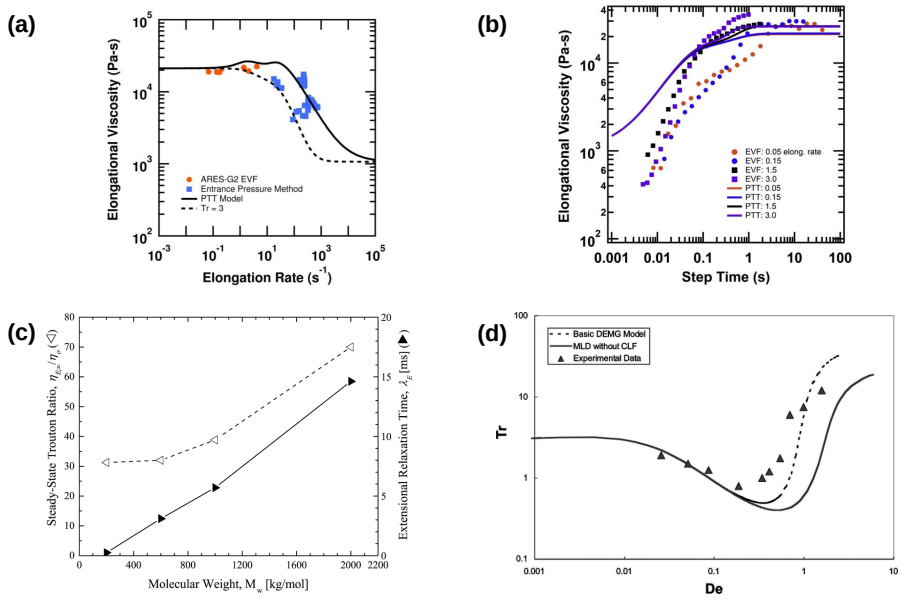


Figure 3.7: (a) Representative extensional rheology data for PLA at 170°C obtained using both the Sentmanat extensional rheology fixture (TA Instruments SER) and Cogswell analysis of entrance pressure method. The solid line represents the Phan-Thien-Tanner model fits to the experimental data while the dashed line represents a Tr of 3 (image reprinted from [Phan et al., 2020] with permission from Elsevier); (b) Evolution of extensional viscosity as a function of time at different extension rates for PLA at 170°C measured using the extensional fixture in a rheometer. The solid lines represent the Phan-Thien-Tanner model fits to the experimental data (image reprinted from [Phan et al., 2020] with permission from Elsevier); (c) Effect of polymer molecular weight on the steady-state Trouton ratio and extensional relaxation time (image reprinted from [Khandavalli and Rothstein, 2014] Copyright 2014 The Society of Rheology); and (d) The steady extensional viscosity of a concentrated polystyrene solution (6.0 wt.%, $M_w = 10.2 \times 10^6$ g/mol) with $Z \sim 26$ entanglements per molecule and the associated prediction of the Doi-Edwards-Marrucci-Grizutti (DEMG) model and the Mead-Larson-Doi (MLD) model without contour length fluctuations relaxation mechanisms. In order to calculate Z, the values of M_w and M_e can be obtained using gel-permeation chromatography and linear rheology, respectively (image reprinted from [McKinley and Sridhar, 2002] with permission from Annual Reviews).

3.6.7 Extensional rheological characterizations: Missing links for MatEx

The effect of MW and MWDs are often overlooked in the context of FFF. At low Hencky strains, Tr of approximately 3 is reported which rapidly increases with increasing Hencky strains due to enhanced molecular alignment. Moreover, significant strain-hardening effects occur at the higher molecular weights [Khandavalli and Rothstein, 2014]. Polymers with high MW already have high zero-shear viscosities associated with them and strain hardening makes it even challenging to process using MatEx, provided the polymer melts exhibit similar shear-thinning behavior. Figure 3.7(c) highlights the dependence of the extensional relaxation time ($_e$) and steady-state Tr on the polymer MW. The monotonic increase in Tr and $_e$ with MW suggests the elasticity as well as the deformation of the entangled polymer chains play a vital role in controlling the strain hardening mechanisms at higher MWs.

In case of entangled polymer chain networks, it is important to understand the dependence of Tr on the De. Figure 3.7(d) highlights the effect of characteristic timescales (De) on the steady extensional viscosity of the entangled polymer melt. The experimental results were found to be in close agreement with constitutive model predictions [McKinley and Sridhar, 2002, Bhattacharjee et al., 2002]. In the range of low De (less than 0.5), a Tr value of 3 is observed, as is the case for uniaxial Newtonian flows. These characterizations can be performed using filament-stretching rheometry [Bhattacharjee et al., 2002] but such approaches have not yet been realized in relation to the MatEx process. For De in the range between 0.5 and three times the entanglement number ($Z = M_w/M_e$), the stress and hence, the extensional viscosity decreases due to chain relaxation in timescale of the flow field and therefore Tr less than 3 is observed. However, at higher De values, significant chain stretch can occur resulting in the strain hardening of the polymer chain network. It is interesting to note that the transition from extension-thinning to extension-thickening occurs at $De \sim 1$; modifying the print speed can allow for a polymer melt that is extrudable through the nozzle but also has enough integrity to hold its shape post-extrusion.

Barczewski et al. [Barczewski et al., 2020] performed a comprehensive analysis of the flow instabilities associated with extrusion of linear LDPE by carrying out detailed rheological characterizations using rotational, extensional, and capillary rheometry. Moreover, the authors devised a novel method to detect the onset of sharkskin instability during extrusion through a dynamic pressure signal analysis [Barczewski et al., 2020]. This approach can be

extended to the extrusion process during MatEx to develop novel nozzle designs that would allow for in-situ monitoring and hence provide valuable information regarding the origin of flow instabilities at different processing conditions. Details regarding real-time in-situ measurements to monitor rheological properties and structural changes during extrusion of thermoplastics have been reviewed elsewhere [Hilliou and Covas, 2021]. It is expected that establishing relationships between polymer rheology and morphological features will aid in tailored material development for MatEx.

Rheological characterizations on potential feedstocks for MatEx based on shear-rate sweeps can provide valuable insights into the "printability" of the material. Such experimental investigations that relate die swell with rheology are lacking in current literature. Recently, Mehrjerdi et al. [Mehrjerdi et al., 2020] investigated the shear-thinning nature of talc filled high density polyethylene (HDPE) at shear rates relevant to the printing process (1-10^4 s^{-1}); while characterizing the extrudate swelling characteristics of the polymers. Increasing the amount of filler drastically reduces the melt elasticity that resulted in a reduction in the die swell by hindering the polymer chain mobility in the melt. Although independent of the temperature, the die swell for talc/HDPE composites was found to be strongly influenced by the shear rate126; these results can be the basis of intelligent process parameter selection for MatEx processing for such materials where print speed (rather than the print temperature) can be employed to control the extrudate swelling.

3.7 Dynamics of post-deposition on the print bed

3.7.1 Interlayer chain diffusion and bond formation

During the next step of the MatEx process, the extrudate that has exited the nozzle and traveled through the standoff region is deposited on the print bed or onto a previously deposited layer. After deposition, the polymer layers undergo solidification during high cooling rates. This is a critical stage since parts processed using AM tend to be mechanically inferior to those processed using conventional manufacturing approaches, attributed to the poor interlayer adhesion along the axis perpendicular to the print direction. The weld lines generated along this axis serve as stress concentration points that can cause premature mechanical failure compared to traditionally processed/injection molded parts.

Generally, the mechanical properties of MatEx printed parts tested perpendicular to the print direction are significantly inferior to those obtained when testing the parts parallel to the print direction [Ahn et al., 2002, Masood et al., 2010]. Polymer chain reptation dynamics and hence diffusion across the interface controls the interlayer bonding in the printed parts. Both the print temperature and print speed can influence the polymer chain reptation in the deposited layers [Rodriguez et al., 2003, Yan et al., 2000]. Therefore, understanding the physics governing the interfacial bond formation and development through interface healing [Wool et al., 1989, de Gennes, 1971] during the AM process is of critical importance. In order to have a polymer interface completely "healed" (i.e., when the interface properties approach bulk properties), the polymer chains in two adjacent layers must undergo chain rearrangement and surface approach, surface wetting, diffusion across the interface, and finally equilibration and randomization. The first two steps are controlled by surface tension of the polymer melts while the latter two are dominated by the relaxation timescales of the polymer. Detailed description of the welding process as well as polymer interface healing is beyond the scope of the current manuscript and has been detailed elsewhere in excellent review articles [Grewell and Benatar, 2008, Zhang and Li, 2016].

In the context of MatEx, when the interface between two deposited layers achieves a high degree of healing, the mechanical properties of the final part are generally homogenous and approach that of parts processed using traditional manufacturing techniques. Figure 3.8 highlights the healing process through molecular diffusion across an interface. It is worth mentioning that although surface tension of the polymer melt controls the interlayer bonding process on the print bed, for the sake of clarity in the illustration it is assumed that the surface tension forces are negligible and only the rheological aspects of the process are emphasized. The thermo-mechanical and rheological characteristics as well as the localized thermal history associated with the deposited layers strongly affect the healing across the interface in MatEx printed parts and thereby control their mechanical properties [McIlroy and Olmsted, 2017b, Snijkers et al., 2015]. Detailed information regarding the thermal history related to both interlayer and intralayer bonding are essential to ensure decent printed part properties and several experimental techniques have been developed to specifically monitor the thermal profile during printing of the deposited layers on the print bed [Seppala and Migler, 2016, Prajapati et al., 2020, Ravoori et al., 2019a].

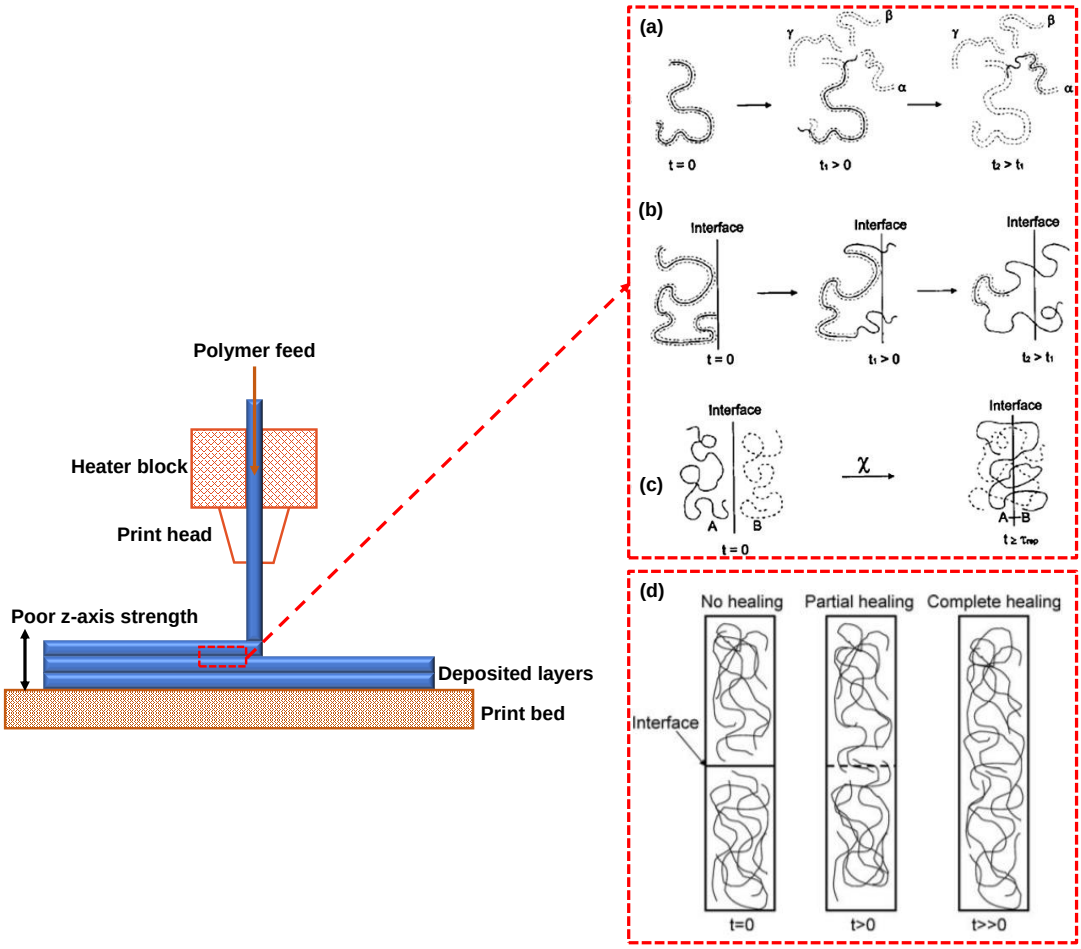


Figure 3.8: Overall depiction of the interfacial polymer diffusion that takes place post-deposition on a print bed during MatEx. (a-c) illustrates the reptation mechanism for molecular diffusion and randomization behavior across the interface during healing for a single polymer chain (χ is the average distance of the segments from the interface between the two adjacent chains) (image reprinted with permission from [Bousmina et al., 1998] Copyright 1998 American Chemical Society); and (d) highlights the details of entire polymer chain networks across the interface during healing (image reprinted with permission from [Grewell and Benatar, 2007] Copyright 2007, Carl Hanser Verlag, Munich)

3.7.2 Sintering models and printed part properties

As is the case with other processing techniques, upon the deposition of successive layers during MatEx interlayer bonding takes place between the adjacent layers through a combination of surface wetting, neck growth, and interfacial polymer chain diffusion and entanglements [Coogan and Kazmer, 2017a, Bellehumeur et al., 2004]. Immediately following the surface wetting staging, viscous sintering of the adjacent layers takes place leading to coalescence [Bellehumeur et al., 2004, Cole et al., 2016]. Pokluda et al. developed a bond formation model that predicted the growth of the bond width, as highlighted in Equation 3.21 [Pokluda et al., 1997].

$$\frac{d\theta}{dt} = \frac{\frac{\Gamma}{a_0\mu}\left(2^{-\frac{5}{3}}\cos\theta\sin\theta(2-\cos\theta)^{\frac{1}{3}}\right)}{(1-\cos\theta)(1+\cos\theta)^{\frac{1}{3}}} \tag{3.21}$$

$$\theta = \sin^{-1}\frac{x}{a} \tag{3.22}$$

where θ is the bond width, given by Equation 3.22, x is the radius of the neck at time t, a is the particle radius at time t, t is time, μ is viscosity, a_0 is initial particle radius, and Γ is the surface tension. Bhalodi et al. [Bhalodi et al., 2019] extended this analysis to include a temperature dependent term to account for the non-isothermality of MatEx. It is worth mentioning that the sintering model developed by Pokluda et al. [Pokluda et al., 1997] is based on the welding of two spheres; recent work has aimed to model the sintering of two cylindrical rods that is more representative of interlayer welding of the extrudate taking place during the MatEx process [Polychronopoulos and Vlachopoulos, 2020].

The final mechanical properties of the printed parts are controlled by the extent of coalescence and hence the quality of interlayer adhesion between the deposited layers [Sun et al., 2008]. The neck growth can only occur when the melt is above its T_g; for a typical MatEx process this is approximately about 2-3 seconds [Seppala and Migler, 2016] and hence only partial neck growth and incomplete coalescence can occur prior to the chains losing mobility [Bhalodi et al., 2019, Polychronopoulos and Vlachopoulos, 2020]. The short timescales for polymer chain diffusion results in the formation of a weld interface where the interdiffusion length is smaller than the radius of gyration (R_g) of the polymer leading to printed parts that recover only a fraction of the bulk properties [Seppala et al., 2017]. The strength of the weld (σ_{weld})

compared to ultimate tensile strength of the polymer (σ_{UTS}) is a function of the welding time (t_{weld}) and the time-averaged reptation time ($\bar{\tau}_{rep}$) as highlighted in Equation 3.23:

$$\frac{\sigma_{weld}}{\sigma_{UTS}} = \left(\frac{t_{\text{weld}}}{\bar{\tau}_{rep}}\right)^{\frac{1}{4}} = \left(\frac{t_{weld} \times D_S}{R_g^2}\right)^{\frac{1}{4}} \tag{3.23}$$

3.7.3 Effect of print parameters on printed part properties

Modifying the printing parameters can significantly affect the thermal history associated with a deposited layer and strength of the corresponding interlayer bonds in a MatEx printed part. Increasing the printing temperature is an option to increase the time the deposited polymer melt stays above the T_g, provided the material exhibits enough thermal stability [Coasey et al., 2020]. Broadening the time window the polymer chains remain above T_g can also be achieved by printing with higher layer thicknesses and/or increased layer widths; a technique that is more commonly used in the BAAM scale rather than FFF [MacDonald et al., 2018], as will be discussed in a later section related to large-format AM. Rheological analysis can be performed using the time-temperature superposition (TTS) principle to calculate the time available for bond formation under isothermal conditions, although MatEx is inherently a non-isothermal process [Coogan and Kazmer, 2017a, Peterson, 2019]. In an effort to extrapolate the rheological response over a wider temperature/time window shift factors based on Williams-Landel-Ferry (WLF), Vogel-Fulcher-Tammann (VFT), and Arrhenius equations can be used depending on the material properties and processing conditions. The WLF equation and the corresponding temperature dependent reptation time (τ_{rep}) are given by Equations 3.3 and 3.24, respectively.

$$\tau_{rep}(T) = \tau_{rep}\left(T_{\text{ref}}\right) \times a_T(T) \tag{3.24}$$

Recent work has investigated the possibility of coupling the neck growth and polymer chain diffusion phenomena to predict the interlayer strength of the printed parts [Coogan and Kazmer, 2020]. The limited amount of polymer chain diffusion caused due to the long relaxation times of the polymer was held responsible for the poor interlayer bond strength. Characterizations performed on a traditional rotational rheometer were used to determine number average relaxation time (τ_n), as highlighted in Equation 3.25, which served as a

metric to predict the interlayer diffusion limitations [Coogan and Kazmer, 2020].

$$\tau_n = \frac{\eta_0(T)}{G_N^0} \tag{3.25}$$

where, η_0 and G_N^0 are the zero-shear viscosity and plateau modulus, respectively. Figure 3.9(a) compares the values of τ_n for three different polymer filaments (high-impact polystyrene, HIPS, ABS, and PC) as a function of localized temperature. The temperature dependence of τ_n) was quantified by estimating η_0 as a function of temperature (using shear rate sweeps) and G_N^0 (using TTS). The temperature of interest for such calculation is the average temperature at the interlayer welds that was experimentally determined to be in the range of 140-170°C; but is also strongly dependent on the processing conditions (cooling rates; thermal gradients; bed and/or environmental temperature). The results indicated PC and HIPS prints achieved complete healing through chain diffusion whereas ABS print healing was limited by diffusion. The high η_0 value of ABS (as highlighted from the steady shear rate sweeps conducted at 190°C presented in Figure 3.9b) was deemed responsible for the higher relaxation timescales that led to incomplete healing since the polymer chains did not have enough time to relax during the printing process to recover the bulk properties. The authors studied the welding phenomena in great detail and the model framework presented was found to be in good agreement with experimental results obtained using amorphous polymers [Coogan and Kazmer, 2020]. Combining semicrystalline polymers, that have issues associated with volumetric shrinkage and mobility restriction due to crystallinity development, within such a framework will pave the way for a more complete understanding the MatEx process that is necessary for future advancements.

For polymers with relatively higher molecular weights, interface healing can take place before the polymer chain can move a distance of the order of its R_g and hence the welding time is lower than the reptation time for such polymers [Coogan and Kazmer, 2020]. In a more comprehensive study, McIlroy et al. [McIlroy and Olmsted, 2017b] modeled the chain relaxation and stretch, entanglement recovery, and chain diffusion to predict the interfacial fracture toughness in a MatEx printed part. Figure 3.9(c) highlights the effect of polymer chain alignment during flow that can lead to anisotropic diffusions and therefore hinder the welding process by limiting the inter-filament chain diffusion. The authors commented on the high levels of chain stretching and disentanglement due to shear at the nozzle which was not fully recovered due to the rapid cooling post-deposition on the printer bed. The higher shear rates caused greater deformation that takes additional time to relax and hence there

is reduced time for chain entanglement to occur prior to the polymer melt cooling below T_g which decreases the mechanical strength at the weld [McIlroy and Olmsted, 2017b].

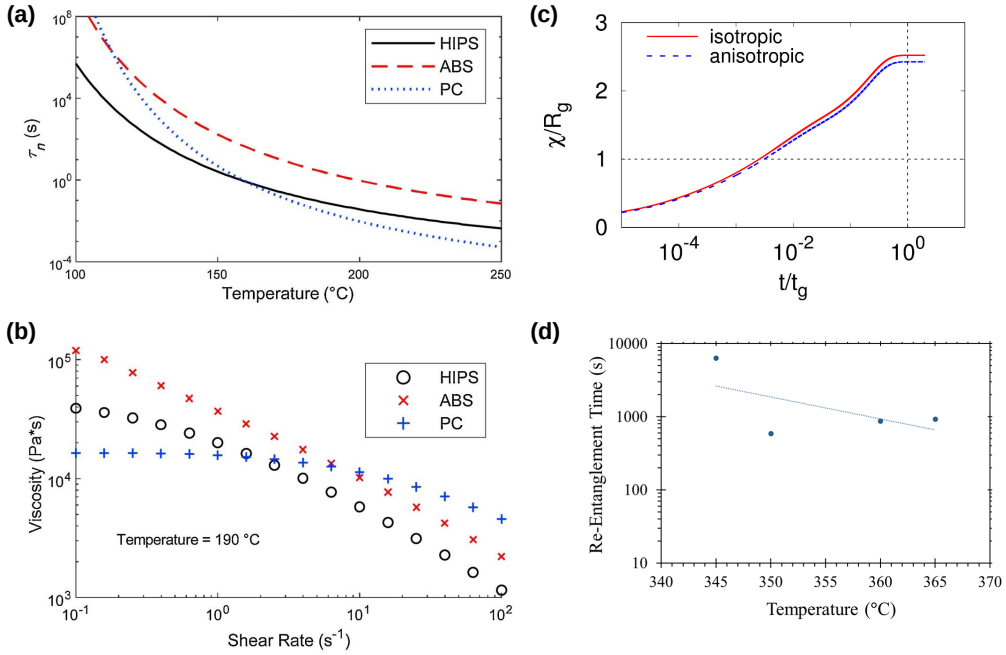


Figure 3.9: (a) Effect of temperature on the number averaged relaxation timescales of three different polymer filaments (image reprinted from [Coogan and Kazmer, 2020] with permission from Elsevier); (b) steady shear rate sweeps performed using a rotational rheometer on the three materials at 190°C (image reprinted from [Coogan and Kazmer, 2020] with permission from Elsevier); (c) The polymer interdiffusion distance (χ) normalized to the radius of gyration of the polymer size, as a function of time. The X-axis is scaled by the time taken to reach T_g such that at $t/t_g = 1, T = T_g$. Details of the model can be found in [McIlroy and Olmsted, 2017b] (image reprinted from [Das et al., 2021c] with permission from Springer Nature); and (d) The dependence of complete re-entanglement time of PEI on the temperature of the print, obtained using interrupted shear measurements performed on a cone and plate rheometer (image reprinted from [Gilmer et al., 2019] Copyright 2019 American Chemical Society).

The mechanical properties at the interlayer region are controlled by the MW between entanglements at the welds and as such, the fracture toughness of the welds (G_c^{weld}) can be estimated using Equation 3.26. In this case, although the interdiffusion lengths were higher than R_g of the polymer, reduced re-entanglement density resulted in poor interfacial bond toughness in the printed parts [McIlroy and Olmsted, 2017b]. An important finding from

these studies was that polymer chain interdiffusion and entanglements (and not the neck growth during surface wetting) dictate the properties of interfacial welds [Gao et al., 2021].

$$G_C^{\text{weld}} \sim \left(1 - \frac{1}{q v_W Z}\right) \tag{3.26}$$

In the above equation, q is a factor accounting for the fraction of entanglements post-deformation (or post-printing) compared to the bulk (initial state) [Berger, 1990] and ν_w is the weld entanglement fraction (which provides a measure of the robustness of the entangled network) [McIlroy and Olmsted, 2017b].

3.7.4 Mechanical integrity of the deposited extrudate

The print bed temperature is often controlled in order to ensure sintering of the polymer layers by imparting enough thermal energy so that the polymer chains can diffuse across the layers. However, too high a bed temperature can result in the deposited material transitioning into its flow state by losing its mechanical stability as more and more layers are deposited on it. Since the effects of shear are minimal when the polymer is deposited on the print bed, the effect of chain disentanglement at different cooling rates, representative of the MatEx process, can be studied in a rotational rheometer operating in the zero-shear regime.

Higher values of zero shear viscosity (η_0) result in printed parts that exhibit better shape retention and mechanical integrity, as highlighted in Table **??**. In addition, the deposited polymer melt should exhibit elastically dominant behavior (such that $G"/G' = tan\delta$ is less than unity) as well as having a high yield stress (σ_y) to prevent the extrudate from cracking post-extrusion. The former behavior can be rheologically characterized using frequency sweeps under the relevant temperatures and an appropriate linear viscoelastic (LVE) strain while the σ_y can be obtained using the shear stress sweeps under MatEx relevant process conditions. Moreover, the rapid switching between the magnitudes of G' and G" under the influence of shear must be ensured to guarantee consistent extrusion through the nozzle and ensuring molecular interdiffusion ($G" > G'$) while properly controlling the mechanical and shape integrity of the deposited layers on the printer bed ($G' > G"$) [O'Mahony et al., 2020].

Sanchez et al. [Sanchez et al., 2019] investigated the effect of rheological properties on the print quality of PLA and ABS parts. The viscosity at the print temperature needs to be low enough to extrude but also high enough to retain its shape once the polymer chain

has relaxed. The low viscosity assists the coalescence between the adjacent layers since the polymer chains have enough molecular mobility to diffuse and entangle across the interface. But too low a viscosity results in poor resolution of the deposited layers that adversely affects the shape and dimensional accuracy of the final part. Moreover, a deposited layer should be able to support the subsequent layers without collapsing due to the creep phenomena. The authors proposed that a trade-off between the viscous and elastic nature of the polymer melt as well as parameter optimization can result in prints with excellent dimensional stability and geometric accuracy that exhibit minimal surface roughness [Sanchez et al., 2019]. However, drawing such conclusions from results obtained from only two polymers processed under selected conditions might be a bit premature and further research is required to verify the claims.

3.7.5 Quantifying the extent of chain interdiffusion

To quantify the required time for the interdiffusion of the polymer chains to return the mechanical properties of the weld to those of the bulk, Pisipati and Baird performed interrupted shear rheology using a rotational shear rheometer [Pisipati and Baird, 1984]. The corresponding time is referred to as the complete re-entanglement time, or the time required for the polymer chains on either side of the weld to diffuse across the interface and re-entangle to a state similar to that of the bulk. The test involves a two-step shearing process with a specified relaxation time between the shearing steps. Due to the inception of shear, a stress overshoot is produced at the start of each shearing step. The relationship between the two transient stress overshoot values can provide information on the re-entanglement of the polymer. The amount of recovery, or healing, can be calculated using Equation 3.27.

$$\% \text{ recovery } = \frac{\left[\tau_m\left(\dot{\gamma}, t_r\right) - \tau_{ss}\right] / \tau_m\left(\dot{\gamma}, t_r\right)}{\left[\tau_m(\dot{\gamma}, \infty) - \tau_{ss}\right] / \tau_m(\dot{\gamma}, \infty)} \tag{3.27}$$

where, $\tau_m\left(\dot{\gamma}, t_r\right)$ is the value of the stress overshoot after the relaxation time, $\tau_m(\dot{\gamma}, \infty)$ is the value of the stress overshoot after infinite relaxation time, and τ_{ss} is the steady state stress value. This test can be performed at multiple relaxation times and the results can be extrapolated to 100% recovery. Although, the authors developed the method for injection molding applications, these characterizations can be easily extended for MatEx processing [Gilmer et al., 2019]. Gilmer et al. [Gilmer et al., 2019] estimated the re-entanglement

times for polyether imide (PEI) at different print temperatures using cone and plate fixtures on a rotational rheometer in an effort to explain the nonisothermal behavior of the chain diffusion at the layer interfaces, as highlighted in Figure 3.9(d). The logarithmic dependence of the re-entanglement time on the print temperature suggested the rapid evolution of the interfacial bond strength, presumably within the first few seconds after deposition. In other words, the major portion of the entanglements across the interface takes place rapidly while only a small amount of entanglements are formed over the remaining time period, thereby restoring bulk properties of the polymer [Gilmer et al., 2019]. Previous work has highlighted the importance of re-entanglement density (instead of interdiffusion length-scales higher than the polymer's R_g [McIlroy and Olmsted, 2017b]) in dictating the mechanical properties of the interface under typical processing conditions [McIlroy and Olmsted, 2017b]. Finally, the repeated nonisothermal thermal history associated with FFF affects the interfacial strength of the printed parts by controlling the time windows for surface wetting, chain diffusion, and chain re-entanglement.

3.7.6 Routes to promote interlayer welding in printed parts

In a very recent study, researchers employed molecularly aware rheological models (Rolie-Poly equations) and coupled with experimental birefringence measurements to investigate the weld strength of an amorphous polymer [Costanzo et al., 2020]. The authors reported that the dynamic orientation of the entangled polymer chains in the printed parts resulted in lower weld strength and interdiffusion across the deposited layers did not play a significant role, as has been reported in prior literature. The molecular rigidity of polymers such as PEI is higher than that of PLA resulting in reduced chain mobility in the former polymer where chain diffusion controls the weld properties.

Thermal annealing of parts post-printing has been reported as a facile way of improving the mechanical properties for both amorphous and semi-crystalline polymers; often resulting in properties comparable to injection molded counterparts [Das et al., 2020b, Hart et al., 2018a, Hart et al., 2020, Fitzharris et al., 2018, Dunn et al., 2019]. Although, the annealing is usually performed at temperatures approximately 20-40°C lower than the temperatures at which the polymers begin to flow; there is no adequate prediction about the duration of thermal treatment. Hart et al. [Hart et al., 2018a, Hart et al., 2020] calculated the required annealing time for sufficient healing ($t_{annealing}$) based on surface-wetting controlled healing

models using Equation 3.28.

$$t_{\text{annealing}} = \frac{3a_0\eta}{\Gamma} \tag{3.28}$$

where, a_0, Γ, and η are the radius of the deposited extrudate, surface tension and viscosity of the polymer of the polymer at the annealing temperature, respectively. Based on their experimental findings on semicrystalline PLA and amorphous ABS, the authors concluded that the healing times for semicrystalline polymers to be 2-3 orders of magnitude lower than that for amorphous polymers [Hart et al., 2020]. Although Equation 3.28 provides an acceptable rule-of-thumb, further research must be performed to validate it's the applicability for other polymers, especially ones having a higher degree of crystallinity than PLA.

Polyvinyl chloride (PVC) based polymers were evaluated for use in FFF and proper processing conditions were selected based on a buckling analysis, similar to that highlighted in Equations 3.3-3.7 [Calafel et al., 2020]. Further, the interlayer adhesion was studied using the Dahlquist criterion for the relaxation modulus as a metric to ensure welding of the interfaces. However, molecular interpretation of the results in terms of chain stretch and extent of disentanglement was not provided. Along similar lines, Peñas et al. [Peñas et al., 2020] investigated the extrusion based AM of PVC/acrylate copolymers and found filament buckling to be a serious issue in FFF of the material. However, the polymer was still printable using a screw-based extrusion system and the associated viscoelastic and rheological characteristics to ensure interlayer welding was studied. Stress-relaxation experiments carried out in a parallel-plate fixture revealed that interlayer welding can occur for approximately 1s at 100°C; these findings help in tuning the printing parameters.

The current material library for MatEx is largely dominated by amorphous polymers with the semicrystalline polymers being largely relegated to academic research. The majority of industrial AM involving semicrystalline polymers is done through PBF and hence application in MatEx is fairly limited. As a result, the importance of rheology of such polymers has not been addressed in great detail in the current manuscript with respect to the deposition process during MatEx. In case of such polymers, the viscosity can reduce substantially (2-3 orders of magnitude) after melting which can lead to destabilization of the deposited filaments [Mackay, 2018]. Moreover, the interlayer bonding initiated by the neck growth of the adjacent layers occurs within a very short time window when the polymer melt remains above the crystallization temperature [Shahriar et al., 2017]. Shahrier et al. [Shahriar et al.,

2017] applied Equation 3.21 to a semicrystalline polymer (PEEK) and demonstrated that the model is unable to accurately predict the coalescence of a semicrystalline polymer below the melting temperature (T_m), although it is in good agreement with experimental values when the material coalesces above T_m.

Candal et al. investigated the rheological properties of biodegradable semicrystalline polyesters in relation to extrusion through a printer nozzle and subsequent interlayer welding [Candal et al., 2020]. Continuous flow and SAOS measurements on a parallel plate fixture indicated the viscosity of the polymers to be in range for successful extrusion. TTS analysis was performed to calculate Z and it was correlated to the interlayer weld strength of the printed parts. However, contradictory results were obtained since low Z values (compared to PLA) resulted in decent strength across the interface. In general, lower Z suggests higher M_e, i.e., fewer entanglements and therefore it is possible that, for these polymers, molecular chain diffusion might not be the controlling factor during weld formation.

Srinivas et al. [Srinivas et al., 2020] incorporated low molecular weight amorphous additives to arrest the fast crystallization of PLA and help in MatEx processing. SAOS results collected at the print temperature indicated both an upper limit (5000 Pa.s) and a lower limit (500 Pa.s) of the blend's η_0 values for successful extrusion. Blends with values higher than the upper threshold did not extrude while those with values lesser than the lower threshold failed due to poor shape retention. The results also revealed that at an optimum loading of the additives, the printed parts had decent interlayer diffusion and re-entanglement across the deposited layers. This along with a phenomenon known as co-crystallization that occurred at the interface, resulted in a 15% improvement in weld strength of the printed parts166. The impact of such additives can be qualitatively estimated through rapid melt flow index measurements while the effect on welding time can be investigated by calculating the reptation time for the blends from a TTS mastercurve obtained from SAOS experiments [Ko et al., 2019].

Finally, the effect of the printing conditions on the adhesion between the deposited polymer filaments can be quantitatively assessed through tack testing in modified rheometer setups [Tripathi et al., 2000]. Valuable information regarding the force needed to initiate debonding and insights into the failure modes can be obtained through such characterizations [Sanatgar et al., 2017]. Although such experimental techniques do not constitute the classical rheological experimentation for MatEx; they provide useful tools for better interpreting the characteristics of the polymer extrudate deposited on the print bed. Equipped with these

results, it would be possible to design printers and modify processing conditions in a way to maximize the interlayer bonding during MatEx in order to print parts that approach injection molded properties.

3.8 Discussion and future outlook

3.8.1 Print nozzle

The understanding of the thermal, rheological, and flow behaviors of polymeric materials inside the nozzle has recently been expanded by a substantial amount. A molecular study exploring the chain orientation imposed during extrusion followed by relaxation and inter-diffusion would provide significant insight into the resultant properties and how they are influenced by the printing parameters such as filament feed rate and liquefier temperature. Furthermore, most current research studies a material's behavior outside the nozzle to estimate the accuracy of the models representing a material inside the nozzle. However, a more direct measurement of the temperature, pressure, and velocity profiles inside the liquefier would be more useful for validation of these modeling approaches. While a number of studies demonstrate an ability to perform these measurements, they do not agree on agree on their accuracy and application to studying the rheological behavior of the polymer, most likely due to the transient nature of the printing process60,61. More definitive and consistent measurement techniques are vital to furthering the understanding of various behaviors inside the nozzle that will translate to the properties in the stand-off region and subsequent deposition. Finally, since multimaterial extrusion is gaining popularity in the 3D printing community, collective viscosity models that can predict the shear viscosities inside the nozzle for different polymer melts must be studied in the context of MatEx [Kim, 2020].

3.8.2 Stand-off region

Although significant experimental and numerical research have been realized for the MatEx process in the standoff region, die swelling, and strand deposition, further work needs to be performed to investigate the effects of additional nozzle configuration with different angularity, gap, and cylindricity as well as speed ratio on the cross-section of the strand. The deposition of multiple layers must be simulated by accounting for the complex multiphysics

associated with the process along with its rheological implications to predict the porosity and void density of the printed part. Die-swell can be controlled by tuning the print temperature or by printing at a velocity slightly higher than the filament feed rate (the filament stretching caused by this reduces the die-swell). However, the filament stretching imparts additional deformations to the polymer chains that impact the relaxation behavior of the extrudate and subsequently affects final part properties. The effects of gravity can also help with drawing of the extrudate to reduce swelling; however, this is rarely achieved due to the high print speeds and small heights of the stand-off region, largely because it is desired to transfer as much thermal energy to the previous layer to enhance interlayer adhesion following deposition on the printer bed/prior layer. Both extensional rheology and interrupted shear measurements can provide valuable insights regarding these effects.

3.8.3 Printer bed

As far as the extrudate behavior post-deposition on the printer bed is concerned, proper rheological insights can help in enhancing the printed part properties and isotropy through intelligent process modeling and modifications. For example, localized heating at the interface of the deposited layers can provide mobility to the polymer chains for a longer time period, allowing them to diffuse across the interface to a higher extent and therefore the interface can heal to a greater degree. Too much heat input can lead to the deposited material losing its shape resolution and adversely affecting the geometric accuracy of the printed parts. However, the degree of heating and its temporal distribution can only be predicted once detailed knowledge about the rheology (under the influence of the complex multiphysics associated with the process) that governs the welding dynamics is obtained. Moreover, such processing customization can greatly reduce the time required for manufacturing if they can be performed in-situ rather than subjecting the feedstock or the prints to different treatments before or after the print (e.g., thermal annealing); this can greatly advance the potential of MatEx, especially for more widespread industrial adoption.

3.8.4 Big Area Additive Manufacturing (BAAM)

Recent advances in BAAM have led to the development of capabilities that can process neat and/or filled thermoplastics using extrusion based techniques at high speeds. The

major difference between BAAM and FFF is the use of an extruder to process pelletized polymer feedstocks instead of a heated nozzle with filament-based feeds. Most of the research associated with rheological implications in BAAM are in the preliminary stage, focusing on the printability of the polymers and are therefore discussed in the future outlook section of the current manuscript. Ajinjeru et al. [Ajinjeru et al., 2016] performed SAOS on ABS, polyphenylsulfone (PPSU), carbon fiber (CF) reinforced ABS and PPS to characterize the shear thinning behavior of the polymers at shear rates relevant to BAAM (100-250s^{-1})171. The viscosity was found to increase drastically upon the addition of CFs due to their stiffness while increase in temperature decreased the viscosity and promoted flowability.

Figures 3.10(a-c) illustrates the dependence of complex viscosity on the angular frequency at different CF loading and processing temperatures. The addition of CF enhances the shear thinning behavior of PPSU compared to the neat polymer (exhibiting a typical Newtonian plateau with the onset of shear thinning at approximately $\sim$100s^{-1}), thereby aiding the flowability during extrusion stage of the printing process. Moreover, the effect of temperature on reducing the complex viscosity is quite apparent from the presented data; reiterating its importance as a controlling parameter to ensure smooth extrusion.

Figures 3.10(d) and 3.10(e) highlights the results from a typical SAOS test (10^{-1}-10^{3} rad s^{-1}) obtained using parallel plate rheology for neat and CF reinforced PPSU. Prior to fiber incorporation, G" > G' in PPSU indicating the viscous dominated behavior of the material (addition of the fibers restores the G' to the same order as G") [Ajinjeru et al., 2018b]. In order to ensure proper deposition of the viscous polymer melt on the print bed and subsequent shape retention (low viscosity polymer melts hinders this), it is imperative that the deformation strains are able to relax to a significant extent. This can be ensured by printing with longer layer times (or slower print speeds), allowing a deposited layer to have certain mechanical integrity before the deposition of the next layer. However, too long of a layer time can result in the layer cooling below T_g and the chains losing molecular mobility to re-entangle across the interface resulting in printed parts with poor interlayer adhesion. The impact of polymer rheology on the final printed part properties can be studied by analyzing the interlayer bonding during the printing process. Figure 3.10(f) highlights a scanning electron micrograph of the interlayer region of glass fiber reinforced ABS composite and provides evidence of poor interlayer adhesion and void formation caused due to processing induced defects [Schnittker et al., 2019]. The orientation of the fibers in the polymer matrix also controls the part properties; as highlighted in Fig. 3.10(f) most of the glass fibers are

oriented in the extrusion direction while a minor number of fibers are aligned in a direction diagonal to the extrusion flow.

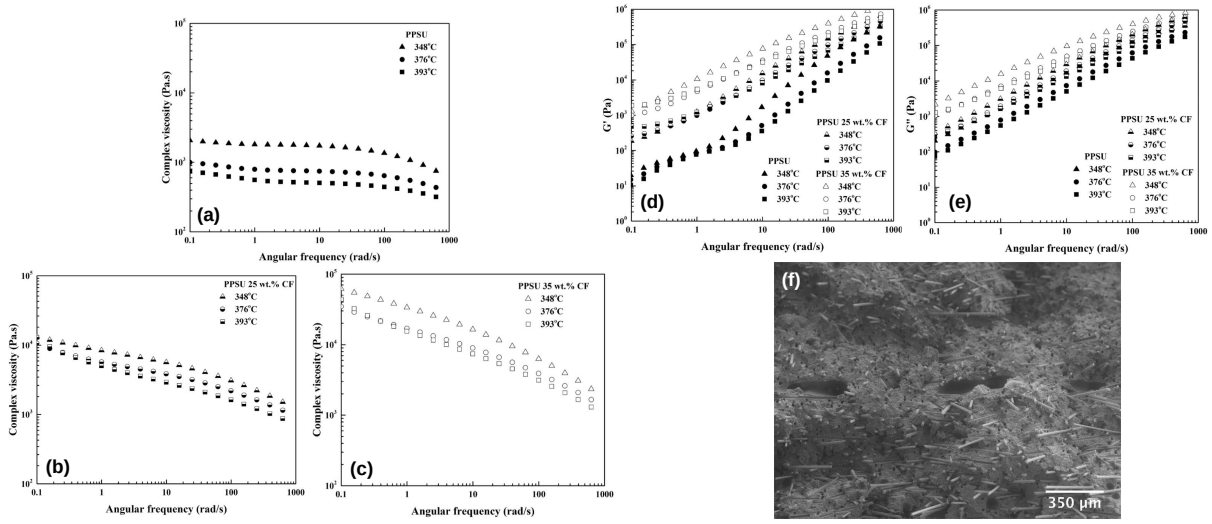


Figure 3.10: Variation in the complex viscosity of (a) neat, (b) 25 wt% CF reinforced PPSU, and (c) 35 wt% CF reinforced PPSU as a function of angular frequency; variation in the (d) storage and (e) loss modulus for neat and CF reinforced PPSU as a function of angular frequency obtained at three different processing temperatures using a linear viscoelastic strain of 1%; The rheology tests were performed in a 25mm parallel plate fixture with a gap height in the range of 1.5-1.8mm and in nitrogen environment to limit any thermally triggered side reactions and/or degradation of the polymers (all the images are reprinted from [Ajinjeru et al., 2018b] with permission from Elsevier); and (f) a typical SEM image of the interlayer bond obtained during BAAM scale printing of 20 wt% glass fiber reinforced ABS using a Cincinnati BAAM-100 system (image reprinted from [Schnittker et al., 2019] with permission from Elsevier).

Subsequent work from the same group established a pressure-dependent extrusion criteria for identifying printing parameters using a thermo-rheological model based on SAOS tests over the shear rates of interest ($\sim$30-100^{-1}) [Ajinjeru et al., 2017]. A similar study with CF reinforced thermoplastics revealed the increased elastic response (necessary for extrudate shape retention post-extrusion) and greater shear-thinning behavior (ensuring higher flow rates) after fiber incorporation compared to the neat polymers [Ajinjeru et al., 2019]. SAOS tests performed on neat and CF reinforced polyether imide (PEI) revealed G" $> G$' over the processing window investigated [Ajinjeru et al., 2018a]. Although this guarantees uniform

flow through the extruder, process modifications (such as longer layer times) are necessary to ensure that the extrudate can retain its shape post-extrusion. Compared to the neat polymer, CF reinforced versions significantly augmented the shear thinning behavior and viscosity [Ajinjeru et al., 2018a], a trend that has been reported previously with ABS and PPSU [Ajinjeru et al., 2016]. An inherent assumption of these studies is the applicability of Cox-Merz's rule which might not hold for fiber reinforced composites and polymers (such as PEI, PPS, etc.) that might experience crosslinking/degradation at high processing temperatures. However, the rheological approach outlined can be extended to a variety of thermoplastics and can serve as a rapid screening technique to recognize suitable print temperatures and print speeds (shear rates) for proper extrudability and printability of the material.

As evident from the above discussion, there is a great deal of research addressing the rheological properties of polymers that are of importance during the extrusion stage of BAAM. However, only a limited amount of work specifically relates polymer rheology with print properties post-extrusion in BAAM, specifically, in the stand-off region and post-deposition on the print bed. Given the significantly higher thermal mass associated with BAAM compared to FFF, the increased thermal gradients can play an important role in controlling property evolution in the extrudate. Issues arising from such steep thermal gradients can be addressed to varying extents by heating the print bed (up to polymer's T_g) or by introducing additional heating accessories to have a more controlled cooling profile resulting in better mechanical properties in the printed parts [Kishore et al., 2017b, Nycz et al., 2020]. The rheological characteristics of the extrudate will be very sensitive to any changes in thermal profile and hence monitoring the temperature distribution post-extrusion is of utmost importance.

Kishore et al. [Kishore et al., 2017a] investigated the origin of sharkskin type instabilities in BAAM extrudates and related it to the polymer's viscoelastic nature and processing history. The authors performed capillary rheology on neat and CF reinforced polyether ketone ketone (PEKK) at different shear rates (100-4000s^{-1}) and studied the extrudate surface for the appearance of any instabilities. For neat PEKK and 30wt% CF/PEKK, no defects were observed within the shear rates studied. However, for the 40wt% CF/PEKK samples, sharkskin was observed at shear rates >100s^{-1}. SAOS results indicated that the origin of the instabilities might be due to the elastic effects dominating over the viscous effects ($G' > G''$), in contrast to the PEI results discussed above, at increased shear rates [Kishore et al., 2017a].

As the case within many of the studies in FFF, most of the investigations involving BAAM

limit their focus on a particular stage of the printing process (commonly, the flow through the extruder). With the development of more sophisticated experimental techniques and modeling frameworks, it is expected that the future studies in BAAM will aim to study the entire printing process to better establish the processing-property relationships that are critical in advancing the understanding of the process and will potentially lead to more widespread industrial adoption of BAAM as a manufacturing technique.

3.8.5 Combining experimental and modeling approaches

From the modeling perspective, employing molecularly aware rheological models have provided significant insights into the weld formation upon deposition on the print bed [McIlroy and Olmsted, 2017a, McIlroy and Olmsted, 2017b]. Figure 3.11(a) highlights the dependence of the weld fracture toughness on Z and the print temperature. For certain printing condition, there is an upper limit of polymer MW that can be successfully printed to achieve weld fracture strengths that are equal to the bulk strength. At increased Z values the weld strength is greatly affected by the disentanglement effects, substantiated by the drop-off in the normalized strength values in Figure 3.11(a) [McIlroy and Olmsted, 2017b]. Such models not only capture the orientation of the chains but also the disentanglement of the polymer chains caused due to extrusion through the nozzle. Prior knowledge about the conformational states of the polymer chains during deposition will aid in predicting the mechanism of interlayer diffusion. The degree of healing in the printed parts is dictated by the extent of chain entanglement recovery through reptation post-extrusion on the print bed. However, the effects of different molecular weights and molecular weight distributions is yet to be accounted for in these models; but preliminary research to address this limitation has already been initiated employing Rolie-Double-Poly models [Boudara et al., 2018].

In order to better characterize the polymers, large amplitude oscillatory shear (LAOS) analysis can also be performed. Experimental characterizations of the high levels of chain stretching and deformation can be obtained through LAOS experiments that can be employed to substantiate the claims of the molecularly aware models. Valuable insights into the polymer chain microstructure and morphology development can be obtained from such analysis [Hyun et al., 2011] that can lead to a more physics-guided polymer feedstock design for MatEx by better elucidation of the associated structure-processing relationships. In-situ rheological measurements can also provide experimental validation for the model predictions but de-

signing such a setup is a non-trivial task and should be the focus of future research. The entire idea behind such an approach is to achieve a holistic understanding of the process and address the current disconnect between model predictions and experimental findings as well as how that translates to printed part properties.

3.8.6 Incorporating semicrystalline polymers

In the case of semicrystalline polymers, the crystallization process in the extrudate is also controlled by the associated flow and temperature fields that can affect the final part properties [McIlroy, 2019]. Printing parameters and nozzle wall shear rates can significantly affect the crystallization kinetics for such polymers [Northcutt et al., 2018]. Figure 3.11(b) highlights the time required to achieve 10% of the maximum crystallinity in PCL as a function of wall shear rates. Increased wall shear rates can be achieved during printing at increased temperatures due to the lower resistance to flow under such conditions; however, the higher shear rates augmented the crystallization kinetics to a greater extent when printing at lower temperatures [Northcutt et al., 2018]. A possible reason for the increased crystallization rate might be the incomplete melting of the semicrystalline regions before extrusion through the print nozzle. Any unmelted crystalline nuclei in the extrudate can serve as a building block for crystalline domains to develop thereby increasing the rate of crystallization at low print temperatures [Lorenzo et al., 2006]. Further research is needed to understand the impact of flow-induced crystallization under the complex flow and thermal fields present inside the nozzle [Peng et al., 2018].

McIlroy et al. [McIlroy et al., 2019] the effect of chain deformation during extrusion through the nozzle and during the deposition process on the development of crystalline morphology in PLA printed parts. Crystallization on the surface of the deposited extrudate is promoted by the chain stretching and a gradient in crystalline nuclei density is observed from the surface to the interior of the extrudate. Post-thermal annealing, spherulites are observed in the interlayer welds due to flow induced crystallization effects [McIlroy et al., 2019]. The extent of chain stretching as well as the variation in nucleation density was also modeled in this work and validated against experimental findings. The importance of flow on the crystallization behavior and the timescales associated with flow induced crystallization can be described using De defined as the ratio of the stretch relaxation time (τ_R) to the time required for the polymer melt to cool to its melting temperature (τ_m) [McIlroy, 2019]. Recent

experimental research has probed the stability and features of the flow induced crystalline morphology through in-situ small angle X-ray scattering techniques184 but the gap between such findings and model predictions is yet to be breached.

It is generally difficult to monitor the rheological properties during crystallization because of the complex temperature dependence. However, correlating the crystallization behavior and rheological properties are of utmost importance in order to understand implications of the processing history on printed part properties. Successful coupling of a rheometer with a Raman spectrometer provides a unique capability to track polymer crystallization using correlative spectroscopy that can detect complex modulus fluctuations (rheology) with structural conformational changes (spectroscopy) in the crystallizing melt [Kotula and Migler, 2017]. Such an approach allows for better elucidation of the structure-property-processing relationships associated with MatEx. In a very recent work, Kotula and Migler [Kotula and Migler, 2021] discuss the latest advancements in experimental characterizations techniques for simultaneous monitoring of crystallinity and rheology along with recent simulations studies.

Models accounting for such enhanced shear flow-induced crystallization kinetics have been recently developed and can successfully correlate the crystallinity evolution to the complex shear modulus over a wide frequency range [Kotula, 2020]. However, these models did not account for the two-phase viscoelastic behavior of a semicrystalline polymer melt. Recently, a FEM modeling framework has been established that accounts for the associated transport phenomena (mass, momentum, and energy) along with the nonlinear viscoelastic response and crystallization behavior of isotactic PP in a filament stretching extensional rheometer [van Berlo et al., 2020]. The effect of flow on the rheological characteristics and the relaxation spectra prior to the onset of crystallization have been studied. Future work can aim to verify model predictions by studying the processing-property relationships that lead to different morphological and rheological characteristics.

3.8.7 Rheological implications of incorporating fillers

Another important aspect that needs to be investigated in greater details is the effect of fiber reinforcements and other fillers in polymers on the rheological properties relevant to the printing process. Developing a rapid technique based on rheological characterizations to screen a variety of feedstocks containing different fiber type and varying fiber loadings

will provide a better understanding of the "printability" criterion as well as provide insights into the evolution of interlayer adhesion during MatEx [Lamm et al., 2020]. Nguyen et al. [Nguyen et al., 2018] studied the effect of lignin and CF addition to an amorphous polymer in relation to its rheological characteristics and printed part properties. The phase separation and extent of intermolecular interactions between the filler and the polymer matrix was characterized from SAOS measurements by utilizing van Gurp-Palmen plots [Van Gurp and Palmen, 1998]. The van-Gurp Palmen plot is often employed to check the validity of a TTS from a set of oscillatory shear measurements obtained at different temperatures. Provided the material is thermorheologically "simple", the oscillatory data should superpose into a single van Gurp-Palmen plot without any shifting [Qian and McKenna, 2018, Dealy and Plazek, 2009]. The van-Gurp Palmen plot can provide significant insights into the molecular architecture but is also highly sensitive to changes in MW and polydispersity of a polymer [Qian and McKenna, 2018].

Liu et al. [Liu et al., 2018b] investigated CF filled polyphenylene sulfide (PPS) composite through SAOS in an effort to shed insights into the microstructure developed during printing. The prints filled samples exhibited enhanced interlayer chain diffusion that resulted in almost double the interlayer welding strength compared to that of the neat polymer. PPS had minimal levels of chain branching below 340°C but the number of linear chains drastically reduced above that temperature (as evidenced by the breakdown of the superposition analysis illustrated in the van-Gurp Palmen plot in Figure 3.11c). The resulting branched structure exhibited a higher resistance to flow compared to its linear counterpart having similar molecular weights [Stadler et al., 2006, Malmberg et al., 2002]. The increased resistance meant a lower propensity of the polymer chains to diffuse across the interface resulting in limited interlayer bond strength. Moreover, since PPS is semicrystalline, the mobility of the chains reduces significantly as the temperature of the layers drops below T_m and is almost completely arrested as it approached T_g. Finally, to better understand trans-crystallization across the deposited layers and evolution of interlayer bonding under non-isothermal conditions, future research should examine the coupled effects of chain rigidity, MW, and MWD on the relaxation spectra of the composites by performing detailed rheological measurements that can succinctly capture both the transient viscoelastic response as well as the chain interdiffusion kinetics.

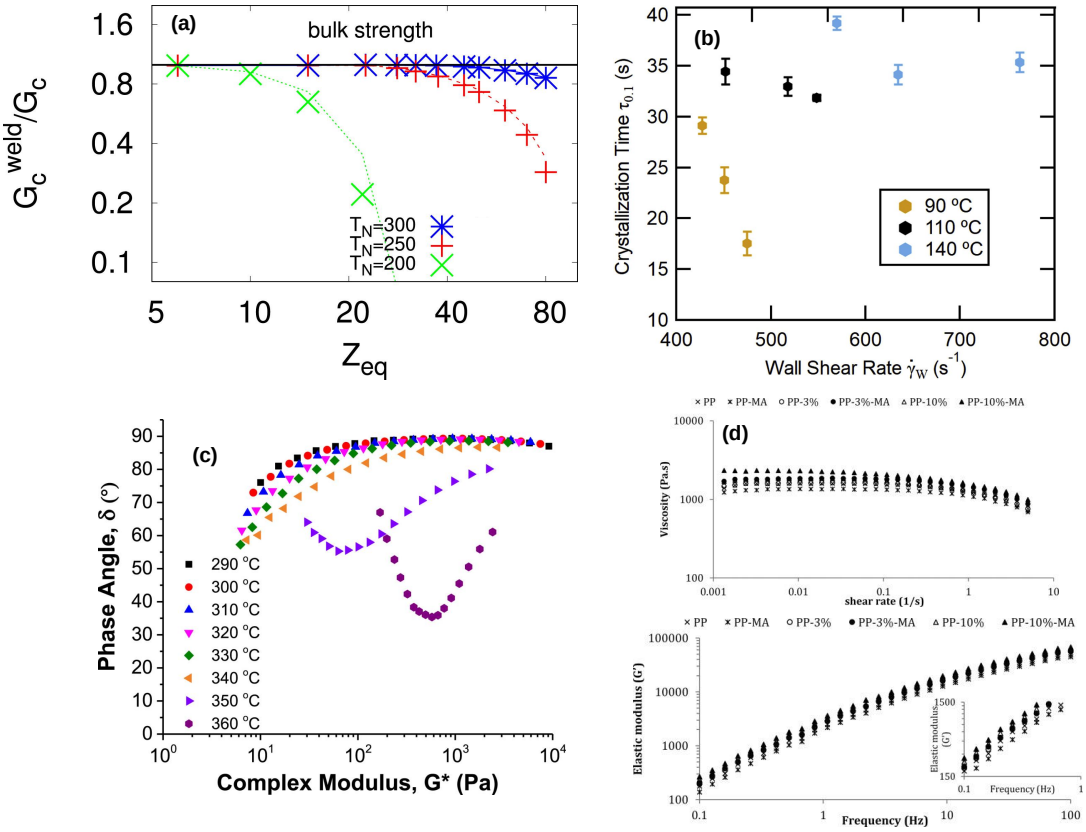


Figure 3.11: (a) Effect of print temperature (200, 250, and 300°C) and entanglement number on the interfacial weld strength of a polycarbonate part printed at constant speed (10 mm s^{-1}). The solid lines represent Equation 3.26 (image reprinted from [McIlroy and Graham, 2018] with permission from Elsevier); (b) Time required to achieve 10% of the maximum crystallinity in PCL printed parts as a function of the corrected nozzle wall shear rates under varying print temperatures (90, 110, and 140°C) (image reprinted from [Northcutt et al., 2018] with permission from Elsevier); (c) The van Gurp-Palmen plots illustrating the variation of phase angle with complex modulus of neat PPS. The data presented in the figure were obtained by performing isothermal frequency sweeps at different temperatures (image reprinted from [Liu et al., 2018b] with permission from Elsevier); and (d) Variation in viscosity (η) and elastic modulus (G') of PP/CNF composites as a function of shear rate and frequency, respectively, obtained from steady shear flow and SAOS tests. The sample nomenclature in the figure represents PP (main component)-X% (weight percent of CNFs in the blends)-MA (maleic anhydride modified PP) (image reprinted from [Wang et al., 2018a] with permission from John Wiley & Sons).

Moreover, z-axis adhesion is a limiting factor for parts manufactured using AM that can

be addressed to a certain extent with the use of fillers with higher aspect ratios. The incorporation of such fibers can lead to be a higher wetted interfacial area across which enhanced polymer chain diffusion and entanglements are promoted that helps in better stress dissipation [Bréchet et al., 2001]. Therefore, rheological studies that address the implications of filler shape on the printing process will lead to a physics-guided development of tailored fiber-reinforced feedstocks for MatEx. Moreover, the shape of the fillers can lead to flow instabilities during filament preparation and FFF-based printing. Baldi et al. [Baldi et al., 2014] reported that the presence of lamellar talc particles stabilized the flow in HDPE melt while spherical glass beads and needle-shaped discontinuous glass fibers led to a stick-slip effect.

Fillers have also been used to arrest the high degrees of volumetric shrinkage associated with MatEx of semicrystalline polymers [Carneiro et al., 2015, Spoerk et al., 2017, Spoerk et al., 2018b]. Cellulose based materials, such as cellulose nanofibril (CNF) and cellulose nanocrystal (CNC), are two such filler materials that have garnered recent research interests. Due to its relatively higher aspect ratios and high entanglement density, CNF can serve as a bridge between two successive deposited layers during MatEx and additionally enhance the mechanical properties of the printed parts. Although detailed characterizations of such nanocellulose materials have been reported in prior literature, but there is only limited work on estimating the rheological properties at MatEx relevant conditions [Sutliff et al., 2020]. Detailed rheological characterizations of CNF based polymer composites is fairly limited in current literature; although Wang et al. [Wang et al., 2018a] reported increased resistance to flow and higher elastic modulus under the shear rates (and frequencies) investigated upon CNF addition to neat PP, as evidenced in Figure 3.11(d). The addition of CNF imparted rigidity to the composite and improved interaction between the filler and the polymer matrix was held responsible for such observations. However, the applicability of these results to MatEx processing is still questionable since the authors performed all the rheological characterizations at fairly low shear rates (0.001-10s^{-1}) which is not representative of the shear rates encountered during MatEx (100-500s^{-1}). Additionally, thermal stability of CNFs also limits the MatEx processability of such composites and future rheological studies should aim to study the shear and temperature dependent behavior of the material in the context of MatEx.

Research on graphene/polyamide 6 composites have investigated the MatEx printability of the percolated composites employing suitable rheological protocols [Lee et al., 2020]. The

increased viscosity under zero-shear conditions along with the shear-thinning behavior of the composites led to the development of a model that can predict the processing window based on the polymer melt flow inside the nozzle. A major finding of this study was that the 3D printable filaments should have a η_0 values that are $\sim$15% of the maximum printable viscosity in order to ensure successful MatEx based processing [Lee et al., 2020].

3.9 Conclusions

In this manuscript, we review the relevant rheological characterizations required for each stage of the MatEx printing of polymers. A trend that has been observed in current literature is the use of empirical relationships and "rules-of-thumb" to examine the "printability" of a feedstock; a few studies exist that perform detailed rheological analysis for MatEx but are invariably limited to certain sections of the process (for example, the most common approach is to study the polymer melt behavior inside the nozzle but not postextrusion). We have attempted to extend the paradigm by offering physics-based models that allow for intelligent process parameter selection based on the polymer's rheological properties. The implications of the processing physics associated with each stage; nozzle extrusion, stand-off region, and finally deposition on print bed; on the structure-property-processing relationships have been elucidated. We have highlighted the necessary rheological characterizations required to screen a polymer feedstock in terms of its extrudability and interlayer welding characteristics to obtain parts that not only have excellent mechanical properties but also exhibit minimal surface defects. The results obtained from such robust characterizations can assist in developing new polymer formulations for MatEx. Furthermore, process modifications and new process designs based on the rheological response can result in printed parts with mechanical properties approaching that of traditional manufacturing techniques. Ultimately, these rheological analyses can be directly leveraged in tasks such as design for AM (DfAM) including details such as toolpath planning, print parameter optimization, and materials selection, all of which are of critical importance for widespread adoption of MatEx-based manufacturing of functional parts.

Chapter 4

Advances in modeling transport phenomena in material-extrusion additive manufacturing: Coupling momentum, heat, and mass transfer

Arit Das[1,2], Claire McIlroy[3], Michael J. Bortner[1,2]

[1]Department of Chemical Engineering, Virginia Polytechnic and State University, Blacksburg, VA 24061, USA

[2]Macromolecules Innovation Institute, Virginia Polytechnic and State University, Blacksburg, VA, 24061, USA

[3]School of Mathematics and Physics, University of Lincoln, Lincoln, LN6 7TS, UK

Arit Das and Claire McIlroy are co-first authors and contributed equally

This chapter was originally published in the **Progress in Additive Manufacturing** journal.

Prog. Addit. Manuf. 2021, 6(1), 3-17. https://doi.org/10.1007/s40964-020-00137-3

Abstract

Material-extrusion (MatEx) additive manufacturing involves layer-by-layer assembly of extruded material onto a printer bed and has found applications in rapid prototyping. Both material and machining limitations lead to poor mechanical properties of printed parts. Such problems may be addressed via an improved understanding of the complex transport processes and multiphysics associated with the MatEx process. Thereby, this review paper describes the current (last five years) state of the art modeling approaches based on momen-

tum, heat and mass transfer that are employed in an effort to achieve this understanding. We describe how specific details regarding polymer chain orientation, viscoelastic behavior and crystallization are often neglected and demonstrate that there is a key need to couple the transport phenomena. Such a combined modeling approach can expand MatEx applicability to broader application space, thus we present prospective avenues to provide more comprehensive modeling and therefore new insights into enhancing MatEx performance.

Keywords: material extrusion; flow deposition; heat transfer; constitutive models; flow-induced crystallization

4.1 Introduction

Additive manufacturing (AM) is a processing technique that employs computer aided design (CAD) file to fabricate three dimensional objects using metals, ceramics, polymers, and composite materials [Herzog et al., 2016, Deckers et al., 2014, Jasiuk et al., 2018, Ning et al., 2015]. However, filament-based material extrusion (MatEx) of thermoplastic polymers is one of the most common and economical AM techniques due to the easy operability, low material and energy requirements [Ambrosi and Pumera, 2016, Gomez-Gras et al., 2018, Northcutt et al., 2018]. MatEx is also a relatively uncomplicated forming method that can be used to manufacture three dimensional parts with intricate geometric features [Sun et al., 2008]. MatEx is being widely used in different industries mainly because it can be used to print functional prototypes like brackets, wire harnesses, ducts, fixtures, and jigs rather than just lab-scale prototypes by carefully selecting the material and processing conditions [Huang et al., 2015]. Although MatEx has progressed significantly, its complexity demands further research to gain an in-depth understanding of the process and consequently ensure the repeatable production of consistent parts [Gao et al., 2015].

The typical MatEx based AM process has been schematically illustrated in Figure 4.1. In this method, a thermoplastic polymer feed (either in the form of solid pellets or filament) is used to print parts of desired shapes. Briefly, the polymer is melted and extruded through a heated liquefier block (heated section in Figure 4.1) via a pinch-roller mechanism (that maintains the feed flow rate). The polymer melt experiences shear rates $\sim 100\ s^{-1}$ inside the nozzle that can have appreciable effect on the polymer chain orientation and stretch (denoted by Region 1 in Figure 4.1) [Northcutt et al., 2018, McIlroy and Graham, 2018]. After deposition on the

build plate the extrudate cools down and the polymer chains relax (denoted by Region 2 in Figure 4.1). Subsequently, the solid filament pushes more material through the nozzle which gets laid on the initially deposited layer where the material undergoes solidification and weld together to fabricate the final product. The print head then moves in the x-y direction and print bed in the z-direction to continue the print in a layer by layer manner till the entire part has been built. The interactions among the process controls, material properties, process parameters, and printed part properties (mechanical properties, surface roughness, surface finish, etc.) have been reviewed in great detail in previous reported literature [Turner et al., 2014, Gold and Turner, 2015, Parandoush and Lin, 2017].

In summary, flow of viscoelastic material through a nozzle, typically at elevated shear rates, coupled with rapid cooling and solidification (and crystallization in the case of some thermoplastics), affects part geometry, porosity, and mechanical strength [Turner et al., 2014, Gold and Turner, 2015]. Ultimately, the part micro-structure determines the buildup of residual stresses and interlayer (weld) strength. Thus, MatEx involves the simultaneous and co-dependent transfer of momentum, heat, and mass, which are intimately linked to end-part properties. An overview of these transport phenomena typical to polymer processing in general is provided by Bird [Bird, 2002]. A systematic way to analyze MatEx is via multi-scale multi-physics models that can simulate the entire print, accounting for four fundamental processes:

(a) flow behavior of the polymer melt [Bird, 2002, George, 2009],

(b) heat transfer [Incropera et al., 2013],

(c) viscoelastic properties (which affect anisotropy and inter-diffusion) [Ferry, 1980], and

(d) solidification and crystallization [Reiter and Sommer, 2003, Reiter and Strobl, 2007].

These processes occur across various length scales; from the size of a polymer molecule (nm) to the scale of the part itself (mm to m).

The modelling approaches to be reviewed here provide powerful tools to explore these complex phenomena occurring across disparate length scales and aim to predict material-specific optimal printing parameters, as well as the mechanical performance of the final printed part.

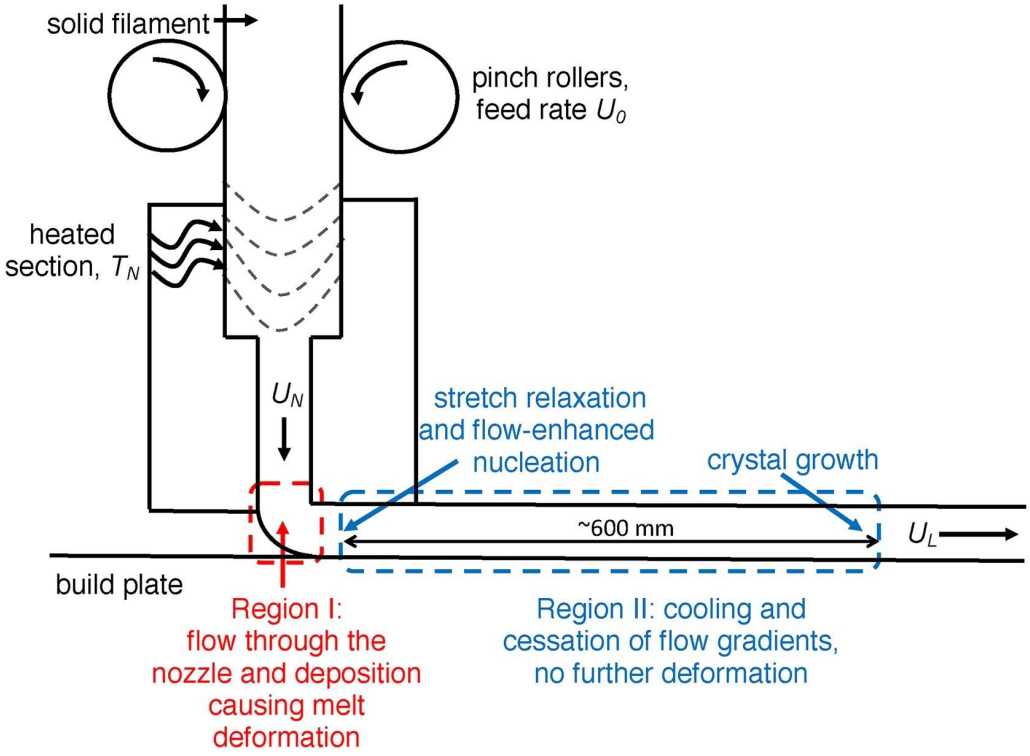


Figure 4.1: Schematic of the MatEx based 3D printing process. The solid polymer filament is fed into the heated section (at a temperature of T_N) at a constant rate (U_0) using the pinch roller mechanism. The polymer melt is deposited on the build plate (print bed) at a constant extrusion speed (U_N) which is usually kept equal to the print bed speed (U_L). The flow profile inside the nozzle is highlighted by the dotted lines. Region 1 highlights the melt flow region in the nozzle and subsequent deposition on the print bed while Region II represents the rapid cooling of the polymer extrudate and relaxation of the polymer chains. For a crystalline material, the crystallization process is initiated in Region II (image reprinted from [McIlroy and Graham, 2018] with permission from Elsevier).

Although there is a substantial amount of current literature that investigate the effect of process variables on the print part properties through various experimental measurements [Lubombo and Huneault, 2018, Mahmood et al., 2017, García Plaza et al., 2019, Young et al., 2019, Tsouknidas et al., 2016, Zandi et al., 2020] such approaches typically focus on empirical data fits rather than a fundamental understanding and model analysis of the key physics. Therefore, the ultimate goal of such models is to provide tools for quality control during MatEx that respond to the physical phenomena to help guide machine and material design

(e.g. changes to heat capacity and thermal conductivity) for improved printing. However, deriving equations that link processing parameters directly to part properties is non-trivial.

In general, transport phenomena are described by three governing equations [Bird, 2002]: conservation of mass, conservation of momentum and the heat equation. That is for an evolving velocity field u(x,t), stress field (x,t), and temperature field T(x,t), which vary in both time t and space x, the governing equations are given by

$$\frac{\partial \rho}{\partial t} + (\nabla \cdot \rho u) = 0 \tag{4.1}$$

$$\rho \frac{Du}{Dt} = -\nabla p - [\nabla \cdot \sigma] + \rho g \tag{4.2}$$

$$\rho C_P \frac{\partial T}{\partial t} = \alpha \nabla^2 T + \dot{q}_V \tag{4.3}$$

where, ρ is the density, $\frac{Du}{Dt}$ is the material derivative of the flow velocity, p is the pressure, C_P is the specific heat capacity, α is the thermal diffusivity of the material, and $\dot{q}_V$ is the volumetric heat source term. Analytic solutions to these equations prove challenging even for simple fluids. For more complex materials, such as the polymer melts used in MatEx, the velocity, stress and temperature fields must also be coupled to an appropriate constitutive equation [Larson, 2013]. Whilst simple relations can be employed to capture shear-dependent viscosity, these do not capture complex (viscoelastic) phenomenon arising from the microstructure of the material. Also, semi-crystalline polymers require further consideration, since the crystallization kinetics [Piorkowska and Rutledge, 2013] affect both the rheology and temperature (via, shear heating and latent heat). Moreover, flow can have interesting implications on the crystallization process [McIlroy, 2019] and hence the ultimate properties of the printed product. Figure 4.2 provides an overview of the multi-physics associated with the MatEx and further illustrates how improper control of one or more of these processes can lead to failure of the MatEx printing process.

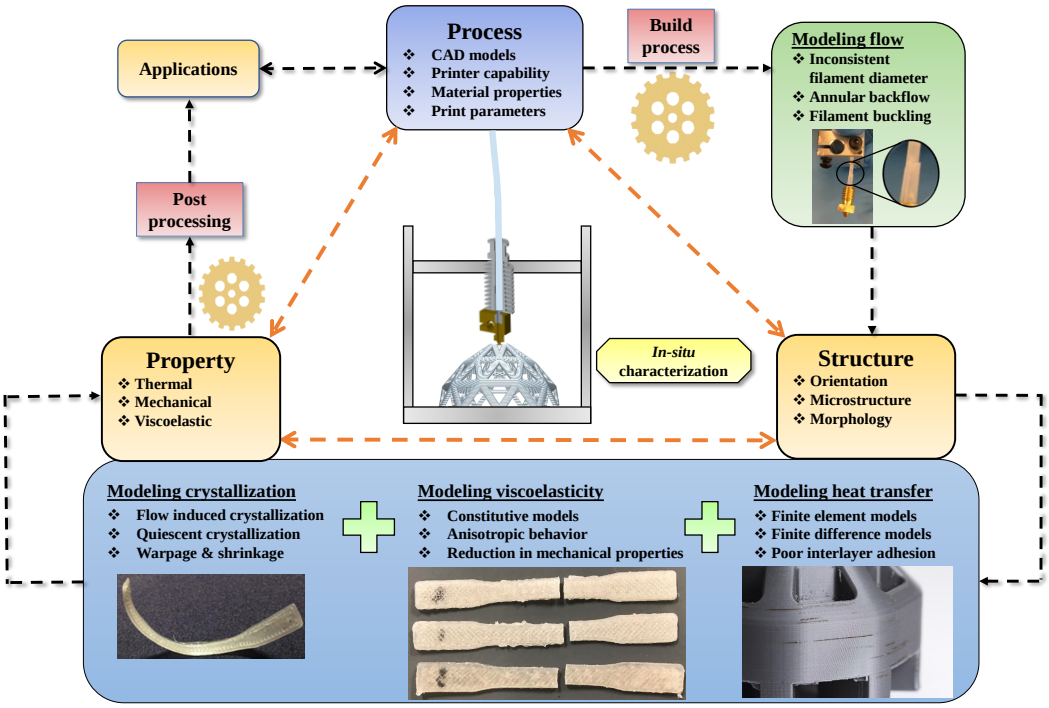


Figure 4.2: Overview of the process-structure-property relationships in material extrusion (MatEx) based additive manufacturing (AM). Green boxes indicate the critical physical phenomena associated with the process and the modeling approaches toward these phenomena are reviewed in this paper.

A full computational model of the MatEx process would require evolving Equations 4.1-4.3, forward in time across the spatial domain (which is also time-dependent due to the layer-by layer process), together with full non-linear coupling to a constitutive equation that is molecularly-aware and accounts for the multi-phase nature of semi-crystalline polymers. Despite the increase in computational power, this is an unwieldy task. Instead, a fundamental understanding of MatEx may be gained by simplifying the problem in various ways. (For example, considering steady-state behavior, reducing the spatial dimension, and decoupling the processes.) In this paper, we review recent advances (over the last five years) in modeling these complex transport phenomena for applications in MatEx AM. Table 4.1 highlights the current state of the art in modeling approaches for MatEx with reference to the fundamental processes modeled as well as the scale at which the simulations were performed.

Table 4.1: Summary of the modeling approaches in material extrusion based additive manufacturing along with the polymer materials that were used to validate the models. The checkmarks indicate the fundamental models that were analyzed in the corresponding studies. The terms within parenthesis in the Material column indicate the scale (road/part) of the simulation performed. It is worth mentioning that the term "road" has been used to denote both the extrudate exiting the nozzle and the material that is deposited on the printer bed.

Study	**Flow model**	**Heat transfer**	**Viscoelasticity /Rheology**	**Crystallization**	**Material (Scale)**
[McIlroy and Graham, 2018]	✓	✓	✓	✓	PCL (road)
[Serdeczny et al., 2018a]	✓				PLA (road)
[Agassant et al., 2019]	✓	✓	✓		ABS (road)
[Gleadall et al., 2018]	✓				PLA (road)
[Costa et al., 2017]		✓			ABS (multi-roads)
[Bakrani Balani et al., 2019]	✓		✓		PLA (road)
[Hebda et al., 2019]	✓				PLA & ABS (road)
[Comminal et al., 2018a]	✓				PLA (road)
[Xia et al., 2019a]	✓	✓	✓		PLA (road)
[Gilmer et al., 2019]		✓			PEI (road)
[Xia et al., 2019b]	✓	✓	✓		PLA (multi-roads)

Table 4.1 – continued from previous page

Study	Flow model	Heat transfer	Viscoelasticity /Rheology	Crystallization	Material (Scale)
[Heller et al., 2016a]	✓		✓		ABS (road)
[Mackay et al., 2017]	✓	✓			PLA & ABS (road)
[Ravoori et al., 2019a]		✓			PLA (road)
[Compton et al., 2017]		✓			CF/ABS (part)
[Osswald et al., 2018]	✓	✓			ABS (road)
[Costa et al., 2015]		✓	✓		ABS (multi-roads)
[D'Amico and Peterson, 2018]		✓			ABS (multi-roads)
[Zhang et al., 2017a]		✓			PLA (multi-roads)
[Zhou et al., 2017a]		✓			PLA (part)
[Zhou and Hsieh, 2017]		✓			PLA (part)
[Zhang and Shapiro, 2018]		✓			ABS (part)
[Luo et al., 2020]		✓			ABS (road)
[Coasey et al., 2020]		✓			ABS (part)

Table 4.1 – continued from previous page

Study	Flow model	Heat transfer	Viscoelasticity /Rheology	Crystallization	Material (Scale)
[Edwards and Mackay, 2020]		✓			ABS & PLA (road)
[Ravoori et al., 2019b]		✓			PLA (multi-roads)
[Prajapati et al., 2018]		✓			ABS (road)
[Phan et al., 2018]	✓	✓	✓		PLA (road)
[Brenken et al., 2019]		✓	✓	✓	CF/PPS (part)
[Phan et al., 2020]	✓	✓	✓		PLA (road)
[McIlroy and Olmsted, 2017b]	✓	✓	✓		PC (multi-roads)
[McIlroy et al., 2019]	✓	✓	✓	✓	PLA (multi-roads)
[McIlroy and Olmsted, 2017a]	✓		✓		PC (road)
[Anderegg, 2020]		✓	✓	✓	PEI (multi-roads)
[Duty et al., 2018]	✓		✓		CF/ABS (multi-roads)
[Stupp, 2019]	✓	✓	✓		–

We discuss models that consider material flow to predict the shape of the deposited layers in Section 4.2. Heat-transfer models that predict the thermal profiles over multiple length scales (from inside the nozzle to the final part) are discussed in Section 4.3. In Section 4.4, we review how these models can be coupled with classical polymer constitutive analyses to provide valuable insights into the micro-structural evolution and ultimate strength of a printed part after solidification. Classical polymer crystallization models can also be incorporated where appropriate to reveal details of the crystal content and morphology, which depend on both thermal and flow history. Finally, we address the challenges associated with these approaches, potential methodologies to address these challenges, and recommendations on developing comprehensive models to accurately represent the intricate transport phenomena occurring during the MatEx process.

4.2 Momentum transport: Flow and geometry

In traditional polymer processing techniques (e.g. injection molding, extrusion etc.) where both shear and elongation flow of the polymer melt are of critical importance [Bird, 2002, George, 2009], geometry of the extrudate is not usually significant since well-defined molds typically dictate the final geometry of the manufactured parts. In contrast, polymer flow through the nozzle and subsequent deposition determines the geometry of extruded roads in MatEx, and thus the fully assembled shape of the part itself [Hebda et al., 2019, Comminal et al., 2018a]. The road geometry depends on both the print resolution and print speed [Serdeczny et al., 2018a] and is ultimately a result of the polymer's viscoelastic properties. Agassant et al. [Agassant et al., 2019] highlight the relationship between print head velocity and pressure at the nozzle outlet. This relationship leads to an optimal operation window (Fig. 4.3a) that eliminates the risk of buckling (as illustrated in Figure 4.2), ensures continuous road deposition, and provides sufficient pressure to encourage inter-layer diffusion and subsequent adhesion. The shape of the roads also provides information regarding porosity [Gleadall et al., 2018], inter-road bonding [Rodriguez et al., 2000], and thermal history [Costa et al., 2017]. The effect of the print parameters on the road geometry [Serdeczny et al., 2018a, Agassant et al., 2019] and surface roughness [Anitha et al., 2001] of a printed part has also been investigated. The print speed, extrusion flow rate, and, gap between

the nozzle head and print bed were found to have a pronounced effect on the shape of the deposited roads as well as the mechanism of extrude spreading on the print bed (hydrodynamically controlled vs. surface tension controlled) [Serdeczny et al., 2018a, Agassant et al., 2019]. On the other hand, layer thickness was found to have a significant effect in determining the surface roughness of a printed part [Anitha et al., 2001]. Bakrani Balani et al. [Bakrani Balani et al., 2019] studied the effect of the printing parameters, rheological and thermal characteristics on the geometry of deposited roads of polylactic acid (PLA) during MatEx. The authors further developed a two-phase flow model that was employed to model the geometry of the deposited roads [Bakrani Balani et al., 2019]. The simulation results (suggesting deformation of the extrudate during deposition on the printer bed) were in close agreement with the experimental findings using an optical microscope, demonstrating the robustness of the modeling approach [Bakrani Balani et al., 2019].

Simple analytic models based on conservation of mass have been developed to predict the height, width and cross-sectional area of a single deposited road [Hebda et al., 2019, Comminal et al., 2018a]. While this approach gives a reasonable agreement with CT-scanning images, it is unable to provide a full description of the ovality of the road, which impacts the weld contact area between adjacent roads (in both the x and z directions), or the part shape. Thus, a number of full computational fluid dynamics (CFD) models have recently been presented [Comminal et al., 2018a, Xia et al., 2019a] and validated against optical microscopy experiments [Serdeczny et al., 2018a], as well as SEM images [Gilmer et al., 2019], as shown in Figures 4.3(b) and 4.3(c), respectively. These analyses illustrate a range of road shapes, from circular to elongated rectangle, depending of print parameters (Fig. 4.3b). A new computationally-efficient volume conserving (VOLCO) model has also been developed [Gleadall et al., 2018] to capture the geometry at road-road interfaces and the porosity within a full 3D lattice. The flow model described was able to represent the printing of a full-size 3D lattice, rather than just a single filament and successfully described the experimental observations (Fig. 4.3d).

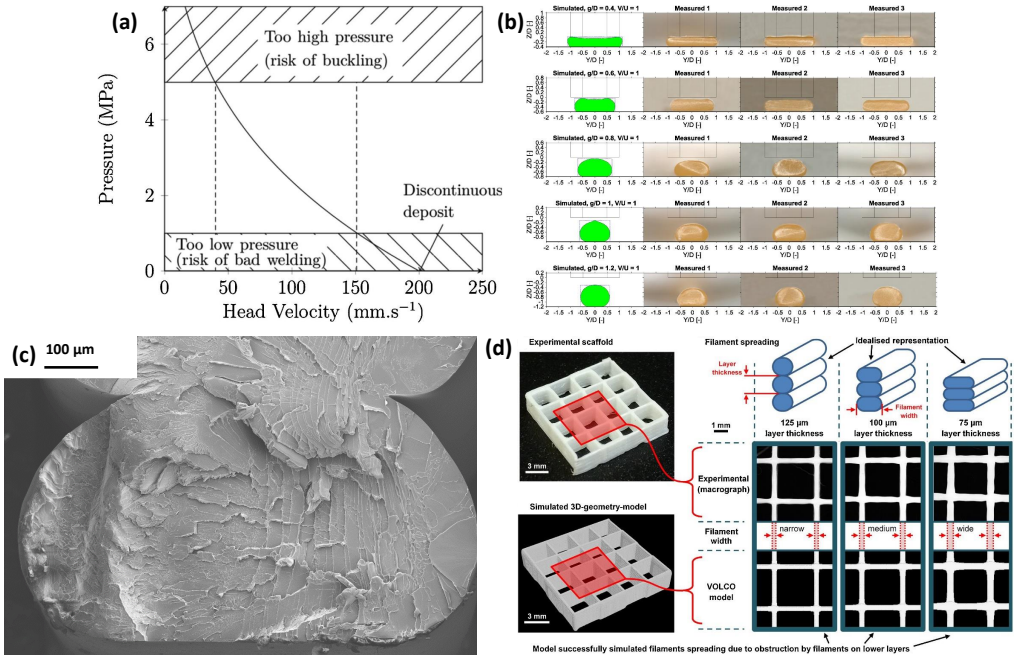


Figure 4.3: (a) Phase map of the pressure across the printer nozzle as a function of print velocity showing the risks associated that can lead to print failure (image reprinted from [Agassant et al., 2019] with permission from Elsevier); (b) Cross-sectional shapes of the extruded filaments from CFD simulations and as observed experimentally using optical microscopy using PLA (image reprinted from [Serdeczny et al., 2018a] with permission from Elsevier); (c) SEM image of a cross-section of a single layer of print using polyether imide (PEI) (image reprinted with permission from [Gilmer et al., 2019] Copyright 2019 American Chemical Society); (d) Experimental 3D printed lattices and simulations of the lattice models as generated by the VOLCO model as a function of layer thickness. The filament spreading as a function of layer thickness was accurately captured by the VOLCO model (image reprinted from [Gleadall et al., 2018] under the terms of the Creative Commons CC-BY license).

Other important geometrical aspects that have recently been considered via numeral modeling include surface instabilities along the road [Bakrani Balani et al., 2019], and sagging of freely-supported roads [Xia et al., 2019b]. While this progress has significantly enhanced our ability to simulate geometry, temperature-dependent viscoelasticity and crystallization must be coupled to these models to fully understand the complex flow dynamics. While power-law models have provided some insight to the spreading dynamics [Agassant et al., 2019], a constitutive model that incorporates normal stress differences is necessary to capture extrudate swell effects [Heller et al., 2016a]. Moreover, density changes during cooling,

which are exaggerated during crystallization, are responsible for part shrinkage and warping (as highlighted in Figure 4.2 as well).

4.3 Heat transfer

Melt-based processing of polymers is associated with complex interactions between fluid mechanics and heat transfer in a non-Newtonian fluid system [Incropera et al., 2013, Denn, 2008]. Similarly, in the MatEx process the filament must be molten to flow through the nozzle and hence heat transfer significantly impacts the print speed [Mackay et al., 2017]. The thermal profile of the polymer from nozzle through to deposition (Fig. 4.4a) also controls inter-road adhesion (also known as welding) through polymer diffusion, significantly impacting final part properties [Gilmer et al., 2019, Davis et al., 2017, Pourali and Peterson, 2019, Seppala et al., 2017, Seppala and Migler, 2016]. Thus, the ability to accurately predict heat transfer is crucial to fully understanding MatEx.

Transient one-dimensional heat-transfer models considering conduction and natural convection, which can be solved via finite-difference methods, have been implemented to calculate inter-road bond strength of acrylonitrile butadiene styrene (ABS) with reasonable accuracy [Coogan and Kazmer, 2017a]. A similar approach, with the addition of radiation, has also been developed for big-area AM (BAAM), and is able to predict the temperature profiles and thermal gradients in thin walls which was validated by infrared imaging of carbon fiber (CF) reinforced ABS prints [Compton et al., 2017]. A 2-D approach with order-of-magnitude analysis was adopted by Osswald et al. [Osswald et al., 2018] for a shear-thinning quasi-Newtonian fluid, which was validated using a custom piston-driven capillary setup. However, these models are insufficient to properly represent the temperature gradient within the deposited roads [Compton et al., 2017, Osswald et al., 2018]. Accurate prediction of this thermal gradient is key to determining the cooling rate after deposition, and hence the evolution of weld strength in the printed parts [Gilmer et al., 2019].

With the improvement in computational capabilities, 3-D heat-transfer models for MatEx, which can be solved using finite-element (FE) methods, have been investigated [Costa et al., 2017, Costa et al., 2015]. For example, a simulated thermal profile within the nozzle head is shown in Figure 4.4(b) [Wang et al., 2019b]. FE models have also been developed to capture rapid cooling during the deposition process [D'Amico and Peterson, 2018], however

assumptions regarding interlayer bonding resulted in predicted trends which overestimate the heat transfer measured using infrared imaging techniques. The entire MatEx process (die extrusion, road deposition, and subsequent cooling and consolidation) has also been modeled recently; the thermal profile of an extruded road from such an analysis is illustrated in Figure 4.4(c) [Gilmer et al., 2019]. Zhang et al. [Zhang et al., 2017a] developed a space resolved, time dependent 3-D model to capture the thermal behavior during and after MatEx. The integrity of the welds formed between the layers was found to strongly dependent on the printing speed while residual stresses inside a print could be controlled by manipulating the cooling rate [Zhang et al., 2017a]. Zhou et al. [Zhou et al., 2017a] also developed a 3-D FE thermal model to describe temperature and stress distribution in a printed part of PLA. The simulation studies revealed that lower print temperature, reduced print speed, and lower layer thickness can mitigate the residual thermal stress and part distortion. Further examples of 3-D FE heat-transfer models can be found in Refs. [Zhou and Hsieh, 2017, Zhang and Shapiro, 2018].

Arguably more important is the validation of analytical and numerical models via comparison to experimental measurements. Luo et al. [Luo et al., 2020] recently developed a heat transfer model based on previous modeling efforts on polymer melt flow in tubes [Agur and Vlachopoulos, 1981] and 3D printer nozzles [AtifYardimci et al., 1997]. The thermal model provides an upper limit of the polymer feed rates that can be successfully printed using MatEx without jamming [Luo et al., 2020]. The authors validated their simulation results by performing experiments on a modified extruder setup and found that their model was in good agreement with model predictions, especially at a nozzle wall temperature range of 210°C-260°C [Luo et al., 2020]. A non-isothermal welding model was developed by Coasey et al. [Coasey et al., 2020] and experimentally verified by interlaminar fracture toughness measurements. The model describes the effect of processing parameters and rheological properties on the degree of healing of the printed parts [Coasey et al., 2020]. The melting behavior of PLA inside a MatEx nozzle was computationally modeled and validated using experiments [Phan et al., 2020]. The authors coupled a generalized Newtonian fluid model with the Phan-Thein-Tanner viscoelastic model to model the melting behavior and subsequent melt flow in the nozzle under high shear rates [Phan et al., 2020]. Edwards and Mackay [Edwards and Mackay, 2020] also developed a post-extrusion heating model for both amorphous and semicrystalline polymers to minimize the formation of "shark-skin" defects during MatEx. Key works that account for radiative heat transfer effects have shown excellent agreement between the temperature profile in the nozzle prior to and after deposition [Ravoori et al.,

2019b], in the standoff region (between nozzle & bed) [Prajapati et al., 2018], and on the print bed [Ravoori et al., 2019a].

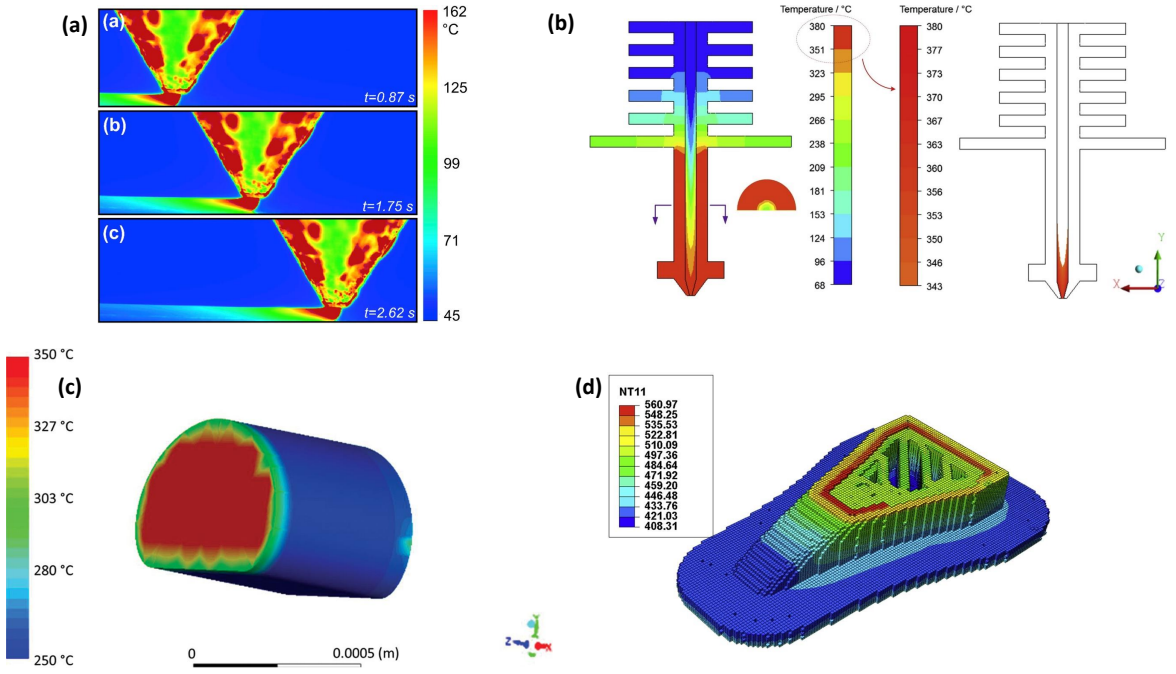


Figure 4.4: (a) Infrared thermographs obtained at three different times for rastering of a single road of print where the nozzle moves from left to right (image reprinted from [Ravoori et al., 2019a] with permission from Elsevier); (b) FE simulations of the thermal profile inside a typical MatEx nozzle (image reprinted from [Wang et al., 2019b] with permission from Elsevier); (c) the thermal profile at a cross-section of the filament (image reprinted from [Gilmer et al., 2019] Copyright 2019 American Chemical Society); (d) simulated thermal profile of an entire printed part (image reprinted from [[Brenken et al., 2019] with permission from Elsevier).

Despite this progress, it is apparent that the rheological properties of the melt significantly affect the heat transfer by influencing the flow characteristics (e.g. viscous heating) [D'Amico and Peterson, 2018]. Hence, to completely understand the complexities of the heat-transfer process, appropriate polymer constitutive models must be considered. Mackey et al. analyzed the problem in the nozzle (where melting and extrusion occurs) using a generalized Newtonian fluid framework to model the rheological behavior [Phan et al., 2018], reporting that heat-transfer affects the pressure drop across the nozzle and limits print speed. On the scale of a final printed part, Brenken et al. coupled a 3-D heat-conduction model with temperature-dependent viscoelasticity to simulate the transient thermal profile in a func-

tional part as highlighted in Figure 4.4(d) [Brenken et al., 2019]. Moreover, polymer crystallization and material shrinkage are also incorporated into their model-crucial ingredients for predicting latent heat effects and part geometry.

4.4 Anisotropy and inter-diffusion

Viscoelasticity plays a crucial role in polymer processing [Tadmor and Gogos, 2013] and hence it is of considerable importance in MatEx as well [Phan et al., 2018, Mackay, 2018]. It has been shown that typical shear rates are sufficient to orient and stretch the polymer molecules [McIlroy and Olmsted, 2017b]. Thus, as well as affecting heat transfer in the nozzle via shear heating [Gutowski et al., 2017], and influencing the geometry of a deposited road via extrudate swell [Heller et al., 2016a], polymer deformation (anisotropy) may persist at solidification. For an amorphous polymer, Fig. 4.5a illustrates the typical degree of residual alignment across a single road locked in due to the glass transition, as predicted by the numerical model of McIlroy et al. [McIlroy and Olmsted, 2017b].

Moreover, the key to ensuring part strength is successful welding of the polymer chains at road-road interfaces via inter-diffusion [Ge et al., 2013]. The poor interlayer bonding between the printed layers is highlighted in Figure 4.2. As a rule of thumb, if there is sufficient time above the glass-transition temperature, T_g, for the polymer to diffuse its radius of gyration, then bulk strength should be recovered in the weld region [Agrawal et al., 1996]. Fig. 4.5b demonstrates a typical cooling profile found in MatEx; for these print conditions (and thermal properties) there is approximately one second above T_g available for inter-diffusion [D'Amico and Peterson, 2018]. Polymer alignment leads to anisotropic diffusion (in the direction of chain orientation) [Hunt and Todd, 2009] and may hinder this welding process, although this effect is found to be small for polycarbonate (PC) [McIlroy and Olmsted, 2017b] and for PLA as shown in Fig. 4.5c [McIlroy and Olmsted, 2017b].

The role of polymer entanglements is also crucial to ensuring strength at road-road interfaces [Ge et al., 2013]. It is proposed that MatEx can lead to flow-induced disentanglement of the polymer network [Ianniruberto and Marrucci, 2013] and that only partial re-entanglement of the network is achieved during cooling [McIlroy and Olmsted, 2017b]. McIlroy et al. [McIlroy and Olmsted, 2017b] suggest that it is this partial entanglement, rather than anisotropic diffusion, that is responsible for weld weakness in amorphous parts. However, this is yet to

be validated experimentally. Nevertheless, residual viscoelastic stresses affect part properties, in particular reducing the tensile properties of printed parts (Fig. 4.5d).

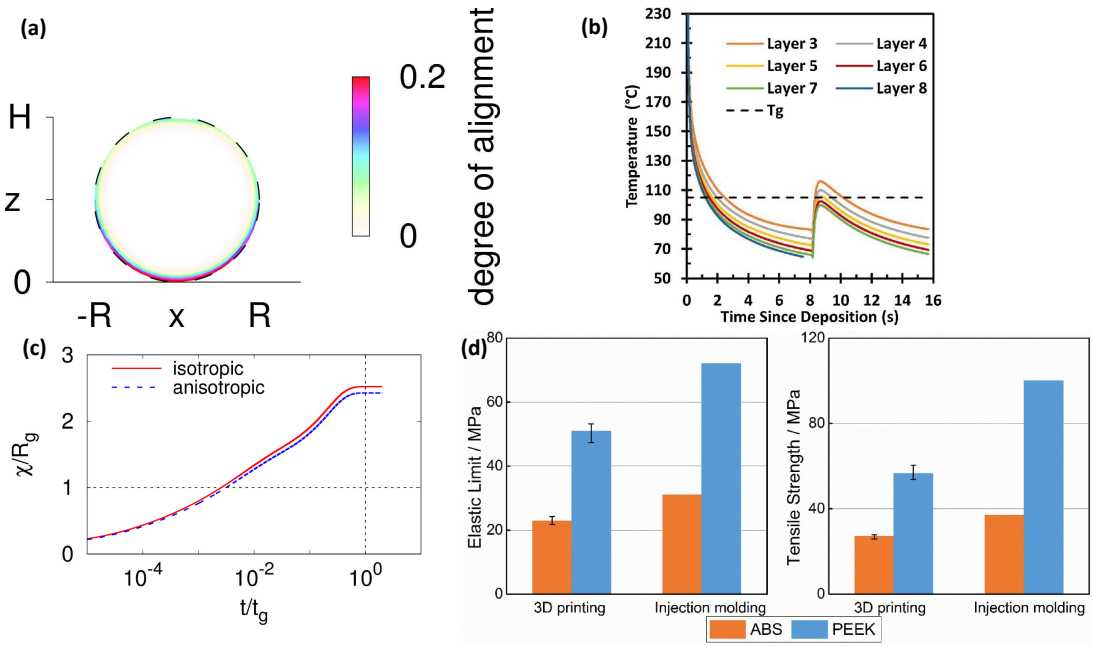


Figure 4.5: (a) Residual alignment in a single deposited road of PLA printed at 120 mm/s and 190°C, as predicted by the numerical model described in [McIlroy and Olmsted, 2017b]; (b) Prediction of the thermal profiles of the deposited layers using FE simulations; the different layers spend varying time periods above T_g which determines the extent of their mobility (image reprinted from [D'Amico and Peterson, 2018] with permission from Elsevier); (c) The polymer diffusion distance, χ, scaled by the polymer size, R_g (radius of gyration), as a function of time. Time scaled by the time taken to reach the glass transition temperature, so that at $t/t_g = 1, T = T_g$. The effects of polymer alignment in the flow give rise to anisotropic diffusion, which hinders diffusion between filaments, i.e., in the transverse z-direction. See [McIlroy and Olmsted, 2017b] for details of the model; (d) Reduction in tensile properties of printed ABS and polyether-ether-ketone (PEEK) samples compared to injection molded parts (image reprinted from [Wu et al., 2015] under the Creative Commons Attribution License).

Since power-law models are not sufficient to capture this molecular-scale behaviour, recent works by McIlroy et al. have employed a molecularly-aware constitutive model [McIlroy and Olmsted, 2017b, McIlroy and Graham, 2018, McIlroy et al., 2019, McIlroy and Olmsted, 2017a], which requires knowledge of both the reptation and Rouse times of the polymer (obtained from linear rheology). In particular, McIlroy and Olmsted [McIlroy and Olmsted,

2017b] prescribes the geometry of the deposited road, which enables the flow field to be solved directly from conservation of mass independently of the constitutive (Rolie-Poly) equation using finite-difference methods. The authors find that the melt experiences significant strain rates within the nozzle, which are able to substantially stretch and orient the polymers. Furthermore, the deposition process involving the 90° turn dominates the deformation and significantly disentangles the melt. Although this approach [McIlroy and Olmsted, 2017b] provides a computationally efficient method to investigate a range of printing conditions, the interplay between viscoelasticity and the weld geometry is neglected. Since the Rolie-Poly model provides a simple one-mode constitutive equation for the stress tensor, it can be readily integrated into full CFD calculations to capture this behavior. Recent advances by Xia et al. [Xia et al., 2019a] incorporate a reduced Rolie-Poly model into a full finite-element computation of the flow field to investigate the effect of these viscoelastic stresses on the deposition geometry.

4.5 Polymer crystallization

The fundamental mechanisms of polymer crystallization are detailed in a review article elsewhere [Zhang et al., 2017b]. The use of semi-crystalline polymers in MatEx has sparked significant interest but is largely relegated to academic studies [Das et al., 2020b, Schirmeister et al., 2019, Peng et al., 2019a, Spoerk et al., 2018a, Stoof and Pickering, 2018]. Briefly, the crystalline regions in these polymers act as physical crosslinks that restrict movement of the polymer chains, thereby strengthening the material [Reiter and Sommer, 2003, Reiter and Strobl, 2007]. Thus, crystallinity is a major factor to determining tensile properties, and ultimately dictates the application of printed parts. For example, Figure 4.6(a) highlights the variation in tensile strength of a common engineering thermoplastic, polyphenylene sulfide (PPS), with the percent crystallinity of the printed parts. The tensile strength increases by 37% with increasing crystalline content due to variations in printing conditions.

The most common approach to modeling polymer crystallization considers the formation of nuclei and subsequent growth into a stable crystalline framework. However, traditional isothermal models fail to capture the complex effects of the steep temperature gradients and cooling rates found in MatEx. As noted in the heat transfer section, Brenken et al. [Brenken et al., 2019] track the thermal profile and crystallization process during MatEx using a dual (Velisaris) non-isothermal model which has been summarized in Figure 4.4(d).

Further to this work, a finite-difference model has been developed to account for multiple crystallization mechanisms, shear stress evolution, and more complicated thermal histories [Anderegg, 2020]. The model predicts both the thermal distribution and evolution of the crystal fraction throughout a printed part, and these processes which are then applied to novel models for predicting the degree of healing and residual stress at each layer. This is the first healing model that accounts for crystallinity and the experimentally determined bond strength was found to be close to the theoretical predictions.

In the models discussed thus far, the polymers are assumed to crystallize quiescently, i.e. the effect of flow is neglected. However, it is well known that even slight alignment of the polymers at the onset of nucleation can strongly enhance the nucleation rate [Graham, 2019], and consequently lead to accelerated crystallization times. McIlroy et al. [McIlroy and Graham, 2018, McIlroy et al., 2019] have recently extended their finite-difference modelling approach (incorporating the Schneider rate equations) to show that there exists a MatEx-operation window in which crystallization times are reduced due to shear in the nozzle (Fig. 4.6b). Furthermore, it is shown that this flow-enhanced crystallization is localized to a thin boundary layer near to the road surface, leading to the development of smaller crystal structures in the weld region (Fig. 4.6c). These results are in agreement with in-situ Raman spectroscopy and optical microscopy measurements.

Shmueli et al. [Shmueli et al., 2019a] coupled in-situ wide angle X-ray scattering with infrared imaging during MatEx of PLA filaments to study the morphology development. The authors found that thermal profile as well the printing direction (with respect to the X-ray beam) significantly affected the structure of the deposited roads [Shmueli et al., 2019a]. Subsequent work performed by the same group [Shmueli et al., 2019b] using polypropylene (PP) by connecting a MatEx printer with a X-ray scattering beamline. The authors observed the formation of shish-kebab crystal structure post printing, which nucleated at the surface of the filaments and gradually advanced toward the center of the filament [Shmueli et al., 2019b] . The experimental method provided both time and space dependent data for the crystallization process and can be a valuable resource for capturing the detailed kinetics as well as the microstructure development during a print. Welding at the interface of two successive printed layers was found to occur due to polymer chain relaxation and diffusion [Shmueli et al., 2019b].

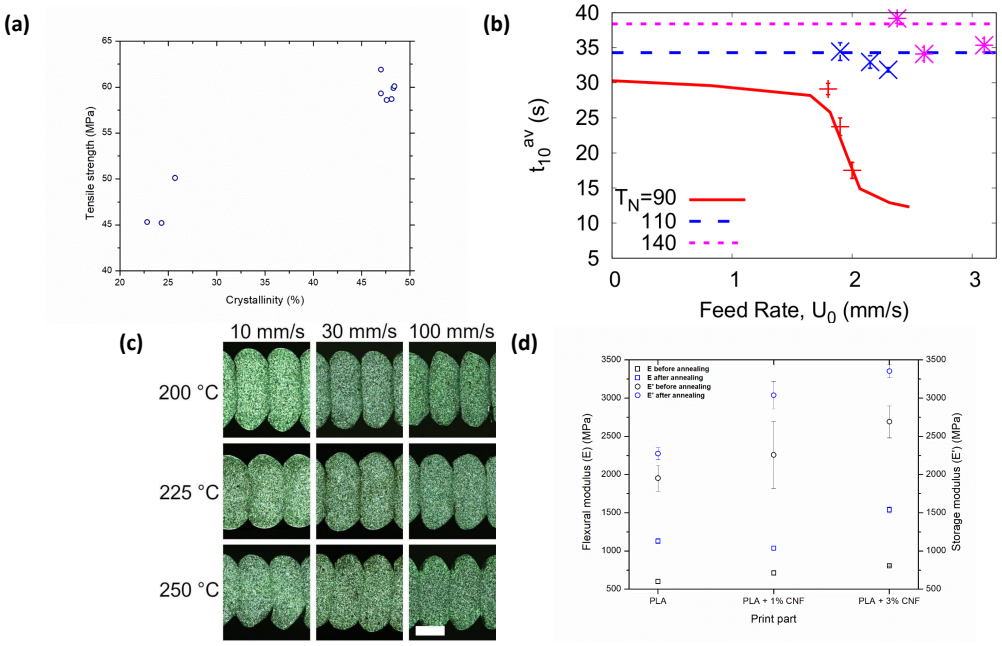


Figure 4.6: (a) Effect of changes in percent crystallinity of printed part on the tensile strength of polyphenylene sulfide (data adapted from [Fitzharris et al., 2018] with permission from Elsevier); (b) Flow-induced crystallization plot (image reprinted from [McIlroy and Graham, 2018] with permission from Elsevier); (c) Optical microscopy of annealed PLA printed cross-sections. Darker regions in the weld correspond to smaller sized spherulites due to flow-enhanced crystallization. The scale bar is 200 μm. (image reprinted with permission from [McIlroy et al., 2019] Copyright 2019 American Chemical Society); (d) Improvement in tensile and flexural properties post-annealing for 3D printed PLA and PLA/cellulose nanofiber (CNF) composites (data adapted from [Dong et al., 2019a] with permission from Elsevier).

In a more recent study, Nogales et al. [Nogales et al., 2019] monitored the microstructure development and weld formation during MatEx of PP by performing in-situ X-ray scattering experiments in the synchrotron beamline. The crystallization mechanism during printing of the layers was found to be similar to that encountered during quiescent crystallization of PP. Moreover, the printed layer had increased crystalline content in the bulk with respect to the interfacial regions indicating a gradient in crystallinity across a single layer [Nogales et al., 2019]. The authors suggested that this can improve interlayer welding and hence improve the mechanical properties of MatEx printed parts since interlayer welding is directly related with the extent of polymer chain diffusion between the layers [Nogales et al., 2019]. Whilst inter-diffusion must precede the crystallization to ensure sufficient inter-road adhesion, the

development of smaller crystal structures may be considered beneficial to improving weld properties [McIlroy and Olmsted, 2017b]. Moreover, McIlroy et al. [McIlroy and Olmsted, 2017b, McIlroy and Graham, 2018] propose a simple comparison of time scales, which can be applied to any printing material, so that print conditions can be optimized to ensure (or eliminate) flow-enhanced crystallization.

4.6 Discussion and future directions

Numerous limitations exist in 3D printing technology, as discussed in Ref. [Oropallo and Piegl, 2016]; multi-scale molecular modeling approaches are critical in addressing challenges in material diversity and print speed. A useful tool to evaluate the 'printability' of a range of materials, including high-temperature thermoplastics, fiber-reinforced thermoplastics, and low-viscosity thermosets has been presented by Duty et al. [Duty et al., 2018], and a range of approaches have been tested for improving part properties:

- Since molecular weight can significantly affect the welding dynamics [McIlroy and Olmsted, 2017b], tuning the molecular-weight distribution may be used as an avenue for optimization. In particular, Levenhagen et al. [Levenhagen and Dadmun, 2018] show that a bi-modal distribution can improve mechanical properties and isotropy of printed parts; the addition of a small-molecular weight tail enhances the inter-diffusion at the welds. Current printing models consider only a single mode description of the molecular-weight distribution, however new capabilities are emerging [Boudara et al., 2018], offering exciting opportunities for a more detailed modeling approach.

- The addition of particulate additives can also improve part properties. In particular, Brenken et al. [Brenken et al., 2018] and Fallon et al. [Fallon et al., 2019] review a range of different composite systems, comprising of discontinuous and continuous fiber-reinforced polymers. The materials are characterized by the fiber alignment, which is oriented parallel to the direction of the deposited road, thus can lead mechanical limitations in the transverse direction. Some progress has been made in modeling the material flow and orientation in these systems [Stupp, 2019], but many open question remain including wetting properties, bond formation, and thermo-mechanical solidification behavior.

- There is also precedent for the employment of post-printing annealing to remove residual viscoelastic stresses and increase the final crystal fraction, thereby improving thermal [Prajapati et al., 2019] and mechanical properties (Fig. 4.6d) [Hart et al., 2018a]. However, it has been shown that annealing may not result in the desired uniformity of spherulite sizes [McIlroy et al., 2019]. In particular, the model of McIlroy et al. [McIlroy et al., 2019] shows that a higher nucleation density may be 'templated' into the road by the flow during printing. Thus, on annealing, smaller flow-enhanced spherulites are revealed in the weld regions, as evidenced by optical microscopy (Fig. 4.6c). Nevertheless, it is proposed that these smaller spherulites can give rise to more ductile fracture.

Although great progress has been in made understanding MatEx using the modelling approaches discussed, many challenges remain; foremost being that coupling viscoelastic flow, heat transfer, and crystallization kinetics is computationally demanding [Xia et al., 2019a, Gilmer et al., 2019]. Table 4.1 provides a list of recent literature on modeling the MatEx process. As evident from the data, there are very few works that take into account all four of the fundamental processes that occur simultaneously during the printing process. Future research must address this concern even though it requires substantial computation power. Another important observation from Table 4.1 is the amount of research on modeling the extrudate exiting the printer nozzle or on the deposition of roads on the printer bed which comfortably outnumber the research works that deal with simulating actual functional parts. It is expected that this trend will start to change in the near future with more industries and academic groups investigating large area AM [Duty et al., 2017, Kishore et al., 2017b, Chesser et al., 2019, Russell et al., 2018] and bridge the gap between the current simulation scale ($\sim \mu$m-mm) and part dimensions ($\sim$m).

Quantitative predictions also rely on thorough materials characterization, including linear viscoelasticity, nucleation and crystal growth rates, as well as thermal properties, which remains non-trivial since the thermoplastic polymer properties for elevated temperature processing in MatEx are usually highly temperature dependent [Ravoori et al., 2018]. The Additive Manufacturing Benchmark (AM-Bench), focused primarily on MatEx and selective laser sintering, has been created as a platform for performing extensive in-situ and ex-situ to generate a huge repository of experimental data. The goal of the AM-Bench is to gain valuable insights into the current modeling endeavors by comparing the simulation results against the rigorously controlled benchmark data [Levine et al., 2020]. One of the current

limitations of the simulation capabilities is the failure to describe spatial evolution of microstructure in a printed part but strides have been made in modeling the same for smaller build volumes. It is expected that incorporating the multiphysics described in this paper with the mechanics (e.g. residual strain/stress) of the printed part and optimizing the computational demands will lead to the development of models that can be of great industrial relevance [Levine et al., 2020].

Moreover, the profound effects of flow on polymer crystallization is still not fully understood [Graham, 2019] - in fact, even assumptions must be made on the nature of quiescent nucleation - and continuum-level models that are able to incorporate the full complexity of the crystallization process remain in their infancy. Finally, there is experimental evidence of a phenomenon known as co-crystallization [Awaja and Zhang, 2015, Bonten and Schmachtenberg, 2001, Xue et al., 2000], which results in improved mechanical properties of a part, but models that account for this mechanism during MatEx are yet to be developed.

Chapter 5

Rheological investigation of nylon-carbon fiber composites fabricated using material extrusion based additive manufacturing

Arit Das[1,2], Martin Etemadi[1,2], Bradley A. Davis[3], Steven H. McKnight[4,5], Christopher B. Williams[2,6], Scott W. Case[2,7], Michael J. Bortner[1,2]

[1]Department of Chemical Engineering, Virginia Polytechnic and State University, Blacksburg, VA 24061, USA

[2]Macromolecules Innovation Institute, Virginia Polytechnic and State University, Blacksburg, VA, 24061, USA

[3]Hume Center for National Security and Technology, Virginia Polytechnic and State University, Blacksburg, VA 24060, USA

[4]Virginia Tech Alexandria Campus (National Capital Region), Arlington, VA 22203, USA

[5]Department of Biomedical Engineering and Mechanics, Virginia Polytechnic and State University, Blacksburg, VA 24061, USA

[6]Department of Mechanical Engineering, Virginia Tech, Virginia Polytechnic and State University, VA 24061, USA

[7]Civil and Environmental Engineering, Virginia Polytechnic and State University, Blacksburg, VA 24061, USA

This chapter was originally published in the *Additive Manufacturing of Polymer Composites* special issue of **Polymer Composites** journal.

Polym. Compos. 2021, 42(11), 6010-6024. https://doi.org/10.1002/pc.26281

Declaration

The authors acknowledge the Department of the Navy award number N00014-19-1-2736 issued by the Office of Naval Research for financial support. The United States Government has a royalty-free license throughout the world in all copyrightable material contained herein. Any opinions, findings, and conclusions or recommendations expressed in this material are those of the authors and do not necessarily reflect the views of the Office of Naval Research.

Abstract

Fused filament fabrication (FFF) has seen broad industrial adoption as it is capable of making large complex parts from robust thermoplastics in a cost-effective manner. However, the mechanical performance of the printed parts is limited due to poor interlayer bonding and the presence of voids. In order to overcome these drawbacks, the addition of short or continuous fibers into the polymer matrix have been investigated, as the fibers can act as a mechanical reinforcement while also mitigating residual stress resulting from the material's rapid solidification following extrusion. Therefore, understanding the implications of process parameters and fiber reinforcements on printed part properties through detailed crystallization analysis and rheological characterizations is of paramount importance.

The goal of this study is to understand the process-structure-property relationships of short carbon fiber reinforced polyamide 6 (CF-PA6) by comparing the melt rheology and crystallinity of CF-PA6 versus a neat PA6 polymer. Differences in the melting and crystallization behavior resulting from the reinforcing fibers revealed an increased time window for crystallization in the fiber reinforced matrix. Rheological characterizations at the recommended printing temperatures demonstrate the shear thinning behavior of the samples at shear rates relevant to FFF. From a statistical design of experiments analysis, layer thickness was found to be the most significant parameter affecting the tensile properties of a printed part at constant printing temperature and printing speed. The tensile fracture surfaces of the printed specimens using scanning electron microscopy was analyzed to provide insights into the failure mechanisms as a function of FFF processing variables.

Keywords: additive manufacturing; 3D printing; rheology; polyamides; composites

5.1 Introduction

Fused Filament Fabrication (FFF) additive manufacturing (AM) technology manufactures parts a layer-by-layer fashion by extruding polymeric filament through a heated nozzle and deposited on a build platform [Gibson et al., 2015]. Widespread industrial application of FFF is limited by its poor mechanical properties, which result from poor interlayer bonding between the deposited layers. In order to overcome this issue, reinforcement fillers are added to the neat polymer to improve printed part strength and stiffness [Ning et al., 2015]. Reinforcement materials in the form of particles, fibers, and nanomaterials can be added to the neat polymers to fabricate polymer composites, leading to improved printability and reduced part warpage.

Printable polymer composite materials reinforced by fibers have been studied in the last decade [Ozkoc et al., 2005, Tian et al., 2016] and generally can be divided into two categories: continuous fiber reinforced thermoplastic (CFRT) composites and short fiber reinforced thermoplastic (SFRT) composites. The mechanical properties of SFRT composites generally depend on the fiber length, fiber orientation, fiber content, and void fraction [Tekinalp et al., 2014]. Ning et al. [Ning et al., 2015] fabricated carbon fiber (CF)-filled filaments by adding CF powders with two different average fiber lengths of 150 μm and 100 μm and fiber diameter of 7.2 μm into acrylonitrile butadiene styrene (ABS). Composite filaments were produced in different CF contents to study the effects of fiber contents on the tensile and flexural properties. The results showed that the tensile strength of specimens with 5 wt% of 150 μm length short CF increases up to 22.5% in comparison with that of neat ABS specimens. Also, it was shown that adding 5 wt% CF could improve almost all the flexural properties up to 21.86% as compared to the neat plastic specimen.

Spoerk et al. [Spoerk et al., 2018b] used polypropylene (PP) filled with short carbon fibers (CF) to evaluate the impact of the carbon fiber orientation on mechanical properties and thermal conductivity of composite parts fabricated via FFF. Results showed that addition of only 10 vol% of short carbon fibers into PP, leads to an increase of 100% in filament yield stress and more than 400% in the filament Young's modulus, compared with neat PP. It was also observed that there are significant differences in the flexural stresses and moduli between 0° and 90° printed road orientation. This occurs since the carbon fibers are aligned within the extrudate due to the shear forces imposed during extrusion. Thus, the full length of the fibers (250 μm) can support the load in the 0° orientation, whereas only the width of the fiber

(7 μm) reinforces PP in the bending direction in the case of 90° printing orientation. This anisotropic behavior is also found in thermal conductivity, wherein the thermal conductivity along the printing, and thus the fiber, direction was three times higher than perpendicular to that direction.

The FFF printed parts of fiber reinforced polymers generally do not achieve their maximum potential (bulk) mechanical properties due to limited interfacial bonding and non-homogenous filler dispersion. Zhang et al. [Zhang et al., 2018] further studied the interfacial bonding properties between printed strands of acrylonitrile-butadiene-styrene (ABS), short carbon fiber reinforced ABS (CF/ABS) and carbon nanotube reinforced ABS (CNT/ABS) fabricated by FFF, by two shear rate methods. Specimens were made by different stacking sequences, which in FFF processing, is equivalent to different printing raster angles. The tensile strength of CF/ABS was found to be superior to that of CNT/ABS for a raster angle of 0°; both the composites exhibited better properties compared to neat ABS. However, when printing with a raster angle of 90°, the tensile strength of CF/ABS specimen was smaller than those of ABS and CNT/ABS specimens. The authors claimed that the addition of short carbon fiber in CF/ABS specimens introduced more voids and weakened the interfacial bonding quality. It was also observed that tensile moduli increased in the order of 90°, ± 45°, and 0° for all ABS, CNT/ABS and CF/ABS specimens. In addition, the effects of printing speed and layer thickness on shear strength of the specimens were investigated. The authors showed that the maximum shear load decreased with increasing printing speed. The effect of layer thickness on the shear strength of CF/ABS printed specimens was characterized using a double notch shear test and the maximum shear load was found to decrease with increasing layer thickness. The observed behavior is likely due to the existence of increased void fraction between the printed layers at higher layer thicknesses and speeds.

Fiber content is another important factor influencing mechanical properties of printed composite materials. Multiple studies have been performed to study the relationship between fiber content and mechanical properties of printed parts [Wang et al., 2017, Papon and Haque, 2019]. Tekinalp et al. [Tekinalp et al., 2014] performed tensile strength and modulus measurements on short fiber (0.2–0.4 mm) reinforced ABS composites dog-bones. Their study showed that both the tensile strength and tensile modulus increased as the fiber content increased, and a maximum 115% and 700% increase could be obtained at 40wt% fiber loading. However, there is limited research on fiber reinforced thermoplastics where the fiber content goes beyond 40wt% because of the nozzle clogging challenges encountered when printing

higher fiber loadings [Fallon et al., 2019].

In this work, we aim at studying the impact of crystallization and rheological behavior of commercially available CF-PA6 filament feedstock and correlating the findings with the mechanical properties of the printed parts. The bulk crystallization behavior and the interlayer polymer chain diffusion under the repeated nonuniform temperature profile during the printing process have been analyzed. The melt flow behavior of the materials, relevant to the printing conditions, has been extensively characterized using both steady shear and oscillatory rheometry. The effect of three print parameters (layer thickness, raster angle, and infill pattern) on the tensile properties of the printed CF-PA6 parts has been investigated using a design of experiments (DOE) approach. Scanning electron microscopy has been employed to highlight surface topography in the printed parts of CF-PA6 as well as to examine the fracture surfaces of the prints to probe the associated failure mechanisms.

5.2 Materials and methods

5.2.1 Filament materials

Two different filaments have been used in this work: neat polyamide 6 (PA6) filament and short CF-reinforced polyamide 6 (with the trade name of Onyx). Both filaments (provided by Markforged) have a nominal diameter of 1.75 mm. The material was dried overnight under vacuum at 80°C before performing the necessary characterizations.

5.2.2 Taguchi approach for determining printing parameters and design of experiments

The Taguchi method of experimental design [Roy, 2010] was used in this analysis. Instead of testing all possible combinations of the process parameters, like the factorial design or other classical DOE methods, the Taguchi only probes pairs of combinations to determine which factors significantly affect process output with minimum experiments. Table 5.1 illustrates three process parameters at three different levels that were examined in this research. The goal was to maximize tensile strength, elongation at break, and elastic modulus. Table 5.2 shows the different levels of process parameters and their combinations determined by design

of experiment analysis using the Taguchi method.

Table 5.1: Printing parameters employed in this study and their levels

Parameter	Unit	L1	L2	L3
Layer thickness	mm	0.1	0.125	0.2
Raster angle	degree	0	45	90
Infill pattern	–	Triangular	Hexagonal	Rectangular

Table 5.2: Printing conditions employed for printing the carbon-fiber reinforced polyamide 6 (CF-PA6) filament

Run No.	Layer thickness (mm)	Infill pattern	Raster angle (°)
1	0.1	Rectangular	90
2	0.1	Hexagonal	45
3	0.1	Triangular	0
4	0.125	Rectangular	0
5	0.125	Hexagonal	90
6	0.125	Triangular	45
7	0.2	Rectangular	45
8	0.2	Hexagonal	0
9	0.2	Triangular	90

Thus, there were nine different combinations of process parameters for experimental investigations. Three identical test specimens were fabricated for each combination, which resulted in a total of 27 test specimens. The analysis of variance (ANOVA) method was employed to identify statistically significant process parameters and their contribution to maximum tensile strength, elongation at break, and tensile modulus.

5.2.3 Thermogravimetric analysis

Thermogravimetric analysis (TGA) was performed on the two materials to ensure provide evidence of minimal thermal degradation at the printing temperature as well as to quantitatively evaluate the fiber content in the composite material. The thermal stability of the

PA6 and CF-PA6 filaments as well as the CF-PA6 printed parts were investigated through TGA using a TGA 5500 (TA Instruments, USA). Weighed amounts of samples (8-10 mg) were tested under a nitrogen environment from room temperature to 600°C at a ramp rate of 10°C min^{-1}. The amount of residue left at the end of the TGA runs for the CF-PA6 samples was indicative of the weight of carbon fibers present in the CF-PA6 filament or printed part (since carbon fibers undergo minimal thermal degradation at 600°C [Dhami et al., 1991].

5.2.4 Dynamic scanning calorimetry

Dynamic scanning calorimetry (DSC) was carried out to determine the changes in melting and crystallization behavior between the filaments and the printed CF-PA6 parts. Changes in total crystalline content of semicrystalline polymers play a major role in dictating the mechanical properties of the 3D printed parts [Bhandari et al., 2019, Das et al., 2020b]. Weighed amounts (5-8 mg) of samples were loaded and pressed into a TA Instruments aluminum T_{zero} pan and DSC was carried out using a Q2000 Series TA Instruments differential scanning calorimeter. The tests were performed using a 50 ml min^{-1} nitrogen flow in order to minimize polymer degradation. Samples were heated to 250°C at a ramp rate of 10°C/min to remove previous thermal history and held at 250°C for two minutes to ensure complete melting; then cooled to 25°C at 10°C/min, below the glass transition temperature of nylon; and finally heated to 250°C at 10°C/min. The crystallinity of the CF-PA6 samples was determined by normalization to the amount of nylon present in the composite (filament or print) via the following equation

$$X_c = \frac{\Delta H_m}{\Delta H_f \times (1 - w_f)} \times 100\% \tag{5.1}$$

where, ΔH_m is the enthalpy of melting of the CF-PA6 composites, ΔH_f is the reference enthalpy of melting of 100% crystalline PA6 which was taken to be 188 J/g [Rwei et al., 2019] , and w_f is the weight fraction of carbon fiber present in the Onyx composite (filament or printed part); as obtained from the TGA runs.

5.2.5 Rheology

Steady shear and oscillatory rheological tests were performed using a TA Instruments ARES G2 rheometer with parallel plate geometry (25 mm) in order to evaluate the shear rate-dependent flow behavior of the materials. Printed discs (25 mm in diameter and 1.6 mm thick with 35% infill) of PA6 and CF-PA6 were used for the rheological characterizations. Steady shear (0.01–10 s^{-1}) was carried out at the recommended printing temperature of the materials (275°C for PA6 and 280°C for CF-PA6). On the other hand, oscillatory (0.1–100 rad s^{-1}) measurements were carried out using a strain amplitude of 0.1% (within the linear viscoelastic regime) at different temperatures (265-280°C for PA6 and 270-285°C for CF-PA6). Both the steady shear and oscillatory measurements were performed using a constant gap height of 1 mm.

5.2.6 Tensile testing

The printed parts of CF-PA6 were tensile tested using an Instron 5969 with a 50 kN load cell at a rate of 3 mm min^{-1} until failure. The tensile characterizations were performed at 22°C, and the reported mechanical properties are an average of at least three tests. The gauge length for all the tests was fixed at 40 mm, and it was assumed that the parts deformed between the Instron grips. Hence, the distance between the crosshead (40 mm) was used to calculate the strain during testing. The width and thickness of the printed parts were 6.35 and 1.45 mm, respectively.

5.2.7 Scanning electron microscopy (SEM)

Cross sections of the tensile tested CF-PA6 prints were imaged using a desktop Phenom Pro scanning electron microscope operated at an accelerating voltage of 10 kV in medium vacuum mode. The cross section of the failed sample was placed onto a double-sided carbon tape and attached to the SEM pedestal prior to imaging.

5.3 Results and Discussion

5.3.1 Thermal characterization

Thermogravimetric analyses (TGA) of the as received PA6 and CF-PA6 filaments along with the printed CF-PA6 parts were performed in nitrogen environment and the corresponding thermograms are presented in Figure 5.1. Table B.1 in the supplementary information lists the different degradation temperatures of as received PA6, CF-PA6, and printed CF-PA6 part; where $T_{x\%}$ denotes the temperature at which x% of the initial sample has decomposed. The onset of thermal degradation (denoted by 5% weight loss) for the PA6 filament initiated at 418°C and the sample was almost completely degraded at 500°C. Both the as received CF-PA6 filament and the printed part exhibits similar thermal degradation pattern where the polymer matrix is burnt off at 500°C. The marginally inferior thermal stability (reduced onset of degradation temperatures) of CF-PA6 filament and print compared to the PA6 filament may be attributed to decomposition of an organic sizing compound present on the carbon fibers [Tranchard et al., 2017]. Also, since PA6 does not undergo charring at high temperatures [Levchik et al., 1999], formation of carbonaceous residue due to interactions between the PA6 and carbon fibers can result in such behavior [Tranchard et al., 2017]. Moreover, the thermal exposure during the printing process can also lead to a final printed part having a lower onset of degradation temperature. The residual amount left after heating the composite samples to 600°C is indicative of the amount of carbon fibers present. For the as received CF-PA6 filament, the weight fraction of carbon fibers was found to be 14.30 $\pm$ 0.26% while that in the printed part was 14.18 $\pm$ 0.09%. Therefore, it can be concluded that the printing process did not significantly alter the amount of carbon fiber present in the printed parts with respect to the feed filament.

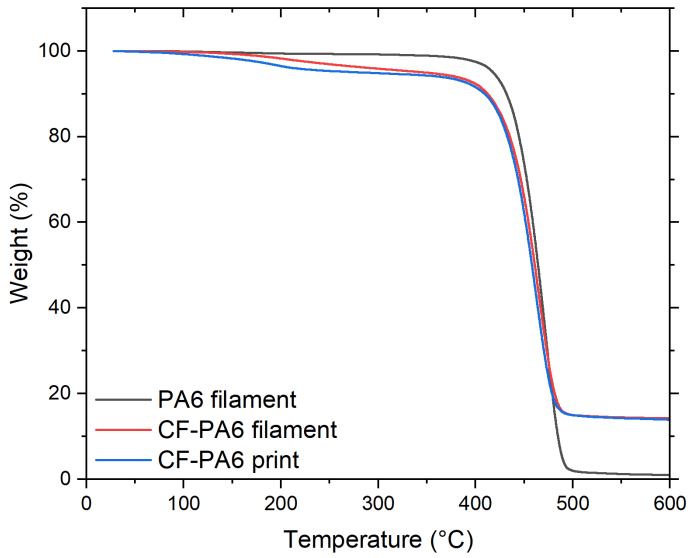


Figure 5.1: TGA profiles for the as received PA6 and CF-PA6 filaments as well as CF-PA6 print performed under nitrogen atmosphere with a heating rate of 10°C min^{-1}.

5.3.2 Melting, crystallization, and crystallinity of PA6 and CF-PA6

The melting and crystallization behavior of PA6 and CF-PA6 plays a crucial role in dictating the time window available for interlayer bond formation during the printing process and therefore directly controls the mechanical properties of the printed parts [Northcutt et al., 2018]. Moreover, the addition of short carbon fibers can significantly impact the peak crystallization temperature, rate, and degree of crystallinity. Broadening the crystallization window (difference between the peak melting temperature and peak crystallization temperature) not only allows for increased time for interlayer chain diffusion, but also assists in relaxation of the residual stresses entrapped in a part during the printing process. Therefore, characterizing the crystallization behavior of the samples under conditions relevant to the printing process is of utmost importance. It is worth mentioning that the cooling rate studied here (10°C min^{-1}) is not representative of the rates encountered by the polymer extrudate upon deposition on the printer bed; however, such analysis can explain differences in

crystallization behavior caused due to the presence of stiff carbon fibers within the polymer matrix.

Figure 5.2 highlights the melting (from the second heat of a nonisothermal experiment) and cooling profiles of the as received PA6 and CF-PA6 filament, as well as that of the filament following thermal exposure from the printing process, as measured by DSC. The printed/extruded PA6 did not have any significant change in the melting and crystallization properties compared to the as-received PA6 filament. Hence, changes observed in the composite filament and print is directly a result of the incorporation of CFs in the PA6 matrix. Details about the peak melting temperature (T_m), peak crystallization temperature (T_c), enthalpy of melting, and enthalpy of crystallization have been provided in Table B.2 of the supporting information section. As illustrated in Figure 5.2, the presence of a homogenous melting peak is indicative of the presence of a single crystalline phase in the samples. The crystallization window ($T_m - T_c$) increased by 5.8°C in the CF-PA6 filament as compared to that of neat PA6 filament. The broader crystallization window ensures the polymer chains stay in the melt state for a longer time prior to coalescence (weld formation, typically occurs above glass transition temperature for amorphous polymers and above the T_c for semicrystalline polymers), which results in better residual stress dissipation due to increase chain mobility and therefore ensures printed parts with minimal warpage and improved dimensional stability [Das et al., 2020b, Chatham et al., 2019a].

The total crystalline content in the samples is an important factor in controlling the mechanical properties of the final printed part. Any adverse effect on the degree of crystallinity needs to be minimized in order to maintain properties in the printed parts comparable to traditionally processed parts. The degree of crystallinity for the neat PA6 and CF-PA6 filament was calculated from the second heating cycle of the nonisothermal DSC experiment using Equation 5.1 and found to be 24.4% and 29.5%, respectively. Such increase in the degree of crystallinity is likely due to the presence of increased number of nucleation sites [Dul et al., 2021] and enhanced crystal growth rate in the fiber reinforced composite [Karsli and Aytac, 2013]. The different processing history as well as the incorporation of CFs can also be responsible for the variation in the degree of crystallinity of the composites as compared to PA6. However, a delicate balance between the fiber content and degree of crystallinity must be achieved since too high a fiber concentration severely limits polymer chain mobility and diffusion [Fornes and Paul, 2003]. Therefore, it is detrimental to the crystal growth within the polymer matrix [Lozano and Barrera, 2001, Ren et al., 2008]. Interestingly, the

crystal size (that dictates mechanical properties) can be tuned by controlling the number of nucleation sites and hindered crystal growth rates in the composites [Fornes and Paul, 2003]. Within the scope of the current work, only one fiber concentration (14.3 wt%) has been investigated; future work can aim to investigate the optimal fiber content in PA6 that corresponds to maximum achievable degree of crystallinity in the composites.

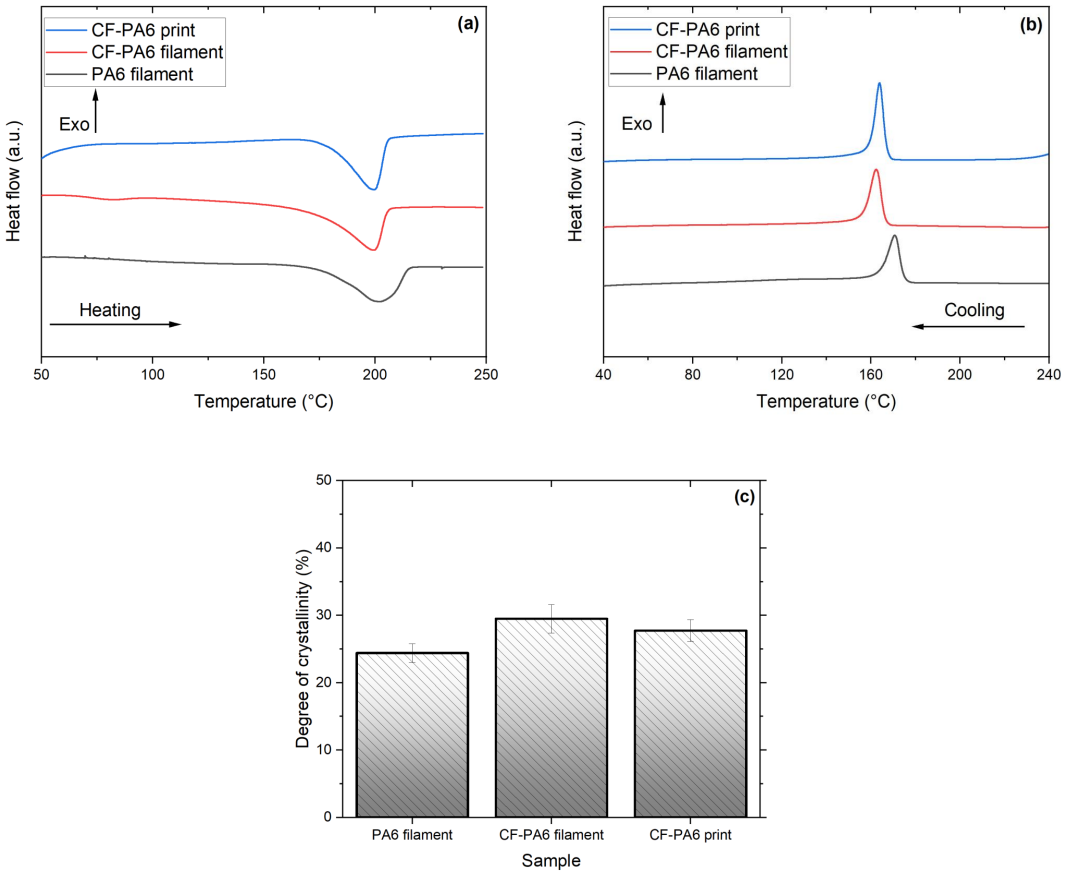


Figure 5.2: (a) DSC melting endotherms from the second heat of the nonisothermal experiments for PA6 and CF-PA6 (Onyx); (b) DSC cooling exotherms from the nonisothermal experiments for PA6 and CF-PA6 (Onyx); (c) Degree of crystallinity as measured using Equation 1 for PA6 and CF-PA6 (Onyx filament and print). The enthalpy of melting was calculated from the second heat of the nonisothermal experiments.

The printed CF-PA6 part was also tested under similar conditions and the behavior was

found to be similar to that of the filament sample, suggesting the shear and thermal history (experienced during the printing process) has a minimal impact on the melting and crystallization characteristics. The degree of crystallinity in the printed part (27.7%) was slightly lower than that in the filament (29.5%), and can be attributed to the changes in relaxation timescales during printing that results in reduced chain orientation effects [McIlroy and Graham, 2018].

5.3.3 Rheological characterization

The rheological behavior of the neat PA6 and short carbon fiber filled CF-PA6 composite was studied. As recommended by the manufacturer, the printing temperature for PA6 and CF-PA6 are 275°C and 280°C, respectively. Therefore, rheological characterizations at these temperatures are most important to describe the extrusion through the nozzle during the printing process. However, in order to better understand the viscoelastic behavior of the polymer melt, a series of oscillatory measurements were performed at different temperatures.

Figure 5.3 illustrates the complex viscosity (η^*) of neat PA6 and CF-PA6 composites as a function of angular frequencies at different temperatures. For both the materials, a Newtonian plateau is observed at lower rates followed by shear thinning region at higher rates. The breadth of the Newtonian plateau diminishes as the temperature increases and the samples exhibit a more pronounced shear thinning behavior, which is ideal for ensuring extrusion through the printing nozzle. The increased mobility of the polymer chains at higher temperatures is held responsible for the observed trends in the complex viscosity data. In case of the composite material, the coupled effects of shear and thermal energy ensures mobility of the fibers, which then rearranges into macro-structures that can strongly impact the rheological response of the composite [Azizi and Faghihi, 2009, Shenoy, 1999].

The obtained complex viscosity data at different temperatures were fitted to the Carreau model, as illustrated in Equation 5.2

$$\eta^* = \eta_0^* \left[1 + (\lambda\dot{\gamma})^a\right]^{\frac{n-1}{a}} \tag{5.2}$$

where, is the η_0^* zero shear complex viscosity, λ is the relaxation timescale, a is a model parameter, and n is the power law index. The values of the Carreau law parameters have been listed in Table B.3 of the supplementary information section. For both PA6 and CF-

PA6, a decrease in the η_0^* and an increase in n is observed with temperature; likely due to the reduced resistance to flow at higher temperatures. The relative increase is the value of n with temperature for the CF-PA6 composite is less than that of PA6 which may be due to the fiber alignment occurring at the high shear rates which hinders the propensity of the polymer chains to flow at higher temperatures [Bertolino et al., 2021]. The shear rate experienced by the polymer melt during extrusion through the nozzle can be calculated using the following equations [Das et al., 2021b, Calafel et al., 2020]:

$$\dot{\gamma} = \frac{32Q}{\pi D^3}\left(\frac{3n+1}{4n}\right) \tag{5.3}$$

$$Q = \frac{\pi d^2 v}{4} \tag{5.4}$$

where, D is the nozzle diameter, d is the filament diameter, v is the printing speed, Q is volumetric flow rate. Using the value of n from the Carreau fits at the printing temperature of CF-PA6 (280°C), we calculate the shear rate inside the nozzle to be in range of 10^4 s^{-1}. Since such high shear rates are not attainable in a rotational rheometer, the melt flow behavior can be described using the Cox Merz rule under the printing conditions as highlighted in the following section.

The addition of the carbon fibers results in a significant increase in the complex viscosity of the CF-PA6 composite compared to PA6 as well as enhancing the shear thinning behavior in the composite sample. The incorporation of the short carbon fibers increases the local shear rates experienced by the polymer melt trapped between the fibers as compared to the neat polymer and leads to a more pronounced shear thinning behavior [Laun, 1984]. Both PA6 and CF-PA6 are in the shear thinning regimes at the shear rates experienced by the polymer melt during extrusion through the print nozzle. The higher zero shear viscosity of CF-PA6 is likely to help in better shape retention post deposition on to the printer bed compared to PA6.

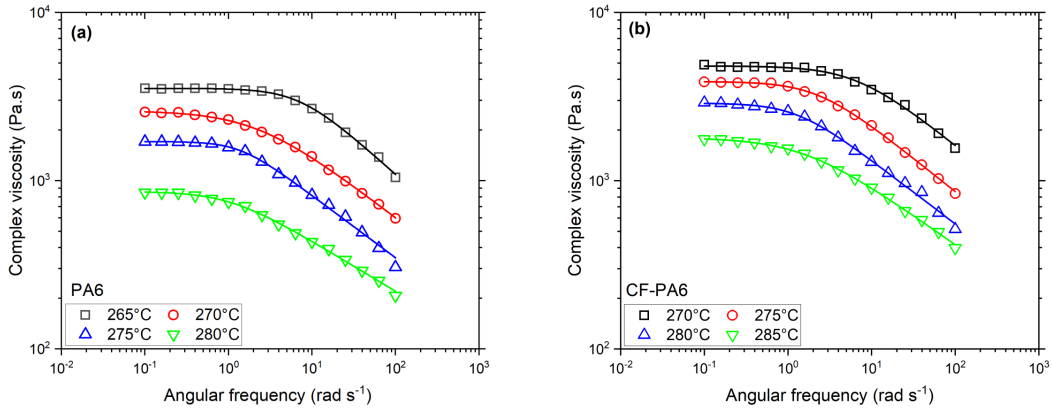


Figure 5.3: Complex viscosity as a function of angular frequency as obtained using SAOS rheometry at different temperatures for (a) PA6 and (b) CF-PA6. The solid lines indicate the data fits to the Carreau model (Equation 5.2).

As an initial approximation of the melt flow behavior of carbon fiber reinforced polymers, researchers have used SAOS measurements previously [Ajinjeru et al., 2018a]. The viscosity (or complex viscosity) of the neat PA6 and CF-PA6 composites as a function of shear rate (or angular frequency) at the respective printing temperatures are presented in Figure 5.4. During the printing process, the polymer melts experience a wide range of shear rates; ranging from $\dot{\gamma} \leq 0.1s^{-1}$ on the print bed to $\dot{\gamma} \sim 100 - 500s^{-1}$ inside the printer nozzle [Gilmer et al., 2019, Ajinjeru et al., 2018b]. Therefore, in order to check the applicability of complex viscosity measurements obtained in a rotational rheometer to the high shear behavior inside the nozzle, the validity of the Cox Merz rule (Equation 5.5) must be investigated.

$$\eta(\dot{\gamma}) = |\eta^*(\omega)| \, for \dot{\gamma} = \omega \tag{5.5}$$

As highlighted in Figure 5.4, the Cox Merz rule is a good approximation for the neat PA6 and the CF-PA6 composite, although there exists some discrepancy in the overlap between the SAOS and steady shear data. It is worth mentioning that fiber alignment along the direction

of shear results in reduction of steady shear viscosity in CF-PA6 composite; a feature that cannot be captured using SAOS rheometry. The Cox Merz rule can serve as a good "rule of thumb" for process design providing qualitative representation of the shear/frequency dependence of the viscosity, but the values obtained using this technique are not strictly representative of the shear dependent flow behavior encountered during the printing process. Therefore, SAOS can more reliably provide relative differences in the flow behavior of PA6 and CF-PA6 as a function of printing conditions and material compositions, rather than directly comparing the exact viscosity values.

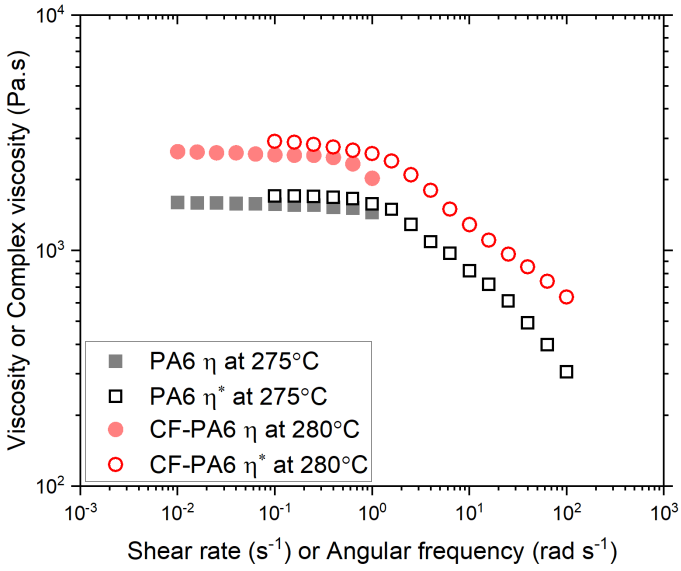


Figure 5.4: Overlay of the steady torsional shear (filled symbols) and small amplitude oscillatory shear (open symbols) rheometry of PA6 and CF-PA6 at the respective printing temperatures of 275°C and 280°C.

Figure 5.5 highlights the storage modulus (G') and loss modulus (G") as a function of frequency at different temperatures for PA6 and CF-PA6. The elastic response associated with each deformation cycle represented by the recovered energy is indicated by G' while the dissipated energy in the corresponding cycles is denoted by G". As presented in Figure 5.5, G' and G" values of both PA6 and CF-PA6 exhibit a strong dependence on the angular frequency, indicating that the samples are predominantly composed of non-covalent bonds [Liu et al., 2019]. Within the temperature range probed (265-280°C for PA6 and 270-285°C

for CF-PA6), the samples exhibit a liquid-like characteristic with G" > G' for all angular frequencies. Such behavior is necessary in ensuring extrusion through the printing nozzle as well as to facilitate interdiffusion of polymer chains between two deposited layers on the printer bed [Das et al., 2021b, O'Mahony et al., 2020]. Compared to neat PA6, the incorporation of short carbon fibers resulted in higher G' and G" values for the CF-PA6 sample. The increased values of the modulus was more pronounced at the lower frequency range (less than 1 rad s^{-1}) compared to the higher frequency range (greater than 10 rad s^{-1}) which is in agreement with results obtained previously for carbon fiber reinforced polyether imide samples [Ajinjeru et al., 2018a]. The comparatively shorter characteristic timescales at the higher frequencies counteracts the presence of fibers in the sample and hence the difference between dynamic modulus values [Greene and Wilkes, 1995, Kim and Song, 1997].

However, once deposited, the polymer melt should rapidly switch to a viscoelastic behavior exhibiting G' > G" to maintain shape retention and print resolution[29]. The loss tangent ($tan\delta = G"/G'$) for both the samples at the temperatures tested was found to be greater than unity; further highlighting the dominant viscous behavior under the processing conditions. Since both the PA6 and CF-PA6 samples exhibit a strong viscous component, longer relaxation times after deposition on the printer bed is recommended in order to ensure mechanical stability of the extrudate during the printing process [Duty et al., 2018]. Moreover, the frequency dependent behavior of the storage modulus (G'), which provides a measure of the elastic nature of the PA6 and CF-PA6 samples, can be expressed using a power-law type model, as illustrated in Equation 5.6:

$$G' = a_1\omega^{a_2} \tag{5.6}$$

where, a_1 and a_2 are the power law parameters representative of magnitude of G' at a particular frequency and the extent of frequency dependence of G' [Purwanti et al., 2011]. The values for these parameters at different temperatures for PA6 and CF-PA6 are listed in Table B.4 of the supporting information and the corresponding G' vs. ω along with the data fits to Equation 5.6 are plotted in Figure B.1. The values of a_1 decreased with temperature while that of a_2 increased and gradually approached unity at the highest temperature. Both the trends suggested the increased propensity (and hence reduced resistance) of the samples to flow which in turn assists in smooth extrusion under shear through the print nozzle.

Generally, in the terminal flow region of relaxed monodisperse polymer chains G' scales with ω^2 with linear architecture [Wang et al., 2008]; however, for PA6 and CF-PA6 investigated

in this study, the relations are given by $G' \sim \omega^{(}0.75 - 1.01)$ and $G' \sim \omega^{(}0.82 - 1.00)$, respectively. The polydispersity of the polymer chains is a likely cause behind this discrepancy [Krishnamoorti and Giannelis, 1997]. Another possible explanation behind this surprising trend is formation of interconnected structures of the carbon fibers in the polymer matrix resulting in increased interactions between the fibers and PA6. Such structures can significantly impact the long range co-operative motion and corresponding relaxation spectra of the polymer chains [Sung et al., 2006] resulting in deviation from the expected scaling laws.

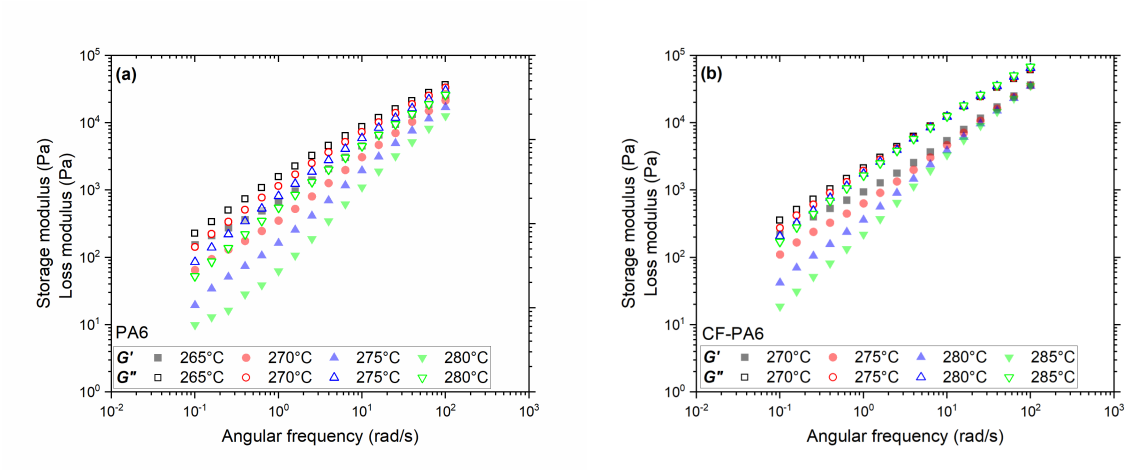


Figure 5.5: Mechanical spectra for storage modulus (closed symbols) and loss modulus (open symbols) as a function of angular frequency for (a) PA6 and (b) CF-PA6 samples at different temperatures.

Post extrusion from the nozzle, the most important factor determining the success of a printed part is the interlayer bond formation (G' > G") on the print bed. The bond formation takes place through multiple steps including surface wetting, neck growth, interfacial chain diffusion, and viscous sintering [Bellehumeur et al., 2004, Coogan and Kazmer, 2017a]. During the diffusion and sintering process, the polymer chains can migrate across the deposited layers and re-entangle. The motion of the polymer chains is however limited by the time the polymer stays above the glass transition temperature, a time window of only 2-3s before molecular motion stops [Seppala and Migler, 2016, Anderegg, 2020]. Within this

timescale, the interlayer weld formation occurs which in turn dictates the properties of the printed parts.

In summary, from the results discussed in this section the rheological differences between neat PA6 and CF-PA6 are apparent and is likely to affect the printing process and subsequently, the printed part properties. The shear rate and temperature associated with the printing process controls the extent of fiber mobility in the PA6 matrix. In turn, the mobility of the CFs in the PA6 matrix plays a crucial role in dictating the interlayer bonding during the printing process and hence determines the final printed part properties. Tuning the rheological properties as a function of process variables can lead to the development of tailored feedstock formulations that can achieve mechanical properties in the vicinity of injection molded parts.

5.3.4 Tensile properties of printed parts: Effect of print parameters

Like all AM processes, FFF features a large number of processing parameters that can affect the final printed part properties. FFF processing parameters include both toolpath parameters (part build orientation, raster angle, raster width, printing speed, infill pattern, infill density, layer thickness) and parameters related to material extrusion and thermoplastic welding (build platform/environment temperature, nozzle temperature, filament feed rate). In our current study, we investigate the effect of layer thickness, infill pattern, and raster angle on the mechanical properties of the printed PA-CF6 parts. Layer thickness controls the total number of printed layers, the geometric accuracy, manufacturing efficiency, and the printed parts' performance in a typical 3D printing process [Tian et al., 2016]. In the case of CF-reinforced thermoplastics, varying the layer thickness can change the fiber content in the final part. Infill pattern and raster angle are also significant parameters that can affect print time, weight, strength, etc. [Chacón et al., 2019].

In order to obtain the effective optimum combination of the process parameters, a number of CF-PA6 composite parts were printed at 40 mm s^{-1} and 280°C with an infill density of 37% using the print parameters listed in Table 5.2. Representative stress strain plots of the nine different samples tested for DOE analysis are presented in Figure 5.6. The tensile properties corresponding to the various process parameters are tabulated in Table 5.3 for the printed specimens manufactured with short carbon fiber reinforced PA6. Reported values

of the tensile properties are based on an average of at least three tests. Table 5.4 compares the tensile properties of the CF-PA6 composites obtained in this study with reported values in the literature for similar fiber reinforced polymer composites processed using FFF. The tensile properties reported in this study are comparable or even superior to that reported by Sauer and Tantillo when using similar CF-PA6 material and Mark Two printer [Sauer, 2018, Tantillo, 2019].

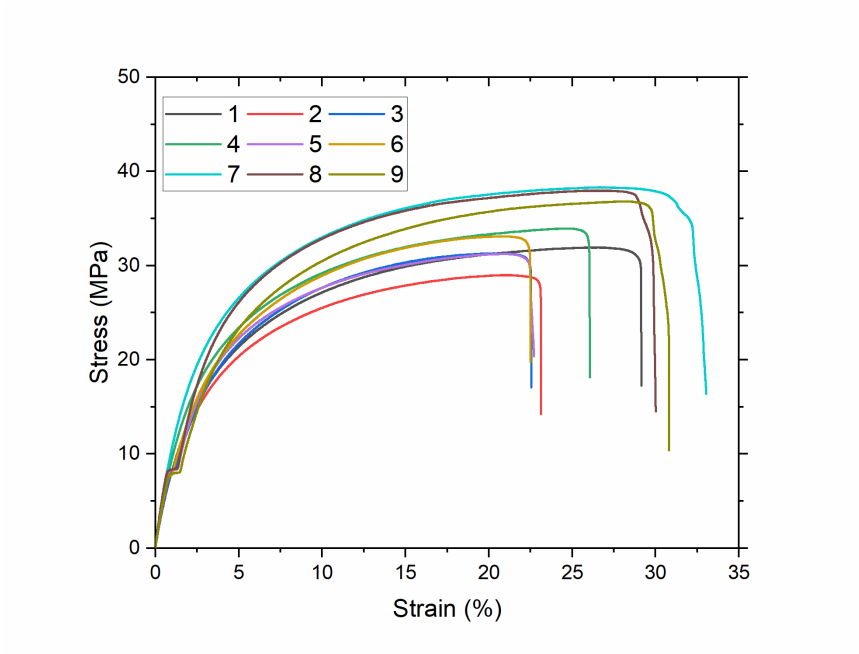


Figure 5.6: Representative stress-strain plots of the different CF-PA6 printed parts used in this study. The numbers in the inset of the figure refers to the sample numbers as listed in Table 5.2 with different layer thickness, raster angle, and infill pattern. The printing temperature, printing speed, and infill density was kept constant at 280°C, 40 mm s−1, and 37% respectively

It was observed that the maximum tensile strength of 38.0 *pm* 0.2 MPa was obtained when the specimen was printed in a raster angle of 0°, layer thickness of 0.2mm, and hexagonal infill pattern. The mechanical test results also revealed that the same print parameter combination results in the maximum tensile modulus values. The reason for the improved tensile strength of the hexagonal pattern prints is attributed to the relative orientation of the deposited layers that ensures better contact. This is consistent with the findings of Naranjo-Lozada et al. [Naranjo-Lozada et al., 2019] who reported the print pattern to have

a significant effect on the tensile properties of both continuous and chopped CF reinforced thermoplastics. The maximum tensile strength of 0.2 mm layer thickness prints increases by 23-30% compared to the 0.1 and 0.125 mm prints. A raster angle of 0° exhibits the maximum tensile strength and modulus values; likely due to the reinforcement effect arising from the continuous layer deposition in the direction of tensile testing.

Table 5.3: Tensile properties of printed specimens of the CF-PA6 material as a function of the processing parameters employed in this study.

Run no.	Layer thickness (mm)	Infill pattern	Raster angle (°)	Maximum tensile stress (MPa)	Elongation at break (%)	Tensile modulus (GPa)
1	0.1	Rec	90	32.0 ± 0.1	26.5± 1.7	1.17± 0.07
2	0.1	Hex	45	29.7 ± 0.5	23.0 ± 0.6	1.09 ± 0.02
3	0.1	Tri	0	31.3 ± 0.1	21.6 ± 1.0	1.16 ± 0.07
4	0.125	Rec	0	34.4 ± 0.3	26.4 ± 1.2	1.23 ± 0.03
5	0.125	Hex	90	31.0 ± 0.5	21.5 ± 0.7	1.22 ± 0.02
6	0.125	Tri	45	33.1 ± 0.7	22.6 ± 0.1	1.17 ± 0.06
7	0.2	Rec	45	38.0 ± 0.8	29.8 ± 1.8	1.31 ± 0.03
8	0.2	Hex	0	38.0 ± 0.2	29.2 ± 0.1	1.37 ± 0.04
9	0.2	Tri	90	36.9 ± 0.3	30.4 ± 0.7	1.22 ± 0.03

On the other hand, maximum elongation at break for CF-PA6 prints was obtained when the sample was printed in a raster angle of 90°, layer thickness of 0.2 mm, and triangular pattern. The CF-PA6 specimens printed with a triangular pattern and 0.2 mm layer thickness exhibited an increase in elongation at break 15-40% higher than that of a 0.1 mm layer thickness printed sample. ANOVA results for maximum tensile strength are exhibited in Table B.5. For a p-value is less than 0.05, the statistical significance of the corresponding parameter is established; therefore, layer thickness has a significant role in dictating the maximum tensile strength of CF-PA6 printed parts. Also, the percentage contribution of each process parameter has been calculated and reflected in Table B.5.

Table 5.4: Comparison of mechanical properties available in the literature for carbon fiber reinforced nylon composite (Onyx) with other filler reinforced polymer composites manufactured using FFF.

Type of material	Tensile strength (MPa)	Elongation at break (%)	Tensile modulus (GPa)	Reference
CF reinforced ABS	42			[Ning et al., 2015]
Short CF reinforced polyamide	9.0 ± 0.4	0.70 ± 0.1	1.41 ± 0.11	[Striemann et al., 2021]
Short CF reinforced PLA	37.76		1.57	[Fan et al., 2020]
Short CF reinforced PA	33.5		1.85	[Blok et al., 2018]
Glass fiber reinforced PP	34		0.39	[Sodeifian et al., 2019]
Onyx	24.9		1.3	[Tantillo, 2019]
Nylon	25.5			[Vishwas et al., 2018]
CNT reinforced ABS		4.0	1.00	[Abeykoon et al., 2020]
Nylon (PA6)	10.4		0.598	[Naranjo-Lozada et al., 2019]
Onyx	15.2		1.293	[Naranjo-Lozada et al., 2019]
Onyx	31.0 ± 2.1		0.88 ± 0.3	[Sauer, 2018]
CF-PA6	38.0 ± 0.2	29.2 ± 0.1	1.37 ± 0.04	This work

Using the Taguchi method, process parameter design converts the output value to signal to noise ratio (S/N), known as a quality characteristic evaluation index. Considering the

S/N ratio, the least variation and the optimal quality design can be obtained. This research aims to maximize the mechanical properties of the printed part using the CF-PA6 composite material. Thus, the Taguchi analysis is implemented to maximize properties, and larger values of the S/N ratio improve values for tensile strength. Figure 5.7(a) illustrates the main effects plots, indicating suggested combinations of the parametric levels for obtaining the maximum tensile strength. It is apparent that the S/N ratio increases with increasing layer thickness, decreases with increasing the raster angle, and it reaches its maximum value when the infill pattern is rectangular. Thus, the tested specimen exhibited maximum ultimate tensile strength at 0.2mm layer thickness, raster angle of 0°, and rectangular infill pattern.

ANOVA results for elongation at break of the CF-PA6 printed parts are presented in Table B.6 while the corresponding main effects plot is highlighted in Figure 5.7(b). Based on the p-values obtained using the statistical analysis, it can be concluded that the layer thickness is the most significant parameter affecting the elongation at break. The percentage contributions of other process parameters are also calculated. As demonstrated in Figure 5.7(b), maximum elongation at break was obtained maximum at 0.2mm layer thickness, 90° raster angle, and rectangular infill pattern.

Table 5.5: Optimum factor levels for maximum tensile strength, elongation at break, and tensile modulus of the CF-PA6 printed parts

Factors	Maximum tensile strength	Elongation at break	Tensile modulus
Layer thickness (mm)	0.2	0.2	0.2
Raster angle (°)	0	90	0
Infill pattern	Rectangular	Rectangular	Rectangular
Significant	Layer thickness		

Figure 5.7(c) illustrates the main effects plot for the tensile modulus of the CF-PA6 printed parts while the ANOVA statistical analysis based on the tensile modulus is presented in Table B.7. Of those evaluated ,the process parameters that provided the highest tensile modulus are 0.2mm layer thickness, 0° raster angle, and rectangular infill pattern, as indicated from the main effects of the S/N ratio highlighted in the figure. The optimum levels of three factors for each response of the printed part can be obtained from the main effect plots for the S/N ratio in Figs. 5.7(a-c). Optimum factor levels with significant factors and interactions for the printed part strength are summarized in Table 5.5.

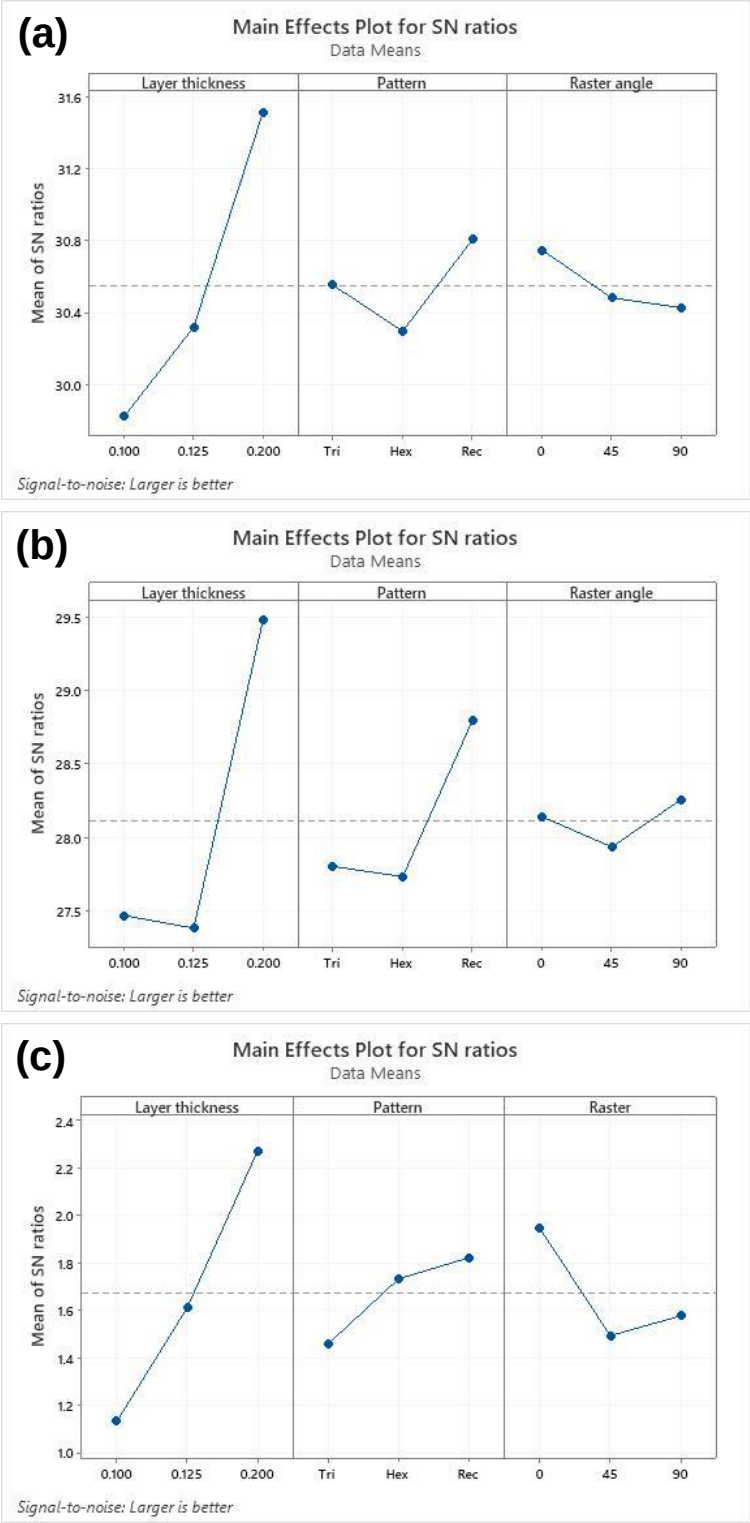


Figure 5.7: Signal to noise ratios for (a) maximum tensile strength, (b) elongation at break, and (c) tensile modulus of printed parts of CF-PA6 as a function of layer thickness, raster angle, and infill pattern.

The importance of surface roughness of the printed parts (and hence the layer thickness employed during printing) on the mechanical properties have been studied previously [Durgun and Ertan, 2014]. The mechanical properties, microstructure, and failure mechanisms of the printed parts are strongly influenced by layer thickness [Terekhina et al., 2020]. Generally, the microscopic surface defects in a part led to the formation of crack initiation sites. The effect of layer thickness on the surface finish and surface roughness in the printed parts has been recently reported using 3D laser-scanning confocal microscopy by Striemann et al. [Striemann et al., 2021] The results suggested a linear increase in the primary surface texture with layer thickness.

From the surface roughness measurements, an effective load bearing cross sectional area can be defined (based on a correction factor), which is lower than the nominal load bearing area. As a result, an increase in the tensile strength and modulus have been observed with increasing layer thickness, consistent with the trend reported in the current manuscript. The larger layer thickness during printing will result in a part that has fewer layer interfaces and hence during tensile testing lower number of crack propagation sites are generated as compared to a part printed with lower layer thickness values. Moreover, larger layer thickness results in increased road dimensions and hence higher interlayer contact area across which polymer chains can migrate and form interlayer bonds. The raster angle of 0° resulted in prints with the highest tensile strength and modulus likely due to the layer alignment along the direction of tensile testing.

From the rheological stand-point, during the printing process a deposited layer must be robust enough to support the successive layers. However, having an extrudate with lower viscosity allows the melt to flow more post-extrusion through the nozzle and can assist in pore fill-up through intelligent toolpath designs. Print parameter optimization and a balance between the viscous (G") and elastic (G') nature of the polymer melt (as discussed earlier in the manuscript) can ensure printed parts with minimal surface roughness. Although, as mentioned in the previous section, increased surface roughness can lead to increased tensile properties; generally, it is undesired for printed parts for functional applications. The interplay between the G' and G" components of the modulus can assist in shape retention during the printing process as well as ensure proper surface finish on the printed parts thereby affecting the mechanical properties. The window available for switching between $G' < G"$ (smooth extrusion through nozzle and interlayer chain diffusion) and $G' > G"$ (shape retention and stable extrudate) is the time spent by the polymer chains in the melt state prior

to the onset of crystallization. Optimizing the layer thickness can help in achieving optimum tensile properties at the cost of surface finish; while tuning the rheological properties can aid in limiting the extent of surface roughness imparted to a part during the printing process. Therefore, simultaneous characterization of the crystallization, rheological, and mechanical behavior as presented in this study is of utmost importance in order to achieve a comprehensive understanding of the printing process for fiber reinforced polymers.

5.3.5 SEM analysis

The tensile fracture surfaces of the printed short carbon fiber PA6 (Onyx) composites were analyzed via SEM in order to provide insights into the failure mechanisms as a function of processing variables. The associated SEM micrographs of the CF-PA6 composites are presented in Figure 5.8. It is evident that the fibers were embedded within the polymer matrix and during testing most of the fibers were pulled out. This is attributed to the poor interfacial adhesion between the carbon fibers and PA6. Another interesting observation is that all the prints failed through fiber pull-out from the PA6 matrix and not through polymer matrix fracture since the stresses encountered during tensile testing are insufficient to cause the latter [Li and Zhang, 2009]. In some cases, localized deformation of the PA6 matrix in the vicinity of the fibers resulted in the formation of dark patterns (Figure 5.8c) between the fibers and the polymer [Lozano and Barrera, 2001]. Finally, the surfaces of the fiber post-testing were clean further corroborating the limited wetting of the fibers by the matrix [Li and Cai, 2011]. This observation is indicative of interlaminar failure suggesting the inconsistent bonding of the fibers to the PA6 matrix. The insufficient wetting and hence the poor bonding is further aggravated at higher fiber loadings resulting in printed parts with increased voids [Dickson et al., 2017]. An easy way to counteract this problem is to subject the carbon fibers to specialized surface treatments that would significantly improve the fiber/matrix interface [Dickson et al., 2017, Li and Cai, 2011].

5.4 Conclusions

In this study, the effect of layer thickness, raster angle, and infill pattern on the tensile properties of FFF processed short carbon fiber reinforced PA6 parts have been evaluated using a DOE approach. The crystallization profiles along with the total crystalline content of

the neat PA6 and composite have been characterized to highlight changes in the time window available for crystallization (and solidification) during the printing process. The composite material exhibits a broader crystallization window allowing the polymer chains to remain in the melt state longer, thereby significantly reducing the residual stress state in the printed parts (evidenced by the extent of warpage in the CF-PA6 printed parts compared to that of neat PA6). Steady shear and SAOS measurements demonstrate the importance of shear thinning behavior of PA6 and CF-PA6 in order to ensure successful FFF processing. Within the temperature range studied, both materials exhibit viscous dominant behavior, which is ideal for ensuring interdiffusion of the polymer chains. The higher zero shear viscosity of CF-PA6 compared to PA6 ensures better shape retention of the extrudate post printing. Finally, the tensile properties of the printed parts were characterized, and layer thickness (>25% improvement in maximum tensile strength and tensile modulus) and print pattern (>30% improvement in elongation at break) were found to have a profound impact on the maximum tensile strength and tensile modulus.

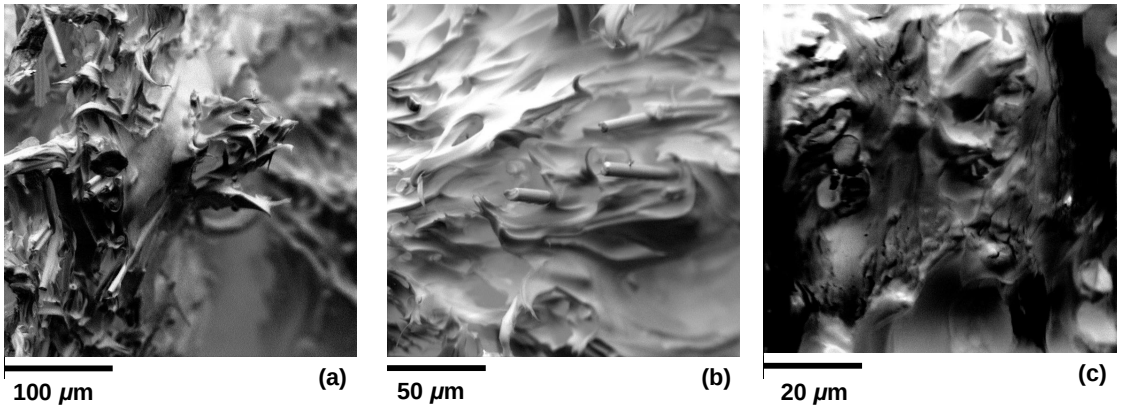


Figure 5.8: Scanning electron micrographs of the fracture surface of CF-PA6 prints after tensile testing (a) fiber pullout from the polymer matrix but no evidence of matrix cracking of layer delamination; (b) clean surface of the carbon fibers suggesting poor interfacial adhesion with the polymer matrix; and (c) dark patches in the polymer matrix due to localized deformations near the fibers.

The process-induced effects of layer thickness on the mechanical properties of the printed parts must be coupled with the crystallization and rheological characteristics of the polymer melt in order to generate parts with optimum properties and quality. The results presented in this manuscript aim to lay the framework for physics-based optimization of print properties of carbon fiber reinforced polymer composites based on their thermal, crystallization, and rheological properties for multifunctional applications (e.g., electromagnetic antennas, accessories for space vehicles, sensors for structural health monitoring, etc.). Future research can attempt to model the polymer melt flow coupled with the fiber orientation effects in fiber reinforced polymer composites. Although there are a few recent works in this topic [Wang and Smith, 2018, Heller et al., 2016b, Russell et al., 2018], there is still much to investigate regarding the polymer wetting at the interface of deposited layers, evolution of interlayer bond strength, and thermo-mechanical consolidation post deposition on the printer bed [Das et al., 2021c].

Chapter 6

Material extrusion-based additive manufacturing with blends of polypropylene and hydrocarbon resins

Arit Das[1,2], Alexandra E. C. Marnot[1], Jacob J. Fallon[2,3], Stephen M. Martin[1,2], Eugene G. Joseph[1], and Michael J. Bortner[1,2]

[1]Department of Chemical Engineering, Virginia Polytechnic and State University, Blacksburg, VA 24061, USA

[2]Macromolecules Innovation Institute, Virginia Polytechnic and State University, Blacksburg, VA 24061, USA

[3]Department of Macromolecular Science and Engineering, Virginia Tech, Blacksburg, VA 24061, USA

This chapter was originally published in the **ACS Applied Polymer Materials** journal.

ACS Appl. Polym. Mater. 2020, 2, 2, 911–921. https://doi.org/10.1021/acsapm.9b01127

Abstract

Filament-based material extrusion additive manufacturing (MEAM) is one of the most commonly used techniques in additive manufacturing (AM). In spite of recent notable development in the MEAM process, there is still a need to develop more materials that can be printed consistently using this technique. Isotactic polypropylene (PP), a popular thermoplastic material, undergoes rapid crystallization and subsequent volume contraction. This can lead to residual stress buildup in PP parts when processed using MEAM, resulting in poor adhesion to the printing platform, poor geometric tolerance, and mechanical performance. In this work, the effects of varying composition of low molecular weight hydrocarbon resins incorporated to PP are investigated. Specifically, the thermal behavior, crystallization, morphology,

and printability of the blends are studied. The rapid crystallization of PP has been delayed by the addition of hydrocarbon resins that provided a larger time window for the residual stresses to relax. The addition of the resins to the pure PP matrix lowers the crystallization temperature of PP from 121.8 to 116.0 °C, which further enables additional diffusion during the solidification process. Polarized optical microscopy demonstrates the differences in crystalline morphology, which is expected to impact the structure at the interlayer boundaries between deposited layers. The combination of modifications in crystallization rate, time, and morphology significantly affects the interlayer adhesion and residual stress state, which directly controls the mechanical properties and part warpage of printed parts. Tensile bars of the different blends were printed in two different orientations to analyze the mechanical performance and study part anisotropy. The maximum tensile stress of pure PP (26.8 ± 2.1 MPa) printed at a ±45° raster angle increased with addition of 20 wt% hydrocarbon resin (32.4 ± 3.0 MPa) when printed under the same conditions. The improvement in the tensile strength is due to a combination of changes in crystallinity, morphology, and improved interlayer adhesion during printing. The parts were annealed postprinting to improve polymer chain diffusion across the layers, thereby improving interlayer adhesion and resulting in tensile modulus and strength values in excess of 90% of injection-molded PP parts.

Keywords: additive manufacturing; semicrystalline polymers; polypropylene; crystallinity; mechanical properties

6.1 Introduction

Additive manufacturing (AM) is one of the fastest growing processing approaches and is rapidly becoming an alternative to subtractive manufacturing or milling. The term 3D printing refers to the digitally controlled AM process of three dimensional items through the continuous deposition of sequential layers of material to achieve intricate structures [Gebhardt, 2012, Jerez-Mesa et al., 2016]. The process has advantages over existing manufacturing techniques due to its ability to control and maintain the composition as well as the configuration of the final product [Kim and Oh, 2008, Pham and Gault, 1998]. This has led to widespread applications in industries which manufacture automotive and aerospace parts [Ahn et al., 2002]. Over the last 30 years a variety of printing methods have been developed that aid the rapid prototyping of the printed parts and products [Fleck et al., 2017]. There are many techniques used to manufacture products using AM such as stereolithography [Hague

et al., 2004, West et al., 2001], direct ink writing [Li et al., 2019a, Lewis, 2006], selective laser sintering11,12, and layered object manufacturing [Gibson and Shi, 1997, Majewski and Hopkinson, 2011]; however, the most commonly used method for polymers is filament based material extrusion AM (MEAM) due to its operational flexibility, facile maintenance, low energy demands, low material wastage, and low cost [Gomez-Gras et al., 2018, Ambrosi and Pumera, 2016]. It is well documented that key enablers to advance MEAM are optimizing the process speed with respect to print quality and broadening the material selection library [Kellens et al., 2017].

There is strong interest in broadening the available polymeric materials which can be used in MEAM. Thermoplastic polymers like polyethylene (PE) and polypropylene (PP) have attracted attention due to their availability and widespread applications in packaging, automotive, and other industries [Mukherjee et al., 2018, Karger-Kocsis, 1994]. PP is a possible material choice in MEAM due to its desirable physical, mechanical, chemical, and optical properties for a broad range of applications [Cimmino et al., 1999, Cimmino et al., 2004, Menyhárd et al., 2009]. However, significant amount of warpage is associated with the additively manufactured PP parts [Spoerk et al., 2017, Spoerk et al., 2019b] which affects geometric accuracy during the print. This observation has been attributed to the built-in residual stresses caused due to rapid crystallization of PP during the MEAM process. This is different to what is observed in traditional melt processing techniques such as extrusion or injection molding, which can accommodate the rapid crystallization behavior through more controlled thermal profiles [Coxon and White, 1980, Kalay and Bevis, 1997]. Another consequence of part warpage is the printed part "lifting off" from the printer bed. Previous studies suggest application of an adhesive layer to the printing platform to solve this issue [Nazan et al., 2017]. However, this solution is less than ideal since the adhesive application has to be repeated after each part is built.

MEAM using semicrystalline thermoplastics like PE and PP has been studied recently but the approach has been more focused on the printing parameters and machine settings rather than the material itself [Carneiro et al., 2015, Wang and Gardner, 2017, Jin et al., 2018]. Recommendations can be found in literature that suggest heating the print bed and applying PE tape to the print bed can overcome the limitations [Chong et al., 2017]. Schirmeister et al. [Schirmeister et al., 2019] optimized the processing parameters for MEAM of high density polyethylene (HDPE) filaments by modifying the print bed to improve adhesion and applying a gradient in the extrusion rate to arrest void formation during printing. The

tensile strength and modulus of the warp-free printed parts approached injection molded (IM) properties, which was attributed to print conditions that allowed enhanced chain diffusion and entanglements across the interface. Most of the work that has been done with PP printing employs commercially available composite PP with different filler materials that potentially impact the inherent properties of the PP printed parts. For example, the mechanical properties of printed parts using a filled PP filament was studied as a function of different MEAM process parameters [Wang and Gardner, 2017], which found that high print temperature, slow print speed, and small layer height resulted in parts approaching IM properties due to enhanced chain diffusion [Wang and Gardner, 2017]. Prior works have also investigated MEAM of both natural fiber and glass fiber filled PP composites [Carneiro et al., 2015, Stoof and Pickering, 2017, Milosevic et al., 2017]. Although the alignment of fibers improves the dimensional stability, the porous nature of the parts decreases their tensile strength [Milosevic et al., 2017]. Carbon fiber and carbon nanotube filled PP can address warpage issues, but at elevated loading levels, nozzle clogging becomes a significant problem [Spoerk et al., 2018b, Stanciu et al., 2019, Fallon et al., 2019]. The interaction between the filler and polymer matrix is of significant importance with respect to MEAM, in order to develop an approach for printing a broad range of PP grades. Such an approach would likely address material or process parameter specific limitations without significantly affecting the mechanical properties.

The effect of incorporating low molecular weight terpene and hydrogenated resins to PP has been studied extensively in literature [Karger-Kocsis, 1994, Lorenzo et al., 2001, Cimmino et al., 1991, Cimmino et al., 2004, Silvestre et al., 1999, Cimmino et al., 1993, Caponetti et al., 1996]. The focus of these studies was to understand the phase behavior, morphology, crystallization kinetics, and their effects on the mechanical and diffusion properties. Specifically, the addition of the resins shifted the onset of crystallization temperature and peak crystallization temperatures to lower values compared to pure PP [Lorenzo et al., 2001, Cimmino et al., 1991, Cimmino et al., 2004]. At higher resin loadings, a two phase morphology was evidenced by SEM [Cimmino et al., 1999] with some of the blends being more brittle than pure PP19. Therefore, these additives can adversely affect the mechanical properties of pure PP by influencing the spherulite size and nucleation site density [Lorenzo et al., 2001, Cimmino et al., 1991].

While prior works have investigated the effect of the resins on the crystallization behavior of the blends, these studies have not identified relevant issues in polymer diffusion at the

interface and morphology evolution that is of significance for MEAM. In this work, we aim to study the impact of the repeated non-uniform thermal history, polymer chain diffusion, and overall bulk crystallization profiles of PP blends processed using MEAM. The crystallinity, morphology, and thermal properties of the blends have been investigated along with the mechanical properties of the parts from the MEAM process.

We have found in our studies that the addition of a low molecular weight hydrocarbon resin can eliminate or significantly reduce warpage in parts made by the MEAM process, which is a significant development. We attribute this observation to the slower crystallization kinetics of the blends, verified by differential scanning calorimetry (DSC) studies, which in turn provides a larger time window for the residual stresses to relax during the MEAM process. The presence of hydrocarbon resin-rich domains that are "softer" at elevated temperatures during MEAM processing of the parts leads to stronger interlayer adhesion.

6.2 Materials and methods

6.2.1 Materials

Isotactic polypropylene 5E16S pellets were obtained from Braskem America, Inc., with a heat deflection point of 104°C, a melting point of 164°C, a melt flow rate of 40 g/10 min, and a glass transition temperature estimated between 0 and −20°C. Two low molecular weight hydrocarbon resin powders having different degrees of hydrogenation were obtained from Arakawa Chemical Industries. The fully hydrogenated resin (termed FH) is ARKON P-100, which has a degree of hydrogenation of 98%, softening point of 100°C, molecular weight (M_N) of 850 g mol^{-1}, and a glass transition temperature of 45°C. The partially hydrogenated resin (termed PH) is ARKON M-100, which has a degree of hydrogenation of 50−60%, a softening point of 100°C, a molecular weight (M_N) of 810 g mol^{-1}, and a glass transition temperature of 45°C. The two hydrocarbon resins were chosen for adequate solubility in pure PP at the compositional ratios analyzed in this study.

6.2.2 Preparation of Blends of PP and Hydrocarbon Resins

The composition (by weight percent) ratios of PP/hydrocarbon resin blends evaluated in this study are 100/0, 95/5, 90/10, 85/15, and 80/ 20 as summarized in Table C.1. Controlled ratios of PP and hydrocarbon resins were added into a Brabender mixer which was heated to 190°C for the PH blends and to 170°C for the FH blends. The mixing temperature was selected such that it was above the melting point of PP but below the degradation temperature of the respective hydrocarbon resins. The mixing was done in batches of 45g, which is the maximum capacity of the mixer. Mixer blades were rotated at 32 rpm and mixing was continued for 10 min. Following the mixing period, the blends were scraped off from the mixing blades and collected. During mixing, temperature was monitored carefully to evaluate viscous heating and potential degradation of the hydrocarbon resins. The final temperature achieved after 10 min of mixing was 198°C and 176°C for the PH and FH blends, respectively.

6.2.3 Thermogravimetric Analysis (TGA)

Thermogravimetric analysis was performed in air in a TGA5500 (TA Instruments, USA). The hydrocarbon resins, pure PP, and their blends were heated from room temperature to 600°C at a heating rate of 10°C/min. The thermal stability of the hydrocarbon resins over the temperature range provided a basis for choosing the processing temperature and the overall thermal stability of the prepared blends. The TGA results for the pure resins and prepared blends are presented in Figure C.1 and C.2 respectively.

6.2.4 Differential Scanning Calorimetry (DSC)

10-15 mg of each blend composition was loaded and pressed into a TA Instruments aluminum T_zero pan and tested using a Q2000 Series TA Instruments DSC. Samples were evaluated under non-isothermal heat-cool-heat cycles. Using a 50 mL min^{-1} nitrogen flow rate, the samples were first heated at 10°C min^{-1} to 190°C to ensure complete melting and to erase any previous thermal history, then cooled to -50°C at 5°C min^{-1}, past the glass transition temperature of PP, and finally heated at 10°C min^{-1} again to 190°C. Crystallinity was determined by normalization to the amount of PP present in the blends using the following

equation:

$$\%Crystallinity = \frac{H_M}{H_M^0 * (1 - w_r)} * 100\% \tag{6.1}$$

where, H_M is the enthalpy of melting of the blends; H_M^0 is the reference enthalpy of melting of 100% crystalline PP which was taken to be 207.1 J/g [Bagheriasl et al., 2015], and w_r is the weight fraction of hydrocarbon resin in the respective blends.

The isothermal crystallization profiles were obtained at a given cooling rate for varying crystallization temperatures (120°C, 122°C, 125°C, 127°C, and 130°C). The isothermal experiments were carried out by heating the samples to 190°C at 10°C min^{-1}; holding it at temperature for two minutes to completely melt the sample, ramping down to the designated crystallization temperature, and holding at constant temperature for a specified time interval. The effect of cooling rate (10°C/min and 50°C/min) on the isothermal crystallization profile of the prepared blends was also investigated. The results from the isothermal DSC experiments are discussed in the Supplementary Information section (Figures C.7 and C.8).

6.2.5 Hot Stage Polarized Light Microscopy (HS-PLM)

The morphology of the blends and spherulite formation during cooling was investigated using an Olympus BX51-P polarized light microscope. A Linkam THMS 600 hot stage equipped with a TMS 92 temperature controller was used for heating the microscope stage. The pressed film of each sample was placed on a microscope slide and then positioned inside the hot stage oven. The samples were first heated to 190°C at 20°C min^{-1} and held isothermal for 2 min to ensure complete melting, followed by cooling at 10°C min^{-1} to the desired crystallization temperature. Optical micrographs of the spherulitic morphologies were captured for diameter measurement using ImageJ software.

6.2.6 Rheology of PP/Hydrocarbon Resin Blends

Pure PP and the 80/20 blends with FH and PH resins were compression molded into 25 mm discs at 200°C under 5 ton m^{-2} using a Carver press (Carver Inc., USA). Steady shear measurements (0.01−10 s^{-1}) were performed on a TA AR-G2 rheometer (TA Instruments, USA) with parallel plate geometry (25 mm) at 180°C (MEAM printing temperature of the

blends).

6.2.7 Scanning Electron Microscopy (SEM) of Blends

The as-prepared PP blends with PH and FH resins were cryo-fractured and imaged using a desktop Phenom Pro SEM operated at an accelerating voltage of 5 kV in medium vacuum mode. The cross section of the blend sample was imaged by placing it onto a double-sided copper tape attached to an SEM pedestal.

6.2.8 Filament Generation and MEAM

The blended material obtained from the Brabender was cut down to smaller pieces and fed through a single screw extruder (Filabot EX2 filament extruder: hopper volume of approximately 426.1 cm^3 and screw void volume of 28.8 cm^3. Screw design: outer diameter of 5/8"; L/D of 12; pitch 0.5"; and compression of rate 2.5:1) at 180°C to generate a filament that was re-pelletized to obtain uniform pellets. The pellets were then extruded again through the Filabot EX2 extruder to generate a homogenous and consistent filament. The extrusion speed (18 rpm) as well as the spooling speed was monitored in order to achieve appropriate filament diameter (1.75 ± 0.1mm) for successful MEAM printing. Tensile bars were printed using the extruded filament with a Flashforge (Creator Pro) 3D printer equipped with a Flexion extruder head at an extruder temperature of 180°C and a bed temperature of 120°C. The print speed was maintained at 1000 mm/min with 100% infill and 45° raster angle. For comparison purposes, tensile bars were also printed with a 0° raster angle to investigate the effect of print orientation on the mechanical properties of the printed parts. Tensile bars were printed with 90° raster angle for an assessment of the interlayer strength in the printed parts.

6.2.9 Tensile Testing of Printed Parts

Printed tensile bars were measured using an Instron 5944 with a 2kN load cell at a rate of 3 mm/min until breakage. All tests were performed at room temperature (∼22°C). Reported mechanical properties are an average of five tests. It was assumed that the deformation of the samples took place in the gauge length between the two grips of the Instron and

therefore the distance between the crosshead was used to calculate the strain. The printed tensile bars were annealed in a convection oven (Fisher Scientific Isotemp Oven) for 24 hours at 120°C to evaluate the effect of post-treatment on the mechanical properties of the parts. The annealed parts were cooled to room temperature inside the oven after the annealing period was completed.

6.3 Results and Discussion

The crystallization process of the PP blends with the hydrocarbon resins plays a major role in understanding the weld formation between the deposited layers and hence dictates the mechanical performance of the MEAM printed parts [Yang et al., 2017, Northcutt et al., 2018]. Therefore, it is of significant importance to study the effect of hydrocarbon resins on the crystallization temperature and total crystalline content of the blends. Any changes in these parameters will directly translate to changes in timescales for interlayer diffusion and adhesion prior to crystallization. Moreover, the impact of incorporating resins to pure PP on the morphology of the blends must be analyzed since it can affect the mechanical properties of the final MEAM printed part.

6.3.1 Melting, crystallization and crystallinity of the blends

Differential scanning calorimetry (DSC) was performed to determine the crystallization behaviors of the PP blends in conditions relevant to the MEAM process. The melting (from the second heating cycle in the non-isothermal DSC) and cooling profiles for the PP/PH blends are illustrated in Figure 6.1 (The melting and cooling profiles for the PP/FH blends are highlighted in Fig. C.3). As observed in the heating scans, both pure PP and the blends show a relatively homogenous melting peak suggesting no separate crystalline phases in the blends, likely resulting from the good solubility of the resins in the PP matrix. The peak in the melting endotherm shifts to lower temperatures with increasing resin content in the blends. For both the PP/FH and PP/PH blends, increasing resin content in the blends increases the driving force behind crystallization as compared to pure PP and expands the crystallization window for the blends. These results suggest that the resins delay the onset of crystallization, which is further corroborated by the peak melting temperature, peak crystallization temperature, and the enthalpy of melting and crystallization of pure PP, PP/FH,

and PP/PH blends listed in Table C.3. Further, non-isothermal DSC experiments on the pure resins indicate no discernable exotherm peak is observed in the cooling scans (Fig. C.4).

The degree of hydrogenation can affect the crystallization behavior of the blends due to variable extents of interactions with the pure polymer matrix by reducing the intermolecular interactions in pure PP and reducing the crystallizability [Kang et al., 2013]. Moreover, the resins tend to form thinner lamellae and crystals with reduced size compared to pure PP, while significantly reducing the overall crystallization rate in the blends [Kang et al., 2013]. As illustrated in Figure C.5, complete melting of PP/PH blend occurs at a temperature higher than that for PP/FH blend, suggesting that FH resin interferes with the PP matrix chain mobility to a greater extent than the PH resin [Kang et al., 2013, Silvestre et al., 2007]. Isothermal crystallization results further substantiate this hypothesis and are discussed in the Section C.8.

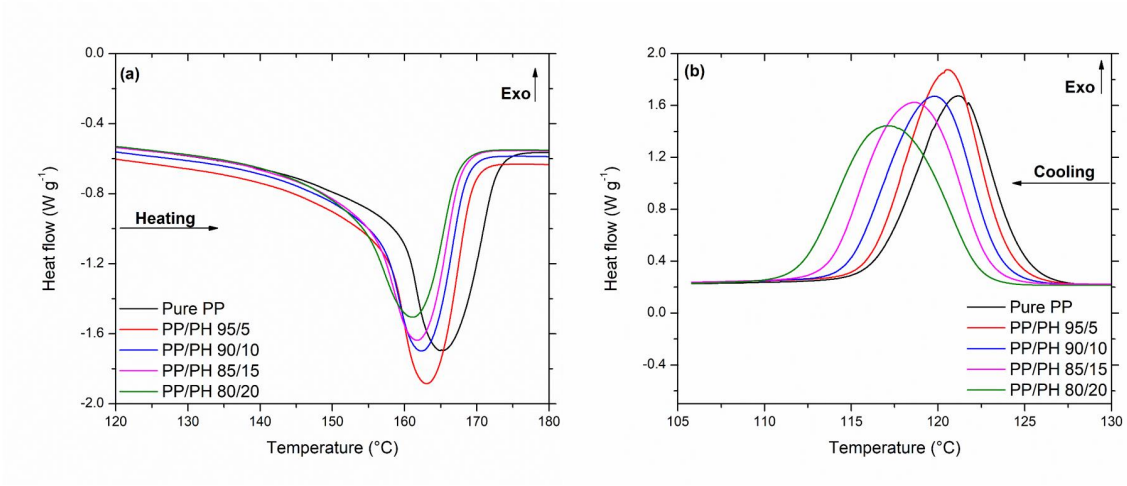


Figure 6.1: (a) DSC melting endotherms from the second heat of non-isothermal experiments for the different compositions of PP/PH blends (b) DSC cooling exotherms from the non-isothermal experiments for the different compositions of PP/PH blends. Data for PP/FH blends are provided in Figure C.3

The 2^{nd} heating scan of the heat-cool-heat DSC experiments is used to obtain degree of crystallinity data for the PP/hydrocarbon resin blends, which plays a vital role in dictating the

thermomechanical performance of the blends. Since this work aims to retain the properties of pure PP as closely as possible in a 3D printed geometry, it is important to limit the effects on crystallinity of the PP/FH and PP/PH blends. The percent crystallinity of the blends with respect to the amount of PP content were calculated using the enthalpies of melting of the blends according to Equation 6.1, and are plotted in Figure C.6. Total crystalline content does not significantly reduce until a compositional ratio with 20 wt% resin is realized. A maximum decrease of 4.3% and 2.5% in the average measured crystallinity of the 80/20 PP/FH and 80/20 PP/PH blend respectively is observed. Similar reduction in the degree of crystallinity has been reported for blends of hydrogenated petroleum resins with PP [Kang et al., 2013].

6.3.2 Hot stage polarized light microscopy of PP/hydrocarbon resin blends

Isothermal crystallization experiments were performed on a hot stage polarized light microscope with the PP/hydrocarbon resin blends to investigate the effect of resin addition on the morphology developed under different crystallization conditions at temperatures (printer bed temperature) that we anticipate crystallization to occur during the printing process. While the printing process is highly non-isothermal, and the repeated thermal history presents additional challenges in developing a protocol for morphology analysis, the goal here is to identify the sole impact of the resins on the resulting morphology to explain differences in printed part morphology between the compositions analyzed. Compositional extremes are analyzed to determine the range of expected effects.

Experiments were carried out on the pure PP and on the 80/20 ratio PH and FH blends at a crystallization temperature of 120°C. Figure 6.2 illustrates the optical micrographs of pure PP and 80/20 blends with the hydrogenated resins. The addition of hydrocarbon resins affects the morphology by interfering with the crystallization process and reduces the size of spherulites. This observation is attributed to the presence of increased nucleation sites in FH and PH blends compared to pure PP, potentially a direct result of the increase in viscosity in the melt state of the blends, which can be a consequence of the confinement effect of the hydrocarbon resins on the motion of the polymer chains. The formation of larger spherulites can result in the deposition of additional material at the boundaries of the spherulites. These spherulites do not undergo crystallization as readily due to reduced chain

mobility, which can significantly impact the mechanical properties by forming weak grain boundaries [Schultz, 1984].

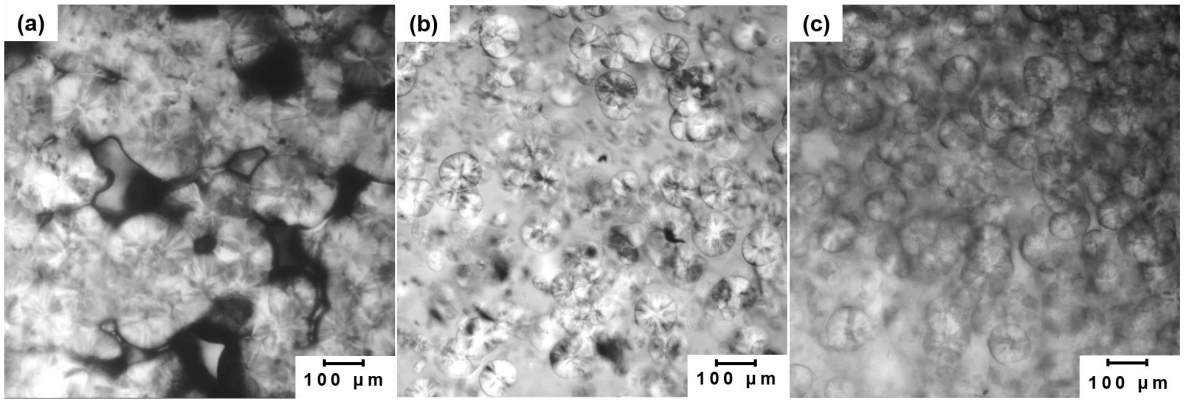


Figure 6.2: Hot stage polarized optical micrographs taken at comparable times for (a) pure PP, (b) 80/20 blends of PP/PH, and (c) 80/20 blends of PP/FH resins obtained after cooling from the melt and held isothermal at 120°C

Figure C.9 shows the effect of added resin type and crystallization temperature on the size of the spherulites formed during crystallization from the melt. The size distribution of the spherulites can be affected by the presence of nucleating agents and the crystallization conditions. Moreover, the type of resin used for the blends also plays an important role in influencing the spherulite density and size. As observed in Figure 6.2, a variation in the spherulite sizes results from nucleation events initiated at different times at the crystallization temperature. As expected based on kinetic theory of crystallization [Erukhimovitch and Baram, 1994], increasing the crystallization temperature (130°C) results in a greater average spherulite diameter than the lower crystallization temperature (120°C).

6.3.3 Rheology of the prepared PP/FH and PP/PH blends

Steady shear rheology was performed on compression molded samples of pure PP and 80/20 blends with hydrocarbon resins. The raw data from the rheometer was corrected using the single point correction method proposed by Carvalho et al. for parallel plate rheometer [Carvalho et al., 1994]. Both PP and the blends exhibit a classical shear-thinning behavior as illustrated in Figure 6.3 with the onset of shear thinning at a shear rate of approximately $0.7s^{-1}$. Therefore, the longest relaxation time for the materials is estimated to be approximately 1.4s (inverse of the shear rate at which the onset off shear thinning occurs) [Xu et al., 2004]. In order to tie this timescale with the printing process, we tune the printing speed during MEAM such that the Deborah number, or the ratio of the relaxation timescale to the process timescale, is approximately 1. This should ensure that the blended materials are relaxed sufficiently during the printing process such that orientation induced effects do not play a significant role in the crystallization behavior.

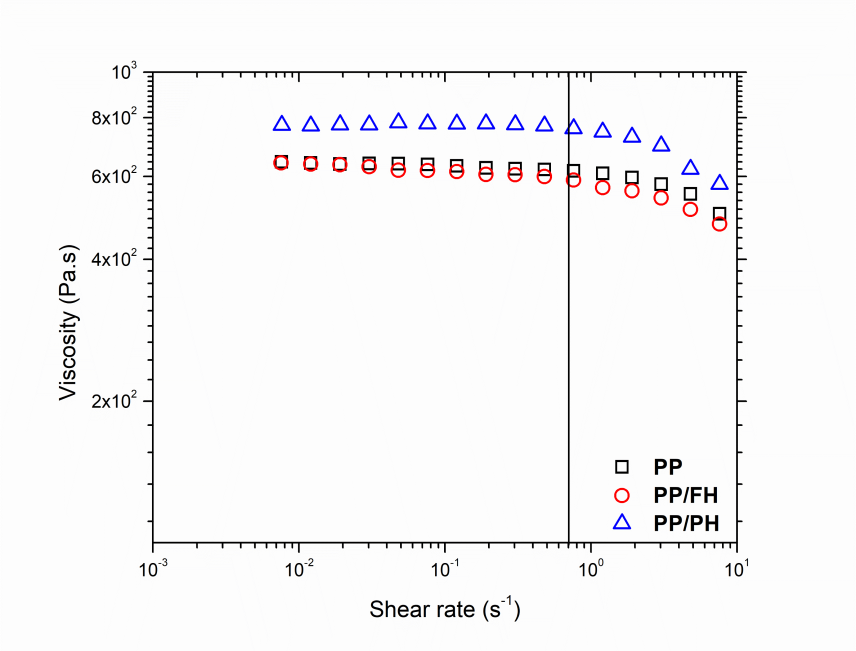


Figure 6.3: Shear thinning behavior of PP and 80/20 blends with FH and PH resins at 180°C performed under steady shear in a TA ARG2 rheometer. The vertical line indicates the onset of shearing thinning behavior, which is observed at a shear rate of $0.7s^{-1}$ for all the systems.

6.3.4 Printed part bed adhesion and warpage

Initial printing experiments were carried out with PP to establish a baseline for comparison to the performance with the PP/resin blends. With pure PP, parts with significant warpage and poor dimensional accuracy are obtained. By comparison, printing experiments with the PP/PH blends have shown significant improvements in reduced warpage and dimensional stability, as observed in Figure 6.4 for the 90/10 and 80/20 PH blends. With the PP/FH blend, improvement in printing is achieved but part warpage is not completely eliminated, although it reduces significantly in comparison to the pure PP print. Warpage was measured as the amount the printed part lifted off from the printed bed at the end of the printing process. The measurement was performed using a Vernier Caliper Gauge Micrometer and the values reported are an average of five measurements.

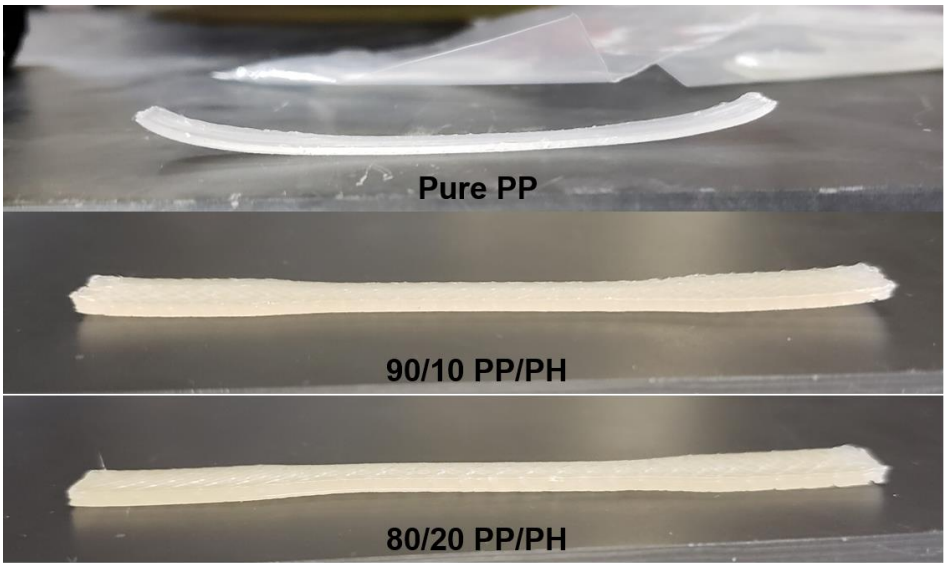


Figure 6.4: Printed parts of pure PP, 90/10 PP/PH, and 80/20 PP/PH blends. The pure PP parts shows significant warpage which reduces progressively as resin content is increased in the blends.

When printing with the PP/PH blend, significant improvement in adhesion to the printing platform and minimal warpage of the part is achieved as highlighted in Figure 6.5. The parts with 80/20 resin content have minimal warpage (∼0.25mm) with the part geometry and

printing conditions implemented for this study. The resins appear to stabilize PP during the printing process by increasing the time during which the blend remained in the melt state and promoting mobility of the polymer chains, which ensures better interlayer adhesion. Moreover, more time spent in the melt state allows for the residual stresses to relax and results in dimensionally accurate prints. These results are consistent with the crystallization behavior (Figure C.7 and C.8), with the 80/20 blend ratio providing the longest time delay for the onset of crystallization from the melt among the blend ratios evaluated in this study. In order to test the mechanical properties of the PP/hydrocarbon resin blends, multiple dogbones (five) were printed using the ASTM D638 standard.

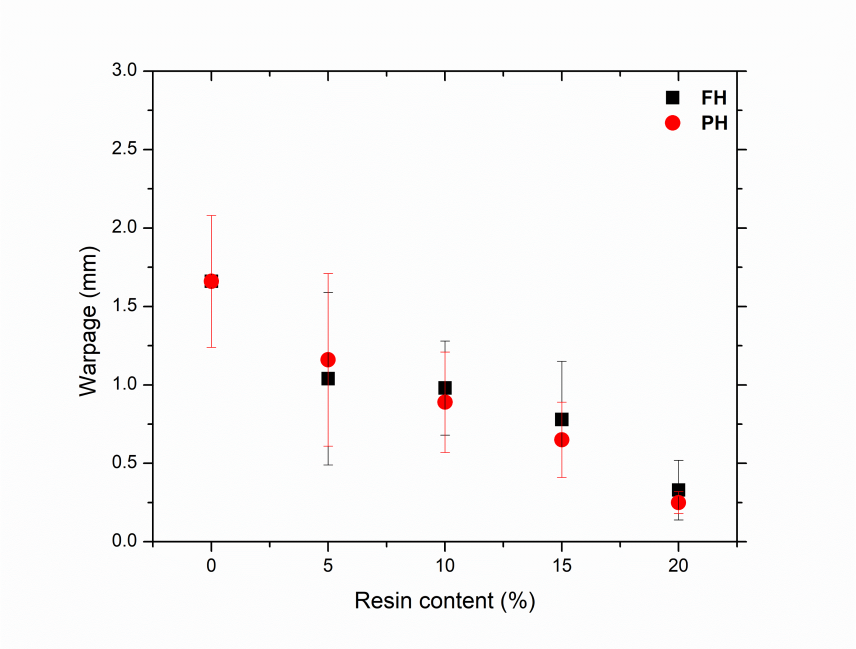


Figure 6.5: Warpage in printed parts of PP/FH and PP/PH blends as a function of increasing resin concentration.

6.3.5 Mechanical properties of printed parts

The mechanical properties of PP/PH printed parts (45° raster angle) compared to injection molded (IM) PP and MEAM printed PP are illustrated in Figure 6.6. The corresponding plots for PP/FH printed parts are highlighted in Figure C.10. The tensile modulus, elongation at break, and tensile strength values reported in the figures are based on an average of

five tests. All samples underwent brittle fracture which is consistent with previous literature [Carpinteri et al., 1986]. The printed parts of pure PP and both blends have tensile strengths less than that of IM PP (32 MPa). In the case of the PP/PH blends, as the PH content increases, the tensile modulus values remain almost unchanged as the PH content increases, and a marginal increase in the tensile strength is observed. Table 6.1 summarizes the tensile properties of pure PP and its blends with hydrocarbon resins when printed at 45° raster angle.

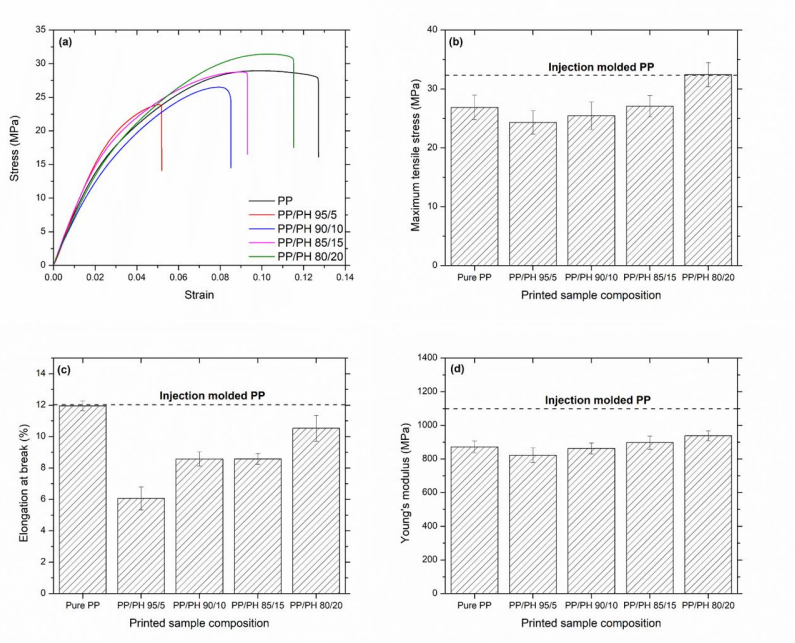


Figure 6.6: (a) Stress-strain curves for the PP/PH printed parts (45° raster angle) in compositional ratios up to 20 wt% resin; (b) effect of increasing PH resin content on the maximum tensile stress; (c) effect of increasing PH resin content on the elongation at break; and (d) effect of increasing PH resin content on the Young's modulus of the printed parts of PP/PH blends.

The tensile modulus of the 80/20 PP/PH blend approaches 86% of the IM value for pure PP. The tensile strength (32.4 ± 2.1) MPa of the same blend is comparable to IM PP an is a 20.7% improvement compared to printed pure PP parts. The tensile strength and modulus of the 80/20 PP/PH blend reported in this study are comparable to those of compression molded sisal-fiber-reinforced PP composites [Joseph et al., 2002] and PP/carbon nanotube composites [Manchado et al., 2005].

The elongation at break initially decreases with the addition of PH resins but then increases to 10.5%, which is 88% of the IM value for PP. Assuming a defect free material, the elongation at break of a material is dictated by the size and number density of the crystalline forms present, which are controlled by the conditions under which the crystallization occurred. For identical degree of crystallinity, the larger spherulites are more brittle than smaller ones [El-Hadi et al., 2002]. The size of the spherulites for the PP/PH blends are smaller than the PP/FH blends, as shown in Figure C.9, which suggests that the PP/PH blends should exhibit higher elongation.

Table 6.1: Tensile properties of printed parts (±45° raster angle) of pure PP and blends with hydrocarbon resins.

Sample	**Tensile strength (MPa)**	**Elongation at break (%)**	**Young's modulus (MPa)**
Pure PP	26.9 ± 2.0	11.9 ± 0.3	872 ± 36.0
PP/FH 95/5	24.9 ± 1.1	9.5 ± 0.7	799 ± 99.0
PP/FH 90/10	21.2 ± 3.2	6.8 ± 0.9	762 ± 52.0
PP/FH 85/15	19.9 ± 1.4	4.9 ± 0.3	801 ± 35.0
PP/FH 80/20	15.3 ± 3.4	4.3 ± 0.5	611 ± 19.6
PP/PH 95/5	24.3 ± 1.9	6.1 ± 0.7	822 ± 43.7
PP/PH 90/10	25.4 ± 2.4	8.6 ± 0.5	863 ± 32.8
PP/PH 85/15	27.1 ± 1.8	8.6 ± 0.3	897 ± 39.0
PP/PH 80/20	32.4 ± 2.1	10.5 ± 0.8	938 ± 29.9

Both the tensile strength and elongation at break reported in this study for PP/PH blends are higher than that of PP/PE blends processed at 190°C and 200°C [Strapasson et al., 2005]. Moreover, the PP/PH blends with higher degree of crystallinity exhibit higher tensile modulus than the PP/FH blends due to increased load bearing capability [Tanniru et al., 2006]. It should be mentioned that crystallinity and morphology are not the only factors that can control the mechanical properties; interactions across the interface and intercrystalline boundaries also play a vital role [Lovinger and Williams, 1980]. The enhanced mechanical properties for the PP/PH blends compared to PP/FH blends is indicative of a reinforcement effect arising from improved interlayer chain entanglements and diffusion prior to crystallization.

6.3.6 Effect of annealing on mechanical properties of printed PP/hydrocarbon resin parts

Figure 6.7 highlights the effect of annealing on the mechanical properties of the printed PP/PH resin blends with respect to IM PP properties. The corresponding plots for PP/FH resin are illustrated in Figure C.11. The tensile strength of the PP/PH printed parts increases after annealing as evidenced in Figure 6.7(a). The tensile strength of the 80/20 blend (34.7 ± 1.3) MPa surpassed that of IM PP (32 MPa). The improved strength may be due to a combination of increased crystallinity after annealing and better miscibility of the PH resin in the PP matrix. The maximum elongation at break for the PP/PH blends decreases after annealing, but to a lower extent than the PP/FH blends.

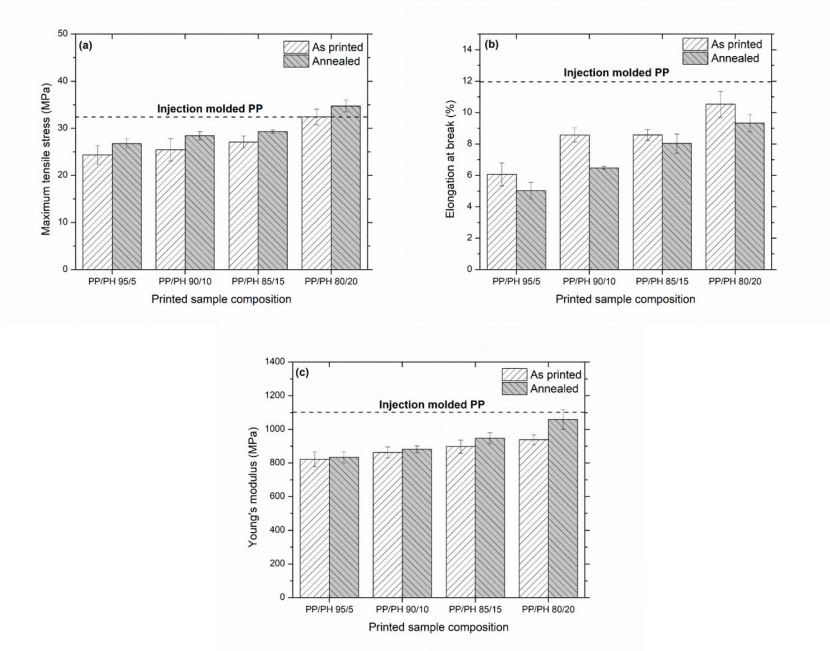


Figure 6.7: Comparison of the (a) maximum tensile stress; (b) elongation at break; and (c) Young's modulus of the as printed and annealed PP/PH parts (45° raster angle) with respect to inection molded PP.

The elongation at break increases by 94% in the 80/20 PP/PH blend to (9.3 ± 0.5)% compared to the corresponding PP/FH blend (4.8 ± 0.3)% after annealing. However, the elongation at break for the 80/20 PP/PH blend decreases by 11.4% after annealing and is 78% of the IM PP value. The most promising result is the Young's modulus of the 80/20 PP/PH

blend (1059 ± 58) MPa which approaches 96% of IM PP properties. The improvement in modulus is again attributed to increased crystallinity and adhesion across the layer interface. Table 6.2 compares the mechanical properties of the annealed and as-printed PP/hydrocarbon blends obtained in this study with several reported values in the literature for PP based composites processed using MEAM. It is worth mentioning that Schirmeister et al.'s group [Schirmeister et al., 2019] printed HDPE using MEAM and achieved tensile strength and modulus similar to what has been reported in this study. Although their approach revolves around print bed optimization for promoting adhesion and material flow gradient out of the nozzle, the method proposed in this study is simpler to implement and can be extended to print polyolefin based materials using most commercially available printers with minimal modifications.

Similiar to the PP/PH printed parts, the maximum tensile stress of the PP/FH printed parts also improved after annealing as evidenced in Figure C.11. The 95/5 blend composition has a tensile strength of (27.7 ± 1.4) MPa which is close 87% of the tensile strength of IM PP parts (32 MPa). Impurities are generally uniformly distributed in the matrix but can migrate towards the grain boundaries when annealed [Heuer et al., 2000]. The crystallinity of the material increases after annealing because at the molecular level, annealing results in a decrease in the number of tie chains by lamellar thickening of the existing spherulites and formation of new spherulites in the amorphous regions [Wright et al., 1988, Dlugosz et al., 1976]. The tensile strength of the 80/20 PP/FH blend improves by 55% after annealing but is still lower than the IM PP value. For the elongation at break of the PP/FH blends, an abrupt 38% drop in the values is observed after annealing for the 95/5 blend. The values decrease slightly with increasing resin content due to increased heterogeneity in the blends. The lower elongation at break after annealing as compared to as-printed parts can be attributed to the increased crystallinity after annealing, which results in a material with lower toughness. Our elongation at break values are comparable to highly filled PP composites with talc and rice husks prepared using traditional melt-mixing techniques [Premalal et al., 2002]. It has been previously reported that the tensile modulus of PP increases with increasing filler content while the elongation at break decreases [Raj et al., 1990], a trend that is in agreement with our results.

Table 6.2: Comparison of mechanical properties of PP/hydrocarbon resin blends obtained in this study with values reported in literature for PP based composites processed using MEAM.

Sample	**Maximum tensile strength (MPa)**	**Reference**
PP	27.5 ± 4.3	[Carneiro et al., 2015]
PP	16.5	[Milosevic et al., 2017]
PP + 20 wt% Harakeke fibers	24.0	[Milosevic et al., 2017]
Recycled PP	20.1 ± 2	[Zander et al., 2019a]
Recycled PP/PS	23.0 ±	[Zander et al., 2019a]
PP	16.4 ± 0.7	[Wang et al., 2018c]
PP + 30 wt% nylon	25 ± 0.5	[Peng et al., 2019b]
PP	29 ± 1	[Zander et al., 2019b]
PP + 0.3 wt% carbon nanotube	29.4 ± 0.60	[Stanciu et al., 2019]
PP	20.9 ± 0.8	[Spoerk et al., 2018b]
PP/PH 80/20 as printed	32.4 ± 1.7	This work
PP/PH 80/20 annealed	34.7 ± 1.3	This work
Sample	**Maximum elongation at break (%)**	**Reference**
PP	14.5 ± 0.3	[Zander et al., 2019b]
PP + 20 wt% carbon fiber	2.9 ± 0.2	[Stanciu et al., 2019]
Recycled PP	0.2 ± 0.02	[Zander et al., 2019a]
Recycled PP/PS	0.1 ± 0.05	[Zander et al., 2019a]
PP + 0.3 wt% carbon nanotube	4.71 ± 0.14	[Stanciu et al., 2019]
PP/PH 80/20 as printed	10.5 ± 0.8	This work
PP/PH 80/20 annealed	9.3 ± 0.5	This work
Sample	**Tensile modulus (MPa)**	**Reference**
PP	1073 ± 203	[Jin et al., 2018]
PP	750 ± 63	[Zander et al., 2019b]
PP	830 ± 10	[Spoerk et al., 2018b]
PP	230	[Milosevic et al., 2017]
PP + 20 wt% Harakeke fibers	325	[Milosevic et al., 2017]
PP	1200 ± 100	[Carneiro et al., 2015]
PP/PH 80/20 as printed	938 ± 29.8	This work
PP/PH 80/20 annealed	1059 ± 57	This work

The Young's modulus for the 85/15 and 80/20 blends of PP/FH increase by 31.5% and 56.4% respectively after annealing. The tensile modulus also provides a measure of the interlayer adhesion, with an improvement in modulus after annealing suggesting better interlayer and interroad bonding as well as reduction in internal stress build-up in the annealed parts; a similar observation was made by Fitzharris et al. when printing with polyphenylene [Fitzharris et al., 2018].

6.3.7 Effect of Print Orientation on Mechanical Properties of PP/Hydrocarbon Resin Blends

Figure 6.8 highlights the effect of print orientation on the tensile modulus of the printed parts by using the PP/hydrocarbon resin blends. The two different print orientations (±45° and 0° raster angles) that were investigated in this study are illustrated in Figure 6.8(a). It is worth mentioning that parts printed in both orientations were tested as printed without annealing. As shown in Figure 6.8(b), the 0° raster angle prints of the 90/10 and 80/20 PP/FH blends respectively show a 30.5% and 45.7% improvement in the tensile modulus as compared to the ±45° raster angle prints while there is a minimal effect of print orientation on the modulus of the 95/5 and 85/15 PP/FH blends. The significant enhancement in the modulus is attributed to the improved interlayer strength arising from continuous polymer road deposition in the direction of tensile testing leading to more chain entanglements across the interfacial layers of the print. The strength of interlayer adhesion is evaluated by printing parts at 90° raster angle, and the results are displayed in Figure C.12.

The tensile modulus of the 80/20 PP/FH blend shows the highest improvement in modulus, but is still only ∼76.5% of the IM PP value. Figure 6.8(c) shows the effect of the print orientation on the tensile modulus of the PP/PH blend printed parts. These results suggest that the PP/PH parts are isotropic and print orientation does not have a significant effect on their tensile moduli. A very slight improvement in the modulus values for the vertically printed parts is observed for all blend ratios. The 80/20 PP/PH blend shows only shows a ∼5% improvement in the modulus values when printed with 0° raster angle, compared to a ∼50% improvement for the 80/20 PP/FH blend.

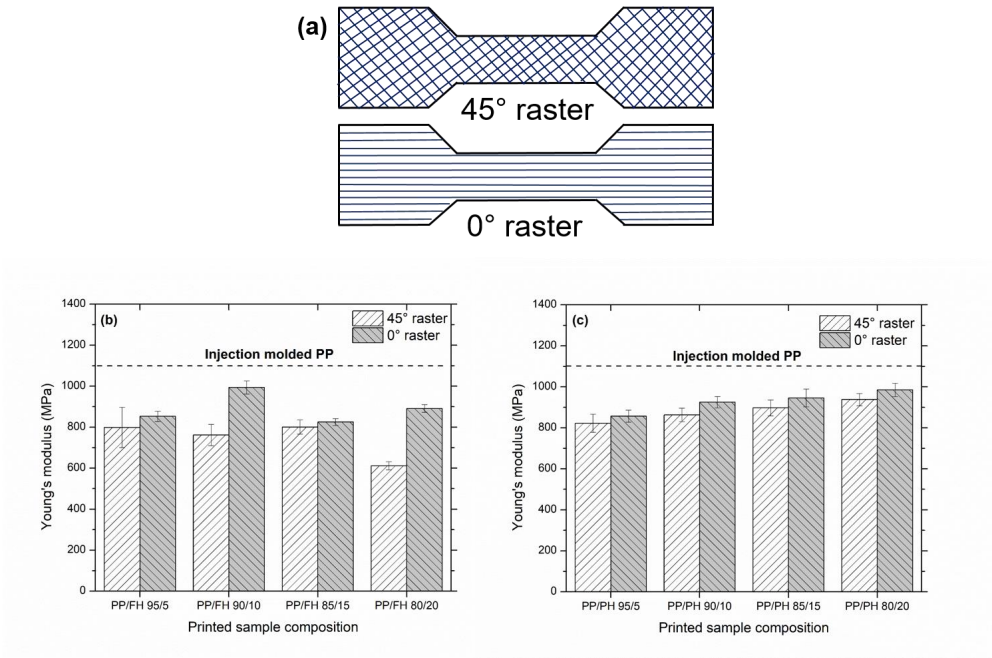


Figure 6.8: (a) ±45° and 0° raster angle print orientation used for printing dogbones in this study; (b) effect of print orientation on the tensile modulus of PP/FH blends; and (c) effect of print orientation on the tensile modulus of PP/PH blends.

Another promising result is that the 0° raster angle printed PP/PH blends are approaching 90% of the IM PP values without annealing. A possible explanation can be that the addition of the PH resins results in better layer adhesion which in turn reduces the number of stress concentration points in the printed parts [Maiti and Sharma, 1992]. Depending upon the print orientation, the mechanical properties of the PP/hydrocarbon resin blends are close to (and in some cases superior than) that of parts printed using bimodal polylactic acid blends, a very popular and widely used material for MEAM [Levenhagen and Dadmun, 2018]. However, further research must be conducted in order to determine why some of the blend compositions did not show a marked improvement in modulus for the different print orientations.

6.3.8 SEM Imaging of the PP/Hydrocarbon Resin Blends

Scanning electron microscopy was performed on the cross sections of cryo-fractured pure PP and its blends with FH and PH resins to investigate the effect on morphology of the fracture

surface. The SEM micrographs are presented in Figure 6.9. For pure PP, the morphology appears to be smooth with rivulets, which is suggestive of brittle failure [Olowojoba et al., 2016]. The cross sections of the 80/20 blends of PP/FH and PP/PH are characterized by the presence of fibrillar structure, suggestive of brittle fracture surfaces. The fibrils are also indicative of the energy dissipation mechanism in the blends [Ferrer-Balas et al., 2002, Ramsteiner et al., 1983] and are responsible for improved interfacial adhesion between the polymer and the resins. The morphology of the PP/FH blend appears to be more uniform as compared to the PP/PH blend.

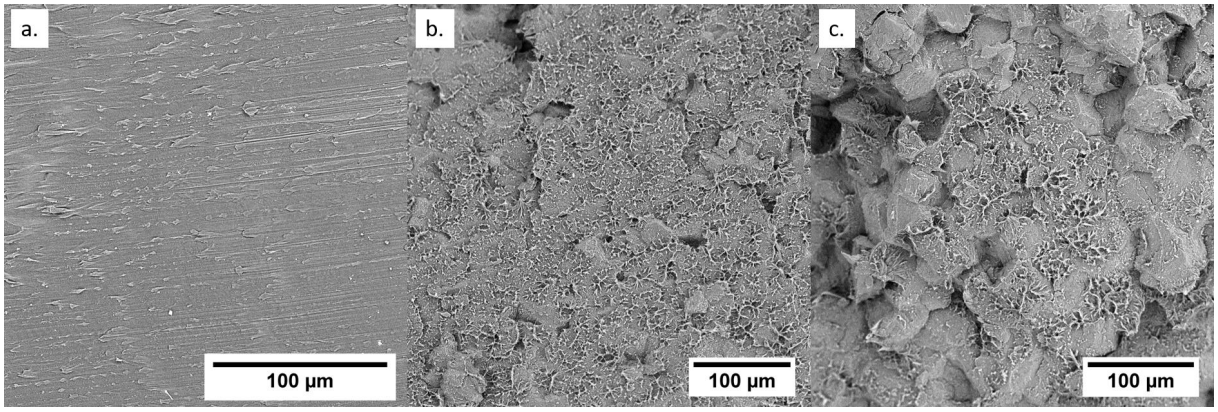


Figure 6.9: SEM micrographs of the cross-section after cryo-fracturing of (a) pure PP, (b) 80/20 blend of PP/FH, and (c) 80/20 blend of PP/PH.

The nodular morphological features in the blends are mostly signatures of the spherulites. We hypothesize that our observations are consistent with that reported in previous literature for blends of PP and poly(D-limonene) [Silvestre et al., 1999]. Prior work with PP and natural terpene resin blended at an 80/20 ratio [Cimmino et al., 1999] showed a two-phase morphology with PP/resin-rich domains dispersed in a continuous phase of PP domains with low resin content. This kind of morphology can also lead to improved adhesion during MEAM printing process due to the resin-rich dispersed domains being more “tacky” (i.e.,

lower modulus) for a slightly longer period of time when cooling from the melt. The tacky nature of the resin may be responsible for the fine threadlike morphology observed in the blends. When tensile tested, the crystalline domain of PP suffers brittle fracture while the blends containing the hydrocarbon resins are initially drawn before their fracture. The phase-segregated morphology (crystalline dominant PP phase and a resin-rich amorphous phase) plays a vital role in dictating the mechanical properties of the printed blends.

6.4 Conclusions

We have demonstrated that significant improvements can be achieved in printing PP using the MEAM approach by blending in low molecular weight hydrocarbon resins at compositions containing up to 20 wt% resin. Among the hydrocarbon resins in this study, the partially hydrogenated resin provides better mechanical performance than the fully hydrogenated resin. The addition of the hydrocarbon resins delays the onset of crystallization from the melt during printing and eliminates, or significantly reduces, the problems associated with adhesion of the part to the printing platform and part warpage. In addition, a two-phase morphology consisting of a PP-rich continuous phase and a resin-rich dispersed phase can be present at 20 wt% loadings. The dispersed phase domains tend to be softer with lower modulus which allows for better adhesion of the layers. The slower crystallization and the two-phase morphology allows for improved printing performance of the PP/hydrocarbon resin blends. Although the as-printed parts have tensile properties lower than IM parts, annealing the as-printed parts recovers over 90% of the IM tensile properties (maximum tensile strength and modulus). Our results suggest that MEAM can be a viable option for the manufacture of highly crystalline, fast crystallizing thermoplastic polymers like PP in an economical manner.

Chapter 7

3D printing of semicrystalline polymer blends: Effect of melt flow rate

Arit Das[1,2], E.M. Dartevelle[1], Eugene G. Joseph[1], and Michael J. Bortner[1,2]

[1]Department of Chemical Engineering, Virginia Polytechnic and State University, Blacksburg, VA 24061, USA

[2]Macromolecules Innovation Institute, Virginia Polytechnic and State University, Blacksburg, VA 24061, USA

This chapter is currently under preparation for submission to the **Chemical Enginnering Journal**.

Abstract

Material extrusion (MatEx) based additive manufacturing (AM) process can produce parts with intricate features that are difficult to fabricate using traditional subtractive manufacturing techniques. However, the MatEx process suffers from to major drawbacks: the mechanical properties of the parts produced using MatEx are often inferior to the bulk material properties and only a limited number of are currently compatible with this mode of AM. Isotactic polypropylene (PP) is a popular thermoplastic material which undergoes rapid crystallization that leads to significant trapped residual stress when processed using MatEx, resulting in poor geometric tolerance and mechanical performance.

In this work, PP having different melt flow rates (MFRs) were blended with low molecular weight hydrocarbon resins having different degree of hydrogenations. The influence of the PP MFI on the crystallinity of the pure polymers and PP/hydrogenated resin blends as well as the melting and crystallization temperature was investigated. For example, the addition of the resins lowered the melting temperature by 7°C while the crystallization temperature of pure PP (MFR=12g/10 min) decreased from 133.3°C to 118.6°C in the

blends; thereby increasing the time required for the material to crystallize from the melt. Next, the blends were extruded using a single screw extruder to obtain filaments that can be used in the MatEx process. An understanding of the modifications in the crystallization process significantly impact the z-axis adhesion and residual stress state, which directly affect mechanical properties and warpage in the printed parts. Tensile bars were printed in two different orientations to analyze the mechanical performance and study the effect on part isotropy. The maximum tensile strength and modulus of the printed parts was found to decrease by 21% and 15% respectively. However, post-printing the printed parts were heat-treated to achieve mechanical properties that approached injection molded PP parts by improving the interlayer bonding of the parts. We can leverage these results to modify processing conditions to optimize mechanical properties of the parts generated using MatEx.

Keywords: 3D printing; polypropylene, semicrystalline polymers; rheology; mechanical properties

7.1 Introduction

Additive manufacturing (AM), also referred to as 3D printing, involves the layer-by-layer fabrication of parts from computer aided design (CAD) models [Das et al., 2020a]. Among the different AM modalities, filament based material extrusion (MatEx), commonly known as fused filament fabrication (FFF) is an attractive choice for processing thermoplastic polymers. However, the material library compatible with FFF is limited largely to amorphous polymers such as polylactic acid (PLA) and acrylonitrile butadiene styrene (ABS). Processing commodity semicrystalline polymers, such as polypropylene (PP) and polyeythlene (PE), through FFF is challenging due to the problems associated with interlayer welding and part warpage resulting from the high levels of volumetric shrinkage encountered during cooling from the melt state [Das et al., 2020b, Schirmeister et al., 2021b]. In a typical FFF process, the adhesion between the successively deposited layers is of critical importance in dictating the final part properties. However, due to the fast cooling of the layers, the extent of interfacial bonding is limited since the polymer chains rapidly lose mobility [Gao et al., 2020].

The issues associated with FFF of semicrystalline polymers have been addressed using two different routes: either by optimizing the processing conditions or through modifications to the material formulation to tune the thermal, crystallization, and rheological properties to

enable successful FFF. There has been a number of studies that investigate the effect of processing parameters such as nozzle temperature and print speed on the printability of both amorphous and semicrystalline polymers, that have been summarized elsewhere in great detail [Peterson, 2019, Vaes and Van Puyvelde, 2021]. The adhesion between the deposited layers can be improved by physical modifications to the printing process. For example, the extent of interlayer chain diffusion and re-entanglement during FFF of PLA was enhanced through the application of ultrasonic vibrations, resulting in parts that exhibit improved interlayer adhesion [Li et al., 2018]. On the other hand, the rheological characteristics of the polymer can be modified to aid interlayer bonding through blending suitable additives or other polymers [Levenhagen and Dadmun, 2018, Levenhagen and Dadmun, 2019a, Rocha et al., 2014, Silva et al., 2021, Levenhagen and Dadmun, 2019b, Alturkestany et al., 2019, Levenhagen and Dadmun, 2017]. Addition of polyamide to ABS assisted in smooth extrusion through the printing nozzle and promoted interlayer welding between the deposited layers [Spreeman et al., 2019]. The enhanced chain mobility also improved the mechanical properties of the blends by reducing the void content in the printed parts. Moreover, by blending low molecular weight fractions of PLA with different molecular architectures, the interlayer adhesion of high molecular weight PLA and ABS prints can be improved significantly [Levenhagen and Dadmun, 2019a, Levenhagen and Dadmun, 2017]. The findings were attributed to the fast diffusion of the low molecular weight fractions across the interface that is essential to the formation of entanglements between the successively printed layers.

However, most of the research on the feedstock modifications to enable FFF has focused on amorphous polymers. Reports of successful FFF of semicrystalline polymers such as PP are fairly limited [Petersmann et al., 2020, Jin et al., 2018, Bertolino et al., 2021]. Specifically, FFF of PP is hindered due to the high melt viscosity at the printing temperatures and the fast crystallization kinetics that result in poor interfacial strength and buildup of significant levels of volumetric shrinkage and internal stress [Bachhar et al., 2020, Das et al., 2021b, Mackay, 2018]. One of the approaches to address the shortcomings of PP in FFF processing is by blending PP with low molecular weight hydrocarbon resins that retards the crystallization kinetics of neat PP and improves the interlayer chain diffusion, thereby, reducing warpage and improving the tensile properties of the printed parts [Das et al., 2020b].

In this work, the process-structure-property relationships associated with FFF of PP/hydrocarbon resin blends are explored through detailed crystallization, rheological, and mechanical characterizations. The effect of varying melt flow rate (MFR) on the printability, interlayer

welding, and printed part properties is investigated. Finally, the processing-induced morphology and polymer chain entanglement at the interface is correlated to the mechanical properties of the different MFR grades of PP.

7.2 Materials and methods

7.2.1 Materials

Three grades of isotactic polypropylene (H521, FT120, and FT200) with differing melt flow rates, were kindly supplied by Braskem America. H521 has the lowest melt flow index of 3.6 g/10 min, FT120 has a melt flow index of 12 g/10 min, and FT200 has the highest melt flow index of 20 g/10 min. Two hydrogenated ARKON resins were obtained from Arakawa Chemical Industries. The fully hydrogenated resin (FH) has a softening point of 100°C, a molecular weight of 1260, and a glass transition temperature of 58.5°C. The partially hydrogenated resin (PH), has a softening point of 100°C, a molecular weight of 1320, and a glass transition temperature of 57°C.

7.2.2 Blend preparation

Each grade of PP was compounded with the two hydrocarbon resins (FH and PH) at different compositions. The blend compositions evaluated in this study were 100/0, 90/10, and 80/20 with respect to weight percent of PP/hydrocarbon resin. The blends were prepared using a Brabender mixer, running the temperature at 190°C for PH blends and at 170°C for FH blends. The mixing was done in batches of 45g and the compounder was run at 32 rpm for 10 minutes at the designated temperatures. After blending, the materials were cooled to room temperature and cut into small pieces for further experiments.

7.2.3 Thermal analysis

Thermogravimetric analysis (TGA) was performed in a thermogravimetric analyzer (TGA 5500, TA Instruments, USA) in air (flow rate: $100\,\mathrm{mL\,min^{-1}}$) from room temperature to 600°C at a heating rate of $10^{\circ}\mathrm{C\,min^{-1}}$.

Differential scanning analysis (DSC) was performed in a Q2000 calorimeter (TA Instruments, USA). Typically, 7 mg of the samples were heated in a nitrogen atmosphere (flow rate: 50 mL min^{-1}) from room temperature to 200°C at a heating rate of 10°C min^{-1} to ensure complete melting, cooled at 5°C min^{-1} to -50°C (below the glass transition of PP), and finally heated to 190°C at a heating rate of 10°C min^{-1}. The crystallinity content (X_c) in the PP blends were determined by the Equation 7.1

$$X_c = \frac{\Delta H_f}{\Delta H_f^\circ \times w} \times 100\% \tag{7.1}$$

where, ΔH_f° is the enthalpy of fusion for 100% PP crystalline material (207 J g^{-1}) [Bagheriasl et al., 2015], $\Delta H_f$is enthalpy of fusion for each sample (measured from the area under the curve of the melting endotherm corresponding to the second heating cycle); and w is the PP mass fraction in the blends (0.9 and 0.8).

7.2.4 Rheology

The rheological properties of PP and its blends with hydrocarbon resins were investigated using a parallel plate rheometer (AR-G2, TA Instruments, USA) with a plate diameter of 25 mm. Samples for the rheology tests were prepared by compression molding in a Carver press at 180°C under a pressure of 2 MPa for 5 minutes. The experiments were performed under nitrogen atmosphere to avoid thermal degradation of the samples. Frequency sweeps (1-100 Hz) in small-amplitude oscillatory shear (SAOS) at a strain amplitude of 1% were conducted at 180°C and 200°C while steady shear rate sweeps (0.01-10 s^{-1}) were conducted at 180°C.

Further, interrupted shear measurements were performed on compression molded discs (25 mm in diameter and 1 mm thick) of the blends in order to investigate the re-entanglement behavior during the printing process as well as to study the interlayer weld formation. The measurements were carried out using 25 mm 0.1 radian cone and plate geometry on the ARES G2 rheometer (TA Instruments, USA) at the printing temperatures of the materials under a constant shear rate of 1 s^{-1}. Details regarding the test procedure and analysis have been described elsewhere [Pisipati and Baird, 1984, Gilmer et al., 2019].

7.2.5 MatEx of PP blends

The blended materials prepared using the Brabender were fed through a single screw extruder (Filabot EX2 filament extruder: hopper volume of approximately 426.1 cm^3 and screw void volume of 28.8 cm^3. Screw design: outer diameter of 5/8 inch; L/D of 12; pitch: 0.5 inch; and compression ratio: 2.5:1) at 180°C using a 1.75 mm die. The extruded filaments were collected, repelletized, and again fed through the single screw extruder under the same conditions to obtain filaments with diameters in the range of 1.65-1.80 mm.

Tensile bars were printed by feeding the prepared filaments to a Flashforge (Creator Pro) 3D printer equipped with a Flexion extruder head. The nominal diameter of the nozzle was measured to be 1.06 mm. The extruder temperature for the blends was kept at 180°C and the bed temperature for all prints was fixed at 120°C. All the parts were printed at 1000 mm min^{-1} and 80% infill density. Scotch tape was applied on the print bed for ease of removal of printed parts. Tensile bars (as per the ASTM D638 Type IV) were printed in ±45° and 0° raster angle patterns to evaluate the effect print orientation on the tensile properties of the printed part. The tensile bars were annealed in a convection oven (Fisher Scientific Isotemp Oven) for 24 hours at 120°C to investigate the effect of post-treatment on the mechanical properties of the printed part.

7.2.6 Tensile testing

The printed tensile bars of each blend were used to measure the stress strain relationship using an Instron 5944 with a max load of 2kN. Sample length, width, and thickness were recorded and each sample was stretched at a rate of 3 mm/min till failure. Care was taken to ensure cylindrical sample geometry with no substantial geometric deviation over the tested filament length, ensuring consistent cross-sectional area. All tests were performed at room temperature (∼22°C). Stress-strain curves provided the measurements necessary to calculate the elastic modulus. The crosshead distance was used as a measurement of the strain with the assumption that all sample deformation occurred in the gauge length between the clamps. The linear region of the stress-strain relationship was used to determine the Young's modulus of each sample by calculating the slope at less than 2% extension.

7.2.7 Geometric accuracy and warpage

The Type IV tensile dogbones printed for tensile property evaluation were used to evaluate the geometric accuracy of prints. Each dimension was measured using calipers and were compared against the targeted design specifications. Warpage of the printed measured as the amount the printed part lifted off from the printed bed at the end of the printing process. The measurement was performed using a Vernier caliper gauge micrometer, and the values reported are an average of five measurements.

7.3 Results and discussion

7.3.1 Melting and crystallization

The smooth extrusion through the printing nozzle and the subsequent consolidation of the deposited layers on the print bed are strongly dependent on the melting and crystallization behavior of PP and PP/hydrocarbon resin blends. Representative DSC melting and crystallization profiles for PP/hydrocarbon resins are presented in Figure 7.1 while the variation in the peak melting (T_m) and crystallization (T_c) temperatures are illustrated in Figure 7.2. The degree of crystallinity in presence of the hydrocarbon resins reduced from 58% (for neat PP) to 42% in agreement with previous work using similar materials [Das et al., 2020b]. The decrease in crystallinity is attributed to the amorphous resins affecting the formation of PP spherulites, likely due to a dilution effect.

The mechanism of interlayer bond formation is dictated by the temperature of the depsoited layers. At temperatures above the T_m, the samples undergo sintering. Once the temperature reaches below T_m the mechanism of interlayer fusion changes and molecular diffusion dominates. The chain motion stops once the temperature drops below the crystallization temperature of the blends since they do not have sufficient thermally induced mobility. The lower crystallization temperature in the blends compared to neat PP allows the samples to remain in the molten state for a longer time period, thereby promoting chain reptation and interdiffusion across the deposited layers.

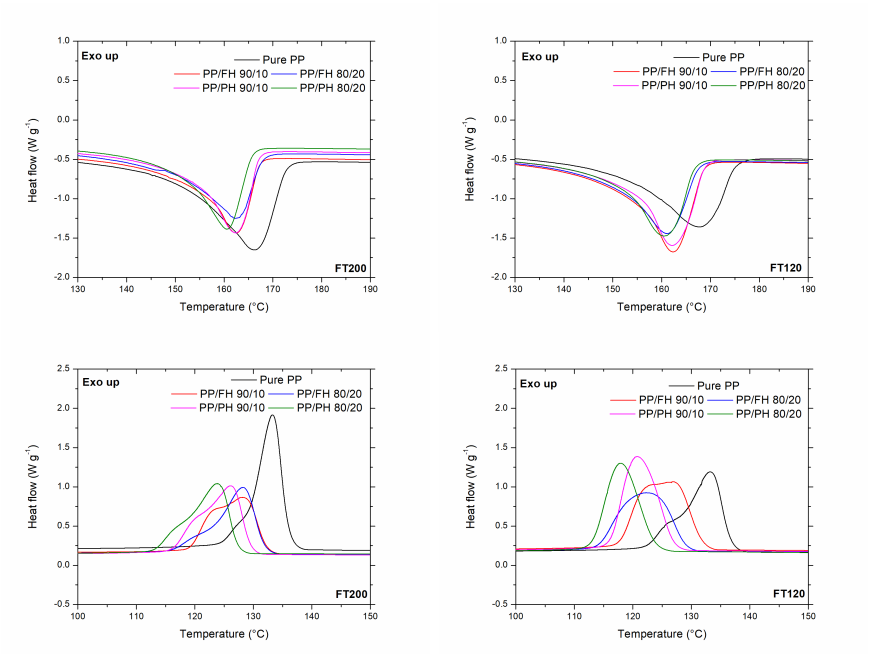


Figure 7.1: DSC melting and crystallization profiles of PP blends with different MFRs

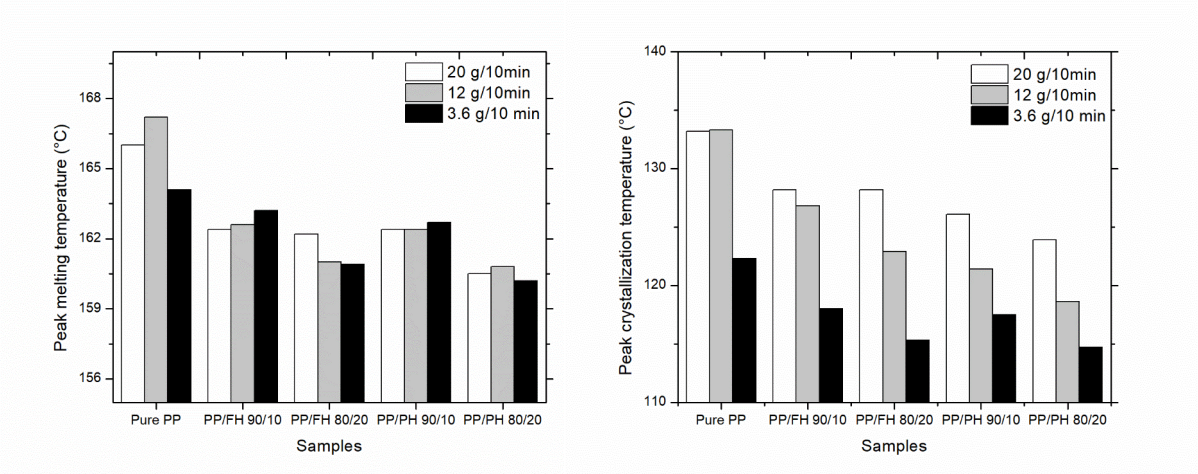


Figure 7.2: Variation in the melting and crystallization temperatures of the blends as a function of blend composition

7.3.2 Shear and oscillatory rheology

Comparing the complex viscosity (η^*) obatined from the small amplitude oscillatory shear measurements to the steady shear viscosity (η) measurements reveals that the conventional Cox-Merz rule (Equation 7.2) is not valid for the PP/hydrocarbon resin blends.

$$\eta^*(\omega) = \eta(\dot{\gamma} = \omega) \tag{7.2}$$

where, $\dot{\gamma}$ is the shear rate in the continuous flow measurements and ω is the angular frequency in the SAOS measurements. A modified version of Cox-Merz rule (Equation 7.3) can be employed to explain the beahvior of the samples.

$$\eta^*(\omega) \times A = \eta(\dot{\gamma} = \omega) \tag{7.3}$$

where A is a parameter that takes into account the effect of shear on the microstructure of the polymer.

Figure 7.3 highlights the overlay between the complex viscosity and the steady shear viscosities based on Equation 7.3 for the PP samples with a MFR of 12g/10min. The steady and oscillatory data for the PP/hydrocarbon resin samples exhibit good agreement with the modified Cox-Merz rule irrespective of the blend composition. The reduction of the viscosity with increasing resin content helps ensure smooth extrusion through the printing nozzle. This observation has been attributed to a phenomenon known as the "ball-bearing" effect that originates from the limited interactions of the PP phase with the amorphous resins at the interfacial regions. the addition of the resins reduces the internal friction resulting from the cooperative motion of the polymer chains [Shenoy et al., 2005]. The shaded region in Figure 7.3 highlights the shear rates relevant to the printing process and as is evident all the blends exhibit shear thinning characteristics; that aids the printing process. Moreover, the higher viscosity values at the low-shear region assures that post-extrusion through the nozzle the extrudate retains its shape with minimal die-swell. Further, high zero-shear viscosities ensure that a deposited layer on the print bed has enough mechanical stability support the weight of the subsequent layers.

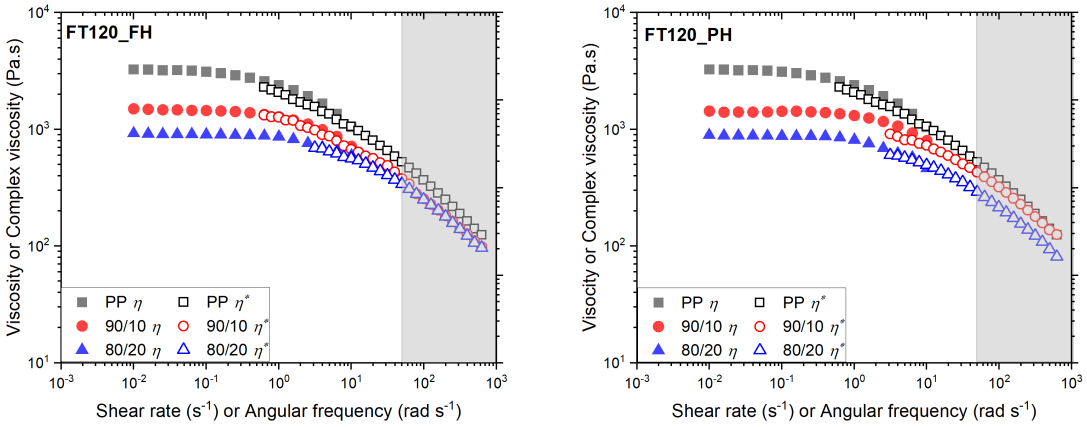


Figure 7.3: Overlay of steady shear (η) and complex (η^*) viscosities normalized by a factor (A) for the PP/hydrocarbon resin blends.

7.3.3 Interrupted shear rheology

Interrupted shear rheometry [Pisipati and Baird, 1984] was employed to characterize the interlayer bonding in the PP/hydrocarbon resin samples during printing by quantifying the extent of bulk property recovery in the printed parts at the printing temperature. Briefly, the test applies a constant shear rate (1s^{-1}) to a sample with infinite relaxation time till equilibrium is achieved; followed by a finite relaxation time where chains can re-entangle after which the shear is reapplied. The typical results from an interrupted shear measurement for PP/hydrocarbon resin blends are presented in Figure 7.4. The percent recovery can be quantified using Equation 7.4:

$$\%\text{recovery} = \frac{\left[\tau_m\left(\dot{\gamma}, t_r\right) - \tau_{ss}\right] / \tau_m\left(\dot{\gamma}, t_r\right)}{\left[\tau_m(\dot{\gamma}, \infty) - \tau_{ss}\right] / \tau_m(\dot{\gamma}, \infty)} \tag{7.4}$$

where, $\tau_m\left(\dot{\gamma}, t_r\right)$ is the value of the stress overshoot after the relaxation time, $\tau_m(\dot{\gamma}, \infty)$ is the value of the stress overshoot after infinite relaxation time, and τ_{ss} is the steady state

stress value, as highlighted in Figure 7.4. The percent recovery for the different MFR grade PP and its blends with the different hydrocarbon resins are also highlighted in Figure 7.4. The higher percent recovery in the blends indicated a printed part with properties approaching that of bulk material whereas, PP could only recover 65% of the bulk properties post re-entanglement. The ideal situation is where the material exhibits 100% recovery (no difference between a printed part and bulk material, i.e., a completely "healed" interface [Zhang and Li, 2016]) but that is extremely challenging to realize during the printing process due to the complex multiphysics and strong processing parameter dependence associated with the process. Using this approach and employing multiple relaxation times, a measure of re-entanglement time can be obtained which is critical in characterizing the thermally driven chain diffusion at the layer interface. Although such measurements provide valuable information regarding the relevant timescales of chain re-entanglement, they are not representative of the polymer's characteristic timescales (Rouse and reptation) and hence these experiments were beyond the scope of the current manuscript.

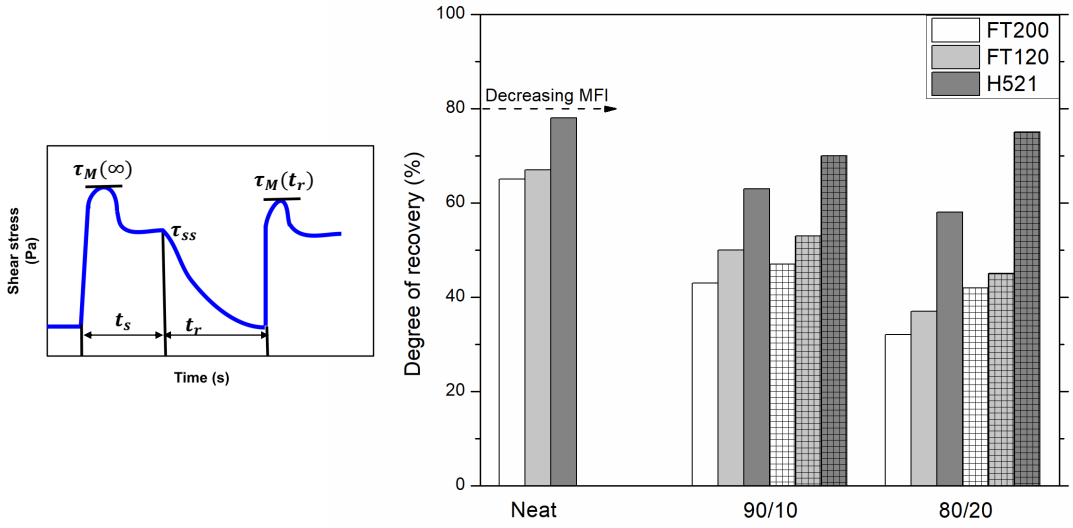


Figure 7.4: Representative plot of the shear stress profile obtained during interrupted shear rheology and effect of blend composition on the degree of recovery.

7.3.4 Printing performance

Following printing parts of the different PP/hydrocarbon resin blends, the warpage of the parts was evaluated as illustrated in Figure 7.5. The observations are consistent with the amount of crystalline content in the blends with blends having higher crystalline content warping to a higher extent than the blends with lower crystalline content. However, addition of hydrocarbon resins drastically decreased the amount of warpage in the printed parts irrespective of the grade of PP employed due to potential improvement in interfacial chain mobility and interlayer adhesion.

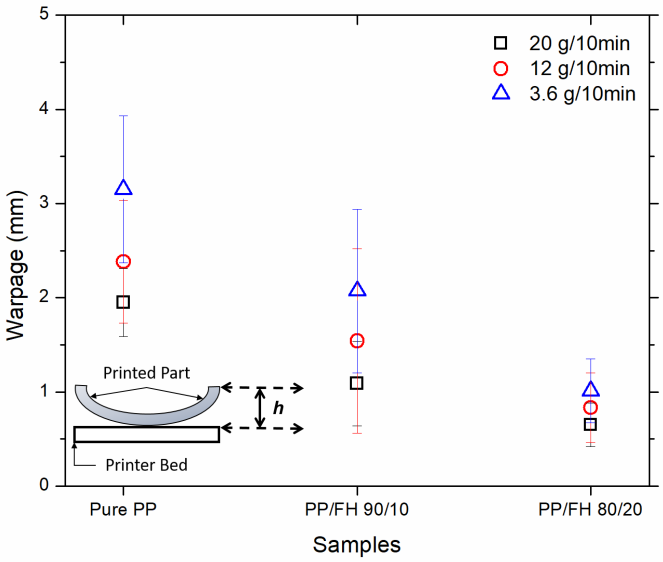


Figure 7.5: Warpage in the printed parts of PP/hydrocarbon resin blends as a function of the blend composition and grade of PP used.

Figure 7.6 highlights the variations in the maximum tensile stress and tensile modulus of the printed parts of PP/hydrocarbon resin blends. The properties for all the blends are inferior to that of injection molded PP values and the parts are heat-treated to evaluate the effect of annealing on the tensile properties. Blends with higher crystalline content have better tensile properties compared to the blends with lower degree of crystallinity. It is interesting to note from Figs.7.5 and 7.6 that the blends with higher MFRs exhibited greater dimensional stability but had lower tensile properties compared to the lower MFR blends. Therefore, a

trade-off must be made when selecting a particular blend for MatEx by taking into account the end application of the printed part (whether it needs to be geometrically accurate or mechanically robust).

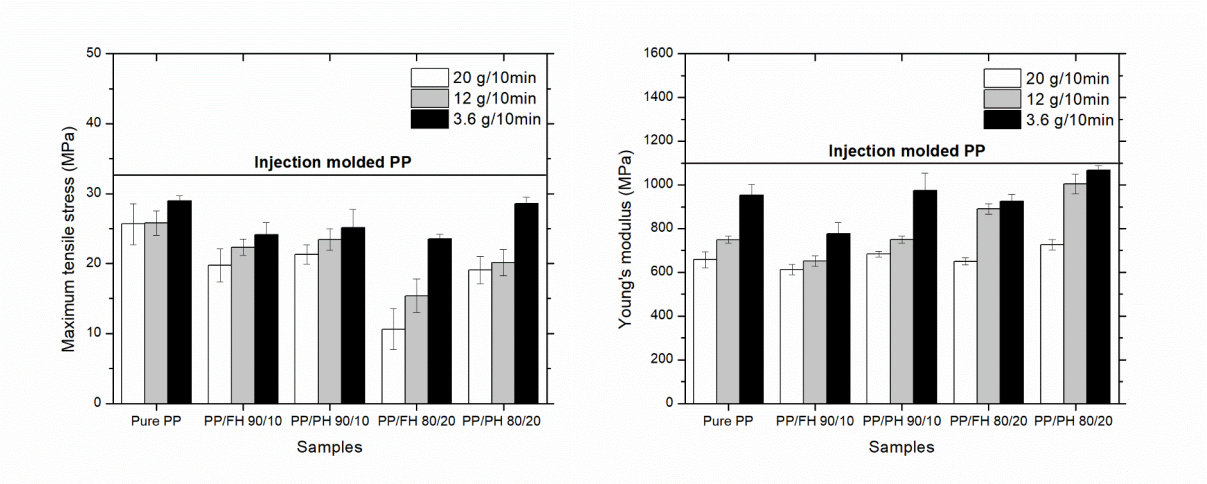


Figure 7.6: (a) Maximum tensile stress and (b) Young's modulus of PP/hydrocarbon resin blends as a function of the blend composition and grade of PP used

Figure 7.7 correlates the maximum tensile stresses with the percent recovery of the PP samples. The properties found to scale linearly with the percent recovery in accordance with Wool's welding theory [Wool et al., 1989]. However, it is worth remembering that lower percent recovery values (<35%) were not achieved under the experimental conditions employed in this study. In order to have a more complete understanding of how the properties evolve as a function of the extent of polymer chain re-entanglement, these lower percent recovery values must be probed by selecting the appropriate relaxation timescales. Moreover, the extent of wetting of the PP matrix with the amorphous resins must be examined in relation to the interrupted shear measurements.

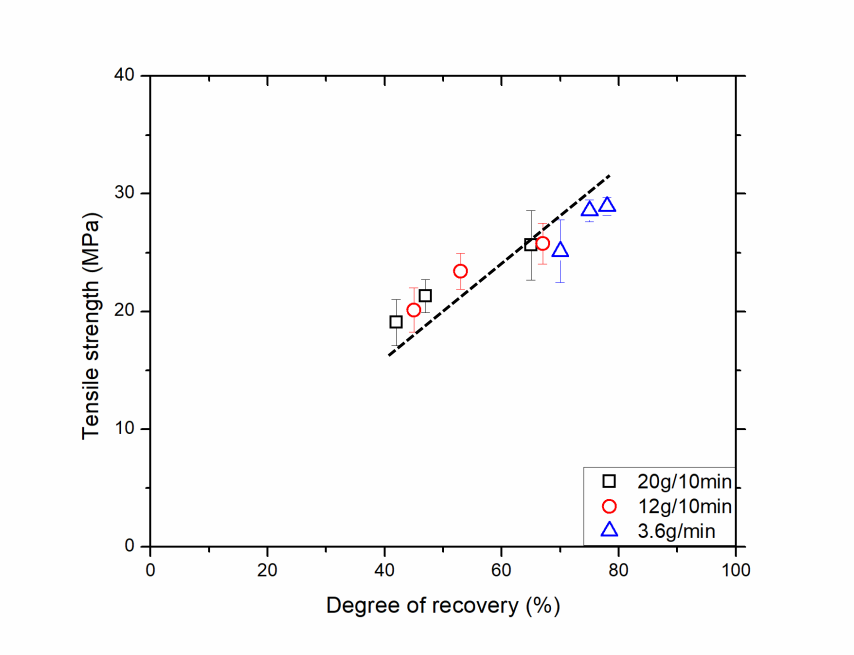


Figure 7.7: Correlating the degree of recovery measured using interrupted shear rheology to the maximum tensile strength of the printed parts

The mechanical properties of the printed parts are controlled by the processing-induced total crystalline content. Post-printing the printed parts were subjected to a thermal annealing procedure that resulted in improvement of the tensile strength and modulus without compromising on the dimensional accuracy of the parts. However, the elongation at break of the annealed parts were inferior to that of the as-printed parts likely due to the formation of more crystalline and hence less tough material. The presence of crystallinity can also hinder the long-range molecular motion and hinder the interdiffusion during annealing. Therefore, increase in crystallinity through the lamellar thickening of the spherulites and reduction in chain mobility due to increased physical crosslinks must be delicately balanced to achieve optimal printed part properties that are suitable for functional applications.

One other important thing to note is the cooling profiles the prints are exposed to once the annealing treatment has been performed. In order to maintain adequate levels of interlaminar toughness, the prints should be cooled at an optimal rate ensuring that the degree of crystallinity is not too high at the end of the treatment.

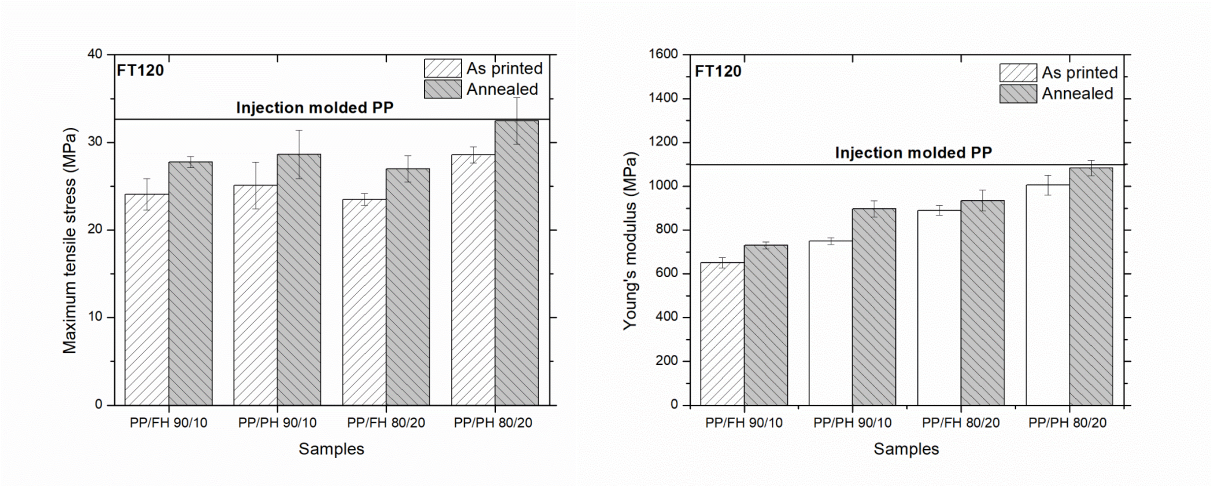


Figure 7.8: Effect of thermal annealing on the tensile properties of PP/hydrocarbon resin blends

7.4 Conclusions

The printability of blends of PP with different MFRs and crystalline content have been studied. The crystallization rate of the PP blends were successfully retarded by adding amorphous hydrocarbon resins. The processability of the blends through MatEx was informed through detailed rheological characterizations (both shear and oscillatory) that revealed details regarding the fluid flow behavior under shear at temperatures that correspond to the printing temperature (180–200°C). The dimensional stability of the printed parts of PP blends improved compared to neat PP through tuning the processing parameters based on the crystallization and rheological analysis. However, the geometric accuracy of the prints can be further improved through tuning the scaling and offset parameters in the build software. Mechanical testing on the as printed and annealed parts were performed to evaluate the tensile properties of the blends. Post-printing isothermal annealing of specimens above their melt temperature increased interfacial contact, eliminating the weak interlaminar interfaces typical of the additive manufacturing process.

Chapter 8

Customized blends of polypropylene for extrusion based additive manufacturing

Arit Das[1,2], Nishanth Shanmugham[1], and Michael J. Bortner[1,2]

[1]Department of Chemical Engineering, Virginia Polytechnic and State University, Blacksburg, VA 24061, USA

[2]Macromolecules Innovation Institute, Virginia Polytechnic and State University, Blacksburg, VA 24061, USA

This chapter is currently under review for publication in *The Role of Additives in Rheology and Processing* special issue of **Journal of Vinyl & Additive Technology**.

Abstract

Filament-based material extrusion (MatEx) additive manufacturing (AM) has garnered great interest due to its simplicity, customizability, and cost-effectiveness. However, AM or 3D printing of semicrystalline polymers is still largely relegated to prototyping applications. Major issues involving volumetric shrinkage and warpage of the printed parts must be addressed in order to employ them for printing functional parts. Moreover, the crystallization behavior and rheology of the polymer are dependent on the MatEx processing conditions. In the current work, the printability of blends of isotactic polypropylene with a soft, low crystallinity propylene based homopolymer is evaluated. Addition of the homopolymer resulted in an increase in the crystallization window of the blends by 6°C that had a profound impact on the interlayer adhesion and residual stress state. The shear-dependent melt flow behavior inside the printing nozzle as well as the interlayer chain diffusion and interlayer welding on the print bed were investigated. Rheological characterizations also indicate sufficient dispersion and

miscibility of the homopolymer in the neat polypropylene matrix. The incorporation of the homopolymer significantly improved the dimensional accuracy of the printed parts through better dissipation of the entrapped residual stresses during MatEx. Moreover, the degree of mechanical anisotropy of the parts was significantly lower than that obtained using many 3D printable grade polymers. The findings from this study can be leveraged in toolpath planning, process parameter optimization, and new feedstock development, highlighting current limitations as well as providing valuable insights into necessary processing modifications in order to enable MatEx of next generation semicrystalline polymers.

Keywords: polypropylene; fused filament fabrication; crystallization; rheology; mechanical properties

8.1 Introduction

Additive manufacturing (AM) or 3D printing of polymers that involves layer-by layer fabrication of a three-dimensional part from its corresponding computer aided design (CAD) model, has emerged has a viable alternative to traditional subtractive manufacturing techniques. Polymer material extrusion (MatEx) includes both filament-fed fused filament fabrication (FFF) and pellet-fed techniques which have garnered significant research interest over the past decade [Turner et al., 2014, Gold and Turner, 2015]. Limited material catalog compatible with the FFF process presents a major roadblock in the widespread adoption of the technique for mass production of functional parts [Das et al., 2020a, Popescu et al., 2018]. The process-structure-property relationships of commodity thermoplastics such as acrylonitrile butadiene styrene (ABS) and polylactic acid (PLA) have been studied in great detail in the context of FFF [Ligon et al., 2017, Peterson, 2019]. However, in order to manufacture parts suitable for high performance applications (such as, in the medical, automotive, aerospace industries), it is necessary to integrate other commodity and engineering semicrystalline polymers within the FFF material library.

Polypropylene (PP) is one of the most commercially relevant polymer in the world and has the potential to revolutionize the economy if successfully incorporated within the AM paradigm. A large body of literature has focused on studying mechanical properties of "3D printing grade" PP feedstocks as a function of printing parameters [Carneiro et al., 2015, Jin et al., 2018] and insights into what makes such material printable is lacking. The

rapid crystallization of PP (or any semicrystalline polymer) due to the high cooling rates associated with the FFF process results in large levels of volumetric shrinkage that in turn leads to entrapment of significant amounts of residual stresses in a printed part [Vaes et al., 2021]. This problem is further exacerbated in case of isotactic PP due to high degree of crystallinity resulting from regular arrangements of the molecular chains [Phillips, 2000].

A common approach to print PP by addressing the warpage issue is by the addition of high aspect ratio fillers such as carbon fibers [Spoerk et al., 2018b, Savandaiah et al., 2021, Spoerk et al., 2020]. The stiff fibers, when aligned along the extrusion direction, counteract the warp deformations during printing while the high thermal conductivity of the carbon fibers result in a more uniform thermal profile within the print; consequently, leading to generation of low levels of internal stresses [Spoerk et al., 2020]. However, addition of fibers results in a printed part that has significantly poor mechanical properties when tested orthogonally to the fiber orientation; since the fillers hinder interlayer polymer chain diffusion [Chacón et al., 2019]. Hence, blending PP with other polymers that can address the warpage and interlayer strength problems during FFF is an interesting alternative to fiber reinforcements and has been utilized with reasonable success [Zander et al., 2019a, Peng et al., 2019b, Ho and Kontopoulou, 2022, Leng et al., 2020, Schirmeister et al., 2021b].

Previous work from our group has investigated the printability of PP blended with amorphous hydrocarbon resins and the printed part performance has been explored [Das et al., 2020b]. However, limited miscibility of the resins in the PP matrix resulted in parts that exhibited inferior tensile properties as compared to injection-molded PP [Das et al., 2020b]. Therefore, improving the miscibility of the fillers in the PP matrix can lead to a more homogenous material that could potentially have comparable mechanical performance to traditionally processed PP. In this context, thermoplastic elastomers are an interesting class of compounds due to their attractive mechanical properties, ease of processing, and recycling potential. Polyolefin-based elastomers comprising of the respective thermoplastic phase along with a plasticizer and suitable additives (filler, compatibilizer, processing aid, etc.) are commonly used for industrial polymer processing.

The crystalline behavior and thermo-mechanical properties of blends of PP with elastomers has garnered significant research interest over the course of the last decade [Zhang et al., 2015, Kannan et al., 2013, Guezzout et al., 2017, Lou et al., 2016, Wang et al., 2014]. Most of these works focus on understanding the structure-property relationships of the blends processed using traditional techniques. The effect of inorganic fillers on blends of isotactic

polypropylene and PP-based elastomers has been studied through detailed structural and rheological characterizations [Alanalp et al., 2019]. The filler geometry was found to have a significant effect on the viscoelastic properties of the blends by modifying the melt flow characteristics as well as the relaxation kinetics [Alanalp et al., 2019]. As evident from the above discussion, the effect of the elastomer addition on the blend properties is strongly dependent on their composition. However, there is limited knowledge about the process-property relationships of such materials in the context of FFF. Such an understanding is critical for highlighting the impact of the non-isothermal repeated thermal profile and inter-layer polymer diffusion on the printability of the blends and eventually dictates the printed part performance.

In this study, the rapid crystallization of isotactic PP has been impeded by the addition of low levels (2.5-10wt%) of a low-crystallinity, low modulus propylene homopolymer (LCPP). The resulting blends were evaluated in terms of their crystallization behavior, rheology, printability using a commercial off the shelf printer, and the tensile properties of the resulting parts in order to gain a complete understanding of the associated processing-structure-property relationships. The addition of the LCPP significantly improved the printing process by expanding the crystallization window and reduced the warpage in the parts. The soft nature of LCPP coupled with its high compatibility with isotactic PP play a vital role in dictating the mechanical properties of the printed parts by controlling the interlayer adhesion during FFF. The current study is critical in gaining valuable insights for developing the next-generation of polymer-based feedstocks for FFF that are machine-agnostic.

8.2 Materials and Methods

8.2.1 Materials

Pellets of isotactic PP 5E16S with a melt flow index of 40g/10min were kindly supplied by Braskem America, Inc. The heat deflection point of the polymer was estimated to be 104°C while the glass transition temperature was between 0°C and -20°C as reported by the supplier. The low-crystallinity PP pellets (L-MODU S400) with a were obtained from Idemitsu Kosan Co., Japan. The low isotacticity was achieved through addition of rubber, copolymerization with ethylene, and tuning the stereochemistry using metallocene catalyst technology. The melting and softening point of the LCPP were reported by the supplier to

be 80°C and 93°C, respectively. All materials were dried under vacuum at 60°C prior to processing.

8.2.2 Preparation of PP/LCPP Blends

PP/LCPP blends were prepared using a single screw extruder ((Filabot EX2 filament extruder) at different LCPP content (2.5, 5, 7.5, and 10wt%). Briefly, weighed amounts of PP and LCPP pellets were hand mixed and fed through the extruder (with a hopper and screw void volume of approximately 426 and 29 cm^3, respectively) at 185°C. In order to ensure proper mixing, the collected extrudate were chopped into small pieces and again fed through the extruder using a 1.75 mm die. The extruded filament was cooled using a water bath and spooled. The extruder screw speed and spooling speed was adjusted such that the diameter of the extruded filament (1.70 ± 0.15 mm) was acceptable for FFF processing. The prepared filaments were stored in airtight containers until further processing.

8.2.3 Differential Scanning Calorimetry (DSC) of PP/LCPP Blends

The melting and crystallization behavior of the prepared blends were characterized using Differential Scanning Calorimetry (DSC Q200, TA Instruments, USA). Weighed amounts of each sample (∼5mg) were placed in aluminum pans and heated at 10°C/min to 200°C under a nitrogen flow of 50 mL/min to erase the thermal history associated with the blends during extrusion. The samples were held at 200°C for a couple of minutes to ensure complete melting and then cooled to -50°C at 5°C/min. Finally, the sample was again heated to 200°C at 10°C/min. The melting temperature (T_m) and enthalpy of melting (ΔH_m) was reported based on the second heating cycle while the crystallization temperature (T_c) and enthalpy of crystallization (ΔH_c) were calculated using the heat flow data from the cooling cycle. The degree of crystallinity (X_c) of each sample was calculated using the following equation:

$$X_c = \frac{\Delta H_m}{\Delta H_m^{100}} \times 100\% \tag{8.1}$$

where, ΔH_m^{100} is the melting enthalpy of 100% crystalline PP and its value was taken to be 207 J g^{-1} [Bagheriasl et al., 2015].

8.2.4 Rheology of PP/LCPP Blends

Circular discs with a diameter of 25 mm and thickness of 1.2 mm were melt pressed at 200°C under a pressure of 5 ton m^{-2} using a Carver Press (Carver Inc., USA). A parallel plate geometry (plate diameter of 25 mm) was employed in DHR 30 rheometer (TA Instruments, USA) to monitor the storage (G') and loss (G") modulus as well as the complex viscosity (η^*) through oscillatory frequency scans between 0.1 rad/s and 100 rad/s. These small amplitude oscillatory shear (SAOS) rheology experiments were performed under a strain amplitude of 1% and a constant gap height of 1mm.

8.2.5 3D Printing of PP/LCPP Blends

A FlashForge Creator Pro 3D printer (with a build volume of 227x148x150 mm) coupled with a Flexion extruder head was used in this study. The printer bed was covered in painter's tape and Cube glue (3D systems, USA) was applied on it in order to improve the adhesion between the printer bed and the deposited layer. The nozzle and bed temperature were fixed at 200°C and 120°C, respectively. All prints were printed with an infill of 100%, print speed of 1200 mm/min, layer thickness of 0.1 mm, and an extrusion multiplier of 1.5mm. Further, to improve bed adhesion the first layer was printed at 750 mm/min while an outline brim was used to prevent warping of the deposited layer. In order to probe the anisotropy in the tensile properties, test specimens were printed using 0° and 90° raster angle; these two configurations allow for evaluation of the properties parallel and perpendicular to the tensile testing direction, respectively.

8.2.6 Tensile Testing of Printed Parts

The printed tensile bars (according to ASTM D638 Type IV) were heat treated at 120°C in a convection oven (Fischer Scientific Isotemp Oven) overnight. Post-annealing, the prints were cooled to room temperature inside the oven prior to tensile testing. An Instron 5944 with a 2kN load cell was used to characterize the tensile properties of the PP/LCPP prints at 3mm/min until failure. Each test was performed at room temperature and a constant gauge length of 25mm was used. The reported tensile properties are an average of at least three replicates.

8.2.7 Dynamic Mechanical Analysis (DMA) of Printed Parts

A qualitative estimation of the mechanical integrity of the different PP/LCPP prints was performed by comparing their storage modulus at room temperature and 120°C using a dynamic mechanical analyzer (Discovery DMA 850, TA Instruments, USA). Frequency sweeps (0.1-100Hz) were performed at different temperatures (25°C and 120°C) under a constant strain of 0.1% (within the linear viscoelastic regime of the printed parts). All the DMA experiments were performed on printed rectangles (40x5x1 mm) using the same printing parameters as outlined in Section 8.2.5.

8.3 Results and Discussions

8.3.1 Melting and Crystallization Behavior of the Blends

The melting and crystallization behavior of isotactic PP blended with the low crystallinity propylene homopolymer (LCPP) were characterized using non-isothermal DSC experiments as highlighted in Figure 8.1. Depending on the melting characteristics of the blends, the printing temperature for FFF can be determined such that the viscosity of the polymer can be lowered while evading issues associated with nozzle clogging [Fallon et al., 2019]. The viscosity of the polymer melts as well as the presence of LCPP affects the melting temperature of the blends. The melting endotherm and the crystallization exotherm are characterized by the presence of a single peak indicative of a single crystalline phase in the blends due to the enhanced miscibility of LCPP in the PP matrix. Further, the appearance of a single melting and crystallization peak has been attributed to the presence of α-crystallites of isotactic PP in the blends [Chen et al., 2005]. Similar results were obtained by Bertolino et al. when using talc filled PP for FFF and as per their definition the prepared blends in this study can be classified as heterophasic copolymers [Bertolino et al., 2021].

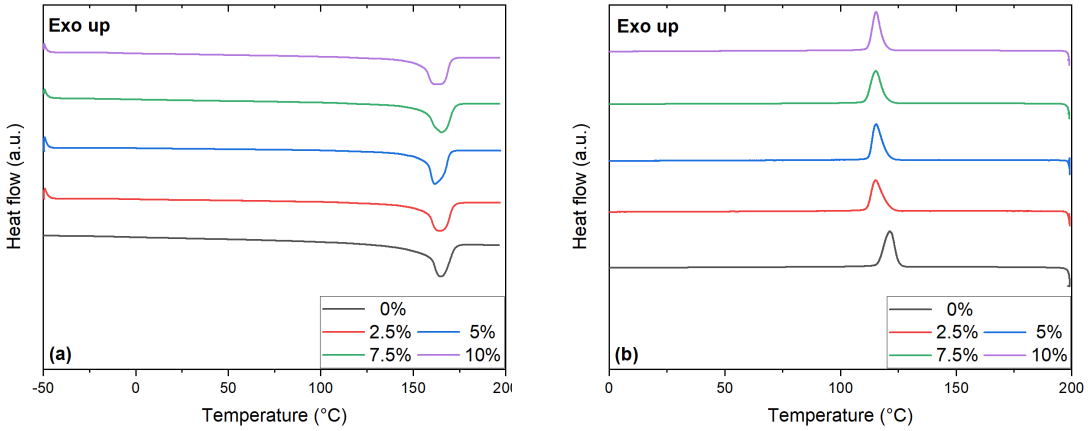


Figure 8.1: (a) Melting endotherms from the second heating cycle of the heat-cool-heat DSC tests for the different blends of PP and LCPP; and (b) crystallization exotherms from the cooling cycle of the heat-cool-heat DSC tests for the different blends of PP and LCPP.

As presented in Table 8.1, the peak melting temperature, the enthalpy of melting, and the degree of crystallinity of the blends decreases with the addition of LCPP as compared to neat isotactic PP. The presence of a broader melting peak and reduction in T_m values of the blends are indicative of slower nucleation and crystallization kinetics [Wu et al., 2020b]. The decrease in the peak melting temperatures is dictated by the extent of miscibility of the homopolymer in the PP matrix. The isotactic PP chains surrounding the LCPP chains are associated with the formation of the α-crystallites of PP and hence the presence of LCPPs results in generation of imperfect crystallites. The reduction in the T_c values of the blends compared to neat PP is attributed to delayed nucleation of the crystallizable domains requiring increased activation energy. Moreover, the relatively imperfect crystallites in the blends compared to neat PP coupled with the dilution effect of the homopolymer chains can also be responsible for the observed trend [Li et al., 2019b]. The crystallization window ($T_m - T_c$) in the blends was found to increase by 5.6°C upon incorporating 2.5wt% LCPP. During FFF of semicrystalline polymers, the interfacial weld formation takes place above the T_c of the polymer. Therefore, the increase in the crystallization window is significant

in the context of FFF since the polymer chains retain mobility for a longer amount of time resulting in increased interfacial diffusion and stress dissipation. However, with the addition of more LCPP, the crystallization window decreased to 2.6°C since higher amounts of LCPP promoted nucleation in the amorphous regions of isotactic PP.

Table 8.1: Peak melting temperature, enthalpy of melting from the second heating cycle as well as the peak crystallization temperature and enthalpy of crystallization from the cooling cycle of the heat-cool-heat DSC tests for the different blends of PP and LCPP. The degree of crystallinity was calculated based on the enthalpy of melting from the second heating cycle as highlighted in Equation 8.1

LCPP content (%)	**Peak melting temperature (°C)**	**Enthalpy of melting (J/g)**	**Peak crystallization temperature (°C)**	**Enthalpy of crystallization (J/g)**	**Degree of crystallinity (%)**
0	164.7	108.5	121.4	111.5	52.4
2.5	164.2	96.5	115.3	97.9	46.6
5	161.7	95.8	115.4	98.4	46.3
7.5	161.0	95.0	115.3	99.3	45.9
10	161.3	92.3	115.4	95.3	44.6

Finally, the of addition of LCPP has a direct impact on the degree of crystallinity of the blends with a maximum decrease of 7.8% compared to neat isotactic PP due to the dilution effect, as discussed earlier. The regular arrangement of the chains in isotactic PP is disrupted in presence of LCPP that can impede the PP chain diffusion when cooling from the melt and influence the stereoregularity of the polymer resulting in crystals growing at slower rates. Both the enthalpy of melting and the final crystalline content in the blends influence the extent of volumetric shrinkage experience during the printing process. Therefore, the amount of LCPP in the blends must be tuned such that the crystallization window is broadened (to aid stress dissipation and limit warpage) without reducing the degree of crystallinity (necessary to retain desirable mechanical properties) to a significant extent. It is expected that such a reduction in the degree of crystallinity will have an adverse effect on the tensile properties of the parts printed using the blends, as will be discussed in the following sections.

8.3.2 Rheological Characterizations of the Blends

The rheology of the prepared blends influences the flow behavior of the material inside the printer nozzle as well as the consolidation and interlayer adhesion characteristics of the layers once deposited on the printer bed [Das et al., 2021b, Mackay, 2018]. The rheological properties dictate the printability of a particular feedstock and is therefore, essential in controlling the final part properties.

As highlighted in Figure 8.2a, the complex viscosity ($\eta^*(\omega)$) of the blends exhibits a typical Newtonian behavior at low frequencies while at higher frequencies, the behavior transitions to a non-Newtonian shear-thinning regime. Addition of the low molecular weight LCPPs did not interfere with the relaxation dynamics of neat PP and hence all of them exhibit a similar viscosity versus angular frequency profile. At low rates (0.1-1 rad/s), a steady Newtonian plateau is observed for all the blend compositions; this is desirable once the material is deposited on the print bed to maintain its shape as well as to support the next layer that is deposited on it. With the increase in rates (>10 rad/s), the blends exhibit a shear-thinning behavior that is exploited for the extrusion through the printer nozzle. At 200°C, the enhanced molecular motion of the polymer chains controls the rheological characteristics of the blends and contributes to desirable behavior in the context of FFF. The rate-dependent complex viscosity of the blends was modeled using the Carreau-Yasuda model as highlighted in Equation 8.2 below:

$$\eta^*(\omega) = \eta_0^* \left[1 + (\lambda\omega)^a\right]^{\frac{n-1}{a}} \tag{8.2}$$

where, η_0^* is the complex viscosity of the blends at low frequencies ($\omega \to 0$), n is the pseudoplasticity index, a is parameter indicative of the width of the transition between the Newtonian plateau and shear-thinning regime, and λ is the characteristic relaxation time of the blends defined as follows:

$$\lambda = \frac{\eta_0^*}{\tau^*} \tag{8.3}$$

where, τ^* is the shear stress at the transition region between the first Newtonian and shear thinning regime [Zare et al., 2019]. Using the values of n calculated by fitting the complex viscosity versus angular frequency data to Equation 8.2 for the different blends, the apparent shear rates ($\dot{\gamma}_{app}$) the polymer melt experiences during extrusion through the printer nozzle

can be calculated using Equations 8.4 and 8.5 [Das et al., 2021b, Calafel et al., 2020].

$$\dot{\gamma}_{app} = \frac{32Q}{\pi D^3}\left(\frac{3n+1}{4n}\right) \tag{8.4}$$

$$Q = \frac{\pi d^2 v}{4} \tag{8.5}$$

where, D is the diameter of the printing nozzle (0.4mm), Q is volumetric material flow rate through the nozzle, d is the nominal diameter of the filament feedstock (1.75mm), and v is the print speed (20 mm/s). Employing the values of n as presented in Table 8.2, the representative shear rates inside the printing nozzle was estimated to be approximately 8.5×10^3 s^{-1}. Such high shear rates cannot be realized successfully (without incurring significant edge fracture) in a rotational rheometer. Previous research on PP based copolymers for FFF has highlighted the applicability of the Cox-Merz rule for such materials [Bertolino et al., 2021, Aumnate et al., 2019] and the η_0^* values (calculated at the FFF relevant rates using the Carreau model) are expected to be similar to steady-shear viscosities.

Moreover, the addition of LCPP to neat PP resulted in a decrease in the complex viscosity over the entire frequency range investigated; a trend previously observed upon blending neat PP with polymers having lower crystalline content [Jiang et al., 2019, Spoerk et al., 2017]. The decrease in the η_0^* values (Table 8.2) in the blends with higher LCPP content is attributed to the dilution of the PP melt upon addition of the copolymers with significantly higher melt flow index (2600g/10min compared to 40g/10min for neat PP). The reduced viscosity in the blends assisted in the flow of the polymer melt through the printer nozzle. The extent of shear-thinning remains relatively unaltered as evidenced by the similar values of the power law index (0.68-0.74). The microstructure of the blends as well as the relative interactions between the LCPP with the nucleating agents present in the commercial PP can also significantly affect the rheological response of the blends. Finally, the gradual decrease in the value of the parameter a suggests that the polymer melt transitions to the shear thinning regime at relatively lower rates for blends with higher LCPP content; a feature that is again ideal for smooth extrusion through the 3D printer nozzle.

Table 8.2: The parameters of the Carreau-Yasuda model obtained by fitting the complex viscosity versus angular frequency data from the small amplitude oscillatory shear rheology experiments along with the corresponding coefficient of determination (R^2) values. The values of the critical shear stress (τ^*) was calculated using Equation 8.3

LCPP content (%)	η_0^* **(Pa.s)**	λ **(s)**	τ^* **(Pa)**	a	n	R^2
2.5	637.2	0.05	12744	1.07	0.74	0.998
5	519.3	0.06	8655	1.06	0.73	0.998
7.5	433.4	0.04	10835	0.98	0.71	0.999
10	292.5	0.02	14625	0.84	0.68	0.999

Figures 8.2(b) and 8.2(c) highlight the effect of angular frequency on the storage modulus (G') and loss modulus (G") for the different blends at 200°C. The rate-dependent modulus data is indicative of the rigidity of the polymer macrostructure and can reveal important information about polymer chain mobility and melt flow behavior of the polymer blends. Both the G' and G" values increase with increasing frequencies; the incorporation of the LCPPs decreased the G' values slightly over the entire frequency range likely due to the dilution effect promoting the long range motion of the polymer chains [Li et al., 2019b]. This observation suggests the formation of a less rigid polymer chain architecture in the blends that is susceptible to deformation. Although the addition of the copolymer resulted in a blend with improved flow properties (evidenced by Figure 8.2a), the stiffness decreased slightly. The storage modulus of the blends exhibits a behavior in line with the linear viscoelastic theory; at low frequencies (terminal region) following the classical $G' \sim \omega^2$ scaling relationship that indicates relaxation of the low molecular weight LCPP chains. Deviations from the scaling law at higher frequencies (lower timescales) is attributed to the relatively slower relaxation of the polymer chains; a phenomenon that is governed by the stereochemistry as well as the molecular architecture of the blends.

In relation to FFF, once deposited on the printer bed, the polymer chains should retain enough mobility in order to facilitate interlayer chain diffusion while having enough mechanical integrity to retain layer shape and support the succeeding layer. The diffusion across the layers is critical in dictating the interlayer weld strength which in turn controls the mechanical properties of the printed part. The G" values are higher than the G' values in the terminal flow regime for all the blends, indicative of a viscous-dominated response promoting chain mobility across the layer interfaces [Das et al., 2021a]. Figure 8.2(d) exhibits the rela-

tive contribution of the elastic (G') and viscous (G") response (stored vs. dissipated energy) of the different blends by tracking the loss tangent ($tan\delta = G"/G'$) at different frequencies. As stated earlier, the terminal region has tanδ»1; however, at higher frequencies (>10rad/s) tanδ approaches unity suggesting crossover between G' and G" curves. The crossover characteristic is important since upon deposition on the bed the extrudate needs to maintain its shape resolution. Therefore, tuning the elastic and viscous response of the blends is critical to ensure successful FFF processing resulting in parts with desired properties. At 200°C the viscous component is dominating irrespective of the blend composition; hence, longer relaxation times are essential in order to ensure retention of the extrudate shape post-deposition [Duty et al., 2018].

The miscibility of individual components in a polymer blend is essential in order to have synergistic material properties. For the PP and LCPP blends presented in this study, the blend miscibility and relaxation dynamics was characterized using Cole-Cole plots [Coombs et al., 2020]. As highlighted in Figure 8.2(e), the imaginary (η") and real (η') contributions of the complex viscosity for each blend composition are plotted against each other. The values of η' and η" are calculated from the G' and G" data collected from the SAOS rheology experiments as demonstrated in Equation 8.6. A smooth semicircular Cole-Cole plot is indicative of enhanced compatibility while deviations is indicative of phase separation or inhomogeneous dispersion of fillers [Jiang et al., 2020a].

$$|\eta^*| = \left(\eta'^2 + \eta''^2\right)^{1/2} = \left[\left(\frac{G''}{\omega}\right)^2 + \left(\frac{G'}{\omega}\right)^2\right]^{1/2} = \frac{|G^*|}{\omega} \tag{8.6}$$

As presented in Figure 8.2(e), all the PP/LCPP blends exhibit a single relaxation characteristic irrespective of the blend composition. Addition of higher contents of LCPP results in retention of the semicircular shape suggesting that the prepared blends are compatible and homogenous. The origin of a single relaxation time (single peak in the η" vs. η' plot) can be explained by the extent of wetting of the LCPP phase with the neat matrix phase leading to enhanced elasticity. The 10wt% PP/LCPP blend is associated with the longest relaxation time (characterized by the peak in the η" vs. η' plot) resulting from hindered PP chain motion. Comparing the Cole-Cole plots for the different blends, it is evident that the radius of the semicircle increases with the increase in LCPP content which is attributed to the transition from a polymer with narrow molecular weight distribution to one with a wider molecular weight as well as the different phases relaxing in a continuous manner [Codou

et al., 2018]. Therefore, based on the findings the miscibility and morphology of the blends can be tuned by modifying the amount of LCPP in the blends. Figure 8.2(f) presents the Han plots (G' vs. G") of the PP/LCPP blends at 200°C; the plots are linear and similar in nature irrespective of the blend composition. With the increase in LCPP content, a slight increase in G' was observed at constant G" values which is attributed to the blends having minimal changes in microstructure at higher loading levels [Aumnate et al., 2020].

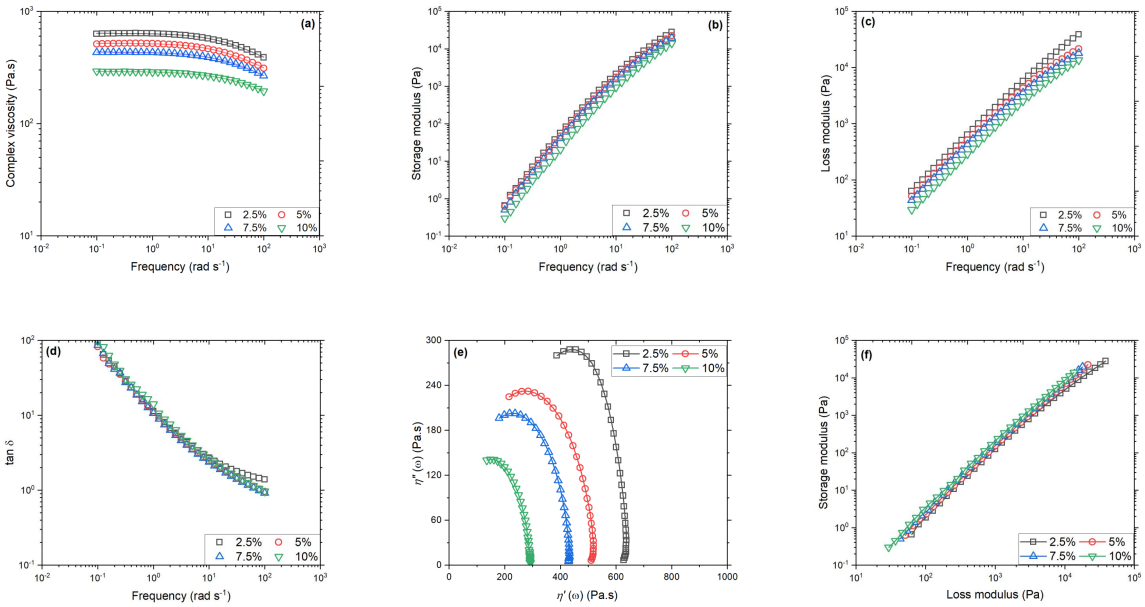


Figure 8.2: (a) Complex viscosity of the different PP/LCPP blends as a function of angular frequency; the solid lines are representative of the non-linear curve fits to the Carreau Yasuda model; (b) storage modulus (G'); (c) loss modulus (G"); (d) tan δ associated with the different blends of PP and LCPP as a function of angular frequency; (e) Cole-Cole plot highlighting the variation of η" vs. η'; and (f) Han plot describing the variation of storage modulus vs. loss modulus. All the experiments were performed at 200°C with a linear viscoelastic strain of 1% using a 25mm parallel plate geometry.

8.3.3 Printing Performance and Mechanical Properties of the Blends

The prepared filaments of the PP/LCPP were employed as a feedstock for FFF based printing using a commercial off the shelf 3D printer. As discussed in Section 8.3.1, the addition of LCPP broadened the crystallization window in the blends through long-range segmental

interactions with the PP matrix. As a result, during printing the mobility of the polymer chains in the melt state is retained for a longer time period allowing enhanced interfacial chain diffusion. The diffusion of chains persists as long as the semicrystalline polymer is above its crystallization temperature and the properties of the printed parts are controlled by the extent of interdiffusion over this 2-3s time period [Seppala and Migler, 2016]. The addition of LCPPs augments this time window allows for better residual stress dissipation and results in parts with improved dimensional stability. Prior to mechanical testing, the as-printed parts were subjected to a mild thermal annealing step, in line with previous research to diminish the effect of internal stress build-up as well as to aid in interlayer bonding [Das et al., 2020b, Fitzharris et al., 2018].

The effect of addition of the LCPP homopolymer on the mechanical properties of the printed PP parts were investigated using tensile tests. Representative stress-strain plots for each of the PP/LCPP blend composition is presented in Figure 8.3(a) and the associated tensile properties are summarized in Table 8.3. All the prints are characterized by the distinctive response of a brittle and stiff material that do not display any yielding behavior before tensile fracture. Figures 8.3(b-d) compares the maximum tensile strength, elongation at break, and tensile modulus of the parts printed at 0° and 90° raster angle. The properties of the printed parts develop through a complex interplay among the crystallinity, morphology, and interfacial interactions between the crystalline and amorphous regions. Increasing the LCPP loading from 2.5wt% to 10wt% increases the tensile modulus from 338 MPa to 464 MPa for the 0° prints; a 37% increase related to enhanced load bearing potential. The soft nature of the LCPPs that leads to improved flexibility (consistent with the G' and G" discussions in the preceding section) of the chain network in blends decent layer adhesion and can lower the number of the stress concentration points. It is hypothesized that the propylene homopolymer serve as tie chains linking the PP crystal lamellae while the rest of the LCPP chains soften and promote chain mobility in the blends; thereby improving the final tensile properties [Li et al., 2019b]. The layer adhesion in the prints can further be improved by optimizing the print parameters such as print temperature, layer thickness, and raster angle [Hertle et al., 2016]; however, the aim of the current study is to highlight the printability of PP/LCPP blends and evaluating the print performance in relation to its crystallization and rheological behavior. The elongation at break for the prints was in the range of 7-9%, further illustrating their brittle nature, and was relatively invariant with LCPP loading. Table 8.4 compares the tensile properties of the PP/LCPP blends with that of that of similarly 3D printed PP based blends and composites.

Table 8.3: Tensile properties of the PP/LCPP blends parts printed at 0° and 90° raster angle. All the parts were printed with a nozzle temperature of 200°C, bed temperature of 100°C, infill of 75%, layer thickness of 0.1mm, and print speed of 20mm/s.

LCPP content (%)	**Raster angle (°)**	**Maximum tensile strength (MPa)**	**Elongation at break (%)**	**Tensile modulus (MPa)**
2.5	0	16.0 ± 2.6	9.0 ± 0.2	338 ± 53
5	0	17.4 ± 2.1	8.8 ± 2.2	352 ± 29
7.5	0	20.1 ± 2.3	8.9 ± 2.4	435 ± 13
10	0	23.8 ± 2.6	9.6 ± 1.8	464 ± 32
2.5	90	14.6 ± 0.9	7.9 ± 1.5	309 ± 21
5	90	14.6 ± 2.3	7.9 ± 2.0	332 ± 46
7.5	90	16.1 ± 1.6	8.4 ± 1.8	395 ± 23
10	90	18.1 ± 2.2	8.4 ± 0.8	478 ± 49

The tensile strength of the 0° prints exhibits a 31% enhancement over the 90° prints, likely due to the deposited layers being continuously aligned in the direction of tensile testing. Moreover, the residual alignment in the polymer chains, imparted during extrusion through the printer nozzle, can lead to anisotropic diffusion that opposes the recovery of bulk properties at the interlayer of the prints [Das et al., 2021c], an effect that is exacerbated for the 90° prints. The difference in the tensile properties can be employed to characterize the mechanical isotropy associated with the printed parts. The importance of interlayer bonding on the part performance is evaluated through the degree of anisotropy (D_a) metric, as defined in Equation 8.7.

$$D_a(\%) = \left(1 - \frac{TS_{90}}{TS_0}\right) \times 100\% \tag{8.7}$$

where, TS_{90} and TS_0 represent the maximum tensile strength of parts printed at 90° and 0° raster angles, respectively. Evidently, D_a is controlled by both the polymer architecture and properties as well as the FFF processing conditions; ideally, low values of D_a (<10%) are desired to ensure isotropic properties. Figure 8.3(e) highlights the variation in the values D_a as a function of PP/LCPP blend composition. The anisotropy increases from 8.7% to 23.7% as the LCPP content increases from 2.5wt% to 10wt%. Commonly used FFF polymers such as polylactic acid (PLA) and acrylonitrile-butadiene-styrene (ABS) have D_a values close to

50% [Gao et al., 2021]. Printed parts of semicrystalline polymer such as polyamide, polyether ether ketone (PEEK), and polyethylene are relatively more isotropic with D_a values in the range of 10-20% [Gao et al., 2020]. As discussed in Section 8.3.2, addition of LCPPs reduces the melt viscosity compared to neat PP and hence assists in the development of robust intralayer bonds [Gao et al., 2019] which is detrimental to the interlayer welding during FFF and as such, the reduction in isotropic nature of the parts with elevated LCPP content is observed in the current study.

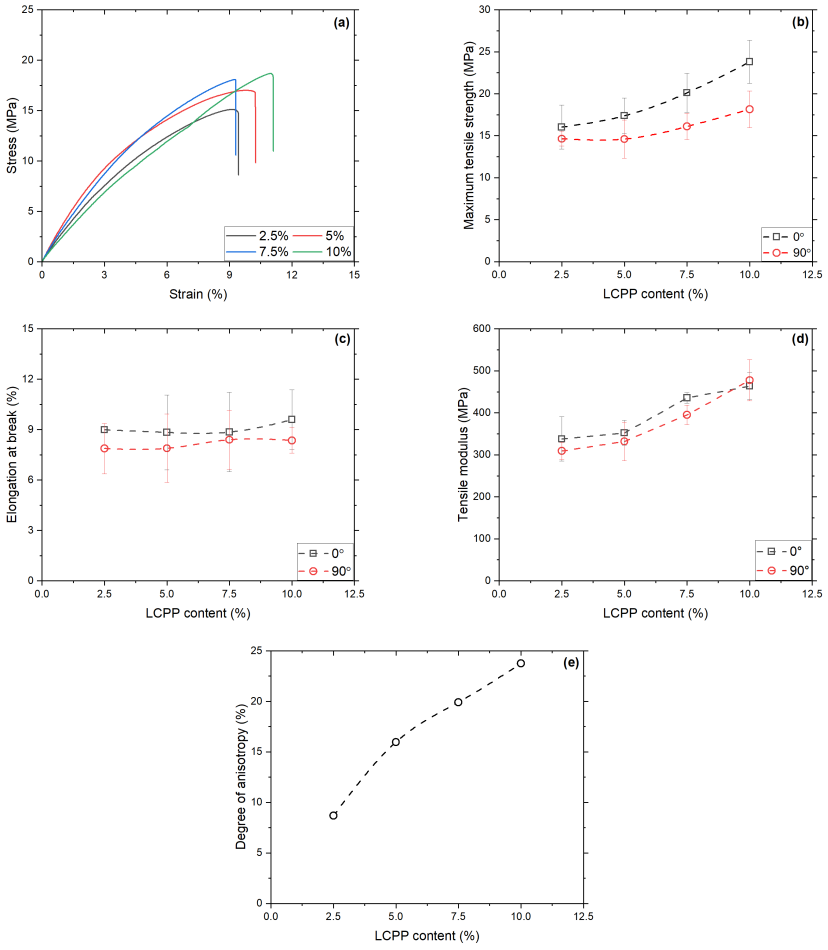


Figure 8.3: (a) Representative stress-strain plots obtained from tensile testing of the printed PP/LCPP (0° raster angle) as a function of blend composition; (b) effect of blend composition on the maximum tensile stress of the printed parts; (c) effect of blend composition on the maximum tensile stress of the printed parts; (d) effect of blend composition on the maximum tensile stress of the printed parts; and (e) variation in the degree of anisotropy, as defined in Equation 8.7, in the printed parts as a function of blend composition.

Table 8.4: Tensile properties of the printed specimens of PP/LCPP blends in comparison to those reported in literature for 3D printed polypropylene based blends and composites.

Sample name	**Maximum tensile strength (MPa)**	**Elongation at break (%)**	**Tensile modulus (MPa)**	**Reference**
PP	8.7	$> 300\%$	220	[Aumnate et al., 2020]
PP	16.5		230	[Milosevic et al., 2017]
PP + alkali treated bamboo fiber	21.8	14.2		[Long et al., 2019]
PP +0.3wt% carbon nanotube	29.4 ± 0.6	4.71 ± 0.14		[Stanciu et al., 2019]
PP	18.0 ± 0.7			[Ai and Vogt, 2022]
Recycled PP	20.1 ± 2	20 ± 2		[Zander et al., 2019a]
PP +10 wt% LCPP	23.8 ± 2.6	9.6 ± 1.8	464 ± 32	This work

8.3.4 Viscoelastic Properties of the Printed Parts

From the results presented in the preceding sections, it is expected that the printed part performance can be affected by the incorporation of LCPP in the blends. The results are also representative of the multilayer prints and are independent of the test geometry dimensions. As highlighted in Sections 8.3.1 and 8.3.2, the broadening of the crystallization window in the blends compared to neat PP coupled with the reduced viscosity of the blends are advantageous to the FFF process since they assist in minimizing the crystallization-induced residual stress buildup in the deposited layers. The reduced viscosity in the blends is also beneficial to interlayer weld formation as the polymer chains have increased mobility. Figure 8.4 highlights the effect of blend composition on the glassy-state storage modulus (at 25°C) along with the storage modulus at an increased temperature (120°C).

At 25°C, the storage modulus value of the 2.5wt% blend was 1.1 GPa which is comparable to that of neat PP with similar degree of crystallinity [Li et al., 2020], indicating the rigidity of

the printed sample. As the LCPP content in the blends increases, the storage modulus values decrease slightly which is due to the increased elasticity of the LCPP polymer. The molecular architecture of the LCPP is such that the polymer chains can easily deform under external force which provides a load transfer mechanism in the blends with increased LCPP content. The storage modulus for all the blend compositions decreases by an order of magnitude when tested at 120°C as compared to the results obtained at 25°C. This has been recently attributed to a combined effect of increased chain mobility and slippage between crystallites [Gunasekaran et al., 2021]. Moreover, the slight decrease in the storage modulus values in the blends with increased LCPP content is likely due to the increased coordinated segmental motion in the amorphous regions of the blends. The results presented in this section suggests that the printed parts exhibit homogeneity and can serve as an alternative to neat PP in functional applications.

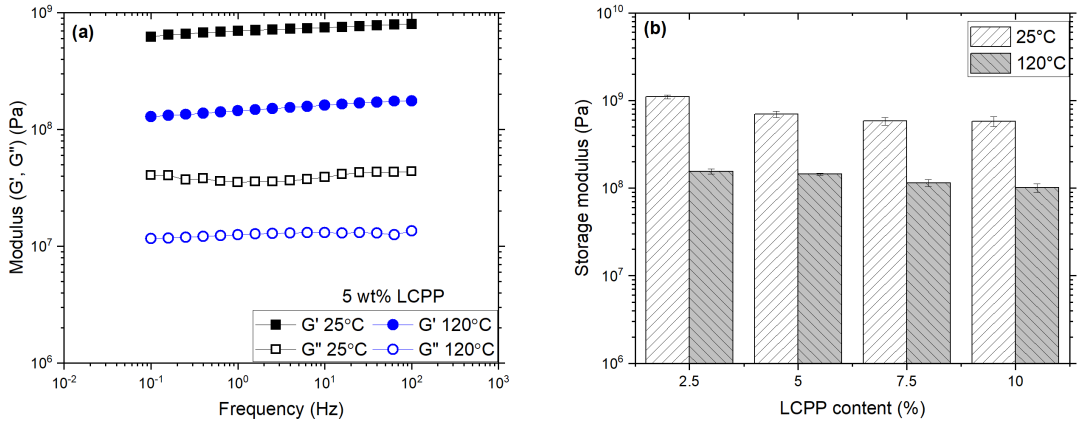


Figure 8.4: (a) Representative plot of storage and loss modulus as a function of frequency performed at 25°C and 120°C for the 5wt% PP/LCPP blend; and (b) variation in storage modulus corresponding to a frequency of 1Hz as a function of LCPP content in the blends at 25°C and 120°C. All the measurements were performed under a linear viscoelastic strain of 0.1%.

8.4 Conclusions

The crystallization and rheological characteristics of semicrystalline polymer feedstocks play a critical role in successful FFF based processing. Significant improvement in PP printing was achieved upon incorporating small amounts of low crystallinity, low modulus PP. The addition of soft LCPP resulted in the polymer chains staying in the mobile state longer and hence assisted with better dissipation of the entrapped residual stresses during FFF. Rheological characterizations highlighted the importance of shear-dependent viscous response to ensure smooth extrusion through the printer nozzle as well as the interfacial chain diffusion once the material is deposited on the printer bed to achieve a part with desirable mechanical properties. Cole-Cole plots highlighted adequate miscibility of the propylene homopolymer in the PP matrix. The printed parts exhibited tensile properties comparable to that reported in literature using similar materials but are inferior to injection molded PP, most likely, due to the defects and voids introduced during the FFF process. Future work will investigate the universality of the proposed approach by printing parts across different size scales. Moreover, addition of a suitable compatibilizer during blending is likely to ensure a more homogenous blend morphology resulting in improved mechanical properties that can rival those obtained using traditional polymer processing techniques. The results presented in this study provides a simplistic approach to enable FFF processing of PP based blends with decent properties while limiting and/or eliminating warpage in the printed parts.

Chapter 9

Conclusions and Scientific Contributions

9.1 Conclusions

The results presented in this dissertation suggest that filament based MatEx is a suitable avenue for manufacturing functional parts from polymers with high levels of crystallinity in a reliable and consistent manner.

- The addition of stiff fibers (specifically, CFs) improve the printing performance of PA6. Using a DOE approach, the tensile properties were optimized with respect to the layer thickness (mm), raster angle (°), and infill pattern. The optimum parameters were evaluated to be 0.2 mm thick, 90° raster, and rectangular pattern. However, the presence of CFs limit the diffusion of polymer chains in the z-direction resulting in mechanical anisotropy in the printeed parts. Further, limited interaction between the CFs and PA6 matrix led to fiber pull-out during tensile testing. The process-structure-property-relationships established using this study must be considered together with the polymer melt rheology and crystallization behavior in order to achieve desirable print properties.
- Semicrystalline blends of PP with low molecular weight hydrocarbon resins exhibit notable improvements in printing performance. The high levels of residual stresses relax over a larger time interval since the addition of resins broaden the crystallization window by affecting the crystallization kinetics. Retention of polymer chain mobility over the aforementioned time window allows for enhanced interfacial chain entanglements across the deposited layers of the printed parts. Although issues associated with part warpage and dimesional accuracy were ameliorated, the tensile properties of the

printed parts were inferior to that of injection molded PP due to the limited compatibility of the resins in the PP matrix. Interestingly, the tensile properties of the prints approached those of injection molded PP when subjected to a mild thermal annealing treatment; a finding that is attributed to the increase in crystallinity post-annealing.

- The melt flow rate of PP and therefore the its molecular weight and viscosity is a major factor in dictating the feasibility of MatEx processing in addition to its crystallization and rheological behavior. All the neat PP prints suffer from warpage and inferior tensile properties due to the high levels of volumetric shrinkage and limited healing of the interlayer welds, respectively. Addition of hydrocarbon resins (upto 20 wt%) improves the flowability as compared to neat PP and assists in smooth extrusion through the printer nozzle. The reduced viscosity of the blends also aids the weld formation between the deposited layers on the print bed. The extent of interdiffusion achieved in the printed parts was quantified through interrupted shear rheology and blends having broader crystallization time window ($T_m - T_c$) were associated with enhanced chain diffusion. The degree of recovery correlates with the increase in tensile strength of the parts suggesting acceptable levels of interfacial fusion. The blends with higher melt flow PP improved dimensional stability in the prints while those with lower melt flow rates exhibited better mechanical properties.

- The crystallization kinetics of PP can also be delayed upon the addition of low-crystalinity propylene based homopolymer. The blends with higher loading levels of the homopolymer experience reduced levels of volumetric shrinkage (and hence residual stress state) when cooling from the melt due to the increased time above T_c. However, the mechanical properties are negatively impacted due to the reduction in the degree of crystallinity compared to neat PP. SAOS measurements indicate enhanced mobility of the polymer chains in presence of the homopolymer resulting in a deformable macrostructure. Further, the blends exhibit a frequency dependent relaxation mechanism as dictated by the polymer stereochemistry. The homopolymer imparts flexibility to the chain structure due to its soft nature resulting in improved interlayer adhesion during printing. The tensile properties of the printed parts improved with addition of the homopolymer due to better load bearing capabilities and exhibited significantly lower values of the degree of anisotropy as compared to commonly used MatEx feedstocks such as, PLA and ABS.

9.2 Scientific Contributions

- Provided a process-structure-property relationship framework to enable reliable processing of semicrystalline polymer feedstocks (blends and composites) via MatEx by coupling detailed crystallization and rheological analysis.
- Demonstrated fiber reinforcements hinder polymer chain mobility and limit interlayer welding during MatEx of filled semicrystalline polymers.
- Highlighted the importance of interfacial adhesion between the fibers and polymer matrix in controlling the mechanical properties of the printed parts.
- Illustrated the impact of subtle variations in the crystallization kinetics of semicrystalline polymers on the residual stress relaxation (by altering the levels of volumetric shrinkage) and interlayer polymer chain diffusion during MatEx.
- Characterized the comprehensive rheological response of the polymer feedstocks relevant to to the different conditions encountered during MatEx (smooth extrusion through the nozzle, shape retention in the stand-off region, and consolidation on the print bed).
- Established the effect of polymer melt flow rate on the dimensional stability and mechanical properties of MatEx processed parts.
- Correlated the extent of polymer chain re-entanglement across the printed layers of semicrystalline polymers with the printed properties.
- Evaluated the feasibility of thermal annealing post-printing step to recover part properties that are comparable to those obtained using traditional manufacturing techniques.
- Examined the importance of miscibility in semicrystalline polymer blends on the mechanical isotropy of MatEx processed parts.

Chapter 10

Future work

The objective of this dissertation is to perform a thorough investigation of semicrytalline polymer feedstocks for application in MatEx-based AM to detail the relevant process-structure-property relationships; thereby developing a fundamental understanding of the associated process physics to achieve a machine agnostic manufacturing framework. Although the results presented in Chapters 5-8 are promising, there remains scope for future research as outlined in the following sections:

10.1 Effect of fiber reinforcements

The interlayer welds formed during MatEx of semicrystalline polymers are largely amorphous due to the high cooling rates (>100°C s^{-1}) while the core of the deposited layer is able to crystallize to an appreciable extent due to the time spent above T_g or T_c [Pu et al., 2021, Shmueli et al., 2019b, Nogales et al., 2019]. The addition of fibers can affect this gradient in crystalline fraction from the core to the sheath of the printed layers. Following on the work described in Chapter 5, further investigation must be performed to evaluate the mechanistic details regarding the interlayer strength evolution during MatEx of semicrystalline polymers reinforced with stiff fibers. Specifically, short carbon fiber reinforced nylon (Onyx) and continuous carbon fiber (CCF) reinforced nylon will be printed using the Mark Two commercial printer from Markforged in two different configurations as illustrated in Figure 10.1. The parts will be printed at constant temperature, print speed, layer height, and fill pattern; as recommended by the manufacturer. In case of the CCF reinforced samples, the alignment of the fibers (0°, 45°, and 90°) with respect to polymer matrix and the number of reinforcement layers (3, 5, and 7) will be varied. The storage modulus under tensile loading (E) of the printed samples will be evaluated using a DMA within the linear visocelastic region at room temperature. The goal of this study will be to predict the E_{perp} and E_{par} to compare with the DMA measurements.

The thermal profile within the print will be simulated using the one-dimensional axisymmetric heat equation with appropriate boundary conditions (Equation 10.1)

$$\frac{\partial T}{\partial t} = \alpha(\varphi)\frac{1}{r}\frac{\partial}{\partial r}\left(r\frac{\partial T}{\partial r}\right) \tag{10.1}$$

where, φ is the volume fraction of carbon fiber in the prints (as determined using TGA) and α is thermal diffusivity (dependent on φ).

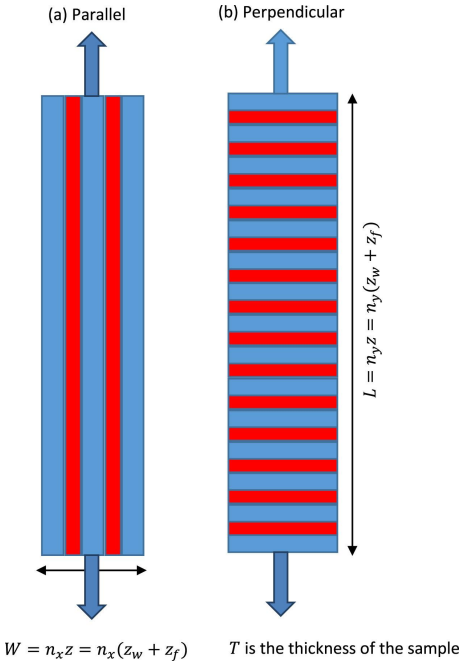


Figure 10.1: Schematic of the (a) parallel and (b) perpendicular printed DMA bars having a length L, width w, and thickness T. The height of each road is given by z and the bars have a total of n_x and n_y roads in the parallel and perpendicular directions, respectively. The red regions indicate the weld between the roads (pure nylon) while the blue regions indicate the CF/nylon roads (image reprinted from Pu et al. [Pu et al., 2021] with permission from Elsevier.

The crystallization of the polymer will be modeled based on the Schneider rate equations, as described below:

$$\dot{\phi}_3 = 8\pi\dot{N}(T), (\phi_3 = 8\pi N) \tag{10.2}$$

$$\dot{\phi}_2 = G(T)\phi_3, (\phi_2 = 8\pi R_{tot}) \tag{10.3}$$

$$\dot{\phi}_1 = G(T)\phi_2, (\phi_1 = S_{tot}) \tag{10.4}$$

$$\dot{\phi}_0 = G(t)\phi_1, (\phi_0 = V_{tot}) \tag{10.5}$$

where, ϕ is the degree of crystallinity of the composite, $\dot{N}(T)$ and $G(T)$ are the nucleation rate and crystal growth rates, respectively adjusted based on the presence of CFs with respect to neat nylon. The storage modulus of the crystalline fraction of the composite ($E_{PA}(\phi)$) will be calculated using the classical Halpin-Kardos theory. Based on previous research assuming continuous and fully aligned fibers in the printed polymer matrix, the final values of E_{perp} and E_{par} are desribed by Equations 10.6 and 10.7 [Pu et al., 2021]

$$\frac{1}{E_{perp}} = \frac{1}{z}\left(\frac{z - z_w}{E_{PA}} + \frac{z_w}{E_w}\right) \tag{10.6}$$

$$E_{\text{par}} = \frac{1}{z}\left[(\varphi E_{CF} + (1-\varphi)E_{PA})\,(z - z_w) + E_w z_w\right] \tag{10.7}$$

where, z and z_w are the height of a single road and height of the weld region, respectively. E_f and E_w are the storage modulii of the road (blue region in Figure 10.1) and the weld region (red region in Figure 10.1), respectively while E_{CF} denotes the storage modulus of CFs.

Supplementary to the above study, detailed crystallization analysis will be performed to calculate crystallization half-times at different isothermal crystallization temperatures, following previously reported protocols [Seo et al., 2019]. Finally, shear and oscillatory rheological characterizations will provide a measure of intrinsic timescales (τ_{rep} and τ_R) of the polymer, that are critical in the evolution of part property during the printing process.

10.2 Effect of crystallinity on interlayer strength

The bulk properties of printed parts are directly controlled by the extent of polymer chain interdiffusion between the layers during the welding process [Das et al., 2021b]. In case of semicrystalline polymers, the presence of crystallites, acting as physical crosslinks, restrict chain motion and can affect the strength of the interlayer welds. The crystalline content in the printed parts is dependent on the printing parameters, specially, print temperature and print speed. Therefore a comprehensive investigation, combining experimental and modeling approaches, of the interlayer strength evolution during printing is of utmost importance.

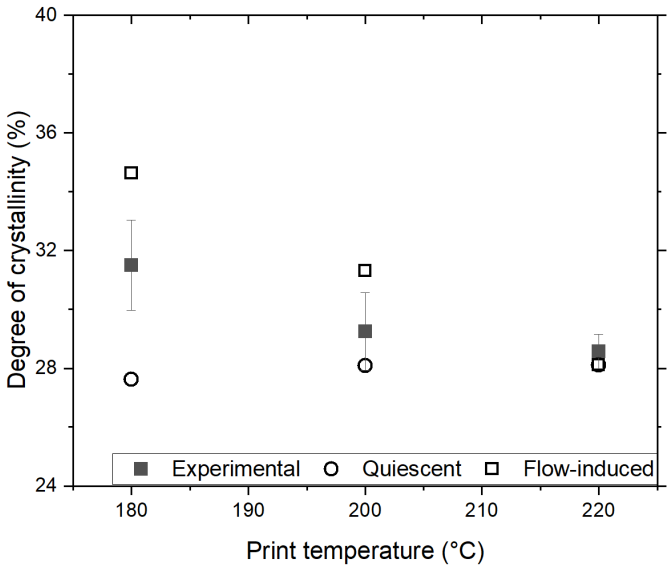


Figure 10.2: Comparison of the degree of crystallinity, as measured by DSC, of the single road width wall PP printed at different print temperatures (180°C, 200°C, and 220°C) and a constant print speed of 10 mm/s with the values predicted from a conventional quiescent and flow induced crystallization model.

Experimentally, single road width walls (SRWWs) of PP were printed at different print temperatures and speeds. The crystallinity of the samples were measured using DSC while the extent of interlayer strength was estimated by measuring the storage modulii (parallel and perpendicular to the tensile loading direction) of the prints using DMA. From the modeling perspective, we use a coupled mutiphysics model accounting for the thermal and crystal-

lization profiles, as outlined in Chapter 4. The model can be tuned to include the effects of both temperature-dependent quiescent nucleation and flow-induced crystallization. The temperature distribution in the SRWW prints were estimated using a two dimensional finite difference heat transfer modeling approach, as outlined by Gilmer et al. [Gilmer et al., 2021]. As highlighted in Figure 10.2, the experimentally measured degree of crystallinity values of PP printed at three different temperatures (and constant speed of 10 mm/s) are in close agreement with that predicted using a coupled constitutive model that considers the flow induced crystallization phenomena.

Preliminary results from the DMA tests are presented in Figure 10.3. The storage modulus of the PP prints tested in the perpendicular direction was lower than that obtained while testing in the parallel direction, likely due to the reduced interlayer weld strength. The storage modulus values trend with the degree of crystallinity values, in accordance with the Halpin Kardos model. Future work will aim to incorporate the mechanical models with the thermo-crystallization model (as described in the previous paragraph).

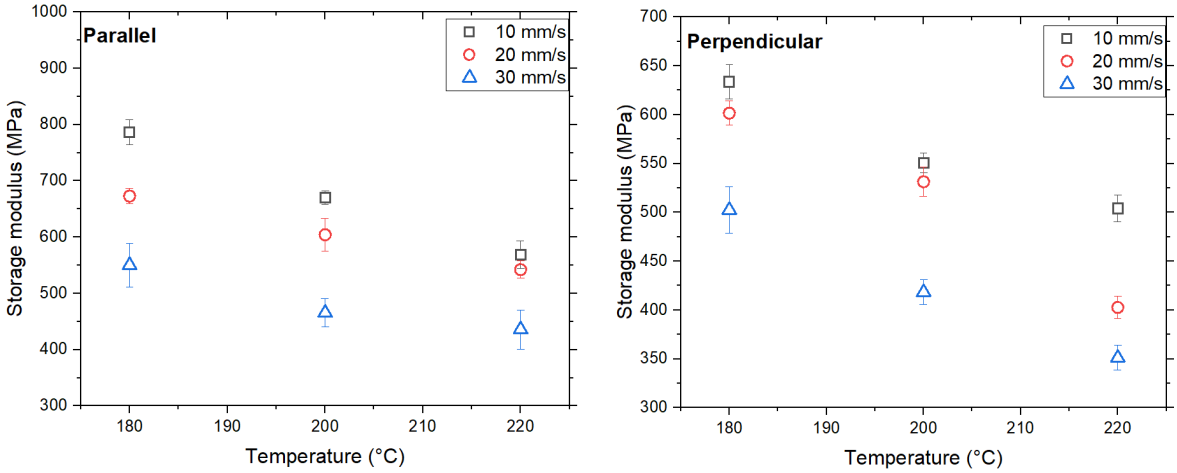


Figure 10.3: Effect of print temperature and print speed on the storage modulii (E') of the SRWW PP prints. The image on the left represents the E' values corresponding to the parallel testing configuration while the image on the right highlights the values for the perpendicular testing configuration.

10.3 Other semicrystalline feedstocks for MatEx

10.3.1 Improving filler matrix adhesion

As discussed in Chapter 5, the tensile fractured prints failed due to fiber pull-out from the matrix arising from the limited adhesion of the fibers with the neat polymer. Since the material used in the study was a commercial one, it was not possible to modify and/or treat the fibers in order to improve fiber adhesion. Therefore, manufacturing MatEx feedstocks in-house employing CFs that are subjected to suitable surface treatments can be an alternative technique to enhance the fiber-matrix interactions.

10.3.2 Tailoring blend composition

The results presented in Chapter 7 suggest that printed parts of the blends of PP with lower melt flow rate exhibit better tensile properties than the blends containing PP with lower molecular weight. On the other hand, the warpage in the printed parts decrease with a increase in melt flow rate (resulting in more mobility in the melt state) of the PP fractions, likely due to the decrease in crystalline content in these blends. Therefore, it will be interesting to study ternary blends of higher melt flow PP with a lower melt flow counterpart in addition to the amorphous hydrocarbon resin. It is hypothesized that the resins will arrest the crystallization kinetics resulting in residual stress dissipation while the two different PP fractions can dictate warpage and mechanical properties, provided the blends do not phase separate.

10.3.3 Enhancing miscibility in blends

As discussed in Chapters 6-8, the addition of low molecular weight hydrocarbon resins or PP-based homopolymers retard the crystallization process of neat PP and significantly aid the printing process by promoting chain mobility above the T_c. However, the properties of the as-printed parts were found to be inferior than injection molded properties of the neat polymer likely due to the limited miscibility of the resins in the PP matrix. Although, thermal annealing of the printed parts at temperatures about 20-40°C lower than the T_m could recover properties close to traditionally processed parts, adding a post-printing step is not

ideal for widespread industrial adoption. Therefore, using compatibilized PP/hydrocarbon resin blends or blending PP with other semicrystalline copolymers having tunable amorphous content (that will ensure enhanced compatibility) is a viable route for achieving printed part properties that are comparable to injection molded grade PP.

In addition to characterizing the rheology of the blends and tensile properties of the prints, hot-stage polarized optical microscopy (Figure 10.4) will be employed to determine the final crystallite size and growth kinetics when cooling from the melt. The goal is to correlate the rheological and morphological findings to print performance. Moreover, the crystallization process, as encountered during MatEx, will be studied using Flash DSC by mimicking the cooling rates observed during printing and can provide valuable insights crucial to understanding the impact of processing variables on the evolution of print properties. Finally, the small angle X-ray scattering (SAXS) will be performed on the printed parts to reveal the effect of MatEx processing on the crystal microstructure development, as a function of location (core vs. shell) on the print.

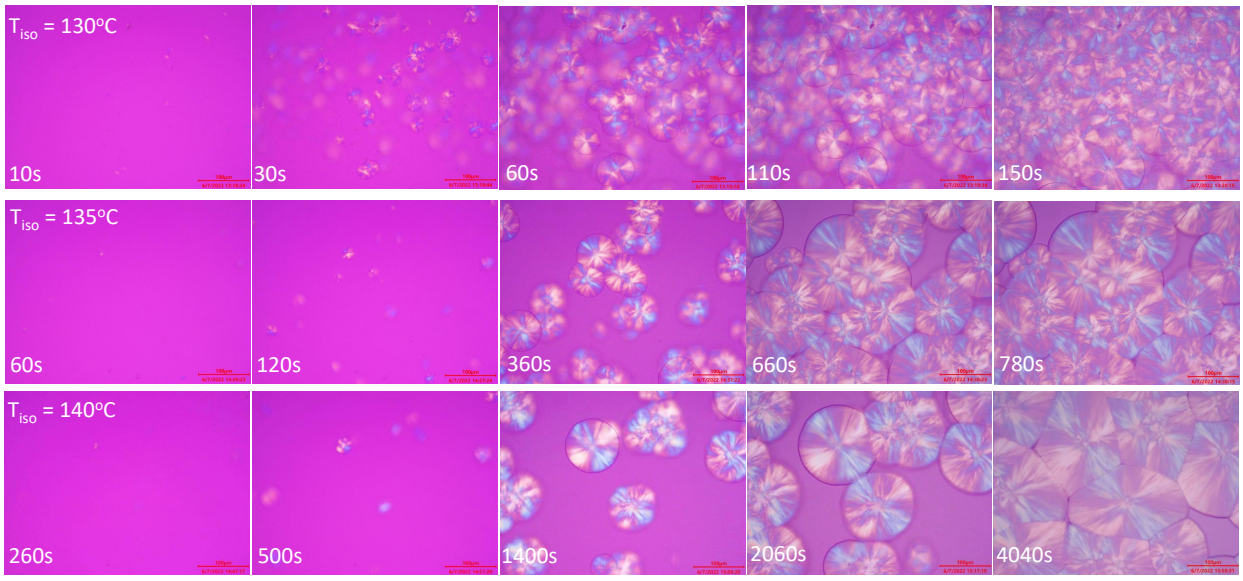


Figure 10.4: Representative hot-stage polarized optical micrographs of isotactic polypropylene during cooling from the melt. Three different isothermal crystallization temperatures (130°C, 135°C, and 140°C) were studied and micrographs were captured at regular time intervals.

Chapter 11

Publications

11.1 Journal publications

1. J.T. Owens, **A. Das**, and M.J. Bortner, "Accelerating heat transfer modeling in material extrusion additive manufacturing: From desktop to big area", **Additive Manufacturing**, 55, 102853, 2022.

2. A.J. Kennedy, M.L. Ballentine, L.R. May, **A. Das**, A.J. Bednar, C.S. Griggs, M.S. Hull, and M.J. Bortner, "Simplifying complex contaminant mixtures: Selective ammonia adsorption and toxicity reduction using 3D printable polymer-zeolite", **Water, Air, & Soil Pollution**, 233, 148, 2022.

3. **A. Das**, G.Y.H. Choong, D.A. Dillard, D.S.A. De Focatiis, and M.J. Bortner, "Characterizing friction for fiber reinforced composites manufacturing: Method development and effect of process parameters", **Composites Part B: Engineering**, 236, 109777, 2022.

4. A.D. McQueen, M.L. Ballentine, L.R. May, C.H. Laber, **A. Das**, M.J. Bortner, and A.J. Kennedy, "Photocatalytic degradation of polycyclic aromatic hydrocarbons (PAHs) in water by 3D printed TiO_2 composites", **ACS ES & T Water**, 2 (1), 137–147, 2022.

5. **A. Das**, M. Etemadi, B.A. Davis, S.H. McKnight, C.B. Williams, S.W. Case, and M.J. Bortner, "Rheological investigation of nylon-carbon fiber composites fabricated using material extrusion based additive manufacturing", **Polymer Composites**, 42 (11), 6010-6024, 2021.

6. **A. Das**, E.L. Gilmer, S. Biria, and M.J. Bortner, "Importance of polymer rheology on material extrusion additive manufacturing: Correlating process physics to print properties", **ACS Applied Polymer Materials**, 3 (3), 1218–1249, 2021.

7. C.A. Chatham, **A. Das**, T.E. Long, M.J. Bortner, and C.B. Williams, "Ageing of PBF-grade poly(phenylene sulfide) powder and its effect on critical printability properties", **Macromolecular Materials and Engineering**, 306 (3), 2000599, 2021.

8. T.W. Seguine, J.J. Fallon, **A. Das**, E.A. Holz, M.R. Bracco, J.E. Yon, E.J. Foster, and M.J. Bortner, "Enabling mechanically adaptive 4D-printing with cellulose nanocrystals", **Green Materials**, 9 (4), 146-156, 2021.

9. A.J. Kennedy, M.L. Ballentine, **A. Das**, C.S. Griggs, K. Klaus, and M.J. Bortner, "Additive manufacturing for contaminants: Ammonia adsorption in 3D printed polymer-zeolite composites", **ACS ES & T Water**, 1 (3), 621–629, 2021.

10. E.G. Joseph, N. Budhavaram, W. DePolo, and **A. Das**, "Nanoribbons fabricated by melt electrospinning", **Polymer Journal**, 53 (3), 493-503, 2021.

11. **A. Das**, C. McIlroy, and M.J. Bortner, "Advances in modeling transport phenomena in material-extrusion additive manufacturing: Coupling momentum, heat, and mass transfer", **Progress in Additive Manufacturing**, 6 (1), 3-17, 2021.

12. **A. Das**, C.A. Chatham, J.J. Fallon, C.E. Zawaski, E.L. Gilmer, C.B. Williams, and M.J. Bortner, "Current understanding and challenges in high temperature additive manufacturing of engineering thermoplastic polymers", **Additive Manufacturing**, 34, 101218, 2020.

13. **A. Das** and M.J. Bortner, "Recent advances in material development and process monitoring in polymer additive manufacturing", **Journal of Advanced Manufacturing and Processing**, 2 (3), e210051, 2020.

14. **A. Das**, A.E.C. Marnot, J.J. Fallon, S.M. Martin, E.G. Joseph, and M.J. Bortner, "Material extrusion based additive manufacturing with blends of polypropylene and hydrocarbon resins", **ACS Applied Polymer Materials**, 2 (2), 911-921, 2020.

15. B.P. Sutliff, **A. Das**, J. Youngblood, and M.J. Bortner, "High shear capillary rheometry of cellulose nanocrystals for industrially relevant processing", **Carbohydrate Polymers**, 231, 115735, 2020.

11.2 Technical report

1. A.J. Kennedy, M.L. Ballentine, A.D. McQueen, C.S. Griggs, **A. Das**, and M.J. Bortner, "Environmental applications of 3D printing polymer composites for dredging operations", **ERDC/TN DOER-C-37**, Vicksburg, MS: U.S. Army Engineer Research and Development Center, 2021.

11.3 Manuscripts under review/in revision

1. **A. Das**, N. Shanmugham, and M.J. Bortner, "Customized blends of polypropylene for extrusion based additive manufacturing", **Journal of Vinyl & Additive Technology**, *In revision*, 2022.

2. **A. Das**, J.S. Bryant, C.B. Williams, and M.J. Bortner, "Melt-based additive manufacturing of polyolefins using material extrusion and powder bed fusion", **Polymer Reviews**, *Under review*, 2022.

11.4 Manuscripts in preparation

1. **A. Das**, E.M. Dartevelle, E.G. Joseph, and M.J. Bortner, "3D printing of semicrystalline polymer blends: Effect of melt flow rate", **Chemical Engineering Journal**, *In preparation*, 2022.

2. A.J. Kennedy, A.D. McQueen, M.L. Ballentine, L.R. May, B.M. Fernando, **A. Das**, C.B. Williams, and M.J. Bortner, "Removal of methylene blue and algal toxin using photocatalytic TiO_2 immobilized in 3D printable polymer", **Chemosphere**, *In preparation*, 2022.

11.5 Refereed conference proceedings

1. **A. Das**, K.J. Chan, D.A. Dillard, D.S.A De Focatiis, and M.J. Bortner, "Effects of sample shape and adhesive type on rheology of unidirectional carbon fiber prepregs", In:

Proceedings of the Annual Technical Conference (ANTEC) of the Society of Plastics Engineers (SPE), Charlotte, North Carolina, June 14-15, 2022.

2. **A. Das** and M.J. Bortner, "Characterization of polypropylene/hydrocarbon resin blends for 3D printing", In: **Proceedings of the Annual Technical Conference (ANTEC) of the Society of Plastics Engineers (SPE)**, Denver, Colorado (The Virtual Edition), May 10-21, 2021.

3. T.W. Seguine, J.J. Fallon, **A. Das**, E.A. Holz, M.R. Bracco, J.E. Yon, E.J. Foster, and M.J. Bortner, "Enabling mechanically adaptive 4D-printing with cellulose nanocrystals", In: **Proceedings of the Annual Technical Conference (ANTEC) of the Society of Plastics Engineers (SPE)**, Denver, Colorado (The Virtual Edition), May 10-21, 2021.

4. B.P. Sutliff, **A. Das**, J. Youngblood, and M.J. Bortner, "Durability of cellulose nanomaterials under industry relevant shear stresses", In: **Proceedings of the 20^{th} Annual Society of Plastics Engineers (SPE) Automotive Composites Conference & Exhibition (ACCE)**, Novi, Michigan (Virtual), September 9-11, 2020.

Bibliography

[noa,] Polymers in Additive Manufacturing | AIChE.

[Abbott et al., 2018] Abbott, A. C., Tandon, G. P., Bradford, R. L., Koerner, H., and Baur, J. W. (2018). Process-structure-property effects on ABS bond strength in fused filament fabrication. *Additive Manufacturing*, 19:29–38.

[Abeykoon et al., 2020] Abeykoon, C., Sri-Amphorn, P., and Fernando, A. (2020). Optimization of fused deposition modeling parameters for improved PLA and ABS 3D printed structures. *International Journal of Lightweight Materials and Manufacture*, 3(3):284–297.

[Agassant et al., 2019] Agassant, J.-F., Pigeonneau, F., Sardo, L., and Vincent, M. (2019). Flow analysis of the polymer spreading during extrusion additive manufacturing. *Additive Manufacturing*, 29:100794.

[Agrawal et al., 1996] Agrawal, G., Wool, R. P., Dozier, W. D., Felcher, G. P., Zhou, J., Pispas, S., Mays, J. W., and Russell, T. P. (1996). Interdiffusion of polymers across interfaces. *Journal of Polymer Science Part B: Polymer Physics*, 34(17):2919–2940. _eprint: https://onlinelibrary.wiley.com/doi/pdf/10.1002/%28SICI%291099-0488%28199612%2934%3A17%3C2919%3A%3AAID-POLB6%3E3.0.CO%3B2-L.

[Agur and Vlachopoulos, 1981] Agur, E. E. and Vlachopoulos, J. (1981). Heat transfer to molten polymer flow in tubes. *Journal of Applied Polymer Science*, 26(3):765–773. _eprint: https://onlinelibrary.wiley.com/doi/pdf/10.1002/app.1981.070260302.

[Ahn et al., 2002] Ahn, S.-H., Montero, M., Odell, D., Roundy, S., and Wright, P. K. (2002). Anisotropic material properties of fused deposition modeling ABS. *Rapid prototyping journal*, 8(4):248–257.

[Aho et al., 2015] Aho, J., Boetker, J. P., Baldursdottir, S., and Rantanen, J. (2015). Rheology as a tool for evaluation of melt processability of innovative dosage forms. *International Journal of Pharmaceutics*, 494(2):623–642.

[Aho et al., 2019] Aho, J., Bøtker, J. P., Genina, N., Edinger, M., Arnfast, L., and Rantanen, J. (2019). Roadmap to 3D-Printed Oral Pharmaceutical Dosage Forms: Feedstock

Filament Properties and Characterization for Fused Deposition Modeling. *Journal of Pharmaceutical Sciences*, 108(1):26–35.

[Ai and Vogt, 2022] Ai, J.-R. and Vogt, B. D. (2022). Size and print path effects on mechanical properties of material extrusion 3D printed plastics. *Progress in Additive Manufacturing*.

[Ajinjeru et al., 2019] Ajinjeru, C., Kishore, V., Chen, X., Hershey, C., Lindahl, J., Kunc, V., Hassen, A. A., and Duty, C. (2019). Rheological survey of carbon fiber-reinforced high-temperature thermoplastics for big area additive manufacturing tooling applications. *Journal of Thermoplastic Composite Materials*, page 0892705719873941. Publisher: SAGE Publications Ltd STM.

[Ajinjeru et al., 2016] Ajinjeru, C., Kishore, V., Chen, X., Lindahl, J., Sudbury, Z., Hassen, A. A., Kunc, V., Post, B., Love, L., and Duty, C. (2016). The influence of rheology on melt processing conditions of amorphous thermoplastics for big area additive manufacturing (BAAM). In *27th Annual International Solid Freeform Fabrication Symposium, Austin, TX*, pages 754–762.

[Ajinjeru et al., 2018a] Ajinjeru, C., Kishore, V., Lindahl, J., Sudbury, Z., Hassen, A. A., Post, B., Love, L., Kunc, V., and Duty, C. (2018a). The influence of dynamic rheological properties on carbon fiber-reinforced polyetherimide for large-scale extrusion-based additive manufacturing. *The International Journal of Advanced Manufacturing Technology*, 99(1):411–418.

[Ajinjeru et al., 2017] Ajinjeru, C., Kishore, V., Liu, P., Hassen, A. A., Lindahl, J. M., Kunc, V., and Duty, C. E. (2017). Rheological evaluation of high temperature polymers to identify successful extrusion parameters. Technical report, Oak Ridge National Lab.(ORNL), Oak Ridge, TN (United States).

[Ajinjeru et al., 2018b] Ajinjeru, C., Kishore, V., Liu, P., Lindahl, J., Hassen, A. A., Kunc, V., Post, B., Love, L., and Duty, C. (2018b). Determination of melt processing conditions for high performance amorphous thermoplastics for large format additive manufacturing. *Additive Manufacturing*, 21:125–132.

[Alanalp et al., 2019] Alanalp, M. B., Durmus, A., and Aydin, I. (2019). Quantifying effect of inorganic filler geometry on the structural, rheological and viscoelastic properties of polypropylene-based thermoplastic elastomers. *Journal of Polymer Research*, 26(2):46.

[Alturkestany et al., 2019] Alturkestany, M. T., Panchal, V., and Thompson, M. R. (2019). Improved part strength for the fused deposition 3D printing technique by chemical modification of polylactic acid. *Polymer Engineering & Science*, 59(s2):E59–E64. _eprint: https://onlinelibrary.wiley.com/doi/pdf/10.1002/pen.24955.

[Ambrosi and Pumera, 2016] Ambrosi, A. and Pumera, M. (2016). 3D-printing technologies for electrochemical applications. *Chemical Society Reviews*, 45(10):2740–2755.

[Amza et al., 2019] Amza, C. G., Zapciu, A., Eyþórsdóttir, A., Björnsdóttir, A., and Borg, J. (2019). Embedding Ultra-High-Molecular-Weight Polyethylene Fibers in 3D-Printed Polylactic Acid (PLA) Parts. *Polymers*, 11(11):1825. Number: 11 Publisher: Multidisciplinary Digital Publishing Institute.

[Anderegg, 2020] Anderegg, D. A. (2020). *In-Situ Monitoring and Simulations of the Non-Isothermal Crystallization of FFF Printed Materials*. Master of Science Thesis, Virginia Tech, Virginia.

[Anderegg et al., 2019] Anderegg, D. A., Bryant, H. A., Ruffin, D. C., Skrip Jr, S. M., Fallon, J. J., Gilmer, E. L., and Bortner, M. J. (2019). In-situ monitoring of polymer flow temperature and pressure in extrusion based additive manufacturing. *Additive Manufacturing*, 26:76–83.

[Anitha et al., 2001] Anitha, R., Arunachalam, S., and Radhakrishnan, P. (2001). Critical parameters influencing the quality of prototypes in fused deposition modelling. *Journal of Materials Processing Technology*, 118(1):385–388.

[Ansari and Ibrahim, 2017] Ansari, M. H. B. M. and Ibrahim, M. H. I. B. (2017). Thermal Characteristic Of Waste-Derived Hydroxyapatite (HA) Reinforced Ultra High Molecular Weight Polyethylene (UHMWPE) Composites For Fused Deposition Modeling (FDM) Process. *IOP Conference Series: Materials Science and Engineering*, 165:012014.

[AtifYardimci et al., 1997] AtifYardimci, M., Hattori, T., Guceri, S. I., and Danforth, S. C. (1997). Thermal analysis of fused deposition. In *1997 International Solid Freeform Fabrication Symposium*.

[Atsani and Mastrisiswadi, 2020] Atsani, S. I. and Mastrisiswadi, H. (2020). Recycled Polypropylene Filament for 3D Printer: Extrusion Process Parameter Optimization. In

IOP Conference Series: Materials Science and Engineering, volume 722, page 012022. IOP Publishing. Issue: 1.

[Aumnate et al., 2019] Aumnate, C., Limpanart, S., Soatthiyanon, N., and Khunton, S. (2019). PP/organoclay nanocomposites for fused filament fabrication (FFF) 3D printing. *eXPRESS Polymer Letters*, 13(10):898–909. Publisher: Budapest University of Technology and Economics, Faculty of Mechanical ….

[Aumnate et al., 2020] Aumnate, C., Potiyaraj, P., Saengow, C., and Giacomin, A. J. (2020). Reinforcing polypropylene with graphene-polylactic acid microcapsules for fused-filament fabrication. *Materials & Design*, page 109329.

[Awaja and Zhang, 2015] Awaja, F. and Zhang, S. (2015). Self-bonding of PEEK for active medical implants applications. *Journal of Adhesion Science and Technology*, 29(15):1593–1606.

[Azizi and Faghihi, 2009] Azizi, H. and Faghihi, J. (2009). An investigation on the mechanical and dynamic rheological properties of single and hybrid filler/polypropylene composites based on talc and calcium carbonate. *Polymer Composites*, 30(12):1743–1748. _eprint: https://onlinelibrary.wiley.com/doi/pdf/10.1002/pc.20685.

[Bachhar et al., 2020] Bachhar, N., Gudadhe, A., Kumar, A., Andrade, P., and Kumaraswamy, G. (2020). 3D printing of semicrystalline polypropylene: towards eliminating warpage of printed objects. *Bulletin of Materials Science*, 43(1):1–8. Company: Springer Distributor: Springer Institution: Springer Label: Springer Number: 1 Publisher: Indian Academy of Sciences.

[Bagheri and Julkapli, 2016] Bagheri, S. and Julkapli, N. M. (2016). Effect of hybridization on the value-added activated carbon materials. *International Journal of Industrial Chemistry*, 7(3):249–264.

[Bagheriasl et al., 2015] Bagheriasl, D., Carreau, P. J., Dubois, C., and Riedl, B. (2015). Properties of polypropylene and polypropylene/poly(ethylene-co-vinyl alcohol) blend/CNC nanocomposites. *Composites Science and Technology*, 117:357–363.

[Bakrani Balani et al., 2019] Bakrani Balani, S., Chabert, F., Nassiet, V., and Cantarel, A. (2019). Influence of printing parameters on the stability of deposited beads in fused filament fabrication of poly(lactic) acid. *Additive Manufacturing*, 25:112–121.

[Baldi et al., 2014] Baldi, F., Briatico-Vangosa, F., and Franceschini, A. (2014). Experimental study of the melt fracture behavior of filled high-density polyethylene melts. *Polymer Engineering & Science*, 54(2):364–377. _eprint: https://onlinelibrary.wiley.com/doi/pdf/10.1002/pen.23580.

[Banerjee et al., 2019] Banerjee, S. S., Burbine, S., Kodihalli Shivaprakash, N., and Mead, J. (2019). 3D-Printable PP/SEBS Thermoplastic Elastomeric Blends: Preparation and Properties. *Polymers*, 11(2):347.

[Barczewski et al., 2020] Barczewski, M., Barczewski, R., and Chwalczuk, T. (2020). The in-line detection method of sharkskin melt flow instability during polyethylene extrusion based on pressure analysis. *Journal of Manufacturing Processes*, 59:153–166.

[Beer and Johnston, 1992] Beer, F. P. and Johnston, E. R. (1992). *Mechanics of Materials*. McGraw Hill, New York, 2nd edition.

[Beesetty et al., 2020] Beesetty, P., kale, A., Patil, B., and Doddamani, M. (2020). Mechanical behavior of additively manufactured nanoclay/HDPE nanocomposites. *Composite Structures*, 247:112442.

[Behdani et al., 2019] Behdani, B., Mason, L., Leu, M., and Park, J. (2019). Computational Fluid Dynamics Simulation of the Fused Deposition Modeling Process: Effect of Temperature-Dependent Viscosity on the Shape of Extruded Strand. Orlando, Florida. American Institute of Chemical Engineers (AIChE).

[Behdani et al., 2020] Behdani, B., Senter, M., Mason, L., Leu, M., and Park, J. (2020). Numerical Study on the Temperature-Dependent Viscosity Effect on the Strand Shape in Extrusion-Based Additive Manufacturing. *Journal of Manufacturing and Materials Processing*, 4(2):46. Number: 2 Publisher: Multidisciplinary Digital Publishing Institute.

[Bellehumeur et al., 2004] Bellehumeur, C., Li, L., Sun, Q., and Gu, P. (2004). Modeling of bond formation between polymer filaments in the fused deposition modeling process. *Journal of Manufacturing Processes*, 6(2):170–178.

[Bellini et al., 2004] Bellini, A., Guceri, S., and Bertoldi, M. (2004). Liquefier dynamics in fused deposition. *Journal of Manufacturing Science and Engineering*, 126(2):237–246.

[Beloshenko et al., 2019] Beloshenko, V. A., Plavan, V. P., Rezanova, N. M., Savchenko, B. M., and Vozniak, I. (2019). Production of high-performance multi-layer fine-fibrous

filter material by application of material extrusion–based additive manufacturing. *The International Journal of Advanced Manufacturing Technology*, 101(9):2681–2688.

[Berger, 1990] Berger, L. L. (1990). On the mechanism of craze fibril breakdown in glassy polymers. *Macromolecules*, 23(11):2926–2934. Publisher: American Chemical Society.

[Bertolino et al., 2021] Bertolino, M., Battegazzore, D., Arrigo, R., and Frache, A. (2021). Designing 3D printable polypropylene: Material and process optimisation through rheology. *Additive Manufacturing*, 40:101944.

[Bhalodi et al., 2019] Bhalodi, D., Zalavadiya, K., and Gurrala, P. K. (2019). Influence of temperature on polymer parts manufactured by fused deposition modeling process. *Journal of the Brazilian Society of Mechanical Sciences and Engineering*, 41(3):113.

[Bhandari et al., 2019] Bhandari, S., Lopez-Anido, R. A., and Gardner, D. J. (2019). Enhancing the interlayer tensile strength of 3D printed short carbon fiber reinforced PETG and PLA composites via annealing. *Additive Manufacturing*, 30:100922.

[Bharath et al., 2020a] Bharath, H., Bonthu, D., Prabhakar, P., and Doddamani, M. (2020a). Three-Dimensional Printed Lightweight Composite Foams. *ACS Omega*, 5(35):22536–22550. Publisher: American Chemical Society.

[Bharath et al., 2020b] Bharath, H. S., Bonthu, D., Gururaja, S., Prabhakar, P., and Doddamani, M. (2020b). Flexural response of concurrently 3D printed sandwich composite. *arXiv:2007.11669 [physics]*. arXiv: 2007.11669.

[Bhattacharjee et al., 2002] Bhattacharjee, P. K., Oberhauser, J. P., McKinley, G. H., Leal, L. G., and Sridhar, T. (2002). Extensional Rheometry of Entangled Solutions. *Macromolecules*, 35(27):10131–10148. Publisher: American Chemical Society.

[Bird, 2002] Bird, R. B. (2002). Transport phenomena. *Applied Mechanics Reviews*, 55(1):R1–R4. Publisher: American Society of Mechanical Engineers Digital Collection.

[Bird et al., 1987] Bird, R. B., Armstrong, R. C., and Hassager, O. (1987). *Dynamics of polymeric liquids*, volume Volume 1. John Wiley and Sons Inc, New York, 2nd edition edition.

[Blok et al., 2018] Blok, L. G., Longana, M. L., Yu, H., and Woods, B. K. S. (2018). An investigation into 3D printing of fibre reinforced thermoplastic composites. *Additive Manufacturing*, 22:176–186.

[Bonten and Schmachtenberg, 2001] Bonten, C. and Schmachtenberg, E. (2001). A new hypothesis to describe the mechanisms acting in a welded joint of semicrystalline thermoplastics. *Polymer Engineering & Science*, 41(3):475–483.

[Bortner et al., 2004] Bortner, M. J., Bhanu, V. A., McGrath, J. E., and Baird, D. G. (2004). Absorption of CO2 in high acrylonitrile content copolymers: dependence on acrylonitrile content. *Polymer*, 45(10):3413–3422. Publisher: Elsevier.

[Boudara et al., 2018] Boudara, V. A. H., Peterson, J. D., Leal, L. G., and Read, D. J. (2018). Nonlinear rheology of polydisperse blends of entangled linear polymers: Rolie-Double-Poly models. *Journal of Rheology*, 63(1):71–91.

[Bourell et al., 2017] Bourell, D., Kruth, J. P., Leu, M., Levy, G., Rosen, D., Beese, A. M., and Clare, A. (2017). Materials for additive manufacturing. *CIRP Annals*, 66(2):659–681.

[Bousmina et al., 1998] Bousmina, M., Qiu, H., Grmela, M., and Klemberg-Sapieha, J. E. (1998). Diffusion at Polymer/Polymer Interfaces Probed by Rheological Tools. *Macromolecules*, 31(23):8273–8280. Publisher: American Chemical Society.

[Brenken et al., 2018] Brenken, B., Barocio, E., Favaloro, A., Kunc, V., and Pipes, R. B. (2018). Fused filament fabrication of fiber-reinforced polymers: A review. *Additive Manufacturing*, 21:1–16.

[Brenken et al., 2019] Brenken, B., Barocio, E., Favaloro, A., Kunc, V., and Pipes, R. B. (2019). Development and validation of extrusion deposition additive manufacturing process simulations. *Additive Manufacturing*, 25:218–226.

[Brites et al., 2019] Brites, F., Malça, C., Gaspar, F., Horta, J. F., Franco, M. C., Biscaia, S., and Mateus, A. (2019). The Use of Polypropylene and High-Density Polyethylene on Cork Plastic Composites for Large Scale 3D Printing. *Applied Mechanics and Materials*, 890:205–225.

[Bréchet et al., 2001] Bréchet, Y., Cavaillé, J.-Y., Chabert, E., Chazeau, L., Dendievel, R., Flandin, L., and Gauthier, C. (2001). Polymer Based Nanocomposites: Effect of Filler-Filler and Filler-Matrix Interactions. *Advanced Engineering Materials*, 3(8):571–577. _eprint: https://onlinelibrary.wiley.com/doi/pdf/10.1002/1527-2648%28200108%293%3A8%3C571%3A%3AAID-ADEM571%3E3.0.CO%3B2-M.

[Calafel et al., 2020] Calafel, I., Aguirresarobe, R. H., Peñas, M. I., Santamaria, A., Tierno, M., Conde, J. I., and Pascual, B. (2020). Searching for Rheological Conditions for FFF 3D Printing with PVC Based Flexible Compounds. *Materials*, 13(1):178. Number: 1 Publisher: Multidisciplinary Digital Publishing Institute.

[Camposeo et al., 2019] Camposeo, A., Persano, L., Farsari, M., and Pisignano, D. (2019). Additive Manufacturing: Applications and Directions in Photonics and Optoelectronics. *Advanced Optical Materials*, 7(1):1800419. _eprint: https://onlinelibrary.wiley.com/doi/pdf/10.1002/adom.201800419.

[Candal et al., 2020] Candal, M. V., Calafel, I., Aranburu, N., Fernández, M., Gerrica-Echevarria, G., Santamaría, A., and Müller, A. J. (2020). Thermo-rheological effects on successful 3D printing of biodegradable polyesters. *Additive Manufacturing*, page 101408.

[Caponetti et al., 1996] Caponetti, E., Martino, D. C., Cimmino, S., Floriano, M. A., Martuscelli, E., Silvestre, C., and Triolo, R. (1996). Small angle scattering study of the structure of isotactic polypropylene-hydrogenated oligo(cyclopentadiene) blends. *Journal of Molecular Structure*, 383(1):75–79.

[Carneiro et al., 2015] Carneiro, O. S., Silva, A. F., and Gomes, R. (2015). Fused deposition modeling with polypropylene. *Materials & Design*, 83:768–776.

[Carpinteri et al., 1986] Carpinteri, A., Marega, C., and Savadori, A. (1986). Size effects and ductile-brittle transition of polypropylene. *Journal of Materials Science*, 21(12):4173–4178.

[Carvalho et al., 1994] Carvalho, M. S., Padmanabhan, M., and Macosko, C. W. (1994). Single-point correction for parallel disks rheometry. *Journal of Rheology*, 38(6):1925–1936.

[Chacón et al., 2019] Chacón, J. M., Caminero, M. A., Núñez, P. J., García-Plaza, E., García-Moreno, I., and Reverte, J. M. (2019). Additive manufacturing of continuous fibre reinforced thermoplastic composites using fused deposition modelling: Effect of process parameters on mechanical properties. *Composites Science and Technology*, 181:107688.

[Chaka et al., 2017] Chaka, K. T., Fambri, L., and Govindan, N. (2017). Kaolinite/Polypropylene Nanocomposites. Part 3: 3D Printing. *International Research Journal of Engineering and Technology*, 4(11).

[Charlon et al., 2021] Charlon, S., Le Boterff, J., and Soulestin, J. (2021). Fused filament fabrication of polypropylene: Influence of the bead temperature on adhesion and porosity. *Additive Manufacturing*, 38:101838.

[Chatham et al., 2021] Chatham, C. A., Das, A., Long, T. E., Bortner, M. J., and Williams, C. B. (2021). Ageing of PBF-Grade Poly(Phenylene Sulfide) Powder and its Effect on Critical Printability Properties. *Macromolecular Materials and Engineering*, 306(3):2000599. _eprint: https://onlinelibrary.wiley.com/doi/pdf/10.1002/mame.202000599.

[Chatham et al., 2019a] Chatham, C. A., Long, T. E., and Williams, C. B. (2019a). A Review of the Process Physics and Material Screening Methods for Polymer Powder Bed Fusion Additive Manufacturing. *Progress in Polymer Science*.

[Chatham et al., 2019b] Chatham, C. A., Zawaski, C. E., Bobbitt, D. C., Moore, R. B., Long, T. E., and Williams, C. B. (2019b). Semi-Crystalline Polymer Blends for Material Extrusion Additive Manufacturing Printability: A Case Study with Poly(ethylene terephthalate) and Polypropylene. *Macromolecular Materials and Engineering*, 304(5):1800764.

[Chaudhry et al., 2020] Chaudhry, A. U., Mabrouk, A., and Abdala, A. (2020). Thermally enhanced pristine polyolefins: fundamentals, progress and prospective. *Journal of Materials Research and Technology*, 9(5):10796–10806.

[Chaunier et al., 2018] Chaunier, L., Guessasma, S., Belhabib, S., Della Valle, G., Lourdin, D., and Leroy, E. (2018). Material extrusion of plant biopolymers: Opportunities & challenges for 3D printing. *Additive Manufacturing*, 21:220–233.

[Chen et al., 2005] Chen, J.-H., Tsai, F.-C., Nien, Y.-H., and Yeh, P.-H. (2005). Isothermal crystallization of isotactic polypropylene blended with low molecular weight atactic polypropylene. Part I. Thermal properties and morphology development. *Polymer*, 46(15):5680–5688.

[Chesser et al., 2019] Chesser, P., Post, B., Roschli, A., Carnal, C., Lind, R., Borish, M., and Love, L. (2019). Extrusion control for high quality printing on Big Area Additive Manufacturing (BAAM) systems. *Additive Manufacturing*, 28:445–455.

[Chirayil et al., 2016] Chirayil, C. J., Joy, J., Maria, H. J., Krupa, I., and Thomas, S. (2016). Polyolefins in Automotive Industry. In Al-Ali AlMa'adeed, M. and Krupa, I., editors, *Polyolefin Compounds and Materials: Fundamentals and Industrial Applications*, Springer

Series on Polymer and Composite Materials, pages 265–283. Springer International Publishing, Cham.

[Choe et al., 2022] Choe, S., Kim, Y., Park, G., Lee, D. H., Park, J., Mossisa, A. T., Lee, S., and Myung, J. (2022). Biodegradation of 3D-Printed Biodegradable/Non-biodegradable Plastic Blends. *ACS Applied Polymer Materials*, 4(7):5077–5090. Publisher: American Chemical Society.

[Choi et al., 2015] Choi, J., Kwon, O.-C., Jo, W., Lee, H. J., and Moon, M.-W. (2015). 4D Printing Technology: A Review. *3D Printing and Additive Manufacturing*, 2(4):159–167.

[Chong et al., 2017] Chong, S., Pan, G.-T., Khalid, M., Yang, T. C.-K., Hung, S.-T., and Huang, C.-M. (2017). Physical Characterization and Pre-assessment of Recycled High-Density Polyethylene as 3D Printing Material. *Journal of Polymers and the Environment*, 25(2):136–145.

[Chong et al., 2020] Chong, S., Yang, T. C.-K., Lee, K.-C., Chen, Y.-F., Juan, J. C., Tiong, T. J., Huang, C.-M., and Pan, G.-T. (2020). Evaluation of the physico-mechanical properties of activated-carbon enhanced recycled polyethylene/polypropylene 3D printing filament. *Sādhanā*, 45(1):57.

[Chortos et al., 2020] Chortos, A., Hajiesmaili, E., Morales, J., Clarke, D. R., and Lewis, J. A. (2020). 3D Printing of Interdigitated Dielectric Elastomer Actuators. *Advanced Functional Materials*, 30(1):1907375.

[Cicala et al., 2018] Cicala, G., Giordano, D., Tosto, C., Filippone, G., Recca, A., and Blanco, I. (2018). Polylactide (PLA) Filaments a Biobased Solution for Additive Manufacturing: Correlating Rheology and Thermomechanical Properties with Printing Quality. *Materials*, 11(7):1191. Number: 7 Publisher: Multidisciplinary Digital Publishing Institute.

[Cimmino et al., 1999] Cimmino, S., D'alma, E., Lorenzo, M. L. D., Pace, E. D., and Silvestre, C. (1999). Blends of isotactic polypropylene and natural terpene resins. I. Phase structure, thermal, and dynamic-mechanical properties. *Journal of Polymer Science Part B: Polymer Physics*, 37(9):867–878.

[Cimmino et al., 1993] Cimmino, S., Di Pace, E., Karasz, F. E., Martuscelli, E., and Silvestre, C. (1993). Isotactic polypropylene/hydrogenated oligo(cyclopentadiene) blends:

phase diagram and dynamic-mechanical behaviour of extruded isotropic films. *Polymer*, 34(5):972–976.

[Cimmino et al., 1991] Cimmino, S., Guarrata, P., Martuscelli, E., Silvestre, C., and Buzio, P. P. (1991). Morphology, phase structure and thermal behaviour of films of isotactic polypropylene/hydrogenated oligocyclopentadiene blends: 1. Extruded isotropic films. *Polymer*, 32(18):3299–3304.

[Cimmino et al., 2004] Cimmino, S., Silvestre, C., and Vecchia, G. d. (2004). Morphology and properties of isotactic polypropylene modified with hydrocarbon resin MBG273. I. Binary blends. *Journal of Applied Polymer Science*, 92(6):3454–3465.

[Coasey et al., 2020] Coasey, K., Hart, K. R., Wetzel, E., Edwards, D., and Mackay, M. E. (2020). Nonisothermal Welding in Fused Filament Fabrication. *Additive Manufacturing*, page 101140.

[Codou et al., 2018] Codou, A., Anstey, A., Misra, M., and K. Mohanty, A. (2018). Novel compatibilized nylon-based ternary blends with polypropylene and poly(lactic acid): morphology evolution and rheological behaviour. *RSC Advances*, 8(28):15709–15724. Publisher: Royal Society of Chemistry.

[Cole et al., 2016] Cole, D. P., Riddick, J. C., Jaim, H. M. I., Strawhecker, K. E., and Zander, N. E. (2016). Interfacial mechanical behavior of 3D printed ABS. *Journal of Applied Polymer Science*, 133(30). _eprint: https://onlinelibrary.wiley.com/doi/pdf/10.1002/app.43671.

[Colón Quintana et al., 2020] Colón Quintana, J. L., Hiemer, S., Granda Duarte, N., and Osswald, T. (2020). Implementation of shear thinning behavior in the fused filament fabrication melting model: Analytical solution and experimental validation. *Additive Manufacturing*, page 101687.

[Comminal et al., 2018a] Comminal, R., Serdeczny, M. P., Pedersen, D. B., and Spangenberg, J. (2018a). Numerical modeling of the strand deposition flow in extrusion-based additive manufacturing. *Additive Manufacturing*, 20:68–76.

[Comminal et al., 2018b] Comminal, R., Serdeczny, M. P., Pedersen, D. B., and Spangenberg, J. (2018b). Numerical simulation of extrusion-based additive manufacturing - Effect of the nozzle geometry on the strand cross-section. In Billington, D., Leach, R. K., Phillips,

D., Riemer, O., and Savio, E., editors, *Proceedings of the 18th International Conference of the european Society for Precision Engineering and Nanotechnology*, pages 285–286, Venice, Italy. The European Society for Precision Engineering and Nanotechnology.

[Comminal et al., 2017] Comminal, R. B., Hattel, J. H., and Spangenberg, J. (2017). Numerical simulations of planar extrusion and fused filament fabrication of non-Newtonian fluids. *Nordic Rheology Society Annual Transactions*, 25:263–270. Publisher: Nordic Rheology Society; 1997.

[Compton and Lewis, 2014] Compton, B. G. and Lewis, J. A. (2014). 3D-Printing of Lightweight Cellular Composites. *Advanced Materials*, 26(34):5930–5935.

[Compton et al., 2017] Compton, B. G., Post, B. K., Duty, C. E., Love, L., and Kunc, V. (2017). Thermal analysis of additive manufacturing of large-scale thermoplastic polymer composites. *Additive Manufacturing*, 17:77–86.

[Coogan and Kazmer, 2017a] Coogan, T. J. and Kazmer, D. O. (2017a). Bond and part strength in fused deposition modeling. *Rapid Prototyping Journal*, 23:414–422.

[Coogan and Kazmer, 2017b] Coogan, T. J. and Kazmer, D. O. (2017b). Healing simulation for bond strength prediction of FDM. *Rapid Prototyping Journal*, 23(3):551–561. Publisher: Emerald Publishing Limited.

[Coogan and Kazmer, 2019] Coogan, T. J. and Kazmer, D. O. (2019). In-line rheological monitoring of fused deposition modeling. *Journal of Rheology*, 63(1):141–155.

[Coogan and Kazmer, 2020] Coogan, T. J. and Kazmer, D. O. (2020). Prediction of interlayer strength in material extrusion additive manufacturing. *Additive Manufacturing*, 35:101368.

[Coombs et al., 2020] Coombs, S. J., Kanso, M. A., and Giacomin, A. J. (2020). Cole–Cole relation for long-chain branching from general rigid bead–rod theory. *Physics of Fluids*, 32(9):093106. Publisher: American Institute of Physics.

[Costa et al., 2015] Costa, S. F., Duarte, F. M., and Covas, J. A. (2015). Thermal conditions affecting heat transfer in FDM/FFE: a contribution towards the numerical modelling of the process: This paper investigates convection, conduction and radiation phenomena in the filament deposition process. *Virtual and Physical Prototyping*, 10(1):35–46.

[Costa et al., 2017] Costa, S. F., Duarte, F. M., and Covas, J. A. (2017). Estimation of filament temperature and adhesion development in fused deposition techniques. *Journal of Materials Processing Technology*, 245:167–179.

[Costakis et al., 2016] Costakis, W. J., Rueschhoff, L. M., Diaz-Cano, A. I., Youngblood, J. P., and Trice, R. W. (2016). Additive manufacturing of boron carbide via continuous filament direct ink writing of aqueous ceramic suspensions. *Journal of the European Ceramic Society*, 36(14):3249–3256.

[Costanzo et al., 2020] Costanzo, A., Spotorno, R., Candal, M. V., Fernández, M. M., Müller, A. J., Graham, R., Cavallo, D., and McIlroy, C. (2020). Residual alignment and its effect on weld strength in material-extrusion 3D-printing of polylactic acid. *Additive Manufacturing*, page 101415.

[Cox and Merz, 1959] Cox, W. and Merz, E. (1959). Rheology of Polymer Melts—A Correlation of Dynamic and Steady Flow Measurements. In *International Symposium on Plastics Testing and Standardization*, pages 178–188, West Conshohocken, PA. ASTM International. Publisher: ASTM International.

[Cox and Merz, 1958] Cox, W. P. and Merz, E. H. (1958). Correlation of dynamic and steady flow viscosities. *Journal of Polymer Science*, 28(118):619–622. _eprint: https://onlinelibrary.wiley.com/doi/pdf/10.1002/pol.1958.1202811812.

[Coxon and White, 1980] Coxon, L. D. and White, J. R. (1980). Residual stresses and aging in injection molded polypropylene. *Polymer Engineering & Science*, 20(3):230–236.

[Das et al., 2020a] Das, A., Chatham, C. A., Fallon, J. J., Zawaski, C. E., Gilmer, E. L., Williams, C. B., and Bortner, M. J. (2020a). Current understanding and challenges in high temperature additive manufacturing of engineering thermoplastic polymers. *Additive Manufacturing*, 34:101218.

[Das et al., 2019] Das, A., Dartevelle, E. M., Joseph, E. G., and Bortner, M. J. (2019). Effect of Polypropylene Melt Flow Index on the Material Extrusion Based Additive Manufacturing of Polypropylene/Hydrogenated Resin Blends. Orlando, Florida. American Institute of Chemical Engineers (AIChE).

[Das et al., 2021a] Das, A., Etemadi, M., Davis, B. A., McKnight, S. H., Williams, C. B., Case, S. W., and Bortner, M. J. (2021a). Rheological investiga-

tion of nylon-carbon fiber composites fabricated using material extrusion-based additive manufacturing. *Polymer Composites*, 42(11):6010–6024. _eprint: https://onlinelibrary.wiley.com/doi/pdf/10.1002/pc.26281.

[Das et al., 2021b] Das, A., Gilmer, E. L., Biria, S., and Bortner, M. J. (2021b). Importance of Polymer Rheology on Material Extrusion Additive Manufacturing: Correlating Process Physics to Print Properties. *ACS Applied Polymer Materials*, 3(3):1218–1249. Publisher: American Chemical Society.

[Das et al., 2020b] Das, A., Marnot, A. E. C., Fallon, J. J., Martin, S. M., Joseph, E. G., and Bortner, M. J. (2020b). Material Extrusion-Based Additive Manufacturing with Blends of Polypropylene and Hydrocarbon Resins. *ACS Applied Polymer Materials*, 2(2):911–921.

[Das et al., 2021c] Das, A., McIlroy, C., and Bortner, M. J. (2021c). Advances in modeling transport phenomena in material-extrusion additive manufacturing: Coupling momentum, heat, and mass transfer. *Progress in Additive Manufacturing*, 6(1):3–17.

[Daver et al., 2016] Daver, F., Baez, E., Shanks, R. A., and Brandt, M. (2016). Conductive polyolefin–rubber nanocomposites with carbon nanotubes. *Composites Part A: Applied Science and Manufacturing*, 80:13–20.

[Davis et al., 2017] Davis, C. S., Hillgartner, K. E., Han, S. H., and Seppala, J. E. (2017). Mechanical strength of welding zones produced by polymer extrusion additive manufacturing. *Additive Manufacturing*, 16:162–166.

[Dayam et al., 2020] Dayam, S., Priyadarshi, S., and Tandon, P. (2020). Simulation of Extrusion of Thermoplastic Binder in Additive Manufacturing Process. In Shunmugam, M. S. and Kanthababu, M., editors, *Advances in Additive Manufacturing and Joining*, Lecture Notes on Multidisciplinary Industrial Engineering, pages 319–328, Singapore. Springer.

[de Ciurana et al., 2013] de Ciurana, J., Serenóa, L., and Vallès, . (2013). Selecting Process Parameters in RepRap Additive Manufacturing System for PLA Scaffolds Manufacture. *Procedia CIRP*, 5:152–157.

[de Gennes, 1971] de Gennes, P. G. (1971). Reptation of a Polymer Chain in the Presence of Fixed Obstacles. *The Journal of Chemical Physics*, 55(2):572–579. Publisher: American Institute of Physics.

[Dealy and Plazek, 2009] Dealy, J. and Plazek, D. (2009). Time-Temperature Superposition—A Users Guide. *Rheology Bulletin*, 78(2):16–31.

[Decker and Yee, 2017] Decker, N. and Yee, A. (2017). Assessing the use of binary blends of acrylonitrile butadiene styrene and post-consumer high density polyethylene in fused filament fabrication. *International Journal of Additive and Subtractive Materials Manufacturing*, 1(2):161–171. Publisher: Inderscience Publishers.

[Deckers et al., 2014] Deckers, J., Vleugels, J., and Kruth, J.-P. (2014). Additive manufacturing of ceramics: A review. *Journal of Ceramic Science and Technology*, 5(4):245–260. Publisher: Goeller Verlag GmbH.

[Deng et al., 2012] Deng, D., Chen, Y., and Zhou, C. (2012). Investigation on PEEK fabrication using Mask-image-projection-based Stereolithography. In *Annual Solid Free Form Fabrication Symposium*, pages 606–616.

[Denn, 2008] Denn, M. M. (2008). *Polymer Melt Processing: Foundations in Fluid Mechanics and Heat Transfer*. Cambridge University Press. Google-Books-ID: 883LCgAAQBAJ.

[Deshpande et al., 2019] Deshpande, A., Ravi, A., Kusel, S., Churchwell, R., and Hsu, K. (2019). Interlayer thermal history modification for interface strength in fused filament fabricated parts. *Progress in Additive Manufacturing*, 4(1):63–70. Publisher: Springer.

[Dhami et al., 1991] Dhami, T. L., Manocha, L. M., and Bahl, O. P. (1991). Oxidation behaviour of pitch based carbon fibers. *Carbon*, 29(1):51–60.

[Dickson et al., 2017] Dickson, A. N., Barry, J. N., McDonnell, K. A., and Dowling, D. P. (2017). Fabrication of continuous carbon, glass and Kevlar fibre reinforced polymer composites using additive manufacturing. *Additive Manufacturing*, 16:146–152.

[Ding et al., 2019] Ding, S., Zou, B., Wang, P., and Ding, H. (2019). Effects of nozzle temperature and building orientation on mechanical properties and microstructure of PEEK and PEI printed by 3D-FDM. *Polymer Testing*, 78:105948.

[Dlugosz et al., 1976] Dlugosz, J., Fraser, G. V., Grubb, D., Keller, A., Odell, J. A., and Goggin, P. L. (1976). Study of crystallization and isothermal thickening in polyethylene using SAXD, low frequency Raman spectroscopy and electron microscopy. *Polymer*, 17(6):471–480.

[Doddamani, 2020] Doddamani, M. (2020). Dynamic mechanical analysis of 3D printed eco-friendly lightweight composite. *Composites Communications*, 19:177–181.

[Dong et al., 2019a] Dong, J., Mei, C., Han, J., Lee, S., and Wu, Q. (2019a). 3D printed poly(lactic acid) composites with grafted cellulose nanofibers: Effect of nanofiber and post-fabrication annealing treatment on composite flexural properties. *Additive Manufacturing*, 28:621–628.

[Dong et al., 2019b] Dong, M., Zhang, S., Gao, D., and Chou, B. (2019b). The study on polypropylene applied in fused deposition modeling. *AIP Conference Proceedings*, 2065(1):030059. Publisher: American Institute of Physics.

[Dontsov et al., 2020] Dontsov, Y. V., Panin, S. V., Buslovich, D. G., and Berto, F. (2020). Taguchi Optimization of Parameters for Feedstock Fabrication and FDM Manufacturing of Wear-Resistant UHMWPE-Based Composites. *Materials*, 13(12):2718. Number: 12 Publisher: Multidisciplinary Digital Publishing Institute.

[Dul et al., 2021] Dul, S., Fambri, L., and Pegoretti, A. (2021). High-Performance Polyamide/Carbon Fiber Composites for Fused Filament Fabrication: Mechanical and Functional Performances. *Journal of Materials Engineering and Performance*.

[Dunn et al., 2019] Dunn, R. M., Hart, K. R., and Wetzel, E. D. (2019). Improving fracture strength of fused filament fabrication parts via thermal annealing in a printed support shell. *Progress in Additive Manufacturing*, 4(3):233–243.

[Durgun and Ertan, 2014] Durgun, I. and Ertan, R. (2014). Experimental investigation of FDM process for improvement of mechanical properties and production cost. *Rapid Prototyping Journal*, 20(3):228–235. Publisher: Emerald Group Publishing Limited.

[Duty et al., 2018] Duty, C., Ajinjeru, C., Kishore, V., Compton, B., Hmeidat, N., Chen, X., Liu, P., Hassen, A. A., Lindahl, J., and Kunc, V. (2018). What makes a material printable? A viscoelastic model for extrusion-based 3D printing of polymers. *Journal of Manufacturing Processes*, 35:526–537.

[Duty et al., 2017] Duty, C. E., Kunc, V., Compton, B., Post, B., Erdman, D., Smith, R., Lind, R., Lloyd, P., and Love, L. (2017). Structure and mechanical behavior of Big Area Additive Manufacturing (BAAM) materials. *Rapid Prototyping Journal*, 23(1):181–189.

[D'Amico and Peterson, 2018] D'Amico, A. and Peterson, A. M. (2018). An adaptable FEA simulation of material extrusion additive manufacturing heat transfer in 3D. *Additive Manufacturing*, 21:422–430.

[D'Amico and Peterson, 2020] D'Amico, T. and Peterson, A. M. (2020). Bead parameterization of desktop and room-scale material extrusion additive manufacturing: How print speed and thermal properties affect heat transfer. *Additive Manufacturing*, 34:101239.

[Edwards and Mackay, 2020] Edwards, D. A. and Mackay, M. (2020). Post-extrusion heating in 3-D printing. *Journal of Heat Transfer*.

[El-Hadi et al., 2002] El-Hadi, A., Schnabel, R., Straube, E., Müller, G., and Henning, S. (2002). Correlation between degree of crystallinity, morphology, glass temperature, mechanical properties and biodegradation of poly (3-hydroxyalkanoate) PHAs and their blends. *Polymer Testing*, 21(6):665–674.

[Elbadawi, 2018] Elbadawi, M. (2018). Polymeric Additive Manufacturing: The Necessity and Utility of Rheology. In *Polymer Rheology*. IntechOpen, London, United Kingdom, 43-63 edition.

[Erukhimovitch and Baram, 1994] Erukhimovitch, V. and Baram, J. (1994). Crystallization kinetics. *Physical Review B*, 50(9):5854–5856.

[Fallon et al., 2019] Fallon, J. J., McKnight, S. H., and Bortner, M. J. (2019). Highly Loaded Fiber Filled Polymers for Material Extrusion: A Review of Current Understanding. *Additive Manufacturing*, page 100810.

[Fan et al., 2020] Fan, C., Shan, Z., Zou, G., Zhan, L., and Yan, D. (2020). Performance of Short Fiber Interlayered Reinforcement Thermoplastic Resin in Additive Manufacturing. *Materials*, 13(12):2868. Number: 12 Publisher: Multidisciplinary Digital Publishing Institute.

[Ferraris et al., 2019] Ferraris, E., Zhang, J., and Van Hooreweder, B. (2019). Thermography based in-process monitoring of Fused Filament Fabrication of polymeric parts. *CIRP Annals*, 68(1):213–216.

[Ferreira et al., 2019] Ferreira, I., Machado, M., Alves, F., and Torres Marques, A. (2019). A review on fibre reinforced composite printing via FFF. *Rapid Prototyping Journal*, 25(6):972–988. Publisher: Emerald Publishing Limited.

[Ferrer-Balas et al., 2002] Ferrer-Balas, D., Maspoch, M. L., and Mai, Y.-W. (2002). Fracture behaviour of polypropylene films at different temperatures: fractography and deformation mechanisms studied by SEM. *Polymer*, 43(10):3083–3091.

[Ferry, 1980] Ferry, J. D. (1980). *Viscoelastic Properties of Polymers*. John Wiley & Sons. Google-Books-ID: 9dqQY3Ujsx4C.

[Filgueira et al., 2018] Filgueira, D., Holmen, S., Melbø, J. K., Moldes, D., Echtermeyer, A. T., and Chinga-Carrasco, G. (2018). 3D Printable Filaments Made of Biobased Polyethylene Biocomposites. *Polymers*, 10(3):314.

[Filip et al., 2020] Filip, P., Hausnerova, B., and Hnatkova, E. (2020). Continuous rheological description of highly filled polymer melts for material extrusion. *Applied Materials Today*, 20:100754.

[Fitzharris et al., 2018] Fitzharris, E. R., Watt, I., Rosen, D. W., and Shofner, M. L. (2018). Interlayer bonding improvement of material extrusion parts with polyphenylene sulfide using the Taguchi method. *Additive Manufacturing*, 24:287–297.

[Fleck et al., 2017] Fleck, T. J., Murray, A. K., Gunduz, I. E., Son, S. F., Chiu, G. T.-C., and Rhoads, J. F. (2017). Additive manufacturing of multifunctional reactive materials. *Additive Manufacturing*, 17:176–182.

[Fornes and Paul, 2003] Fornes, T. D. and Paul, D. R. (2003). Crystallization behavior of nylon 6 nanocomposites. *Polymer*, 44(14):3945–3961.

[Forster, 2015] Forster, A. M. (2015). Materials testing standards for additive manufacturing of polymer materials: state of the art and standards applicability. In *Additive Manufacturing Materials*, pages 67–123.

[Freeman et al., 2019] Freeman, T. B., Spitzer, D., Currier, P. N., Rollin, V., and Boetcher, S. K. S. (2019). Phase-Change Materials/HDPE Composite Filament: A First Step Toward Use With 3D Printing for Thermal Management Applications. *Journal of Thermal Science and Engineering Applications*, 11(5).

[Gao et al., 2016] Gao, B., Yang, Q., Zhao, X., Jin, G., Ma, Y., and Xu, F. (2016). 4D Bioprinting for Biomedical Applications. *Trends in Biotechnology*, 34(9):746–756.

[Gao et al., 2015] Gao, W., Zhang, Y., Ramanujan, D., Ramani, K., Chen, Y., Williams, C. B., Wang, C. C. L., Shin, Y. C., Zhang, S., and Zavattieri, P. D. (2015). The status, challenges, and future of additive manufacturing in engineering. *Computer-Aided Design*, 69:65–89.

[Gao et al., 2021] Gao, X., Qi, S., Kuang, X., Su, Y., Li, J., and Wang, D. (2021). Fused filament fabrication of polymer materials: A review of interlayer bond. *Additive Manufacturing*, 37:101658.

[Gao et al., 2020] Gao, X., Qi, S., Zhang, D., Su, Y., and Wang, D. (2020). The role of poly (ethylene glycol) on crystallization, interlayer bond and mechanical performance of polylactide parts fabricated by fused filament fabrication. *Additive Manufacturing*, 35:101414.

[Gao et al., 2019] Gao, X., Zhang, D., Qi, S., Wen, X., and Su, Y. (2019). Mechanical properties of 3D parts fabricated by fused deposition modeling: Effect of various fillers in polylactide. *Journal of Applied Polymer Science*, 136(31):47824. _eprint: https://onlinelibrary.wiley.com/doi/pdf/10.1002/app.47824.

[García Plaza et al., 2019] García Plaza, E., Núñez López, P. J., Caminero Torija, M. ., and Chacón Muñoz, J. M. (2019). Analysis of PLA Geometric Properties Processed by FFF Additive Manufacturing: Effects of Process Parameters and Plate-Extruder Precision Motion. *Polymers*, 11(10):1581. Number: 10 Publisher: Multidisciplinary Digital Publishing Institute.

[Ge et al., 2013] Ge, T., Pierce, F., Perahia, D., Grest, G. S., and Robbins, M. O. (2013). Molecular Dynamics Simulations of Polymer Welding: Strength from Interfacial Entanglements. *Physical Review Letters*, 110(9):098301. Publisher: American Physical Society.

[Gebhardt, 2011] Gebhardt, A. (2011). Understanding Additive Manufacturing: Rapid Prototyping. *Rapid Manufacturing, and Rapid Tooling*, pages 40–44.

[Gebhardt, 2012] Gebhardt, A. (2012). Understanding Additive Manufacturing: Rapid Prototyping. *Rapid Manufacturing, and Rapid Tooling*, pages 40–44.

[George, 2009] George, K. E. (2009). Non-Newtonian fluid mechanics and polymer rheology. In Thomas, S. and Weimin, Y., editors, *Advances in Polymer Processing*, volume Chapter 2, pages 13–46. Woodhead Publishing.

[Gibson et al., 2015] Gibson, I., Rosen, D., and Stucker, B. (2015). *Additive Manufacturing Technologies: 3D Printing, Rapid Prototyping, and Direct Digital Manufacturing*. Springer-Verlag, New York, 2 edition.

[Gibson and Shi, 1997] Gibson, I. and Shi, D. (1997). Material properties and fabrication parameters in selective laser sintering process. *Rapid prototyping journal*, 3(4):129–136.

[Gilmer et al., 2021] Gilmer, E. L., Anderegg, D., Gardner, J. M., Sauti, G., Siochi, E. J., McKnight, S. H., Dillard, D. A., McIlroy, C., and Bortner, M. J. (2021). Temperature, diffusion, and stress modeling in filament extrusion additive manufacturing of polyetherimide: An examination of the influence of processing parameters and importance of modeling assumptions. *Additive Manufacturing*, 48:102412.

[Gilmer et al., 2019] Gilmer, E. L., Mansfield, C., Gardner, J. M., Siochi, E. J., Baird, D. G., and Bortner, M. J. (2019). Characterization and Analysis of Polyetherimide: Realizing Practical Challenges of Modeling the Extrusion-Based Additive Manufacturing Process. In *Polymer-Based Additive Manufacturing: Recent Developments*, volume In press. ACS Books.

[Gilmer et al., 2018] Gilmer, E. L., Miller, D., Chatham, C. A., Zawaski, C., Fallon, J. J., Pekkanen, A., Long, T. E., Williams, C. B., and Bortner, M. J. (2018). Model analysis of feedstock behavior in fused filament fabrication: Enabling rapid materials screening. *Polymer*, 152:51–61.

[Gleadall et al., 2018] Gleadall, A., Ashcroft, I., and Segal, J. (2018). VOLCO: A predictive model for 3D printed microarchitecture. *Additive Manufacturing*, 21:605–618.

[Go et al., 2017] Go, J., Schiffres, S. N., Stevens, A. G., and Hart, A. J. (2017). Rate limits of additive manufacturing by fused filament fabrication and guidelines for high-throughput system design. *Additive Manufacturing*, 16:1–11.

[Goh et al., 2019] Goh, G. D., Yap, Y. L., Agarwala, S., and Yeong, W. Y. (2019). Recent Progress in Additive Manufacturing of Fiber Reinforced Polymer Composite. *Advanced Materials Technologies*, 4(1):1800271. _eprint: https://onlinelibrary.wiley.com/doi/pdf/10.1002/admt.201800271.

[Gold and Turner, 2015] Gold, S. A. and Turner, B. N. (2015). A review of melt extrusion additive manufacturing processes: II. Materials, dimensional accuracy, and surface roughness. *Rapid Prototyping Journal*, 21(3):250–261.

[Gomez-Gras et al., 2018] Gomez-Gras, G., Jerez-Mesa, R., Travieso-Rodriguez, J. A., and Lluma-Fuentes, J. (2018). Fatigue performance of fused filament fabrication PLA specimens. *Materials & Design*, 140:278–285.

[González-Henríquez et al., 2019] González-Henríquez, C. M., Sarabia-Vallejos, M. A., and Rodriguez-Hernandez, J. (2019). Polymers for additive manufacturing and 4D-printing: Materials, methodologies, and biomedical applications. *Progress in Polymer Science*, 94:57–116.

[Gopanna et al., 2019] Gopanna, A., Rajan, K. P., Thomas, S. P., and Chavali, M. (2019). Polyethylene and polypropylene matrix composites for biomedical applications. In Grumezescu, V. and Grumezescu, A. M., editors, *Materials for Biomedical Engineering*, pages 175–216. Elsevier.

[Graham, 2019] Graham, R. S. (2019). Understanding flow-induced crystallization in polymers: A perspective on the role of molecular simulations. *Journal of Rheology*, 63(1):203–214.

[Greene and Wilkes, 1995] Greene, J. P. and Wilkes, J. O. (1995). Steady-State and dynamic properties of concentrated fiber-filled thermoplastics. *Polymer Engineering & Science*, 35(21):1670–1681. _eprint: https://onlinelibrary.wiley.com/doi/pdf/10.1002/pen.760352103.

[Gregor-Svetec et al., 2020] Gregor-Svetec, D., Leskovšek, M., Vrabič Brodnjak, U., Stankovič Elesini, U., Muck, D., and Urbas, R. (2020). Characteristics of HDPE/cardboard dust 3D printable composite filaments. *Journal of Materials Processing Technology*, 276:116379.

[Grewell and Benatar, 2007] Grewell, D. and Benatar, A. (2007). Welding of Plastics: Fundamentals and New Developments. *International Polymer Processing*, 22(1):43–60. Publisher: Hanser Verlag.

[Grewell and Benatar, 2008] Grewell, D. and Benatar, A. (2008). Semi-empirical, squeeze flow and intermolecular diffusion model. I. Determination of model parameters. *Polymer Engineering & Science*, 48(5):860–867.

[Gudadhe et al., 2019] Gudadhe, A., Bachhar, N., Kumar, A., Andrade, P., and Kumaraswamy, G. (2019). Three-Dimensional Printing with Waste High-Density Polyethylene. *ACS Applied Polymer Materials*, 1(11):3157–3164. Publisher: American Chemical Society.

[Guezzout et al., 2017] Guezzout, Z., Doufnoune, R., and Haddaoui, N. (2017). Effect of graphene oxide on the properties of compatibilized polypropylene/ethylene-propylene-rubber blend. *Journal of Polymer Research*, 24(8):129.

[Guillet and Seriai, 1991] Guillet, J. and Seriai, M. (1991). Quantitative evaluation of extrudate swell from viscoelastic properties of polystyrene. *Rheologica acta*, 30(6):540–548. Publisher: Springer.

[Gunasekaran et al., 2021] Gunasekaran, H. B., Ponnan, S., Thirunavukkarasu, N., Wu, K., Wu, L., and Wang, J. (2021). Investigation of in-situ chemical cross-linking during fused filament fabrication process on parts shrinkage reduction and interlayer adhesion. *Journal of Materials Research and Technology*, 15:2026–2035.

[Gutowski et al., 2017] Gutowski, T., Jiang, S., Cooper, D., Corman, G., Hausmann, M., Manson, J.-A., Schudeleit, T., Wegener, K., Sabelle, M., Ramos-Grez, J., and Sekulic, D. P. (2017). Note on the Rate and Energy Efficiency Limits for Additive Manufacturing. *Journal of Industrial Ecology*, 21(S1):S69–S79.

[Górski et al., 2015] Górski, F., Wichniarek, R., Kuczko, W., Zawadzki, P., and Buń, P. (2015). Strength of ABS parts produced by fused deposition modelling technology – A critical orientation problem. *Advances in Science and Technology. Research Journal*, 9(26):12–19. Publisher: Polish Society of Ecological Engineering (PTIE).

[Hague et al., 2004] Hague, R., Mansour, S., Saleh, N., and Harris, R. (2004). Materials analysis of stereolithography resins for use in rapid manufacturing. *Journal of materials science*, 39(7):2457–2464.

[Hamod, 2014] Hamod, H. (2014). *Suitability of recycled HDPE for 3D printing filament.* Master of Science Thesis, Arcada University of Applied Science, Helsinki, Finland.

[Han et al., 2019] Han, P., Tofangchi, A., Deshpande, A., Zhang, S., and Hsu, K. (2019). An approach to improve interface healing in FFF-3D printed Ultem 1010 using laser pre-deposition heating. *Procedia Manufacturing*, 34:672–677.

[Harris et al., 2019] Harris, M., Potgieter, J., Ray, S., Archer, R., and Arif, K. M. (2019). Acrylonitrile Butadiene Styrene and Polypropylene Blend with Enhanced Thermal and Mechanical Properties for Fused Filament Fabrication. *Materials*, 12(24):4167. Number: 24 Publisher: Multidisciplinary Digital Publishing Institute.

[Harris et al., 2020] Harris, M., Potgieter, J., Ray, S., Archer, R., and Arif, K. M. (2020). Preparation and characterization of thermally stable ABS/HDPE blend for fused filament fabrication. *Materials and Manufacturing Processes*, 35(2):230–240.

[Hart et al., 2018a] Hart, K. R., Dunn, R. M., Sietins, J. M., Hofmeister Mock, C. M., Mackay, M. E., and Wetzel, E. D. (2018a). Increased fracture toughness of additively manufactured amorphous thermoplastics via thermal annealing. *Polymer*, 144:192–204.

[Hart et al., 2020] Hart, K. R., Dunn, R. M., and Wetzel, E. D. (2020). Increased fracture toughness of additively manufactured semi-crystalline thermoplastics via thermal annealing. *Polymer*, page 123091.

[Hart et al., 2018b] Hart, K. R., Frketic, J. B., and Brown, J. R. (2018b). Recycling meal-ready-to-eat (MRE) pouches into polymer filament for material extrusion additive manufacturing. *Additive Manufacturing*, 21:536–543.

[Hebda et al., 2019] Hebda, M., McIlroy, C., Whiteside, B., Caton-Rose, F., and Coates, P. (2019). A method for predicting geometric characteristics of polymer deposition during fused-filament-fabrication. *Additive Manufacturing*, 27:99–108.

[Heller et al., 2015] Heller, B. P., Smith, D. E., and Jack, D. (2015). Effect of extrudate swell, nozzle shape, and convergence zone on fiber orientation in fused deposition modeling nozzle flow. In *Proceedings of the Solid Freeform Fabrication*, pages 1220–1236, Austin, Texas.

[Heller et al., 2016a] Heller, B. P., Smith, D. E., and Jack, D. A. (2016a). Effects of extrudate swell and nozzle geometry on fiber orientation in Fused Filament Fabrication nozzle flow. *Additive Manufacturing*, 12:252–264.

[Heller et al., 2016b] Heller, B. P., Smith, D. E., and Jack, D. A. (2016b). Effects of extrudate swell and nozzle geometry on fiber orientation in Fused Filament Fabrication nozzle flow. *Additive Manufacturing*, 12:252–264.

[Heller et al., 2019] Heller, B. P., Smith, D. E., and Jack, D. A. (2019). Planar deposition flow modeling of fiber filled composites in large area additive manufacturing. *Additive Manufacturing*, 25:227–238.

[Hertle et al., 2016] Hertle, S., Drexler, M., and Drummer, D. (2016). Additive Manufacturing of Poly(propylene) by Means of Melt Extrusion. *Macromolecular Materials and Engineering*, 301(12):1482–1493.

[Herzog et al., 2016] Herzog, D., Seyda, V., Wycisk, E., and Emmelmann, C. (2016). Additive manufacturing of metals. *Acta Materialia*, 117:371–392.

[Heuer et al., 2000] Heuer, J. K., Okamoto, P. R., Lam, N. Q., and Stubbins, J. F. (2000). Relationship between segregation-induced intergranular fracture and melting in the nickel–sulfur system. *Applied Physics Letters*, 76(23):3403–3405.

[Hilliou and Covas, 2021] Hilliou, L. and Covas, J. A. (2021). In-process rheological monitoring of extrusion-based polymer processes. *Polymer International*, 70(1):24–33. _eprint: https://onlinelibrary.wiley.com/doi/pdf/10.1002/pi.6093.

[Ho and Kontopoulou, 2022] Ho, Q. B. and Kontopoulou, M. (2022). Improving the adhesion and properties in the material extrusion of polypropylene by blending with a polyolefin elastomer. *Additive Manufacturing*, 55:102818.

[Hopmann and Michaeli, 2016] Hopmann, C. and Michaeli, W. (2016). *Extrusion Dies for Plastics and Rubber: Design and Engineering Computations*. Carl Hanser Verlag GmbH & Co. KG, München, 3 edition.

[Huang and Schlarb, 2021] Huang, M. and Schlarb, A. K. (2021). Polypropylene/poly(ethylene terephthalate) microfibrillar reinforced composites manufactured by fused filament fabrication. *Journal of Applied Polymer Science*, 138(23):50557. _eprint: https://onlinelibrary.wiley.com/doi/pdf/10.1002/app.50557.

[Huang et al., 2015] Huang, Y., Leu, M. C., Mazumder, J., and Donmez, A. (2015). Additive manufacturing: current state, future potential, gaps and needs, and recommendations. *Journal of Manufacturing Science and Engineering*, 137(1):014001.

[Hunt and Todd, 2009] Hunt, T. A. and Todd, B. D. (2009). Diffusion of linear polymer melts in shear and extensional flows. *The Journal of Chemical Physics*, 131(5):054904. Publisher: American Institute of Physics.

[Hyun et al., 2011] Hyun, K., Wilhelm, M., Klein, C. O., Cho, K. S., Nam, J. G., Ahn, K. H., Lee, S. J., Ewoldt, R. H., and McKinley, G. H. (2011). A review of nonlinear oscillatory shear tests: Analysis and application of large amplitude oscillatory shear (LAOS). *Progress in Polymer Science*, 36(12):1697–1753.

[Ianniruberto and Marrucci, 2013] Ianniruberto, G. and Marrucci, G. (2013). Convective constraint release (CCR) revisited. *Journal of Rheology*, 58(1):89–102. Publisher: The Society of Rheology.

[Ichazo et al., 2001] Ichazo, M. N., Albano, C., González, J., Perera, R., and Candal, M. V. (2001). Polypropylene/wood flour composites: treatments and properties. *Composite Structures*, 54(2):207–214.

[Incropera et al., 2013] Incropera, F. P., DeWitt, D. P., Bergman, T. L., and Lavine, A. S. (2013). *Principles of Heat and Mass Transfer*. John Wiley & Sons, New York, 7th edition edition. Google-Books-ID: YBaNaLurTD4C.

[Iring and Tüdős, 1990] Iring, M. and Tüdős, F. (1990). Thermal oxidation of polyethylene and polypropylene: Effects of chemical structure and reaction conditions on the oxidation process. *Progress in Polymer Science*, 15(2):217–262.

[Ismail and Suryadiansyah, 2002] Ismail, H. and Suryadiansyah (2002). Thermoplastic elastomers based on polypropylene/natural rubber and polypropylene/recycle rubber blends. *Polymer Testing*, 21(4):389–395.

[Jabbari et al., 2018] Jabbari, M., Baran, I., Mohanty, S., Comminal, R., Sonne, M. R., Nielsen, M. W., Spangenberg, J., and Hattel, J. H. (2018). Multiphysics modelling of manufacturing processes: A review. *Advances in Mechanical Engineering*, 10(5):1687814018766188. Publisher: SAGE Publications.

[Jagenteufel et al., 2017] Jagenteufel, R., Hofstaetter, T., Kamleitner, F., Pedersen, D. B., Tosello, G., and Hansen, H. N. (2017). Rheology of high melt strength polypropylene for additive manufacturing. *Advanced Materials Letter*, 8:712–716.

[Jasiuk et al., 2018] Jasiuk, I., Abueidda, D. W., Kozuch, C., Pang, S., Su, F. Y., and McKittrick, J. (2018). An Overview on Additive Manufacturing of Polymers. *JOM*, 70(3):275–283.

[Jeong and Leonov, 2003] Jeong, J.-H. and Leonov, A. I. (2003). Quasi-1D Modeling of Polymer Melt Die Swell in Short Dies. *arXiv:physics/0308013*. arXiv: physics/0308013.

[Jerez-Mesa et al., 2016] Jerez-Mesa, R., Travieso-Rodriguez, J. A., Corbella, X., Busqué, R., and Gomez-Gras, G. (2016). Finite element analysis of the thermal behavior of a RepRap 3D printer liquefier. *Mechatronics*, 36:119–126.

[Jeyachandran et al., 2020] Jeyachandran, P., Bontha, S., Bodhak, S., Balla, V. K., Kundu, B., and Doddamani, M. (2020). Mechanical behaviour of additively manufactured bioactive glass/high density polyethylene composites. *Journal of the Mechanical Behavior of Biomedical Materials*, 108:103830.

[Jiang et al., 2020a] Jiang, G., Wang, F., Zhang, S., and Huang, H. (2020a). Structure and improved properties of PPC/PBAT blends via controlling phase morphology based on melt viscosity. *Journal of Applied Polymer Science*, 137(31):48924. _eprint: https://onlinelibrary.wiley.com/doi/pdf/10.1002/app.48924.

[Jiang et al., 2020b] Jiang, S., Siyajeu, Y., Shi, Y., Zhu, S., and Li, H. (2020b). Improving the forming quality of fused filament fabrication parts by applied vibration. *Rapid Prototyping Journal*, 26(1):202–212. Publisher: Emerald Publishing Limited.

[Jiang et al., 2019] Jiang, Y., Wu, J., Leng, J., Cardon, L., and Zhang, J. (2019). Reinforced and toughened PP/PS composites prepared by Fused Filament Fabrication (FFF) with in-situ microfibril and shish-kebab structure. *Polymer*, 186:121971.

[Jin et al., 2018] Jin, M., Giesa, R., Neuber, C., and Schmidt, H.-W. (2018). Filament Materials Screening for FDM 3D Printing by Means of Injection-Molded Short Rods. *Macromolecular Materials and Engineering*, 303(12):1800507.

[Jin et al., 2020] Jin, M., Neuber, C., and Schmidt, H.-W. (2020). Tailoring polypropylene for extrusion-based additive manufacturing. *Additive Manufacturing*, page 101101.

[Jing et al., 2020] Jing, J., Chen, Y., Shi, S., Yang, L., and Lambin, P. (2020). Facile and scalable fabrication of highly thermal conductive polyethylene/graphene nanocomposites

by combining solid-state shear milling and FDM 3D-printing aligning methods. *Chemical Engineering Journal*, 402:126218.

[Joseph et al., 2002] Joseph, P. V., Joseph, K., and Thomas, S. (2002). Short sisal fiber reinforced polypropylene composites: the role of interface modification on ultimate properties. *Composite Interfaces*, 9(2):171–205.

[Kalay and Bevis, 1997] Kalay, G. and Bevis, M. J. (1997). Processing and physical property relationships in injection-molded isotactic polypropylene. 1. Mechanical properties. *Journal of Polymer Science Part B: Polymer Physics*, 35(2):241–263.

[Kalita et al., 2003] Kalita, S. J., Bose, S., Hosick, H. L., and Bandyopadhyay, A. (2003). Development of controlled porosity polymer-ceramic composite scaffolds via fused deposition modeling. *Materials Science and Engineering: C*, 23(5):611–620.

[Kang et al., 2013] Kang, J., Li, J., Chen, S., Zhu, S., Li, H., Cao, Y., Yang, F., and Xiang, M. (2013). Hydrogenated petroleum resin effect on the crystallization of isotactic polypropylene. *Journal of Applied Polymer Science*, 130(1):25–38.

[Kannan et al., 2013] Kannan, M., Bhagawan, S. S., Thomas, S., and Joseph, K. (2013). Nanoclay effect on transport properties of thermoplastic polyurethane/polypropylene (TPU/PP) blends. *Journal of Polymer Research*, 20(8):201.

[Karger-Kocsis, 1994] Karger-Kocsis, J. (1994). *Polypropylene structure, blends and composites: Volume 2 Copolymers and blends*, volume 2. Springer Science & Business Media.

[Karian, 2003] Karian, H. (2003). *Handbook of Polypropylene and Polypropylene Composites, Revised and Expanded*. CRC Press. Google-Books-ID: C0nzeNPUpoIC.

[Karis et al., 1996] Karis, T. E., Dawson, D. J., Davis, C. R., Kono, R.-N., Kim, G., Jhon, M. S., and Kim, S. J. (1996). Rapid Prototyping Materials Rheology. *Journal of Imaging Science and Technology*, 40(2):147–155.

[Karsli and Aytac, 2013] Karsli, N. G. and Aytac, A. (2013). Tensile and thermomechanical properties of short carbon fiber reinforced polyamide 6 composites. *Composites Part B: Engineering*, 51:270–275.

[Katschnig et al., 2017] Katschnig, M., Arbeiter, F., Haar, B., Campe, G. v., and Holzer, C. (2017). Cranial Polypropylene Implants by Fused Filament Fabrication. *Advanced Engineering Materials*, 19(4):1600676. _eprint: https://onlinelibrary.wiley.com/doi/pdf/10.1002/adem.201600676.

[Kaynak et al., 1996] Kaynak, A., Polat, A., and Yilmazer, U. (1996). Some microwave and mechanical properties of carbon fiber-polypropylene and carbon black-polypropylene composites. *Materials Research Bulletin*, 31(10):1195–1206.

[Kaynak et al., 2018] Kaynak, B., Spoerk, M., Shirole, A., Ziegler, W., and Sapkota, J. (2018). Polypropylene/Cellulose Composites for Material Extrusion Additive Manufacturing. *Macromolecular Materials and Engineering*, 303(5):1800037.

[Kellens et al., 2017] Kellens, K., Baumers, M., Gutowski, T. G., Flanagan, W., Lifset, R., and Duflou, J. R. (2017). Environmental dimensions of additive manufacturing: Mapping application domains and their environmental implications. *Journal of Industrial Ecology*, 21(S1):S49–S68.

[Kennedy et al., 2022] Kennedy, A. J., Ballentine, M. L., May, L. R., Das, A., Bednar, A. J., Griggs, C. S., Hull, M. S., and Bortner, M. J. (2022). Simplifying Complex Contaminant Mixtures: Selective Ammonia Adsorption and Toxicity Reduction using 3D Printable Polymer–Zeolite. *Water, Air, & Soil Pollution*, 233(5):148.

[Khandavalli and Rothstein, 2014] Khandavalli, S. and Rothstein, J. P. (2014). Extensional rheology of shear-thickening fumed silica nanoparticles dispersed in an aqueous polyethylene oxide solution. *Journal of Rheology*, 58(2):411–431. Publisher: The Society of Rheology.

[Kim and Oh, 2008] Kim, G. D. and Oh, Y. T. (2008). A benchmark study on rapid prototyping processes and machines: quantitative comparisons of mechanical properties, accuracy, roughness, speed, and material cost. *Proceedings of the Institution of Mechanical Engineers, Part B: Journal of Engineering Manufacture*, 222(2):201–215.

[Kim and Song, 1997] Kim, J. K. and Song, J. H. (1997). Rheological properties and fiber orientations of short fiber-reinforced plastics. *Journal of Rheology*, 41(5):1061–1085. Publisher: The Society of Rheology.

[Kim, 2020] Kim, S. K. (2020). Collective viscosity model for shear thinning polymeric materials. *Rheologica Acta*, 59(1):63–72.

[Kishore et al., 2017a] Kishore, V., Ajinjeru, C., Liu, P., Lindahl, J., Hassen, A., Kunc, V., and Duty, C. (2017a). Predicting sharkskin instability in extrusion additive manufacturing of reinforced thermoplastics. In *Proceedings of Solid Freeform Fabrication Symposium.*, pages 1696–1704, Austin, TX.

[Kishore et al., 2017b] Kishore, V., Ajinjeru, C., Nycz, A., Post, B., Lindahl, J., Kunc, V., and Duty, C. (2017b). Infrared preheating to improve interlayer strength of big area additive manufacturing (BAAM) components. *Additive Manufacturing*, 14:7–12.

[Klippstein et al., 2018] Klippstein, H., Sanchez, A. D. D. C., Hassanin, H., Zweiri, Y., and Seneviratne, L. (2018). Fused Deposition Modeling for Unmanned Aerial Vehicles (UAVs): A Review. *Advanced Engineering Materials*, 20(2):1700552.

[Knoop et al., 2015] Knoop, F., Schoeppner, V., Knoop, F. C., and Schoeppner, V. (2015). Mechanical and thermal properties of FDM parts manufactured with polyamide 12. In *Proceedings of the 26th Annual International Solid Freeform Fabrication Symposium—An Additive Manufacturing Conference, Austin, TX, USA*, pages 10–12.

[Ko et al., 2019] Ko, Y. S., Herrmann, D., Tolar, O., Elspass, W. J., and Brändli, C. (2019). Improving the filament weld-strength of fused filament fabrication products through improved interdiffusion. *Additive Manufacturing*, 29:100815.

[Konaganti et al., 2016] Konaganti, V. K., Ansari, M., Mitsoulis, E., and Hatzikiriakos, S. G. (2016). The effect of damping function on extrudate swell. *Journal of Non-Newtonian Fluid Mechanics*, 236:73–82.

[Kotlinski, 2014] Kotlinski, J. (2014). Mechanical properties of commercial rapid prototyping materials. *Rapid Prototyping Journal*, 20(6):499–510. Publisher: Emerald Group Publishing Limited.

[Kotula, 2020] Kotula, A. (2020). A frequency-dependent effective medium model for the rheology of crystallizing polymers. *Journal of Rheology*, 64(3):505–515. Publisher: The Society of Rheology.

[Kotula et al., 2019] Kotula, A., Seppala, J., and Snyder, C. (2019). Polymer Additive Manufacturing: Confronting Complexity. In *Polymer-Based Additive Manufacturing: Recent*

Developments, volume 1315 of *ACS Symposium Series*, pages 1–6. American Chemical Society.

[Kotula and Migler, 2017] Kotula, A. P. and Migler, K. B. (2017). Evaluating models for polycaprolactone crystallization via simultaneous rheology and Raman spectroscopy. *Journal of Rheology*, 62(1):343–356. Publisher: The Society of Rheology.

[Kotula and Migler, 2021] Kotula, A. P. and Migler, K. B. (2021). Percolation implications in the rheology of polymer crystallization. *Polymer Crystallization*, 4(2):e10162. _eprint: https://onlinelibrary.wiley.com/doi/pdf/10.1002/pcr2.10162.

[Krishnamoorti and Giannelis, 1997] Krishnamoorti, R. and Giannelis, E. P. (1997). Rheology of End-Tethered Polymer Layered Silicate Nanocomposites. *Macromolecules*, 30(14):4097–4102. Publisher: American Chemical Society.

[Kruth et al., 1998] Kruth, J.-P., Leu, M. C., and Nakagawa, T. (1998). Progress in Additive Manufacturing and Rapid Prototyping. *CIRP Annals-Manufacturing Technology*, 47(2):525–540. Publisher: Technische Rundschau Edition Colibri LTD.

[Kumar et al., 2019] Kumar, S., Singh, R., Singh, T., and Batish, A. (2019). On investigation of rheological, mechanical and morphological characteristics of waste polymer-based feedstock filament for 3D printing applications. *Journal of Thermoplastic Composite Materials*, page 0892705719856063.

[Kwok et al., 2017] Kwok, S. W., Goh, K. H. H., Tan, Z. D., Tan, S. T. M., Tjiu, W. W., Soh, J. Y., Ng, Z. J. G., Chan, Y. Z., Hui, H. K., and Goh, K. E. J. (2017). Electrically conductive filament for 3D-printed circuits and sensors. *Applied Materials Today*, 9:167–175.

[Lamm et al., 2020] Lamm, M. E., Wang, L., Kishore, V., Tekinalp, H., Kunc, V., Wang, J., Gardner, D. J., and Ozcan, S. (2020). Material Extrusion Additive Manufacturing of Wood and Lignocellulosic Filled Composites. *Polymers*, 12(9):2115. Number: 9 Publisher: Multidisciplinary Digital Publishing Institute.

[Larson, 2013] Larson, R. G. (2013). *Constitutive Equations for Polymer Melts and Solutions: Butterworths Series in Chemical Engineering*. Butterworth-Heinemann. Google-Books-ID: 6uMgBQAAQBAJ.

[Laun, 1984] Laun, H. M. (1984). Orientation effects and rheology of short glass fiber-reinforced thermoplastics. *Colloid and Polymer Science*, 262(4):257–269.

[Leal et al., 2017] Leal, R., Barreiros, F. M., Alves, L., Romeiro, F., Vasco, J. C., Santos, M., and Marto, C. (2017). Additive manufacturing tooling for the automotive industry. *The International Journal of Advanced Manufacturing Technology*, 92(5):1671–1676.

[Lee et al., 2020] Lee, K. P. M., Brandt, M., Shanks, R., and Daver, F. (2020). Rheology and 3D Printability of Percolated Graphene–Polyamide-6 Composites. *Polymers*, 12(9):2014. Number: 9 Publisher: Multidisciplinary Digital Publishing Institute.

[Leng et al., 2020] Leng, J., Gu, X., Hong, R., and Zhang, J. (2020). Tailored crystalline structure and enhanced impact strength of isotactic polypropylene/high-density polyethylene blend by controlling the printing speed of fused filament fabrication. *Journal of Materials Science*, 55:14058–14073.

[Levchik et al., 1999] Levchik, S. V., Weil, E. D., and Lewin, M. (1999). Thermal decomposition of aliphatic nylons. *Polymer International*, 48(7):532–557. _eprint: https://onlinelibrary.wiley.com/doi/pdf/10.1002/%28SICI%291097-0126%28199907%2948%3A7%3C532%3A%3AAID-PI214%3E3.0.CO%3B2-R.

[Levenhagen and Dadmun, 2017] Levenhagen, N. P. and Dadmun, M. D. (2017). Bimodal molecular weight samples improve the isotropy of 3D printed polymeric samples. *Polymer*, 122:232–241.

[Levenhagen and Dadmun, 2018] Levenhagen, N. P. and Dadmun, M. D. (2018). Interlayer diffusion of surface segregating additives to improve the isotropy of fused deposition modeling products. *Polymer*, 152:35–41.

[Levenhagen and Dadmun, 2019a] Levenhagen, N. P. and Dadmun, M. D. (2019a). Improving Interlayer Adhesion in 3D Printing with Surface Segregating Additives: Improving the Isotropy of Acrylonitrile–Butadiene–Styrene Parts. *ACS Applied Polymer Materials*, 1(4):876–884. Publisher: American Chemical Society.

[Levenhagen and Dadmun, 2019b] Levenhagen, N. P. and Dadmun, M. D. (2019b). Reactive Processing in Extrusion-Based 3D Printing to Improve Isotropy and Mechanical Properties. *Macromolecules*, 52(17):6495–6501. Publisher: American Chemical Society.

[Levine et al., 2020] Levine, L., Lane, B., Heigel, J., Migler, K., Stoudt, M., Phan, T., Ricker, R., Strantza, M., Hill, M., Zhang, F., Seppala, J., Garboczi, E., Bain, E., Cole, D., Allen, A., Fox, J., and Campbell, C. (2020). Outcomes and Conclusions from the 2018 AM-Bench Measurements, Challenge Problems, Modeling Submissions, and Conference. *Integrating Materials and Manufacturing Innovation*, 9(1):1–15.

[Lewandowski et al., 2016] Lewandowski, K., Piszczek, K., Zajchowski, S., and Mirowski, J. (2016). Rheological properties of wood polymer composites at high shear rates. *Polymer Testing*, 51:58–62. Publisher: Elsevier.

[Lewicki et al., 2017] Lewicki, J. P., Rodriguez, J. N., Zhu, C., Worsley, M. A., Wu, A. S., Kanarska, Y., Horn, J. D., Duoss, E. B., Ortega, J. M., Elmer, W., Hensleigh, R., Fellini, R. A., and King, M. J. (2017). 3D-Printing of Meso-structurally Ordered Carbon Fiber/Polymer Composites with Unprecedented Orthotropic Physical Properties. *Scientific Reports*, 7(1):43401. Number: 1 Publisher: Nature Publishing Group.

[Lewis, 2006] Lewis, J. A. (2006). Direct Ink Writing of 3D Functional Materials. *Advanced Functional Materials*, 16(17):2193–2204.

[Li et al., 2018] Li, G., Zhao, J., Wu, W., Jiang, J., Wang, B., Jiang, H., and Fuh, J. Y. H. (2018). Effect of Ultrasonic Vibration on Mechanical Properties of 3D Printing Non-Crystalline and Semi-Crystalline Polymers. *Materials*, 11(5):826. Number: 5 Publisher: Multidisciplinary Digital Publishing Institute.

[Li and Cai, 2011] Li, J. and Cai, C. L. (2011). The carbon fiber surface treatment and addition of PA6 on tensile properties of ABS composites. *Current Applied Physics*, 11(1):50–54.

[Li and Zhang, 2009] Li, J. and Zhang, Y. F. (2009). The tensile properties of HNO3-treated carbon fiber reinforced ABS/PA6 composites. *Surface and Interface Analysis*, 41(7):610–614. _eprint: https://analyticalsciencejournals.onlinelibrary.wiley.com/doi/pdf/10.1002/sia.3072.

[Li et al., 2020] Li, J., Zhu, Z., Li, T., Peng, X., Jiang, S., and Turng, L.-S. (2020). Quantification of the Young's modulus for polypropylene: Influence of initial crystallinity and service temperature. *Journal of Applied Polymer Science*, 137(16):48581. _eprint: https://onlinelibrary.wiley.com/doi/pdf/10.1002/app.48581.

[Li et al., 2019a] Li, L., Lin, Q., Tang, M., Duncan, A. J. E., and Ke, C. (2019a). Advanced Polymer Designs for Direct-Ink-Write 3D Printing. *Chemistry – A European Journal*, 25(46):10768–10781.

[Li et al., 2019b] Li, Y., Li, Y., Han, C., Yu, Y., and Xiao, L. (2019b). Morphology and properties in the binary blends of polypropylene and propylene–ethylene random copolymers. *Polymer Bulletin*, 76(6):2851–2866.

[Ligon et al., 2017] Ligon, S. C., Liska, R., Stampfl, J., Gurr, M., and Mülhaupt, R. (2017). Polymers for 3D printing and customized additive manufacturing. *Chemical reviews*, 117(15):10212–10290.

[Lim et al., 2012] Lim, S., Buswell, R. A., Le, T. T., Austin, S. A., Gibb, A. G. F., and Thorpe, T. (2012). Developments in construction-scale additive manufacturing processes. *Automation in Construction*, 21:262–268.

[Liu et al., 2018a] Liu, F., Vyas, C., Poologasundarampillai, G., Pape, I., Hinduja, S., Mirihanage, W., and Bartolo, P. (2018a). Structural evolution of PCL during melt extrusion 3D printing. *Macromolecular Materials and Engineering*, 303(2):1700494.

[Liu et al., 2018b] Liu, P., Dinwiddie, R. B., Keum, J. K., Vasudevan, R. K., Jesse, S., Nguyen, N. A., Lindahl, J. M., and Kunc, V. (2018b). Rheology, crystal structure, and nanomechanical properties in large-scale additive manufacturing of polyphenylene sulfide/-carbon fiber composites. *Composites Science and Technology*, 168:263–271.

[Liu et al., 2019] Liu, Y., Yu, Y., Liu, C., Regenstein, J. M., Liu, X., and Zhou, P. (2019). Rheological and mechanical behavior of milk protein composite gel for extrusion-based 3D food printing. *LWT*, 102:338–346.

[Long et al., 2019] Long, H., Wu, Z., Dong, Q., Shen, Y., Zhou, W., Luo, Y., Zhang, C., and Dong, X. (2019). Mechanical and thermal properties of bamboo fiber reinforced polypropylene/polylactic acid composites for 3D printing. *Polymer Engineering & Science*, 59(s2):E247–E260. _eprint: https://onlinelibrary.wiley.com/doi/pdf/10.1002/pen.25043.

[Lorenzo et al., 2006] Lorenzo, A. T., Arnal, M. L., Sánchez, J. J., and Müller, A. J. (2006). Effect of annealing time on the self-nucleation behavior of semicrystalline polymers. *Journal of Polymer Science Part B: Polymer Physics*, 44(12):1738–1750. _eprint: https://onlinelibrary.wiley.com/doi/pdf/10.1002/polb.20832.

[Lorenzo et al., 2001] Lorenzo, M. L. D., Cimmino, S., and Silvestre, C. (2001). Nonisothermal crystallization of isotactic polypropylene blended with poly(-pinene). I. Bulk crystallization. *Journal of Applied Polymer Science*, 82(2):358–367.

[Lorenzo-Bañuelos et al., 2020] Lorenzo-Bañuelos, M., Díaz, A., and Cuesta, I. I. (2020). Influence of raster orientation on the determination of fracture properties of polypropylene thin components produced by additive manufacturing. *Theoretical and Applied Fracture Mechanics*, 107:102536.

[Lou et al., 2016] Lou, C.-W., Huang, C.-L., Pan, Y.-J., Lin, Z.-I., Song, X.-M., and Lin, J.-H. (2016). Crystallization, mechanical, and electromagnetic properties of conductive polypropylene/SEBS composites. *Journal of Polymer Research*, 23(5):84.

[Lovinger and Williams, 1980] Lovinger, A. J. and Williams, M. L. (1980). Tensile properties and morphology of blends of polyethylene and polypropylene. *Journal of Applied Polymer Science*, 25(8):1703–1713.

[Lozano and Barrera, 2001] Lozano, K. and Barrera, E. V. (2001). Nanofiber-reinforced thermoplastic composites. I. Thermoanalytical and mechanical analyses. *Journal of Applied Polymer Science*, 79(1):125–133. _eprint: https://onlinelibrary.wiley.com/doi/pdf/10.1002/1097-4628%2820010103%2979%3A1%3C125%3A%3AAID-APP150%3E3.0.CO%3B2-D.

[Lubombo and Huneault, 2018] Lubombo, C. and Huneault, M. A. (2018). Effect of infill patterns on the mechanical performance of lightweight 3D-printed cellular PLA parts. *Materials Today Communications*, 17:214–228.

[Luo, 2020] Luo, C. (2020). Modeling the temperature profile of an extrudate in material extrusion additive manufacturing. *Materials Letters*, 270:127742.

[Luo et al., 2020] Luo, C., Wang, X., Migler, K. B., and Seppala, J. E. (2020). Upper bound of feed rates in thermoplastic material extrusion additive manufacturing. *Additive Manufacturing*, 32:101019.

[MacDonald et al., 2018] MacDonald, E., Burden, E., Walker, J., Kelly, J., Conner, B., Patterson, C., Schmidt, A., and Bader, A. (2018). Spatial Frequency Analysis for Improved Quality in Big Area Additive Manufacturing (BAAM). American Society of Mechanical Engineers Digital Collection.

[Mackay, 2018] Mackay, M. E. (2018). The importance of rheological behavior in the additive manufacturing technique material extrusion. *Journal of Rheology*, 62(6):1549–1561.

[Mackay and Astarita, 1997] Mackay, M. E. and Astarita, G. (1997). Analysis of entry flow to determine elongation flow properties revisited. *Journal of Non-Newtonian Fluid Mechanics*, 70(3):219–235.

[Mackay et al., 2017] Mackay, M. E., Swain, Z. R., Banbury, C. R., Phan, D. D., and Edwards, D. A. (2017). The performance of the hot end in a plasticating 3D printer. *Journal of Rheology*, 61(2):229–236.

[Mahmood et al., 2017] Mahmood, S., Qureshi, A., Goh, K. L., and Talamona, D. (2017). Tensile strength of partially filled FFF printed parts: experimental results. *Rapid Prototyping Journal*, 23(1):122–128. Publisher: Emerald Publishing Limited.

[Maiti and Sharma, 1992] Maiti, S. N. and Sharma, K. K. (1992). Studies on polypropylene composites filled with talc particles. *Journal of Materials Science*, 27(17):4605–4613.

[Majewski and Hopkinson, 2011] Majewski, C. and Hopkinson, N. (2011). Effect of section thickness and build orientation on tensile properties and material characteristics of laser sintered nylon-12 parts. *Rapid Prototyping Journal*, 17(3):176–180.

[Malmberg et al., 2002] Malmberg, A., Gabriel, C., Steffl, T., Münstedt, H., and Löfgren, B. (2002). Long-Chain Branching in Metallocene-Catalyzed Polyethylenes Investigated by Low Oscillatory Shear and Uniaxial Extensional Rheometry. *Macromolecules*, 35(3):1038–1048. Publisher: American Chemical Society.

[Manchado et al., 2005] Manchado, M. A. L., Valentini, L., Biagiotti, J., and Kenny, J. M. (2005). Thermal and mechanical properties of single-walled carbon nanotubes–polypropylene composites prepared by melt processing. *Carbon*, 43(7):1499–1505.

[Martini et al., 2002] Martini, S., Herrera, M. L., and Hartel, R. W. (2002). Effect of cooling rate on crystallization behavior of milk fat fraction/sunflower oil blends. *Journal of the American Oil Chemists' Society*, 79(11):1055–1062.

[Masood et al., 2010] Masood, S. H., Mau, K., and Song, W. Q. (2010). Tensile properties of processed FDM polycarbonate material. *Materials Science Forum*, 654-656:2556–2559.

[Mazzanti et al., 2019] Mazzanti, V., Malagutti, L., and Mollica, F. (2019). FDM 3D Printing of Polymers Containing Natural Fillers: A Review of their Mechanical Properties. *Polymers*, 11(7):1094.

[McIlroy, 2019] McIlroy, C. (2019). A fundamental rule: Determining the importance of flow prior to polymer crystallization. *Physics of Fluids*, 31(11):113103.

[McIlroy and Graham, 2018] McIlroy, C. and Graham, R. S. (2018). Modelling flow-enhanced crystallisation during fused filament fabrication of semi-crystalline polymer melts. *Additive Manufacturing*, 24:323–340.

[McIlroy and Olmsted, 2017a] McIlroy, C. and Olmsted, P. D. (2017a). Deformation of an amorphous polymer during the fused-filament-fabrication method for additive manufacturing. *Journal of Rheology*, 61(2):379–397.

[McIlroy and Olmsted, 2017b] McIlroy, C. and Olmsted, P. D. (2017b). Disentanglement effects on welding behaviour of polymer melts during the fused-filament-fabrication method for additive manufacturing. *Polymer*, 123:376–391.

[McIlroy et al., 2019] McIlroy, C., Seppala, J. E., and Kotula, A. P. (2019). Combining Modeling and Measurements To Predict Crystal Morphology in Material Extrusion. In *Polymer-Based Additive Manufacturing: Recent Developments*, volume 1315 of *ACS Symposium Series*, pages 85–113. American Chemical Society.

[McKinley and Sridhar, 2002] McKinley, G. H. and Sridhar, T. (2002). Filament-Stretching Rheometry of Complex Fluids. *Annual Review of Fluid Mechanics*, 34(1):375–415. _eprint: https://doi.org/10.1146/annurev.fluid.34.083001.125207.

[McKinley and Tripathi, 2000] McKinley, G. H. and Tripathi, A. (2000). How to extract the Newtonian viscosity from capillary breakup measurements in a filament rheometer. *Journal of Rheology*, 44(3):653–670. Publisher: The Society of Rheology.

[McQueen et al., 2022] McQueen, A. D., Ballentine, M. L., May, L. R., Laber, C. H., Das, A., Bortner, M. J., and Kennedy, A. J. (2022). Photocatalytic Degradation of Polycyclic Aromatic Hydrocarbons in Water by 3D Printed TiO2 Composites. *ACS ES&T Water*, 2(1):137–147. Publisher: American Chemical Society.

[Mehrjerdi et al., 2020] Mehrjerdi, A. K., Bashir, T., and Skrifvars, M. (2020). Melt rheology and extrudate swell properties of talc filled polyethylene compounds. *Heliyon*, 6(5):e04060.

[Menyhárd et al., 2009] Menyhárd, A., Gahleitner, M., Varga, J., Bernreitner, K., Jääskeläinen, P., Øysæd, H., and Pukánszky, B. (2009). The influence of nucleus density on optical properties in nucleated isotactic polypropylene. *European Polymer Journal*, 45(11):3138–3148.

[Mervine et al., 2020] Mervine, N., Br tt, K., and Saloni, D. (2020). A Review of Sustainable Materials Used in Thermoplastic Extrusion and Powder Bed Melting Additive Manufacturing. In Mrugalska, B., Trzcielinski, S., Karwowski, W., Di Nicolantonio, M., and Rossi, E., editors, *Advances in Manufacturing, Production Management and Process Control*, Advances in Intelligent Systems and Computing, pages 95–102, Cham. Springer International Publishing.

[Milosevic et al., 2017] Milosevic, M., Stoof, D., and Pickering, K. L. (2017). Characterizing the Mechanical Properties of Fused Deposition Modelling Natural Fiber Recycled Polypropylene Composites. *Journal of Composites Science*, 1(1):7.

[Mohan et al., 2020] Mohan, D., Teong, Z. K., Bakir, A. N., Sajab, M. S., and Kaco, H. (2020). Extending Cellulose-Based Polymers Application in Additive Manufacturing Technology: A Review of Recent Approaches. *Polymers*, 12(9):1876. Number: 9 Publisher: Multidisciplinary Digital Publishing Institute.

[Mohan and Bhattacharyya, 2020] Mohan, V. B. and Bhattacharyya, D. (2020). Mechanical, electrical and thermal performance of hybrid polyethylene-graphene nanoplatelets-polypyrrole composites: a comparative analysis of 3D printed and compression molded samples. *Polymer-Plastics Technology and Materials*, 59(7):780–796. Publisher: Taylor & Francis _eprint: https://doi.org/10.1080/25740881.2019.1695272.

[Mohd Ishak et al., 2001] Mohd Ishak, Z. A., Ariffin, A., and Senawi, R. (2001). Effects of hygrothermal aging and a silane coupling agent on the tensile properties of injection molded short glass fiber reinforced poly(butylene terephthalate) composites. *European Polymer Journal*, 37(8):1635–1647.

[Mostafa et al., 2009] Mostafa, N., Syed, H. M., Igor, S., and Andrew, G. (2009). A Study of Melt Flow Analysis of an ABS-Iron Composite in Fused Deposition Modelling Process. *Tsinghua Science & Technology*, 14:29–37.

[Mukherjee et al., 2018] Mukherjee, R., Habibi, M., Rashed, Z. T., Berbert, O., Shi, X., and Boreyko, J. B. (2018). Oil-Impregnated Hydrocarbon-Based Polymer Films. *Scientific Reports*, 8(1):11698.

[Münstedt and Schwarzl, 2014] Münstedt, H. and Schwarzl, F. R. (2014). Linear Viscoelastic Deformation Behavior in Simple Shear. In Münstedt, H. and Schwarzl, F. R., editors, *Deformation and Flow of Polymeric Materials*, pages 121–187. Springer, Berlin, Heidelberg.

[Münstedt et al., 2011] Münstedt, H., Triebel, C., and Zatloukal, M. (2011). Elastic Properties of Polymer Melts Filled with Nanoparticles. *AIP Conference Proceedings*, 1375(1):201–207. Publisher: American Institute of Physics.

[Nabipour et al., 2020] Nabipour, M., Akhoundi, B., and Saed, A. B. (2020). Manufacturing of polymer/metal composites by fused deposition modeling process with polyethylene. *Journal of Applied Polymer Science*, 137(21):48717. _eprint: https://onlinelibrary.wiley.com/doi/pdf/10.1002/app.48717.

[Naranjo-Lozada et al., 2019] Naranjo-Lozada, J., Ahuett-Garza, H., Orta-Castañón, P., Verbeeten, W. M. H., and Sáiz-González, D. (2019). Tensile properties and failure behavior of chopped and continuous carbon fiber composites produced by additive manufacturing. *Additive Manufacturing*, 26:227–241.

[Nazan et al., 2017] Nazan, M. A., Ramli, F. R., Alkahari, M. R., Abdullah, M. A., and Sudin, M. N. (2017). An exploration of polymer adhesion on 3D printer bed. *IOP Conference Series: Materials Science and Engineering*, 210:012062.

[Nematollahi et al., 2018] Nematollahi, B., Xia, M., Sanjayan, J., and Vijay, P. (2018). Effect of type of fiber on inter-layer bond and flexural strengths of extrusion-based 3D printed geopolymer. In *Materials science forum*, volume 939, pages 155–162. Trans Tech Publ.

[Ngo et al., 2018] Ngo, T. D., Kashani, A., Imbalzano, G., Nguyen, K. T. Q., and Hui, D. (2018). Additive manufacturing (3D printing): A review of materials, methods, applications and challenges. *Composites Part B: Engineering*, 143:172–196.

[Nguyen et al., 2018] Nguyen, N. A., Bowland, C. C., and Naskar, A. K. (2018). A general method to improve 3D-printability and inter-layer adhesion in lignin-based composites. *Applied Materials Today*, 12:138–152.

[Nikzad et al., 2011] Nikzad, M., Masood, S. H., and Sbarski, I. (2011). Thermo-mechanical properties of a highly filled polymeric composites for Fused Deposition Modeling. *Materials & Design*, 32(6):3448–3456.

[Ning et al., 2015] Ning, F., Cong, W., Qiu, J., Wei, J., and Wang, S. (2015). Additive manufacturing of carbon fiber reinforced thermoplastic composites using fused deposition modeling. *Composites Part B: Engineering*, 80:369–378.

[Nogales et al., 2019] Nogales, A., Gutiérrez-Fernández, E., García-Gutiérrez, M.-C., Ezquerra, T. A., Rebollar, E., Šics, I., Malfois, M., Gaidukovs, S., Gecis, E., Celms, K., and Bakradze, G. (2019). Structure Development in Polymers during Fused Filament Fabrication (FFF): An in Situ Small- and Wide-Angle X-ray Scattering Study Using Synchrotron Radiation. *Macromolecules*, 52(24):9715–9723.

[Northcutt et al., 2018] Northcutt, L. A., Orski, S. V., Migler, K. B., and Kotula, A. P. (2018). Effect of processing conditions on crystallization kinetics during materials extrusion additive manufacturing. *Polymer*, 154:182–187.

[Nycz et al., 2020] Nycz, A., Kishore, V., Lindahl, J., Duty, C., Carnal, C., and Kunc, V. (2020). Controlling substrate temperature with infrared heating to improve mechanical properties of large-scale printed parts. *Additive Manufacturing*, 33:101068.

[Olesik et al., 2019] Olesik, P., Godzierz, M., and Kozioł, M. (2019). Preliminary Characterization of Novel LDPE-Based Wear-Resistant Composite Suitable for FDM 3D Printing. *Materials*, 12(16):2520. Number: 16 Publisher: Multidisciplinary Digital Publishing Institute.

[Olowojoba et al., 2016] Olowojoba, G. B., Eslava, S., Gutierrez, E. S., Kinloch, A. J., Mattevi, C., Rocha, V. G., and Taylor, A. C. (2016). In situ thermally reduced graphene oxide/epoxy composites: thermal and mechanical properties. *Applied Nanoscience*, 6(7):1015–1022.

[Oropallo and Piegl, 2016] Oropallo, W. and Piegl, L. A. (2016). Ten challenges in 3D printing. *Engineering with Computers*, 32(1):135–148.

[Osborn et al., 2015] Osborn, T., Zhou, E., Gerzeski, R., Mollenhauer, D., Tandon, G. P., Whitney, T. J., and Iarve, E. V. (2015). Experimental and theoretical evaluation of stiffness properties of fused deposition modeling parts. In *American Society of Composites-30th Technical Conference*.

[Osswald et al., 2018] Osswald, T. A., Puentes, J., and Kattinger, J. (2018). Fused filament fabrication melting model. *Additive Manufacturing*, 22:51–59.

[Owens et al., 2022] Owens, J. T., Das, A., and Bortner, M. J. (2022). Accelerating heat transfer modeling in material extrusion additive manufacturing: From desktop to big area. *Additive Manufacturing*, 55:102853.

[Ozkoc et al., 2005] Ozkoc, G., Bayram, G., and Bayramli, E. (2005). Short glass fiber reinforced ABS and ABS/PA6 composites: Processing and characterization. *Polymer Composites*, 26(6):745–755. _eprint: https://onlinelibrary.wiley.com/doi/pdf/10.1002/pc.20144.

[O'Mahony et al., 2020] O'Mahony, C., Gkartzou, E., Haq, E. U., Koutsoumpis, S., Silien, C., Charitidis, C. A., and Tofail, S. A. M. (2020). Determination of thermal and thermomechanical properties of biodegradable PLA blends: for additive manufacturing process. *Journal of Thermal Analysis and Calorimetry*.

[Palanikumar et al., 2020] Palanikumar, K., Mudhukrishnan, M., and Soorya Prabha, P. (2020). Technologies in additive manufacturing for fiber reinforced composite materials: a review. *Current Opinion in Chemical Engineering*, 28:51–59.

[Pan et al., 2018] Pan, G.-T., Chong, S., Tsai, H.-J., Lu, W.-H., and Yang, T. C.-K. (2018). The Effects of Iron, Silicon, Chromium, and Aluminum Additions on the Physical and Mechanical Properties of Recycled 3D Printing Filaments. *Advances in Polymer Technology*, 37(4):1176–1184.

[Panin et al., 2020] Panin, S. V., Buslovich, D. G., Kornienko, L. A., Aleksenko, V. O., Dontsov, Y. V., Ovechkin, B. B., and Shil'ko, S. V. (2020). Comparative Analysis of Tribological and Mechanical Properties of Extrudable Polymer–Polymer UHMWPE Composites Fabricated by 3D Printing and Hot-Pressing Methods. *Journal of Friction and Wear*, 41(3):228–235.

[Panin et al., 2019] Panin, S. V., Buslovich, D. G., Kornienko, L. A., Alexenko, V. O., Dontsov, Y. V., and Shil'ko, S. V. (2019). Structure, as well as the Tribological and

Mechanical Properties, of Extrudable Polymer-Polymeri UHMWPE Composites for 3D Printing. *Journal of Friction and Wear*, 40(2):107–115.

[Papazetis and Vosniakos, 2019] Papazetis, G. and Vosniakos, G.-C. (2019). Mapping of deposition-stable and defect-free additive manufacturing via material extrusion from minimal experiments. *The International Journal of Advanced Manufacturing Technology*, 100(9):2207–2219.

[Papon and Haque, 2019] Papon, E. A. and Haque, A. (2019). Fracture toughness of additively manufactured carbon fiber reinforced composites. *Additive Manufacturing*, 26:41–52.

[Parandoush and Lin, 2017] Parandoush, P. and Lin, D. (2017). A review on additive manufacturing of polymer-fiber composites. *Composite Structures*, 182:36–53.

[Parsons et al., 2019] Parsons, P., Larimore, Z., Muhammed, F., and Mirotznik, M. (2019). Fabrication of low dielectric constant composite filaments for use in fused filament fabrication 3D printing. *Additive Manufacturing*, 30:100888.

[Peacock, 2000] Peacock, A. (2000). *Handbook of Polyethylene: Structures: Properties, and Applications*. CRC Press. Google-Books-ID: JU1ZDwAAQBAJ.

[Peng et al., 2019a] Peng, F., Jiang, H., Woods, A., Joo, P., Amis, E. J., Zacharia, N. S., and Vogt, B. D. (2019a). 3D Printing with Core–Shell Filaments Containing High or Low Density Polyethylene Shells. *ACS Applied Polymer Materials*, 1(2):275–285.

[Peng et al., 2018] Peng, F., Vogt, B. D., and Cakmak, M. (2018). Complex flow and temperature history during melt extrusion in material extrusion additive manufacturing. *Additive Manufacturing*, 22:197–206.

[Peng et al., 2019b] Peng, X., He, H., Jia, Y., Liu, H., Geng, Y., Huang, B., and Luo, C. (2019b). Shape memory effect of three-dimensional printed products based on polypropylene/nylon 6 alloy. *Journal of Materials Science*, 54(12):9235–9246.

[Penumakala et al., 2020] Penumakala, P. K., Santo, J., and Thomas, A. (2020). A critical review on the fused deposition modeling of thermoplastic polymer composites. *Composites Part B: Engineering*, 201:108336.

[Peres et al., 2016] Peres, A. M., Pires, R. R., and Oréfice, R. L. (2016). Evaluation of the effect of reprocessing on the structure and properties of low density polyethylene/thermoplastic starch blends. *Carbohydrate polymers*, 136:210–215. Publisher: Elsevier.

[Petersmann et al., 2020] Petersmann, S., Erdely, P., Feuchter, M., Wieme, T., Arbeiter, F., and Spoerk, M. (2020). Process-induced morphological features in material extrusion-based additive manufacturing of polypropylene. *Additive Manufacturing*, page 101384.

[Peterson, 2019] Peterson, A. M. (2019). Review of acrylonitrile butadiene styrene in fused filament fabrication: A plastics engineering-focused perspective. *Additive Manufacturing*, 27:363–371.

[Peterson et al., 2001] Peterson, J. D., Vyazovkin, S., and Wight, C. A. (2001). Kinetics of the Thermal and Thermo-Oxidative Degradation of Polystyrene, Polyethylene and Poly(propylene). *Macromolecular Chemistry and Physics*, 202(6):775–784.

[Peñas et al., 2020] Peñas, M. I., Calafel, M. I., Aguirresarobe, R. H., Tierno, M., Conde, J. I., Pascual, B., and Santamaría, A. (2020). How Is Rheology Involved in 3D Printing of Phase-Separated PVC-Acrylate Copolymers Obtained by Free Radical Polymerization. *Polymers*, 12(9):2070. Number: 9 Publisher: Multidisciplinary Digital Publishing Institute.

[Pham and Gault, 1998] Pham, D. T. and Gault, R. S. (1998). A comparison of rapid prototyping technologies. *International Journal of machine tools and manufacture*, 38(10-11):1257–1287.

[Phan et al., 2020] Phan, D. D., Horner, J. S., Swain, Z. R., Beris, A. N., and Mackay, M. E. (2020). Computational fluid dynamics simulation of the melting process in the fused filament fabrication additive manufacturing technique. *Additive Manufacturing*, 33:101161.

[Phan et al., 2018] Phan, D. D., Swain, Z. R., and Mackay, M. E. (2018). Rheological and heat transfer effects in fused filament fabrication. *Journal of Rheology*, 62(5):1097–1107.

[Phillips, 2000] Phillips, R. A. (2000). Macromorphology of polypropylene homopolymer tacticity mixtures. *Journal of Polymer Science Part B: Polymer Physics*, 38(15):1947–1964. _eprint: https://onlinelibrary.wiley.com/doi/pdf/10.1002/1099-0488%2820000801%2938%3A15%3C1947%3A%3AAID-POLB10%3E3.0.CO%3B2-M.

[Piccarolo et al., 1992] Piccarolo, S., Saiu, M., Brucato, V., and Titomanlio, G. (1992). Crystallization of polymer melts under fast cooling. II. High-purity iPP. *Journal of Applied Polymer Science*, 46(4):625–634.

[Pickering and Stoof, 2017] Pickering, K. and Stoof, D. (2017). Sustainable Composite Fused Deposition Modelling Filament Using Post-Consumer Recycled Polypropylene. *Journal of Composites Science*, 1(2):17.

[Pigeonneau et al., 2020] Pigeonneau, F., Xu, D., Vincent, M., and Agassant, J. F. (2020). Heating and flow computations of an amorphous polymer in the liquefier of a material extrusion 3D printer. *Additive Manufacturing*, 32:101001.

[Piorkowska and Rutledge, 2013] Piorkowska, E. and Rutledge, G. C. (2013). *Handbook of Polymer Crystallization*. John Wiley & Sons. Google-Books-ID: SrvIAgAAQBAJ.

[Pisipati and Baird, 1984] Pisipati, R. and Baird, D. G. (1984). Correlation of Non-Linear Rheological Properties of Polymer Melts With Weld-Line Strength. In Astarita, G. and Nicolais, L., editors, *Polymer Processing and Properties*, pages 215–228. Springer US, Boston, MA.

[Pokluda et al., 1997] Pokluda, O., Bellehumeur, C. T., and Vlachopoulos, J. (1997). Modification of Frenkel's model for sintering. *AIChE Journal*, 43(12):3253–3256. _eprint: https://aiche.onlinelibrary.wiley.com/doi/pdf/10.1002/aic.690431213.

[Polychronopoulos and Vlachopoulos, 2018] Polychronopoulos, N. D. and Vlachopoulos, J. (2018). Polymer processing and rheology. *Functional Polymers. Polymers and Polymeric Composites: A Reference Series, Springer, Cham*, pages 133–180.

[Polychronopoulos and Vlachopoulos, 2020] Polychronopoulos, N. D. and Vlachopoulos, J. (2020). The role of heating and cooling in viscous sintering of pairs of spheres and pairs of cylinders. *Rapid Prototyping Journal*, 26(4):719–726. Publisher: Emerald Publishing Limited.

[Popescu et al., 2018] Popescu, D., Zapciu, A., Amza, C., Baciu, F., and Marinescu, R. (2018). FDM process parameters influence over the mechanical properties of polymer specimens: A review. *Polymer Testing*, 69:157–166.

[Pourali and Peterson, 2019] Pourali, M. and Peterson, A. M. (2019). Thermal Modeling of Material Extrusion Additive Manufacturing. In *Polymer-Based Additive Manufacturing:*

Recent Developments, volume 1315 of *ACS Symposium Series*, pages 115–130. American Chemical Society.

[Prajapati et al., 2019] Prajapati, H., Chalise, D., Ravoori, D., Taylor, R. M., and Jain, A. (2019). Improvement in build-direction thermal conductivity in extrusion-based polymer additive manufacturing through thermal annealing. *Additive Manufacturing*, 26:242–249.

[Prajapati et al., 2018] Prajapati, H., Ravoori, D., and Jain, A. (2018). Measurement and modeling of filament temperature distribution in the standoff gap between nozzle and bed in polymer-based additive manufacturing. *Additive Manufacturing*, 24:224–231.

[Prajapati et al., 2020] Prajapati, H., Salvi, S., Ravoori, D., and Jain, A. (2020). Measurement of the in-plane temperature field on the build plate during polymer extrusion additive manufacturing using infrared thermometry. *Polymer Testing*, page 106866.

[Prasad and Smyth, 2016] Prasad, L. K. and Smyth, H. (2016). 3D Printing technologies for drug delivery: a review. *Drug Development and Industrial Pharmacy*, 42(7):1019–1031.

[Premalal et al., 2002] Premalal, H. G. B., Ismail, H., and Baharin, A. (2002). Comparison of the mechanical properties of rice husk powder filled polypropylene composites with talc filled polypropylene composites. *Polymer Testing*, 21(7):833–839.

[Pritchard et al., 2019] Pritchard, Z. D., Beer, M. P. d., Whelan, R. J., Scott, T. F., and Burns, M. A. (2019). Modeling and Correcting Cure-Through in Continuous Stereolithographic 3D Printing. *Advanced Materials Technologies*, 4(12):1900700.

[Pu et al., 2021] Pu, J., McIlroy, C., Jones, A., and Ashcroft, I. (2021). Understanding mechanical properties in fused filament fabrication of polyether ether ketone. *Additive Manufacturing*, 37:101673.

[Publishing, 2018] Publishing, S. (2018). Additive Manufacturing with Polymers and Plastics. Library Catalog: www.globenewswire.com.

[Purwanti et al., 2011] Purwanti, N., Smiddy, M., Jan van der Goot, A., de Vries, R., Alting, A., and Boom, R. (2011). Modulation of rheological properties by heat-induced aggregation of whey protein solution. *Food Hydrocolloids*, 25(6):1482–1489.

[Qian and McKenna, 2018] Qian, Z. and McKenna, G. B. (2018). Expanding the application of the van Gurp-Palmen plot: New insights into polymer melt rheology. *Polymer*, 155:208–217.

[Raj et al., 1990] Raj, R. G., Kokta, B. V., and Daneault, C. (1990). The use of Isocyanate as a Bonding Agent to Improve the Mechanical Properties of Polyethylene-Wood Fiber Composites. *International Journal of Polymeric Materials and Polymeric Biomaterials*, 14(3-4):223–234.

[Ramanath et al., 2007] Ramanath, H. S., Chandrasekaran, M., Chua, C. K., Leong, K. F., and Shah, K. D. (2007). Modelling of extrusion behaviour of biopolymer and composites in fused deposition modelling. *Key Engineering Materials*, 334-335:1241–1244.

[Ramanath et al., 2008] Ramanath, H. S., Chua, C. K., Leong, K. F., and Shah, K. D. (2008). Melt flow behaviour of poly- -caprolactone in fused deposition modelling. *Journal of Materials Science: Materials in Medicine*, 19(7):2541–2550.

[Ramli et al., 2016] Ramli, M. S., Wahab, M. S., Ahmad, M., and Bala, A. S. (2016). FDM preparation of bio-compatible UHMWPE polymer for artificial implant. *The International Journal of Advanced Manufacturing Technology*, 11(8):5473–5480.

[Ramsteiner et al., 1983] Ramsteiner, F., Kanig, G., Heckmann, W., and Gruber, W. (1983). Improved low temperature impact strength of polypropylene by modification with polyethylene. *Polymer*, 24(3):365–370.

[Ravoori et al., 2018] Ravoori, D., Alba, L., Prajapati, H., and Jain, A. (2018). Investigation of process-structure-property relationships in polymer extrusion based additive manufacturing through in situ high speed imaging and thermal conductivity measurements. *Additive Manufacturing*, 23:132–139.

[Ravoori et al., 2019a] Ravoori, D., Lowery, C., Prajapati, H., and Jain, A. (2019a). Experimental and theoretical investigation of heat transfer in platform bed during polymer extrusion based additive manufacturing. *Polymer Testing*, 73:439–446.

[Ravoori et al., 2019b] Ravoori, D., Prajapati, H., Talluru, V., Adnan, A., and Jain, A. (2019b). Nozzle-integrated pre-deposition and post-deposition heating of previously deposited layers in polymer extrusion based additive manufacturing. *Additive Manufacturing*, 28:719–726.

[Reiter and Sommer, 2003] Reiter, G. and Sommer, J.-U. (2003). *Polymer Crystallization: Obervations, Concepts and Interpretations*. Springer Science & Business Media.

[Reiter and Strobl, 2007] Reiter, G. and Strobl, G. R. (2007). *Progress in Understanding of Polymer Crystallization*. Springer. Google-Books-ID: 3KttCQAAQBAJ.

[Ren et al., 2008] Ren, X., Wang, X. Q., Sui, G., Zhong, W. H., Fuqua, M. A., and Ulven, C. A. (2008). Effects of carbon nanofibers on crystalline structures and properties of ultrahigh molecular weight polyethylene blend fabricated using twin-screw extrusion. *Journal of Applied Polymer Science*, 107(5):2837–2845. _eprint: https://onlinelibrary.wiley.com/doi/pdf/10.1002/app.27354.

[Reynolds et al., 2018] Reynolds, C., Thompson, R., and McLeish, T. (2018). Pressure and shear rate dependence of the viscosity and stress relaxation of polymer melts. *Journal of Rheology*, 62(2):631–642. Publisher: The Society of Rheology.

[Richardson, 1970] Richardson, S. (1970). The die swell phenomenon. *Rheologica Acta*, 9(2):193–199. Publisher: Springer.

[Rocha et al., 2014] Rocha, C. R., Perez, A. R. T., Roberson, D. A., Shemelya, C. M., MacDonald, E., and Wicker, R. B. (2014). Novel ABS-based binary and ternary polymer blends for material extrusion 3D printing. *Journal of Materials Research*, 29(17):1859–1866. Publisher: Cambridge University Press.

[Rodriguez et al., 2000] Rodriguez, J. F., Thomas, J. P., and Renaud, J. E. (2000). Characterization of the mesostructure of fused-deposition acrylonitrile-butadiene-styrene materials. *Rapid Prototyping Journal*, 6:175–186.

[Rodriguez et al., 2003] Rodriguez, J. F., Thomas, J. P., and Renaud, J. E. (2003). Design of Fused-Deposition ABS Components for Stiffness and Strength. *Journal of Mechanical Design*, 125(3):545–551. Publisher: American Society of Mechanical Engineers Digital Collection.

[Romeijn et al., 2020] Romeijn, T., Wells, B., Wei, D., and Paul, G. (2020). Investigation into the shear property of thin-walled additively manufactured structures using staggered fused filament fabrication. *Additive Manufacturing*, 35:101259.

[Rosen, 2007] Rosen, D. W. (2007). Computer-Aided Design for Additive Manufacturing of Cellular Structures. *Computer-Aided Design and Applications*, 4(5):585–594. Publisher: Taylor & Francis _eprint: https://doi.org/10.1080/16864360.2007.10738493.

[Roy, 2010] Roy, R. K. (2010). *A Primer on the Taguchi Method*. Society of Manufacturing Engineers. Google-Books-ID: k5VBsRZfzQsC.

[Rubenstein and Colby, 2003] Rubenstein, M. and Colby, R. H. (2003). *Polymer physics*. Oxford University Press, New York.

[Russell et al., 2018] Russell, T., Heller, B., Jack, D. A., and Smith, D. E. (2018). Prediction of the Fiber Orientation State and the Resulting Structural and Thermal Properties of Fiber Reinforced Additive Manufactured Composites Fabricated Using the Big Area Additive Manufacturing Process. *Journal of Composites Science*, 2(2):26. Number: 2 Publisher: Multidisciplinary Digital Publishing Institute.

[Rwei et al., 2019] Rwei, S.-P., Ranganathan, P., and Lee, Y.-H. (2019). Isothermal Crystallization Kinetics Study of Fully Aliphatic PA6 Copolyamides: Effect of Novel Long-Chain Polyamide Salt as a Comonomer. *Polymers*, 11(3):472. Number: 3 Publisher: Multidisciplinary Digital Publishing Institute.

[Sabyrov et al., 2020] Sabyrov, N., Abilgaziyev, A., and Ali, M. H. (2020). Enhancing interlayer bonding strength of FDM 3D printing technology by diode laser-assisted system. *International Journal of Advanced Manufacturing Technology*, 108(1-2):603–611. Publisher: Springer.

[Sadiku et al., 2017] Sadiku, R., Ibrahim, D., Agboola, O., Owonubi, S. J., Fasiku, V. O., Kupolati, W. K., Jamiru, T., Eze, A. A., Adekomaya, O. S., Varaprasad, K., Agwuncha, S. C., Reddy, A. B., Manjula, B., Oboirien, B., Nkuna, C., Dludlu, M., Adeyeye, A., Osholana, T. S., Phiri, G., Durowoju, O., Olubambi, P. A., Biotidara, F., Ramakokovhu, M., Shongwe, B., and Ojijo, V. (2017). Automotive components composed of polyolefins. In Ugbolue, S. C. O., editor, *Polyolefin Fibres (Second Edition)*, The Textile Institute Book Series, pages 449–496. Woodhead Publishing.

[Sanatgar et al., 2017] Sanatgar, R. H., Campagne, C., and Nierstrasz, V. (2017). Investigation of the adhesion properties of direct 3D printing of polymers and nanocomposites on textiles: Effect of FDM printing process parameters. *Applied Surface Science*, 403:551–563.

[Sanchez et al., 2019] Sanchez, L. C., Beatrice, C. A. G., Lotti, C., Marini, J., Bettini, S. H. P., and Costa, L. C. (2019). Rheological approach for an additive manufacturing printer based on material extrusion. *The International Journal of Advanced Manufacturing Technology*, 105(5):2403–2414.

[Sanders et al., 2020] Sanders, J. E., Wang, L., and Gardner, D. J. (2020). Comparing mechanical properties of impact modified polypropylene-copolymer (IMPP) from injection molding (IM) and fused layer modeling (FLM) processes. *Rapid Prototyping Journal*, ahead-of-print(ahead-of-print).

[Sauer, 2018] Sauer, M. (2018). *Evaluation of the Mechanical Properties of 3D Printed Carbon Fiber Composites*. Master of Science (MS), South Dakota State University.

[Savandaiah et al., 2021] Savandaiah, C., Maurer, J., Gall, M., Haider, A., Steinbichler, G., and Sapkota, J. (2021). Impact of processing conditions and sizing on the thermomechanical and morphological properties of polypropylene/carbon fiber composites fabricated by material extrusion additive manufacturing. *Journal of Applied Polymer Science*, 138(16):50243. _eprint: https://onlinelibrary.wiley.com/doi/pdf/10.1002/app.50243.

[Schawe, 2017] Schawe, J. E. K. (2017). Mobile amorphous, rigid amorphous and crystalline fractions in isotactic polypropylene during fast cooling. *Journal of Thermal Analysis and Calorimetry*, 127(1):931–937.

[Schirmeister et al., 2021a] Schirmeister, C. G., Hees, T., Dolynchuk, O., Licht, E. H., Thurn-Albrecht, T., and Muelhaupt, R. (2021a). Digitally Tuned Multidirectional All-Polyethylene Composites via Controlled 1D Nanostructure Formation during Extrusion-Based 3D Printing. *ACS Applied Polymer Materials*, 3(3):1675–1686. Publisher: American Chemical Society.

[Schirmeister et al., 2019] Schirmeister, C. G., Hees, T., Licht, E. H., and Mülhaupt, R. (2019). 3D printing of high density polyethylene by fused filament fabrication. *Additive Manufacturing*, 28:152–159.

[Schirmeister et al., 2021b] Schirmeister, C. G., Schächtele, S., Keßler, Y., Hees, T., Köhler, R., Schmitz, K., Licht, E. H., and Muelhaupt, R. (2021b). Low Warpage Nanophase-Separated Polypropylene/Olefinic Elastomer Reactor Blend Composites with Digitally Tuned Glass Fiber Orientation by Extrusion-Based Additive Manufacturing. *ACS Applied Polymer Materials*. Publisher: American Chemical Society.

[Schnittker et al., 2019] Schnittker, K., Arrieta, E., Jimenez, X., Espalin, D., Wicker, R. B., and Roberson, D. A. (2019). Integrating digital image correlation in mechanical testing for the materials characterization of big area additive manufacturing feedstock. *Additive Manufacturing*, 26:129–137.

[Schultz, 1984] Schultz, J. M. (1984). Microstructural aspects of failure in semicrystalline polymers. *Polymer Engineering & Science*, 24(10):770–785.

[Seo et al., 2019] Seo, J., Gohn, A. M., Dubin, O., Takahashi, H., Hasegawa, H., Sato, R., Rhoades, A. M., Schaake, R. P., and Colby, R. H. (2019). Isothermal crystallization of poly(ether ether ketone) with different molecular weights over a wide temperature range. *POLYMER CRYSTALLIZATION*, 2(1):e10055. _eprint: https://onlinelibrary.wiley.com/doi/pdf/10.1002/pcr2.10055.

[Seppala et al., 2017] Seppala, J. E., Han, S. H., Hillgartner, K. E., Davis, C. S., and Migler, K. B. (2017). Weld formation during material extrusion additive manufacturing. *Soft Matter*, 13(38):6761–6769.

[Seppala and Migler, 2016] Seppala, J. E. and Migler, K. D. (2016). Infrared thermography of welding zones produced by polymer extrusion additive manufacturing. *Additive manufacturing*, 12:71–76.

[Serdeczny et al., 2021] Serdeczny, M., Comminal, R., Pedersen, D. B., and Spangenberg, J. (2021). Influence of Fibers on the Flow Through the Hot-End in Material Extrusion Additive Manufacturing. In Meboldt, M. and Klahn, C., editors, *Industrializing Additive Manufacturing*, International Conference on Additive Manufacturing in Products and Applications, pages 251–267, Zurich, Switzerland. Springer International Publishing, Cham.

[Serdeczny et al., 2020a] Serdeczny, M. P., Comminal, R., Mollah, M. T., Pedersen, D. B., and Spangenberg, J. (2020a). Numerical modeling of the polymer flow through the hot-end in filament-based material extrusion additive manufacturing. *Additive Manufacturing*, 36:101454.

[Serdeczny et al., 2018a] Serdeczny, M. P., Comminal, R., Pedersen, D. B., and Spangenberg, J. (2018a). Experimental validation of a numerical model for the strand shape in material extrusion additive manufacturing. *Additive Manufacturing*, 24:145–153.

[Serdeczny et al., 2018b] Serdeczny, M. P., Comminal, R., Pedersen, D. B., and Spangenberg, J. (2018b). Numerical Study of the Impact of Shear Thinning Behaviour on the Strand Deposition Flow in the Extrusion-Based Additive Manufacturing. In Billington, D., Leach, R. K., Phillips, D., Riemer, O., and Savio, E., editors, *Proceedings of the 18th*

International Conference of the European Society for Precision Engineering and Nanotechnology, pages 283–284, Venice, Italy. The European Society for Precision Engineering and Nanotechnology.

[Serdeczny et al., 2019a] Serdeczny, M. P., Comminal, R., Pedersen, D. B., and Spangenberg, J. (2019a). Experimental analysis of the filament feeding force in material extrusion additive manufacturing. In Bernard, A., Leach, R. K., Pedersen, D. B., and Taylor, J. S., editors, *Proceedings of the Joint Special Interest Group meeting between euspen and ASPE Advancing Precision in Additive Manufacturing (2019)*, pages 141–145, Ecole Centrale de Nantes, Nantes, France. The European Society for Precision Engineering and Nanotechnology.

[Serdeczny et al., 2019b] Serdeczny, M. P., Comminal, R., Pedersen, D. B., and Spangenberg, J. (2019b). Numerical simulations of the mesostructure formation in material extrusion additive manufacturing. *Additive Manufacturing*, 28:419–429.

[Serdeczny et al., 2020b] Serdeczny, M. P., Comminal, R., Pedersen, D. B., and Spangenberg, J. (2020b). Experimental and analytical study of the polymer melt flow through the hotend in material extrusion additive manufacturing. *Additive Manufacturing*, 32:100997.

[Shadvar et al., 2019] Shadvar, N., Foroozmehr, E., Badrossamay, M., Amouhadi, I., and Dindarloo, A. S. (2019). Computational analysis of the extrusion process of fused deposition modeling of acrylonitrile-butadiene-styrene. *International Journal of Material Forming*.

[Shahmirzadi et al., 2016] Shahmirzadi, S. R., Yousefi, A. A., and Naderpour, N. (2016). Morphology and Rheological Properties of Copper-Polypropylene Composite as a Candidate for Fusion Deposition Modeling (FDM) Filament. page 3, Islamic Azad University, Tehran, Iran.

[Shahriar et al., 2017] Shahriar, B. B., France, C., Valerie, N., Arthur, C., and Christian, G. (2017). Toward improvement of the properties of parts manufactured by FFF (fused filament fabrication) through understanding the influence of temperature and rheological behaviour on the coalescence phenomenon. *AIP Conference Proceedings*, 1896(1):040008. Publisher: American Institute of Physics.

[Shenoy, 1999] Shenoy, A. V. (1999). *Rheology of Filled Polymer Systems*. Springer Netherlands.

[Shenoy et al., 2005] Shenoy, S. L., Bates, W. D., and Wnek, G. (2005). Correlations between electrospinnability and physical gelation. *Polymer*, 46(21):8990–9004.

[Sheoran and Kumar, 2020] Sheoran, A. J. and Kumar, H. (2020). Fused Deposition modeling process parameters optimization and effect on mechanical properties and part quality: Review and reflection on present research. *Materials Today: Proceedings*, 21:1659–1672.

[Sheth et al., 2017] Sheth, S., Taylor, R. M., and Adluru, H. (2017). Numerical investigation of stiffness properties of fdm parts as a function of raster orientation. In *Proceedings of the 28th Annual International Solid Freeform Fabrication Symposium*, Austin, Texas.

[Shibryaeva, 2012] Shibryaeva, L. (2012). Thermal Oxidation of Polypropylene and Modified Polypropylene - Structure Effects. *Polypropylene*.

[Shih et al., 2019] Shih, C.-C., Burnette, M., Staack, D., Wang, J., and Tai, B. L. (2019). Effects of cold plasma treatment on interlayer bonding strength in FFF process. *Additive Manufacturing*, 25:104–111.

[Shmueli et al., 2019a] Shmueli, Y., Jiang, J., Zhou, Y., Xue, Y., Chang, C.-C., Yuan, G., Satija, S. K., Lee, S., Nam, C.-Y., Kim, T., Marom, G., Gersappe, D., and Rafailovich, M. H. (2019a). Simultaneous in Situ X-ray Scattering and Infrared Imaging of Polymer Extrusion in Additive Manufacturing. *ACS Applied Polymer Materials*, 1(6):1559–1567. Publisher: American Chemical Society.

[Shmueli et al., 2019b] Shmueli, Y., Lin, Y.-C., Lee, S., Zhernenkov, M., Tannenbaum, R., Marom, G., and Rafailovich, M. H. (2019b). In Situ Time-Resolved X-ray Scattering Study of Isotactic Polypropylene in Additive Manufacturing. *ACS Applied Materials & Interfaces*, 11(40):37112–37120. Publisher: American Chemical Society.

[Shmueli et al., 2020] Shmueli, Y., Lin, Y.-C., Zuo, X., Guo, Y., Lee, S., Freychet, G., Zhernenkov, M., Kim, T., Tannenbaum, R., Marom, G., Gersappe, D., and Rafailovich, M. H. (2020). In-situ X-ray scattering study of isotactic polypropylene/graphene nanocomposites under shear during fused deposition modeling 3D printing. *Composites Science and Technology*, page 108227.

[Shulga et al., 2020] Shulga, E., Karamov, R., S. Sergeichev, I., D. Konev, S., I. Shurygina, L., S. Akhatov, I., D. Shandakov, S., and G. Nasibulin, A. (2020). Fused Fila-

ment Fabricated Polypropylene Composite Reinforced by Aligned Glass Fibers. *Materials*, 13(16):3442. Number: 16 Publisher: Multidisciplinary Digital Publishing Institute.

[Silva et al., 2021] Silva, P. A. P., da Silva, A. B., Erbetta, C. D. A. C., Santos, J. P. F., de Sousa, R. G., and Oréfice, R. L. (2021). 3D printability of highly ductile poly(ethylene glycol-co-cyclohexane-1,4-dimethanol terephthalate)-EMAA blends. *Polymer Engineering & Science*, 61(6):1695–1705. _eprint: https://onlinelibrary.wiley.com/doi/pdf/10.1002/pen.25693.

[Silvestre et al., 1999] Silvestre, C., Cimmino, S., D'Alma, E., Di Lorenzo, M. L., and Di Pace, E. (1999). Crystallization of isotactic polypropylene/natural terpene resins blends. *Polymer*, 40(18):5119–5128.

[Silvestre et al., 2007] Silvestre, C., Cimmino, S., Duraccio, D., and Schick, C. (2007). Isothermal Crystallization of Isotactic Poly(propylene) Studied by Superfast Calorimetry. *Macromolecular Rapid Communications*, 28(7):875–881.

[Singh et al., 2019a] Singh, A. K., Deptula, A. J., Anawal, R., Doddamani, M., and Gupta, N. (2019a). Additive Manufacturing of Three-Phase Syntactic Foams Containing Glass Microballoons and Air Pores. *JOM*, 71(4):1520–1527.

[Singh et al., 2019b] Singh, R., Kumar, R., Tiwari, S., Vishwakarma, S., Kakkar, S., Rajora, V., and Bhatoa, S. (2019b). On secondary recycling of ZrO2-reinforced HDPE filament prepared from domestic waste for possible 3-D printing of bearings:. *Journal of Thermoplastic Composite Materials*.

[Sirisinha, 1997] Sirisinha, C. (1997). A review of extrudate swell in polymers. *J. Sci. Soc, Thailand*, 23:259–280.

[Snijkers et al., 2015] Snijkers, F., Pasquino, R., Olmsted, P. D., and Vlassopoulos, D. (2015). Perspectives on the viscoelasticity and flow behavior of entangled linear and branched polymers. *Journal of Physics: Condensed Matter*, 27(47):473002. Publisher: IOP Publishing.

[Sodeifian et al., 2019] Sodeifian, G., Ghaseminejad, S., and Yousefi, A. A. (2019). Preparation of polypropylene/short glass fiber composite as Fused Deposition Modeling (FDM) filament. *Results in Physics*, 12:205–222.

[Spiegel and Paulik, 2020] Spiegel, G. and Paulik, C. (2020). Polypropylene Copolymers Designed for Fused Filament Fabrication 3D-Printing. *Macromolecular Reaction Engineering*, 14(1):1900044. _eprint: https://onlinelibrary.wiley.com/doi/pdf/10.1002/mren.201900044.

[Spoerk et al., 2019a] Spoerk, M., Arbeiter, F., Raguž, I., Holzer, C., and Gonzalez-Gutierrez, J. (2019a). Mechanical Recyclability of Polypropylene Composites Produced by Material Extrusion-Based Additive Manufacturing. *Polymers*, 11(8):1318. Number: 8 Publisher: Multidisciplinary Digital Publishing Institute.

[Spoerk et al., 2018a] Spoerk, M., Gonzalez-Gutierrez, J., Lichal, C., Cajner, H., Berger, G. R., Schuschnigg, S., Cardon, L., and Holzer, C. (2018a). Optimisation of the Adhesion of Polypropylene-Based Materials during Extrusion-Based Additive Manufacturing. *Polymers*, 10(5):490.

[Spoerk et al., 2020] Spoerk, M., Holzer, C., and Gonzalez-Gutierrez, J. (2020). Material extrusion-based additive manufacturing of polypropylene: A review on how to improve dimensional inaccuracy and warpage. *Journal of Applied Polymer Science*, 137(12):48545. Publisher: Wiley Online Library.

[Spoerk et al., 2017] Spoerk, M., Sapkota, J., Weingrill, G., Fischinger, T., Arbeiter, F., and Holzer, C. (2017). Shrinkage and Warpage Optimization of Expanded-Perlite-Filled Polypropylene Composites in Extrusion-Based Additive Manufacturing. *Macromolecular Materials and Engineering*, 302(10):1700143.

[Spoerk et al., 2019b] Spoerk, M., Savandaiah, C., Arbeiter, F., Sapkota, J., and Holzer, C. (2019b). Optimization of mechanical properties of glass-spheres-filled polypropylene composites for extrusion-based additive manufacturing. *Polymer Composites*, 40(2):638–651.

[Spoerk et al., 2018b] Spoerk, M., Savandaiah, C., Arbeiter, F., Traxler, G., Cardon, L., Holzer, C., and Sapkota, J. (2018b). Anisotropic properties of oriented short carbon fibre filled polypropylene parts fabricated by extrusion-based additive manufacturing. *Composites Part A: Applied Science and Manufacturing*, 113:95–104.

[Spreeman et al., 2019] Spreeman, M. E., Stretz, H. A., and Dadmun, M. D. (2019). Role of compatibilizer in 3D printing of polymer blends. *Additive Manufacturing*, 27:267–277.

[Srinivas et al., 2018] Srinivas, V., van Hooy-Corstjens, C. S. J., and Harings, J. A. W. (2018). Correlating molecular and crystallization dynamics to macroscopic fusion and thermodynamic stability in fused deposition modeling; a model study on polylactides. *Polymer*, 142:348–355.

[Srinivas et al., 2020] Srinivas, V., van Hooy-Corstjens, C. S. J., Rastogi, S., and Harings, J. A. W. (2020). Promotion of molecular diffusion and/or crystallization in fused deposition modeled poly(lactide) welds. *Polymer*, 202:122637.

[Stadler et al., 2006] Stadler, F. J., Piel, C., Klimke, K., Kaschta, J., Parkinson, M., Wilhelm, M., Kaminsky, W., and Münstedt, H. (2006). Influence of Type and Content of Various Comonomers on Long-Chain Branching of Ethene/ -Olefin Copolymers. *Macromolecules*, 39(4):1474–1482. Publisher: American Chemical Society.

[Stan et al., 2019a] Stan, F., Stanciu, N.-V., and Fetecau, C. (2019a). On the 3D Printability of Multi-Walled Carbon Nanotube/High Density Polyethylene Composites. American Society of Mechanical Engineers Digital Collection.

[Stan et al., 2019b] Stan, F., Stanciu, N.-V., Fetecau, C., and Sandu, I.-L. (2019b). Mechanical Recycling of Low-Density Polyethylene/Carbon Nanotube Composites and Its Effect on Material Properties. *Journal of Manufacturing Science and Engineering*, 141(9). Publisher: American Society of Mechanical Engineers Digital Collection.

[Stanciu et al., 2018] Stanciu, N.-V., Stan, F., Fetecau, C., and Serban, A. (2018). Fabrication and characterization of LDPE and HDPE filaments for 3D printing. *Technical Sciences*, 3(4):299–312.

[Stanciu et al., 2019] Stanciu, N.-V., Stan, F., Fetecau, C., and Susac, F. (2019). On the Feasibility of Printing 3D Composite Objects Based on Polypropylene/Multi-walled Carbon Nanotubes. *MATEC Web of Conferences*, 290:03017.

[Stansbury and Idacavage, 2016] Stansbury, J. W. and Idacavage, M. J. (2016). 3D printing with polymers: Challenges among expanding options and opportunities. *Dental Materials*, 32(1):54–64.

[Stoof and Pickering, 2018] Stoof, D. and Pickering, K. (2018). Sustainable composite fused deposition modelling filament using recycled pre-consumer polypropylene. *Composites Part B: Engineering*, 135:110–118.

[Stoof and Pickering, 2017] Stoof, D. and Pickering, K. L. (2017). 3D Printing of Natural Fibre Reinforced Recycled Polypropylene. In *Processing and Fabrication of Advanced Materials - XXV*, pages 668–691. The University of Auckland.

[Strapasson et al., 2005] Strapasson, R., Amico, S. C., Pereira, M. F. R., and Sydenstricker, T. H. D. (2005). Tensile and impact behavior of polypropylene/low density polyethylene blends. *Polymer Testing*, 24(4):468–473.

[Striemann et al., 2021] Striemann, P., Huelsbusch, D., Niedermeier, M., and Walther, F. (2021). Application-oriented assessment of the interlayer tensile strength of additively manufactured polymers. *Additive Manufacturing*, 46:102095.

[Striemann et al., 2020] Striemann, P., Hülsbusch, D., Niedermeier, M., and Walther, F. (2020). Optimization and Quality Evaluation of the Interlayer Bonding Performance of Additively Manufactured Polymer Structures. *Polymers*, 12(5):1166. Number: 5 Publisher: Multidisciplinary Digital Publishing Institute.

[Stupp, 2019] Stupp, C. (2019). *Enhancing the processing and product design of additive manufactured fiber reinforced polymers by fused filament fabrication.* PhD Thesis, Technische Universiteit Eindhoven, Eindhoven.

[Sun et al., 2008] Sun, Q., Rizvi, G. M., Bellehumeur, C. T., and Gu, P. (2008). Effect of processing conditions on the bonding quality of FDM polymer filaments. *Rapid Prototyping Journal*, 14(2):72–80.

[Sung et al., 2006] Sung, Y. T., Han, M. S., Song, K. H., Jung, J. W., Lee, H. S., Kum, C. K., Joo, J., and Kim, W. N. (2006). Rheological and electrical properties of polycarbonate/multi-walled carbon nanotube composites. *Polymer*, 47(12):4434–4439.

[Sutliff et al., 2020] Sutliff, B. P., Das, A., Youngblood, J., and Bortner, M. J. (2020). High shear capillary rheometry of cellulose nanocrystals for industrially relevant processing. *Carbohydrate Polymers*, 231:115735.

[Szymczyk-Ziółkowska et al., 2020] Szymczyk-Ziółkowska, P., Łabowska, M. B., Detyna, J., Michalak, I., and Gruber, P. (2020). A review of fabrication polymer scaffolds for biomedical applications using additive manufacturing techniques. *Biocybernetics and Biomedical Engineering*, 40(2):624–638.

[Tadmor and Gogos, 2013] Tadmor, Z. and Gogos, C. G. (2013). *Principles of Polymer Processing*. John Wiley & Sons. Google-Books-ID: Qo5SAwAAQBAJ.

[Tan and Low, 2018] Tan, J. C. and Low, H. Y. (2018). Embedded electrical tracks in 3D printed objects by fused filament fabrication of highly conductive composites. *Additive Manufacturing*, 23:294–302.

[Tan et al., 2020] Tan, L. J., Zhu, W., and Zhou, K. (2020). Recent Progress on Polymer Materials for Additive Manufacturing. *Advanced Functional Materials*, n/a(n/a):2003062. Publisher: John Wiley & Sons, Ltd.

[Tang et al., 2020] Tang, T. O., Holmes, S., Dean, K., and Simon, G. P. (2020). Design and fabrication of transdermal drug delivery patch with milliprojections using material extrusion 3D printing. *Journal of Applied Polymer Science*, 137(23):48777. _eprint: https://onlinelibrary.wiley.com/doi/pdf/10.1002/app.48777.

[Tanniru et al., 2006] Tanniru, M., Yuan, Q., and Misra, R. D. K. (2006). On significant retention of impact strength in clay–reinforced high-density polyethylene (HDPE) nanocomposites. *Polymer*, 47(6):2133–2146.

[Tantillo, 2019] Tantillo, A. (2019). *Annealing of Fused Filament Fabricated Nylon 6 with Elevated Isostatic Pressure*. Master of Science Thesis, Rochester Institute of Technology, Rochester, New York.

[Tarrés et al., 2018] Tarrés, Q., Melbø, J. K., Delgado-Aguilar, M., Espinach, F. X., Mutjé, P., and Chinga-Carrasco, G. (2018). Bio-polyethylene reinforced with thermomechanical pulp fibers: Mechanical and micromechanical characterization and its application in 3D-printing by fused deposition modelling. *Composites Part B: Engineering*, 153:70–77.

[Tekinalp et al., 2014] Tekinalp, H. L., Kunc, V., Velez-Garcia, G. M., Duty, C. E., Love, L. J., Naskar, A. K., Blue, C. A., and Ozcan, S. (2014). Highly oriented carbon fiber–polymer composites via additive manufacturing. *Composites Science and Technology*, 105:144–150.

[Terekhina et al., 2020] Terekhina, S., Tarasova, T., Egorov, S., Skornyakov, I., Guillaumat, L., and Hattali, M. L. (2020). The effect of build orientation on both flexural quasi-static and fatigue behaviours of filament deposited PA6 polymer. *International Journal of Fatigue*, 140:105825.

[Thanh, 1974] Thanh, D. H. (1974). *Effect of Capillary Dimensions On Die Swell of Molten Polymers*. Master of Engineering, McMaster University, Hamilton, Ontario, Canada. Accepted: 2015-06-30T14:35:36Z.

[Thompson et al., 2016] Thompson, M. K., Moroni, G., Vaneker, T., Fadel, G., Campbell, R. I., Gibson, I., Bernard, A., Schulz, J., Graf, P., Ahuja, B., and Martina, F. (2016). Design for Additive Manufacturing: Trends, opportunities, considerations, and constraints. *CIRP Annals*, 65(2):737–760.

[Tian et al., 2016] Tian, X., Liu, T., Yang, C., Wang, Q., and Li, D. (2016). Interface and performance of 3D printed continuous carbon fiber reinforced PLA composites. *Composites Part A: Applied Science and Manufacturing*, 88:198–205.

[Tipton et al., 2019] Tipton, R. B., Hou, D., Weller, T. M., and Bhethanabotla, V. R. (2019). Direct Print Additive Manufacturing of Optical Fiber Interconnects for Board Level Computing Devices. Orlando, Florida. American Institute of Chemical Engineers (AIChE).

[Tofangchi et al., 2019] Tofangchi, A., Han, P., Izquierdo, J., Iyengar, A., and Hsu, K. (2019). Effect of Ultrasonic Vibration on Interlayer Adhesion in Fused Filament Fabrication 3D Printed ABS. *Polymers*, 11(2):315. Number: 2 Publisher: Multidisciplinary Digital Publishing Institute.

[Torrado et al., 2015] Torrado, A. R., Shemelya, C. M., English, J. D., Lin, Y., Wicker, R. B., and Roberson, D. A. (2015). Characterizing the effect of additives to ABS on the mechanical property anisotropy of specimens fabricated by material extrusion 3D printing. *Additive Manufacturing*, 6:16–29.

[Tranchard et al., 2017] Tranchard, P., Duquesne, S., Samyn, F., Estèbe, B., and Bourbigot, S. (2017). Kinetic analysis of the thermal decomposition of a carbon fibre-reinforced epoxy resin laminate. *Journal of Analytical and Applied Pyrolysis*, 126:14–21.

[Tripathi et al., 2000] Tripathi, A., Whittingstall, P., and McKinley, G. H. (2000). Using filament stretching rheometry to predict strand formation and "processability" in adhesives and other non-Newtonian fluids. *Rheologica Acta*, 39(4):321–337.

[Tsouknidas et al., 2016] Tsouknidas, A., Pantazopoulos, M., Katsoulis, I., Fasnakis, D., Maropoulos, S., and Michailidis, N. (2016). Impact absorption capacity of 3D-printed components fabricated by fused deposition modelling. *Materials & Design*, 102:41–44.

[Turner and Gold, 2015] Turner, B. N. and Gold, S. A. (2015). A review of melt extrusion additive manufacturing processes: II. Materials, dimensional accuracy, and surface roughness. *Rapid Prototyping Journal*, 21(3):250–261.

[Turner et al., 2014] Turner, B. N., Strong, R., and Gold, S. A. (2014). A review of melt extrusion additive manufacturing processes: I. Process design and modeling. *Rapid Prototyping Journal*, 20:192–204.

[Tymrak et al., 2014] Tymrak, B. M., Kreiger, M., and Pearce, J. M. (2014). Mechanical properties of components fabricated with open-source 3-D printers under realistic environmental conditions. *Materials & Design*, 58:242–246.

[Vaes et al., 2021] Vaes, D., Coppens, M., Goderis, B., Zoetelief, W., and Van Puyvelde, P. (2021). The Extent of Interlayer Bond Strength during Fused Filament Fabrication of Nylon Copolymers: An Interplay between Thermal History and Crystalline Morphology. *Polymers*, 13(16):2677. Number: 16 Publisher: Multidisciplinary Digital Publishing Institute.

[Vaes and Van Puyvelde, 2021] Vaes, D. and Van Puyvelde, P. (2021). Semi-crystalline feedstock for filament-based 3D printing of polymers. *Progress in Polymer Science*, 118:101411.

[Valino et al., 2019] Valino, A. D., Dizon, J. R. C., Espera, A. H., Chen, Q., Messman, J., and Advincula, R. C. (2019). Advances in 3D printing of thermoplastic polymer composites and nanocomposites. *Progress in Polymer Science*, 98:101162.

[Valkenaers et al., 2013] Valkenaers, H., Vogeler, F., Ferraris, E., Voet, A., and Kruth, J.-P. (2013). A novel approach to additive manufacturing: Screw extrusion 3D-printing. In *Proceedings of the 10th International Conference on Multi-Material Micro Manufacture*, pages 235–238. Research Publishing; Singapore.

[van Berlo et al., 2020] van Berlo, F. P. A., Cardinaels, R., Peters, G. W. M., and Anderson, P. D. (2020). A numerical study of extensional flow-induced crystallization in filament stretching rheometry. *Polymer Crystallization*, n/a(n/a):e10154. _eprint: https://onlinelibrary.wiley.com/doi/pdf/10.1002/pcr2.10154.

[Van Gurp and Palmen, 1998] Van Gurp, M. and Palmen, J. (1998). Time-temperature superposition for polymeric blends. *Rheol. Bull*, 67(1):5–8.

[Veer et al., 2017] Veer, F. A., Setaki, F., Riemslag, A. C., and Sakkas, P. (2017). The strength and ductility of glass fibre reinforced 3D-printed polypropylene. *Heron*, 62(2):85.

[Venkataraman et al., 2000] Venkataraman, N., Rangarajan, S., Matthewson, M., Harper, B., Safari, A., Danforth, S., Wu, G., Langrana, N., Guceri, S., and Yardimci, A. (2000). Feedstock material property–process relationships in fused deposition of ceramics (FDC). *Rapid Prototyping Journal*, 6(4):244–253. Publisher: MCB UP Ltd.

[Vidakis et al., 2021] Vidakis, N., Petousis, M., Tzounis, L., Maniadi, A., Velidakis, E., Mountakis, N., Papageorgiou, D., Liebscher, M., and Mechtcherine, V. (2021). Sustainable Additive Manufacturing: Mechanical Response of Polypropylene over Multiple Recycling Processes. *Sustainability*, 13(1):159. Number: 1 Publisher: Multidisciplinary Digital Publishing Institute.

[Vishwas et al., 2018] Vishwas, M., Basavaraj, C. K., and Vinyas, M. (2018). Experimental Investigation using Taguchi Method to Optimize Process Parameters of Fused Deposition Modeling for ABS and Nylon Materials. *Materials Today: Proceedings*, 5(2, Part 2):7106–7114.

[Vogt et al., 2021] Vogt, B. D., Stokes, K. K., and Kumar, S. K. (2021). Why is Recycling of Postconsumer Plastics so Challenging? *ACS Applied Polymer Materials*, 3(9):4325–4346. Publisher: American Chemical Society.

[Volpato et al., 2015] Volpato, N., Kretschek, D., Foggiatto, J. A., and Gomez da Silva Cruz, C. M. (2015). Experimental analysis of an extrusion system for additive manufacturing based on polymer pellets. *The International Journal of Advanced Manufacturing Technology*, 81(9):1519–1531.

[Wang et al., 2014] Wang, J., Guo, J., Li, C., Yang, S., Wu, H., and Guo, S. (2014). Crystallization kinetics behavior, molecular interaction, and impact-induced morphological evolution of polypropylene/poly(ethylene-co-octene) blends: insight into toughening mechanism. *Journal of Polymer Research*, 21(12):618.

[Wang and Gardner, 2017] Wang, L. and Gardner, D. J. (2017). Effect of fused layer modeling (FLM) processing parameters on impact strength of cellular polypropylene. *Polymer*, 113:74–80.

[Wang et al., 2018a] Wang, L., Gardner, D. J., and Bousfield, D. W. (2018a). Cellulose nanofibril-reinforced polypropylene composites for material extrusion: Rheological properties. *Polymer Engineering & Science*, 58(5):793–801.

[Wang et al., 2018b] Wang, L., Gramlich, W. M., Gardner, D. J., Han, Y., and Tajvidi, M. (2018b). Spray-Dried Cellulose Nanofibril-Reinforced Polypropylene Composites for Extrusion-Based Additive Manufacturing: Nonisothermal Crystallization Kinetics and Thermal Expansion. *Journal of Composites Science*, 2(1):7.

[Wang et al., 2019a] Wang, L., Palmer, J., Tajvidi, M., Gardner, D. J., and Han, Y. (2019a). Thermal properties of spray-dried cellulose nanofibril-reinforced polypropylene composites from extrusion-based additive manufacturing. *Journal of Thermal Analysis and Calorimetry*, 136(3):1069–1077.

[Wang et al., 2018c] Wang, L., Sanders, J. E., Gardner, D. J., and Han, Y. (2018c). Effect of fused deposition modeling process parameters on the mechanical properties of a filled polypropylene. *Progress in Additive Manufacturing*, 3(4):205–214.

[Wang et al., 2008] Wang, M., Wang, W., Liu, T., and Zhang, W.-D. (2008). Melt rheological properties of nylon 6/multi-walled carbon nanotube composites. *Composites Science and Technology*, 68(12):2498–2502.

[Wang et al., 2019b] Wang, P., Zou, B., Xiao, H., Ding, S., and Huang, C. (2019b). Effects of printing parameters of fused deposition modeling on mechanical properties, surface quality, and microstructure of PEEK. *Journal of Materials Processing Technology*, 271:62–74.

[Wang et al., 2017] Wang, X., Jiang, M., Zhou, Z., Gou, J., and Hui, D. (2017). 3D printing of polymer matrix composites: A review and prospective. *Composites Part B: Engineering*, 110:442–458.

[Wang and Smith, 2017] Wang, Z. and Smith, D. (2017). The effect of polymer melt rheology on predicted die swell and fiber orientation in fused filament fabrication nozzle flow. In *Proceedings of the 28th Annual International Solid Freeform Fabrication Symposium – An Additive Manufacturing Conference*, pages 1082–1095, Austin, Texas.

[Wang and Smith, 2018] Wang, Z. and Smith, D. E. (2018). Rheology Effects on Predicted Fiber Orientation and Elastic Properties in Large Scale Polymer Composite Additive

Manufacturing. *Journal of Composites Science*, 2(1):10. Number: 1 Publisher: Multidisciplinary Digital Publishing Institute.

[Watanabe et al., 2016] Watanabe, N., Shofner, M., Treat, N., and Rosen, D. (2016). A model for residual stress and part warpage prediction in material extrusion with application to polypropylene. In *2016 Annual International Solid Freeform Fabrication Symposium, Austin*.

[West et al., 2001] West, A. P., Sambu, S. P., and Rosen, D. W. (2001). A process planning method for improving build performance in stereolithography. *Computer-Aided Design*, 33(1):65–79.

[Wolff et al., 2009] Wolff, F., Resch, J. A., Kaschta, J., and Münstedt, H. (2009). Comparison of viscous and elastic properties of polyolefin melts in shear and elongation. *Rheologica Acta*, 49(1):95.

[Wool et al., 1989] Wool, R. P., Yuan, B.-L., and McGarel, O. J. (1989). Welding of polymer interfaces. *Polymer Engineering & Science*, 29(19):1340–1367.

[Wright et al., 1988] Wright, D. G. M., Dunk, R., Bouvart, D., and Autran, M. (1988). The effect of crystallinity on the properties of injection moulded polypropylene and polyacetal. *Polymer*, 29(5):793–796.

[Wu et al., 2020a] Wu, H., Fahy, W. P., Kim, S., Kim, H., Zhao, N., Pilato, L., Kafi, A., Bateman, S., and Koo, J. H. (2020a). Recent developments in polymers/polymer nanocomposites for additive manufacturing. *Progress in Materials Science*, 111:100638.

[Wu et al., 2020b] Wu, M.-H., Wang, C.-C., and Chen, C.-Y. (2020b). Chemical modification of atactic polypropylene and its applications as a crystallinity additive and compatibility agent. *Polymer*, 194:122386.

[Wu et al., 2015] Wu, W., Geng, P., Li, G., Zhao, D., Zhang, H., and Zhao, J. (2015). Influence of layer thickness and raster angle on the mechanical properties of 3D-printed PEEK and a comparative mechanical study between PEEK and ABS. *Materials*, 8(9):5834–5846.

[Xia et al., 2018] Xia, H., Lu, J., and Tryggvason, G. (2018). Fully resolved numerical simulations of fused deposition modeling. Part II – solidification, residual stresses and modeling of the nozzle. *Rapid Prototyping Journal*, 24:973–987.

[Xia et al., 2019a] Xia, H., Lu, J., and Tryggvason, G. (2019a). A numerical study of the effect of viscoelastic stresses in fused filament fabrication. *Computer Methods in Applied Mechanics and Engineering*, 346:242–259.

[Xia et al., 2019b] Xia, H., Lu, J., and Tryggvason, G. (2019b). Simulations of fused filament fabrication using a front tracking method. *International Journal of Heat and Mass Transfer*, 138:1310–1319.

[Xu et al., 2004] Xu, J., Johnson, M., and Wilkes, G. L. (2004). A tubular film extrusion of poly(vinylidene fluoride): structure/process/property behavior as a function of molecular weight. *Polymer*, 45(15):5327–5340.

[Xue et al., 2000] Xue, Y.-Q., Tervoort, T. A., Rastogi, S., and Lemstra, J. (2000). Welding behavior of semicrystalline polymers. 2. Effect of cocrystallization on autoadhesion. *Macromolecules*, 33(19):7084–7087.

[Yan et al., 2000] Yan, Y., Zhang, R., Hong, G., and Yuan, X. (2000). Research on the bonding of material paths in melted extrusion modeling. *Materials & Design*, 21(2):93–99.

[Yang et al., 2017] Yang, C., Tian, X., Li, D., Cao, Y., Zhao, F., and Shi, C. (2017). Influence of thermal processing conditions in 3D printing on the crystallinity and mechanical properties of PEEK material. *Journal of Materials Processing Technology*, 248:1–7.

[Young et al., 2019] Young, D. J., Otten, C., and Czabaj, M. W. (2019). Effect of Processing Parameters on Interlayer Fracture Toughness of Fused Filament Fabrication Thermoplastic Materials. In Kramer, S., Jordan, J. L., Jin, H., Carroll, J., and Beese, A. M., editors, *Mechanics of Additive and Advanced Manufacturing, Volume 8*, Conference Proceedings of the Society for Experimental Mechanics Series, pages 77–79, Cham. Springer International Publishing.

[Yuan et al., 2020] Yuan, Y., Abeykoon, C., Mirihanage, W., Fernando, A., Kao, Y., and Harings, J. A. W. (2020). Prediction of temperature and crystal growth evolution during 3D printing of polymeric materials via extrusion. *Materials & Design*, page 109121.

[Zaldivar et al., 2018] Zaldivar, R. J., Mclouth, T. D., Ferrelli, G. L., Patel, D. N., Hopkins, A. R., and Witkin, D. (2018). Effect of initial filament moisture content on the

microstructure and mechanical performance of ULTEM® 9085 3D printed parts. *Additive Manufacturing*, 24:457–466.

[Zander et al., 2019a] Zander, N. E., Gillan, M., Burckhard, Z., and Gardea, F. (2019a). Recycled polypropylene blends as novel 3D printing materials. *Additive Manufacturing*, 25:122–130.

[Zander et al., 2019b] Zander, N. E., Park, J. H., Boelter, Z. R., and Gillan, M. A. (2019b). Recycled Cellulose Polypropylene Composite Feedstocks for Material Extrusion Additive Manufacturing. *ACS Omega*, 4(9):13879–13888.

[Zandi et al., 2020] Zandi, M. D., Jerez-Mesa, R., Lluma-Fuentes, J., Roa, J. J., and Travieso-Rodriguez, J. A. (2020). Experimental analysis of manufacturing parameters' effect on the flexural properties of wood-PLA composite parts built through FFF. *The International Journal of Advanced Manufacturing Technology*, 106(9):3985–3998.

[Zare et al., 2019] Zare, Y., Park, S. P., and Rhee, K. Y. (2019). Analysis of complex viscosity and shear thinning behavior in poly (lactic acid)/poly (ethylene oxide)/carbon nanotubes biosensor based on Carreau–Yasuda model. *Results in Physics*, 13:102245.

[Zawaski et al., 2019] Zawaski, C. E., Wilts, E. M., Chatham, C. A., Stevenson, A. T., Pekkanen, A. M., Li, C., Tian, Z., Whittington, A. R., Long, T. E., and Williams, C. B. (2019). Tuning the material properties of a water-soluble ionic polymer using different counterions for material extrusion additive manufacturing. *Polymer*, 176:283–292.

[Zhakeyev et al., 2019] Zhakeyev, A., Tobin, J., Wang, H., Vilela, F., and Xuan, J. (2019). Additive manufacturing of photoactive polymers for visible light harvesting. *Energy Procedia*, 158:5608–5614.

[Zhang et al., 2017a] Zhang, J., Wang, X. Z., Yu, W. W., and Deng, Y. H. (2017a). Numerical investigation of the influence of process conditions on the temperature variation in fused deposition modeling. *Materials & Design*, 130:59–68.

[Zhang et al., 2017b] Zhang, M. C., Guo, B.-H., and Xu, J. (2017b). A Review on Polymer Crystallization Theories. *Crystals*, 7(1):4. Number: 1 Publisher: Multidisciplinary Digital Publishing Institute.

[Zhang and Li, 2016] Zhang, P. and Li, G. (2016). Advances in healing-on-demand polymers and polymer composites. *Progress in Polymer Science*, 57:32–63.

[Zhang et al., 2018] Zhang, W., Cotton, C., Sun, J., Heider, D., Gu, B., Sun, B., and Chou, T.-W. (2018). Interfacial bonding strength of short carbon fiber/acrylonitrile-butadiene-styrene composites fabricated by fused deposition modeling. *Composites Part B: Engineering*, 137:51–59.

[Zhang and Shapiro, 2018] Zhang, Y. and Shapiro, V. (2018). Linear-Time Thermal Simulation of As-Manufactured Fused Deposition Modeling Components. *Journal of Manufacturing Science and Engineering*, 140(7):071002.

[Zhang et al., 2015] Zhang, Z., Yu, F., Zhou, N., and Zhang, H. (2015). Compatibilization by Olefin Block Copolymer (OBC) in Polypropylene/Ethylene-Propylene-Diene Terpolymer (PP/EPDM) Blends. *Journal of Macromolecular Science, Part B*, 54(2):159–176. Publisher: Taylor & Francis _eprint: https://doi.org/10.1080/00222348.2014.996497.

[Zhang et al., 2012] Zhang, Z. X., Zhang, J., Lu, B.-X., Xin, Z. X., Kang, C. K., and Kim, J. K. (2012). Effect of flame retardants on mechanical properties, flammability and foamability of PP/wood–fiber composites. *Composites Part B: Engineering*, 43(2):150–158.

[Zhao et al., 2017] Zhao, Z., Peng, F., Cavicchi, K. A., Cakmak, M., Weiss, R. A., and Vogt, B. D. (2017). Three-Dimensional Printed Shape Memory Objects Based on an Olefin Ionomer of Zinc-Neutralized Poly(ethylene-co-methacrylic acid). *ACS Applied Materials & Interfaces*, 9(32):27239–27249. Publisher: American Chemical Society.

[Zhou and Hsieh, 2017] Zhou, X. and Hsieh, S.-J. (2017). Thermal analysis of fused deposition modeling process using infrared thermography imaging and finite element modeling. In *Thermosense: Thermal Infrared Applications XXXIX*, volume 10214, page 1021409. International Society for Optics and Photonics.

[Zhou et al., 2017a] Zhou, X., Hsieh, S.-J., and Sun, Y. (2017a). Experimental and numerical investigation of the thermal behaviour of polylactic acid during the fused deposition process. *Virtual and Physical Prototyping*, 12(3):221–233.

[Zhou et al., 2017b] Zhou, Y.-G., Su, B., and Turng, L.-s. (2017b). Deposition-induced effects of isotactic polypropylene and polycarbonate composites during fused deposition modeling. *Rapid Prototyping Journal*, 23(5):869–880. Publisher: Emerald Publishing Limited.

[Zhou et al., 2018] Zhou, Z., Salaoru, I., Morris, P., and Gibbons, G. J. (2018). Additive manufacturing of heat-sensitive polymer melt using a pellet-fed material extrusion. *Additive Manufacturing*, 24:552–559.

Appendices

Appendix A

Recent advances in material development and process monitoring in polymer additive manufacturing

Arit Das[1,2] and Michael J. Bortner[1,2]

[1]Department of Chemical Engineering, Virginia Polytechnic and State University, Blacksburg, VA 24061, USA

[2]Macromolecules Innovation Institute, Virginia Polytechnic and State University, Blacksburg, VA 24061, USA

This chapter was originally published in the **Journal of Advanced Manufacturing and Processing** journal.

J. Adv. Manuf. Process. 2020, 2, 3, e210051. https://doi.org/10.1002/amp2.10051

Abstract

This article provides an overview of the recent progress made in the field of polymer based additive manufacturing. The research works discussed in this article was presented at the *Polymers in Additive Manufacturing* session of the Next-Gen Manufacturing Topical Conference at the 2019 American Institute of Chemical Engineers Annual Meeting. It is worth noting that the developments reviewed in this paper are by no means exhaustive; however, we focus only on the research presented in the aforementioned session for the sake of conciseness. The major focus of this article is on the utilization of macromolecular systems in the emerging field of additive manufacturing. In particular, the article highlights both experimental and computational efforts that utilize polymers in additive manufacturing. Current research trends addressing all methods of polymer-based additive manufacturing, including material extrusion, stereolithography, and direct ink writing, have been analyzed. Finally,

prospective avenues to achieve more fundamental understanding and hence further insights into improving additive manufacturing of polymers have also been presented.

Keywords: 3D printing; additive manufacturing; material extrusion; polymers; process modeling

A.1 Introduction

Additive manufacturing (AM), otherwise known as 3D printing, is a disruptive technology that can pave the way for the next manufacturing revolution [Gao et al., 2015]. AM has the capability to expedite the production of parts economically without compromising on dimensional accuracy. Although there are different variations of AM depending on the materials employed and machine designs, all AM processes rely on the same basic principle of fabricating an object in an additive (and typically) layer by layer manner, thus drastically reducing material wastage compared to traditional processing techniques while enabling new design geometries that are unachievable with subtractive manufacturing. Polymer based AM has gained much attention over the years since the polymeric parts fabricated using this technique can have applications in broad design spaces ranging from commodity and consumer products to high-performance applications in the aerospace, automotive, and healthcare industries [Kotula et al., 2019].

In this short paper, we report the current developments in the field of polymer based AM as presented during the Polymers in Additive Manufacturing session of the Next-Gen Manufacturing Topical Conference at the 2019 American Institute of Chemical Engineers (AIChE) annual meeting [noa,]. We review the approaches to develop advanced polymeric materials for AM followed by description of the recent research on process monitoring and modeling that allow better understanding of the complex multiphysics associated with the AM process. Moreover, the challenges associated with the approaches are highlighted. Finally, potential routes to address such challenges are presented to help guide future research that will potentially help in gaining valuable insight into the intricate features of polymer based AM process.

A.2 Material Development in Polymer AM

In recent years, improving and expanding the material selection library for AM has garnered significant interest. Increasing demands from both consumers and industry have prompted multiple researchers and companies to enhance the capabilities of the most common and economic form of AM, known as filament material extrusion (MatEx), which involves extrusion of a polymer filament in a layer-by-layer fashion. MatEx was originally developed as a prototyping tool and is now progressively challenged each day to produce end use parts for a wide variety of applications [Huang et al., 2015, Compton and Lewis, 2014]. Semi-crystalline polymers are an attractive class of materials for MatEx due to their improved thermal stability, toughness, and deformability compared to amorphous polymers [Rubenstein and Colby, 2003].

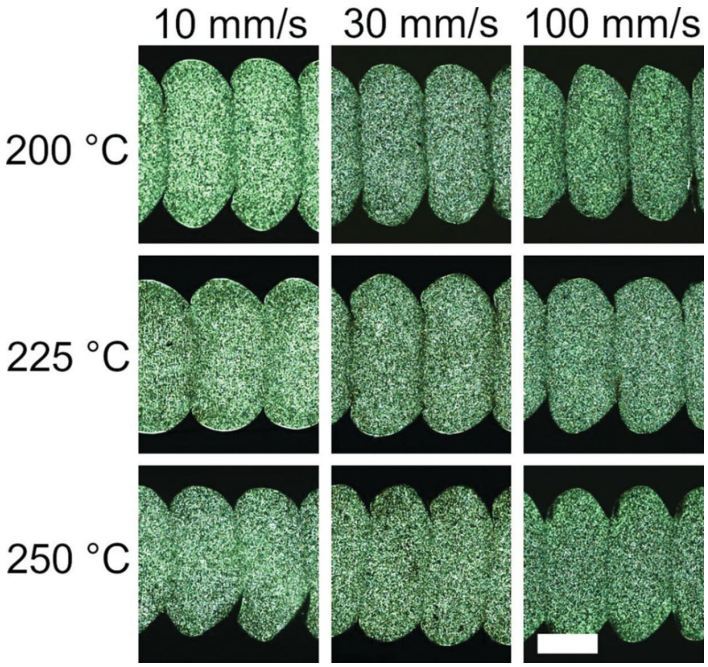


Figure A.1: Cross-polarized optical microscopy of cross sections of printed parts after annealing at 140°C for 1 hour (Scale bar 200 μm). The size of the semicrystalline domains increases after the annealing process. The temperatures on the left indicate the print temperature. (image reprinted with permission from [McIlroy et al., 2019] Copyright 2019 American Chemical Society)

McIlroy et al. [McIlroy et al., 2019] investigated the effect of repeated non-uniform thermal

processing history (as encountered by a polymer during MatEx) on the total crystalline content of a semicrystalline polymer. The authors developed an in-situ Raman spectroscopy technique to quantify the isothermal crystallization kinetics of the polymer during MatEx. Optical microscopy was employed to monitor the crystal growth which revealed that the behavior observed did not obey the classical Lauritzen-Hoffman theory, presumably due to the presence of various additives in the polymers. Post-printing, the parts were annealed to improve the weld strength at the interfacial region by controlling the flow induced crystallization behavior (as illustrated in Figure A.1). Moreover, a theoretical model was developed taking into account the polymer constitutive equations, heat transfer, and crystallization kinetics to describe the interaction between printing parameters and final part properties. Interested readers are referred to the original publication for more details about the model [McIlroy et al., 2019].

Das et al. [Das et al., 2019, Das et al., 2020b] studied the effect of incorporating amorphous hydrocarbon resins into polypropylene (PP) to slow down the crystallization process during MatEx. Increasing resin content in the blends improved the printing process by promoting interfacial adhesion between the deposited layers and reducing warpage. Tensile properties of the 3D printed PP blends obtained using this approach were only 70% of the injection molded (IM) properties. However, moderate annealing of the parts recovered over 90% of the IM tensile stress and modulus at the expense of the elongation at break, as highlighted in Figure A.2. Such improvement in properties after annealing provides further experimental validation for McIlroy et al.'s [McIlroy et al., 2019] simulation results with semicrystalline polymers. Further, the authors found that blends of PP with higher crystalline content exhibited higher mechanical properties but tend to warp more during MatEx [Das et al., 2019].

Another extrusion based AM method, direct ink writing (DIW) has been used to print bioinspired dielectric elastomer actuators that can have potential applications in soft robotics, microfluidics, and artificial muscles [Chortos et al., 2020]. Chortos et al. [Chortos et al., 2020] developed a conductive elastomeric ink for printing electrodes. The rheological characterization of the ink revealed a high storage modulus (G') and a low loss tangent (tan δ) which were necessary to provide mechanical stability during DIW of vertical electrodes with high aspect ratio. The authors demonstrated multi-nozzle DIW and fabricated 3D printed dielectric actuators (DEAs) with multiple interconnected electrodes. The printed DEAs had a breakdown field of 25 V μm^{-1} and actuation strains of up to 9% which are comparable to the

devices obtained using other fabrication techniques such as spray-deposition and multilayer DIW.

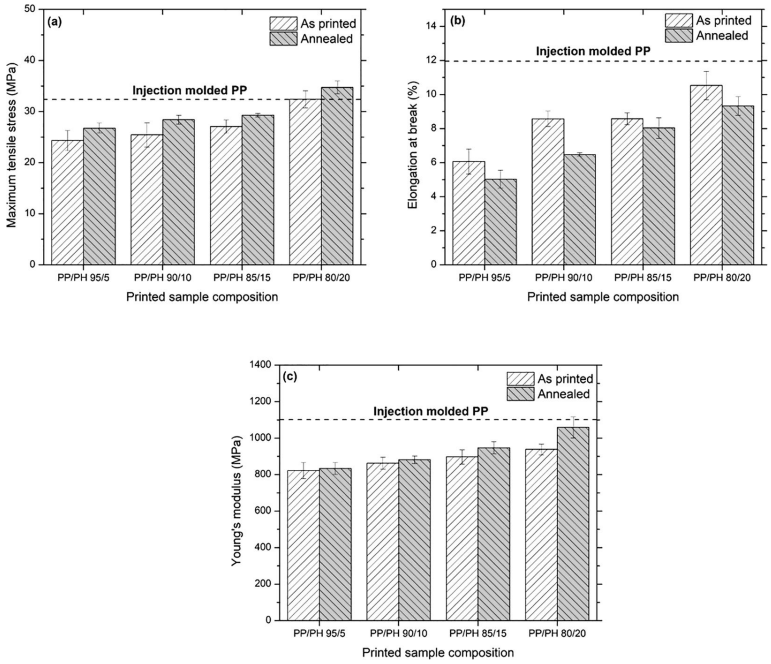


Figure A.2: Effect of post-printing annealing on the (a) maximum tensile stress, (b) elongation at break, and (c) Young's modulus of printed blends of polypropylene/partially hydrogenated resin (PP/PH). The numbers in the X-axis of the plots indicate the composition of PP and PH. (image reprinted with permission from [Das et al., 2020b] Copyright 2020 American Chemical Society)

The versatility of polymer based AM is further evidenced by its application in producing parts for applications in computing and optical communications [Tipton et al., 2019]. Tipton et al. [Tipton et al., 2019] developed a modification of MatEx, termed as direct print AM, that can successfully print single and multi-mode optical fibers with great fidelity. The authors incorporated a picosecond laser processing to improve the surface finish in the printed parts. In order to improve transmission rates, smooth prints with minimal surface roughness were desired. The authors reported a surface roughness of less than 450 nm in a 77 μm diameter optical fiber. Although this was the first reported use of AM to fabricate plastic optical fibers and only 46% optical transmission rate was obtained in the printed parts, it is anticipated that this approach can be employed to develop more sophisticated electronic devices in the near future.

A.3 Process Monitoring in Polymer AM

As highlighted in the work of McIlroy et al. [McIlroy et al., 2019] processing parameters can have a significant impact on the final part properties and quality. In order to provide adequate quality assurance of the printed parts, process control during the AM process is necessary. Numerical modeling coupled with sophisticated experimental procedures can assist in monitoring the AM process and potentially pinpoint the origin of anisotropic properties and poor surface finish in the printed parts. In the current scope of this paper, we provide examples of process modeling and monitoring for MatEx and stereolithography.

Behdani et al. [Behdani et al., 2019] investigated the effects of printing parameters on the morphology of the extruded filaments during MatEx. Non-isothermal simulations for power-law fluids in MatEx was carried out by solving the continuity, momentum conservation, and Fourier's heat equation simultaneously. The volume of fluid was kept constant during the simulation and temperature dependency of the transport properties was taken into account, in contrast to the work of Serdeczny et al. [Serdeczny et al., 2018a] that considered a Newtonian fluid under isothermal conditions. Simulation results for the shape of the extruded filament [Behdani et al., 2019] was found to be in good agreement with previous experimental results [Serdeczny et al., 2018a]. The aspect ratio of the deposited layers was found to increase with temperature whereas the pressure drop decreased, mainly due to a reduction in viscosity at higher print temperatures. Also, the authors claimed that printing at higher temperatures can reduce the surface roughness of the printed parts [Behdani et al., 2019].

Peng et al. [Peng et al., 2018] devised an experimental protocol that can monitor the polymer melt flow and temperature history during MatEx of polycarbonate. Flow visualization was performed by selective incorporation of pigments into the filament feed, followed by subsequently monitoring its distribution in the extruded filament using optical microscopy and X-ray microcomputed tomography. Moreover, ultra-fine thermocouples were embedded into the filaments to capture the complex thermal profile during layer by layer deposition (as highlighted in Figure A.3). Such an approach allows for direct quantification of the changes in flow and thermal fields in the liquefier during MatEx. The results suggest that the process is highly non-isothermal, while the flow field is controlled by the relevant shear rates, entrance effects, and temperature gradients in the nozzle. Finally, results from the study can help improve existing models as well as provide baseline details to develop new multiscale models for better describing polymer based MatEx.

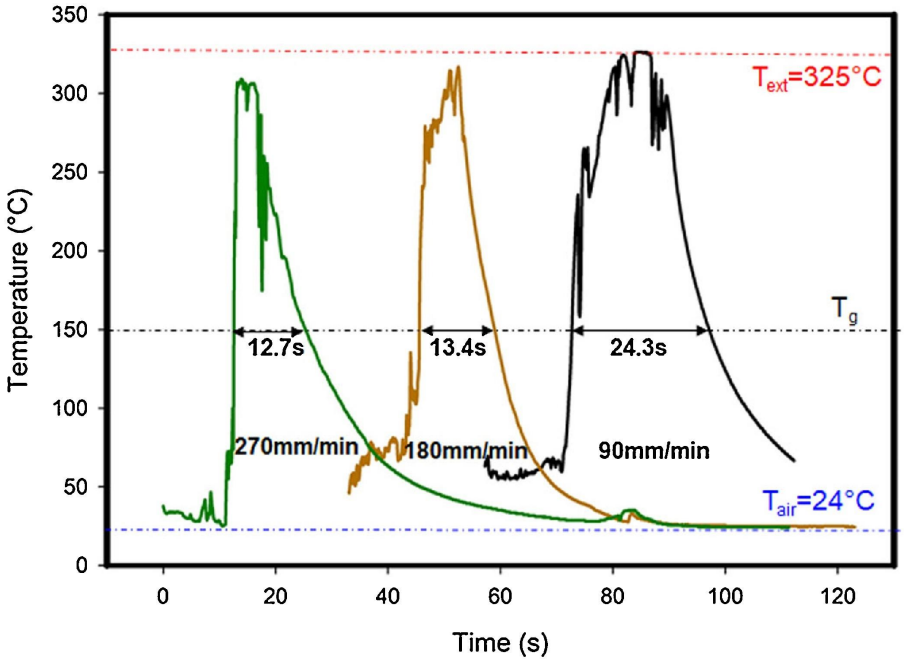


Figure A.3: Complex thermal history during MatEx printing of polycarbonate filaments at 325°C as a function of different print speeds. The timescales highlighted are the times the extruded filament stays above the glass transition temperature. (image reprinted from [Peng et al., 2018] with permission from Elsevier)

Continuous stereolithography (SL) has the advantage of being faster than other layer by layer fabrication processes. The major problem associated with this process is the unwanted curing (also known as overcure) that can lead to internal stress build-up that can lead to part deformation and reduced dimensional stability [Pritchard et al., 2019]. The unwanted curing can be eliminated either by changing resin formulation (a slow process) or by slicing modifications. Pritchard et al. [Pritchard et al., 2019] developed a model coupled with a slice correction algorithm (as illustrated in Figure A.4a) to accurately control light intensity dependent curing and reduce the aforementioned complications in continuous SL. The model took into account the curing threshold as function of print layers by applying a gradient in the slicing procedure which prevents the initiation of unwanted curing. The approach can also be applied for printing intricate parts having controllable porosity by monitoring the regions where curing needs to occur. The robustness of the modeling approach was validated on standard print parts (Figure A.4b and A.4c highlights two benchmark 3D geometries printed using this algorithm) as well as on complex models which was indicative of the universality

of this approach. The details of model development can be found in the original paper by Pritchard et al.[Pritchard et al., 2019] and the printer setup is schematically illustrated in Figure A.4d.

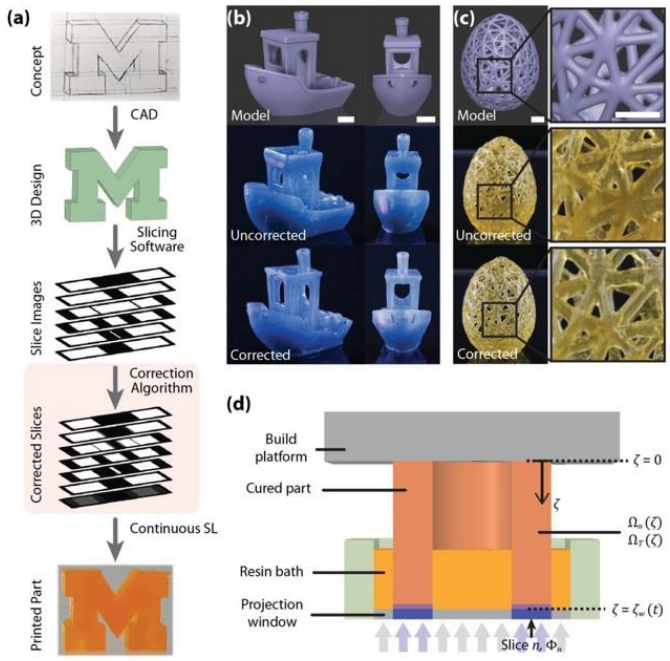


Figure A.4: (a) Illustration of the cure-through correction algorithm implemented by changing the slicing procedure; (b) 3DBenchy and (c) hollow egg printed using the corrected and uncorrected slicing procedure (scale bar 5mm); (d) schematic of the printer apparatus with the important non-dimensionalized parameters, such as, z-position (ζ), dosage (Ω_n), and light intensity (Φ_n) (image reprinted from [Pritchard et al., 2019] with permission from John Wiley and Sons)

A.4 Future Directions

Although great strides have been made in process monitoring and materials development for polymer based AM, there are still scope for further research to better comprehend the interplay between AM process parameters and inherent polymer physics. For example, McIlroy et al.'s work [McIlroy et al., 2019] does not take into account the startup dynamics during printing. Models describing these details will be useful to predict the behavior of the polymer melt during the initial stages of extrusion through the printer nozzle. The simulation

framework described by Behadani et al. [Behdani et al., 2019] fails to capture the effects of polymer viscoelasticity and crystallization kinetics which directly controls the interlayer diffusion and part strength during MatEx. Similarly, the method developed by Pritchard et al. [Pritchard et al., 2019] to improve the consistency in printed parts using continuous SL is limited by the complex flow fields, curing kinetics, and mechanical stability of the polymer resin. Models incorporating these components are expected to further improve the robustness of the predictions. The study from Peng et al. [Peng et al., 2018] suggested inconsistent heat transfer rates leads to diffusion limitations in MatEx. Future studies can aim at quantifying such effects and investigate possible flow instabilities, arising from elastic effects, at higher print speeds.

From the materials development perspective, the approach outlined by Das et al. [Das et al., 2019] provides an interesting way to print semicrystalline polymers. However, the suitability of this method with respect to large format AM needs to be investigated in addition to monitoring the morphology development and welding dynamics during the MatEx process. Chortos et al.'s [Chortos et al., 2020] research on conductive electrode inks highlights the capability of AM in producing parts for many sophisticated applications with tunable mechanical properties. Additional studies (mainly rheological) are required to accurately identify the origin of shape change during printing of such elastomeric inks at sharp directional changes. Dielectric performance can also be enhanced by successful synthesis of inks that can be printed through nozzles less than 10 μm in diameter [Chortos et al., 2020] . Similarly, initial studies of MatEx with flexible materials for optical fiber interconnects provided promising results [Tipton et al., 2019]. Further investigations are warranted to optimize the nozzle design as well as the extrusion process to achieve parts with minimum roughness which will greatly improve the transmission rates in the printed optical fibers. In summary, although there are still research gaps in polymer based AM, current fundamental research trends suggest that significant progress will be made to augment our understanding of the process in the near future.

Appendix B

Rheological investigation of nylon-carbon fiber composites fabricated using material extrusion based additive manufacturing

B.1 Thermal stability of PA6 and CF-PA6

Table B.1: Degradation temperatures for PA6 filament, CF-PA6 filament, and CF-PA6 print along with the residue left after the samples have been heated to 600°C under nitrogen environment (reported values are an average of three runs)

Sample	$\mathbf{T}_{5\%}$	$\mathbf{T}_{10\%}$	$\mathbf{T}_{50\%}$	**Residue (%)**
PA6 filament	418 ± 1.6	432 ± 2.1	464 ± 0.8	1.0 ± 0.1
CF-PA6 filament	348 ± 2.4	412 ± 3.5	461 ± 1.1	14.3 ± 1.1
CF-PA6 print	326 ± 1.9	406 ± 1.5	459 ± 2.3	14.2 ± 0.7

B.2 Melting and crystallization of PA6 and Onyx

Table B.2: Peak melting temperatures (from the second heating scan) and peak crystallization temperatures (from the cooling scan) as well as enthalpy of melting (from the second heating scan) and crystallization (from the cooling scan) of PA6 and CF-PA6 samples obtained using the nonisothermal DSC experiments.

Sample name	Peak melting temperature (°C)	Enthalpy of melting (Jg^{-1})	Peak crystallization temperature (°C)	Enthalpy of crystallization (Jg^{-1})
PA6	202.0 ± 2.3	45.9 ± 1.2	170.8 ± 0.4	30.8 ± 0.5
CF-PA6 filament	199.4 ± 2.6	47.5 ± 0.9	162.4 ± 0.5	36.1 ± 0.8
CF-PA6 print	199.6 ± 2.1	44.7 ± 1.0	163.9 ± 1.3	42.2 ± 1.4

B.3 Complex viscosity of PA6 and CF-PA6

Table B.3: Parameters for the Carreau model fitted to the complex viscosity vs. angular frequency data obtained at different temperatures for PA6 and CF-PA6

Sample	**Temerature (°C)**	η_0^* **(Pa.s)**	λ **(s)**	a	n	R^2
PA6	265	3540.5	0.14	1.66	0.55	0.99
PA6	270	2603.0	0.45	1.05	0.62	0.99
PA6	275	1708.6	0.73	2.11	0.63	0.99
PA6	280	863.1	0.96	1.40	0.70	0.99
CF-PA6	270	4800.9	0.15	1.32	0.60	0.99
CF-PA6	275	3881.6	0.44	1.46	0.60	0.99
CF-PA6	280	2887.5	0.78	1.62	0.62	0.99
CF-PA6	285	1799.2	0.63	1.06	0.65	0.99

B.4 Viscoelastic properties of PA6 and CF-PA6

Table B.4: Power law parameters fitted to the storage modulus vs. angular frequency data obtained at different temperatures for PA6 and CF-PA6

Sample	**Temerature (°C)**	a_1	a_2	R^2
PA6	265	816.4	0.75	0.99
PA6	270	478.6	0.83	0.99
PA6	275	256.1	0.91	0.99
PA6	280	121.0	1.01	0.99
CF-PA6	270	830.6	0.82	0.99
CF-PA6	275	637.7	0.88	0.99
CF-PA6	280	463.2	0.94	0.99
CF-PA6	285	357.2	1.00	0.99

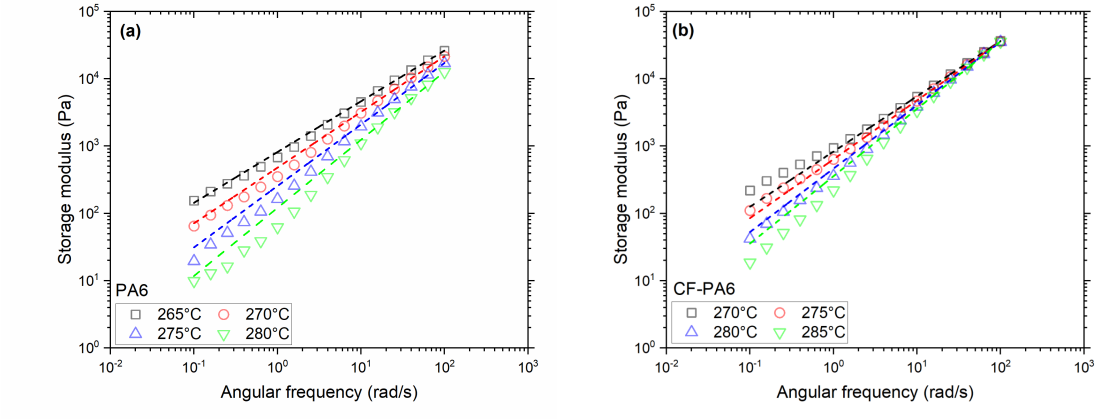


Figure B.1: Frequency dependence of storage modulus of (a) PA6 and (b) CF-PA6 at different temperatures. The dashed lines represent the fits to the power law equation $G' = a_1\omega^{a_2}$

B.5 ANOVA tests for print parameter optimization

Table B.5: Analysis of Variance for maximum tensile strength of printed CF-PA6 parts

Source	**DF**	**Adjusted SS**	**Adjusted MS**	**F-Value**	**P-Value**	**Percentage Contribution**
Layer thickness	2	71.01	35.54	50.73	0.02	88.40
Raster angle	2	2.62	1.311	1.87	0.35	3.26
Infill pattern	2	5.29	2.65	3.78	0.21	6.58
Error	2	1.4	0.70			1.74
Total	8	80.32				100

Table B.6: Analysis of Variance for elongation at break of printed CF-PA6 parts

Source	**DF**	**Adjusted SS**	**Adjusted MS**	**F-Value**	**P-Value**	**Percentage Contribution**
Layer thickness	2	77.45	38.75	8.50	0.11	73.95
Raster angle	2	1.53	0.76	0.17	0.86	1.45
Infill pattern	2	16.67	8.33	1.83	0.35	15.90
Error	2	9.12	4.56			8.70
Total	8	104.77				100

Table B.7: Analysis of Variance for tensile modulus of printed CF-PA6 parts

Source	**DF**	**Adjusted SS**	**Adjusted MS**	**F-Value**	**P-Value**	**Percentage Contribution**
Layer thickness	2	0.019	0.01	0.24	0.81	8.58
Raster angle	2	0.05	0.02	0.56	0.64	20.33
Infill pattern	2	0.079	0.04	0.96	0.51	34.89
Error	2	0.082	0.04			36.20
Total	8	0.23				100

Appendix C

Material extrusion-based additive manufacturing with blends of polypropylene and hydrocarbon resins

C.1 Composition of PP/hydrocarbon resin blends

Table C.1: Different blend compositions of PP and resins along with the mixing temperature used in this study.

Sample designation	Mixing temperature (°C)	Weight percent of PP (%)	Weight percent of resin (%)
Pure PP	170	100	0
PP/FH 95/5	170	95	5
PP/FH 90/10	170	90	10
PP/FH 85/15	170	85	15
PP/FH 80/20	170	80	20
PP/PH 95/5	190	95	5
PP/PH 90/10	190	90	10
PP/PH 85/15	190	85	15
PP/PH 80/20	190	80	20

C.2 Thermal stability of PP/hydrocarbon resin blends

TGA scans were performed on the pure resins to determine whether there are concerns regarding thermal degradation of the resins during processing. From the results, illustrated

in Figure C.1, it is observed that the PH resin undergoes a 5wt% degradation at 216°C while the same occurred for the FH resin at 198°C. This suggests the upper processing temperature limit should be approximately 200°C for the PH blends and 190°C for the FH blends. In order to limit the degradation of PH and FH resins, the maximum temperature used for processing the blends in the Brabender was kept at 190°C.

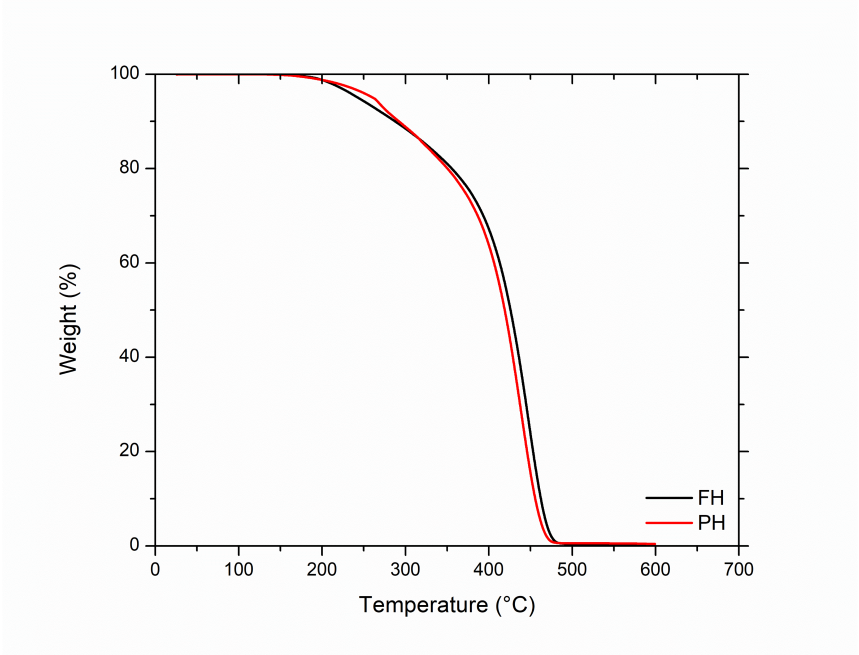


Figure C.1: TGA profiles for the fully hydrogenated (FH) and partially hydrogenated (PH) resins used in this study for blend preparation.

TGA analysis of the PP/hydrocarbon resins blends is highlighted in Figure C.2. The onset degradation temperatures of pure PP and its different blends with the resins has been listed in Table C.2 where $T_{x\%}$ means the temperature at which x% of the initial sample has degraded. The degradation of PP occurs in a single step between 250°C and 400°C, as has been previously reported in literature [Peterson et al., 2001]. The major weight loss in this temperature window has been attributed to oxidative degradation. On further increasing the temperature from 400°C to 600°C, a minor weight loss is observed that is likely due to the degradation of the carbon backbone. All samples degraded completely by 600°C.

Table C.2: Degradation temperature for pure PP and its blends with the FH and PH resins.

Sample Name	$T_{5\%}$ (°C)	$T_{10\%}$ (°C)	$T_{50\%}$ (°C)
Pure PP	277	291	336
PP/FH 95/5	285	303	364
PP/FH 90/10	290	308	363
PP/FH 85/15	289	309	372
PP/FH 80/20	286	307	366
PP/PH 95/5	287	303	354
PP/PH 90/10	285	303	358
PP/PH 85/15	298	317	374
PP/PH 80/20	298	321	383

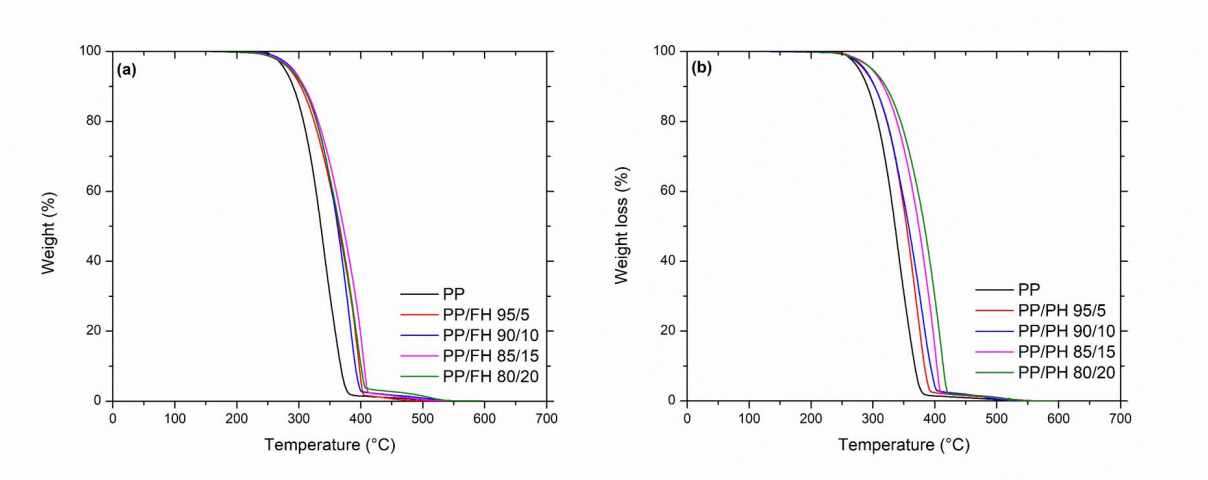


Figure C.2: TGA profiles for the prepared blends of (a) PP/FH and (b) PP/PH.

The incorporation of the hydrocarbon resins to PP increases the degradation temperature for both the PH and FH blends. The improved thermal stability of the blends is due to the interaction between the thermal degradation mechanisms of the hydrocarbon resins and pure PP. The functionalities present in the hydrocarbon resins that act as free radical scavengers

also slow down the thermal degradation of the blends. The hydrocarbon resins dispersed in the PP matrix can undergo dehydrogenation upon heating. These reactions result in the formation of a homogeneous oxidatively stable carbonaceous coating on the surface of the material which slows down the thermal degradation process, and thus the overall thermal stability of the blends is enhanced [Iring and Tüdős, 1990, Shibryaeva, 2012]. The FH blends shows a lower onset degradation temperature compared to the PH blends since the excess hydrogenation makes it more susceptible to thermal deterioration.

C.3 Melting and crystallization profiles of PP/FH blends

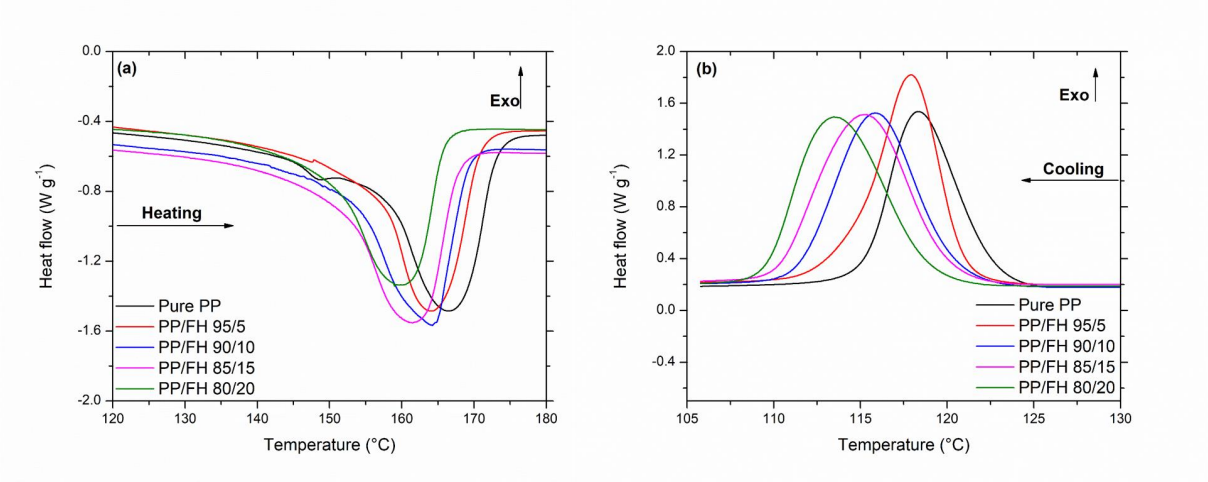


Figure C.3: (a) DSC melting endotherms from the second heat of non-isothermal experiments for the different compositions of PP/FH blends (b) DSC cooling exotherms from the non-isothermal experiments for the different compositions of PP/FH blends.

C.4 Cooling scans of pure hydrocarbon resins from non-isothermal DSC experiments

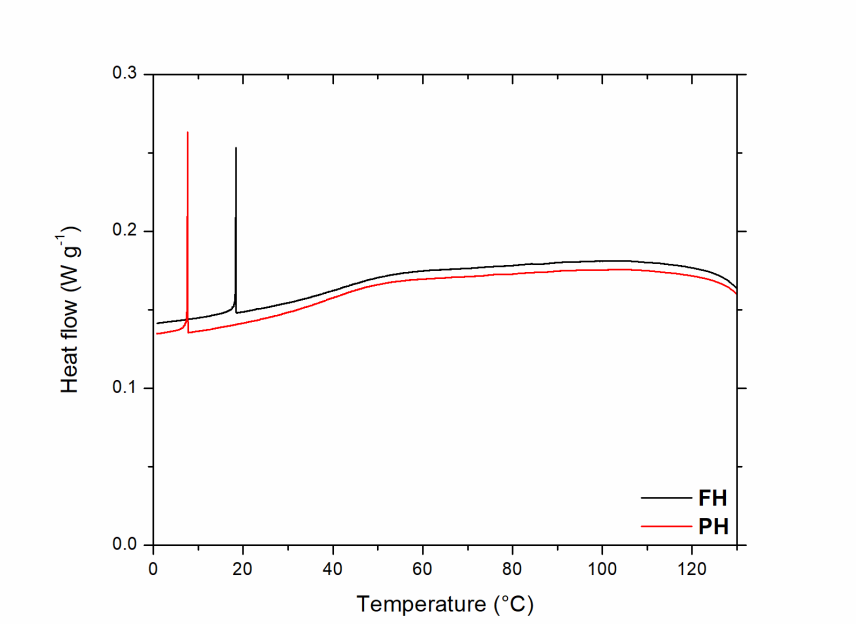


Figure C.4: Cooling scan from the non-isothermal DSC experiments for the pure FH and PH resins.

C.5 DSC melting endotherms of PP and blends zoomed in the region of 160-180°C

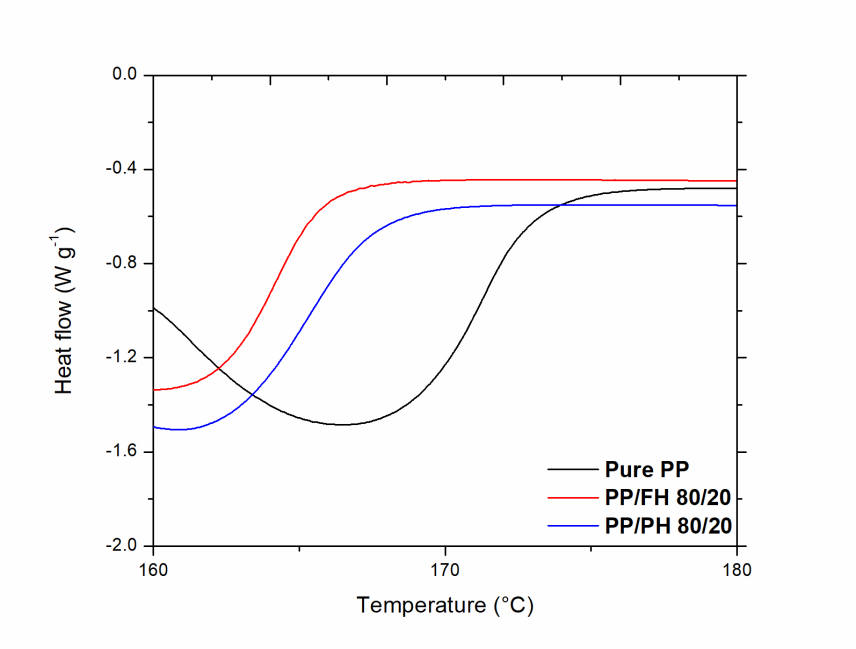


Figure C.5: DSC melting endotherm of pure PP, 80/20 blends of PP/FH and PP/PH zoomed in the region of 160°C-180°C.

C.6 Melting and crystallization temperature and enthalpy of PP/hydrocarbon resin blends

Table C.3: Peak melting temperatures (from the 2^{nd} heating scan) and peak crystallization temperatures (from the cooling scan) as well as enthalpy of melting (from the 2^{nd} heating scan) and crystallization (from the cooling scan) of the prepared PP/FH and PP/PH blends obtained using the non-isothermal DSC experiments.

Sample name	Peak melting temperature (°C)	Enthalpy of melting (Jg^{-1})	Peak crystallization temperature (°C)	Enthalpy of crystallization (Jg^{-1})
Pure PP	165.4	110.0	121.8	110.6
PP/FH 95/5	164.5	103.6	118.7	107.0
PP/FH 90/10	162.9	98.1	118.5	101.2
PP/FH 85/15	162.4	89.6	116.4	98.3
PP/FH 80/20	161.7	80.8	116.1	94.2
PP/PH 95/5	163.3	104.0	120.5	108.9
PP/PH 90/10	162.5	96.5	118.7	99.4
PP/PH 85/15	161.6	90.1	117.5	95.7
PP/PH 80/20	160.7	83.8	116.0	90.2

C.7 Degree of crystallinity of PP/hydrocarbon resin blends

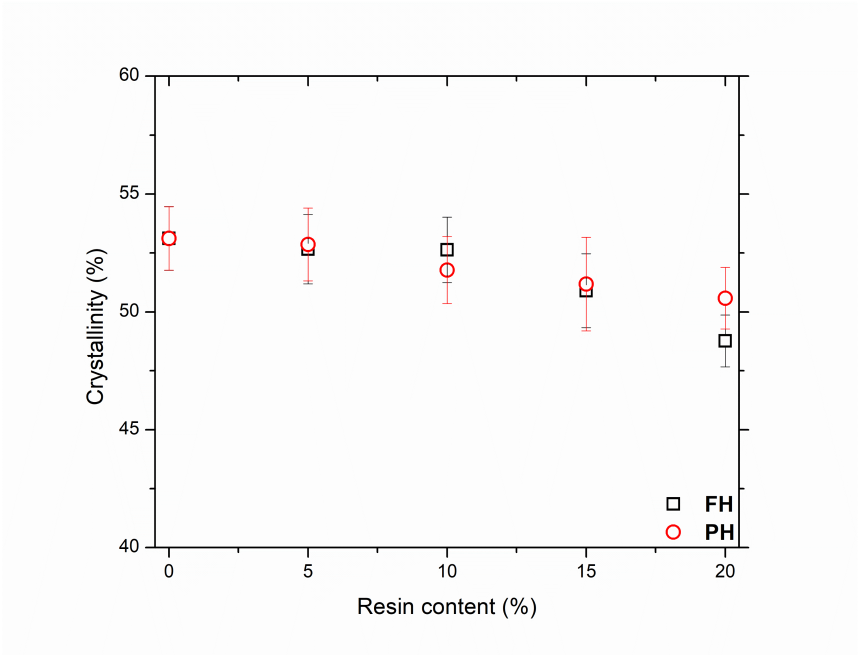


Figure C.6: Variation in percent crystallinity of the PP/FH and PP/PH blends as a function of the content of hydrocarbon resin present in the blends.

C.8 Isothermal crystallization and print bed temperature

During the deposition of polymer filament on the printer bed and subsequent solidification, adhesion to the bed and interlayer adhesion plays a significant role in successfully printing a part. The adhesion is promoted if the deposited layers are in the melt state for a longer period of time. The polymer chains at the interface can remain mobile for longer times, which helps in dissipating the residual stress build-up during crystallization. Therefore, isothermal crystallization studies were carried out using DSC to understand the differences in crystallization from the melt among pure PP, PP/FH, and PP/PH blends. However, it must be kept in mind that MEAM is highly non-isothermal and hence the goal here is to

identify the impact of the resins on the crystallization behavior of the blends.

The crystallization experiments were performed in the temperature range of 120°C to 130°C and the resulting DSC scans are illustrated in Figure C.7. During crystallization, all the samples produced an exothermic peak at each of the crystallization temperatures. At lower temperatures the peak was sharper and gradually broadened with increasing temperature. Figure C.7(a) highlights the isothermal heat flow data for PP and as the temperature increases from 120°C to 130°C, the time required for complete crystallization increases. This behavior is expected and is due to the decrease in degree of supercooling, the driving force behind crystallization, and subsequent crystalline growth. Similar behavior is also observed for the 80/20 PP/FH and PP/PH blends, which are illustrated in Figures C.7(b) and C.7(c) respectively. The incorporation of the hydrocarbon resins into the pure PP matrix results in an increase in the time required for crystallization at a constant crystallization temperature.

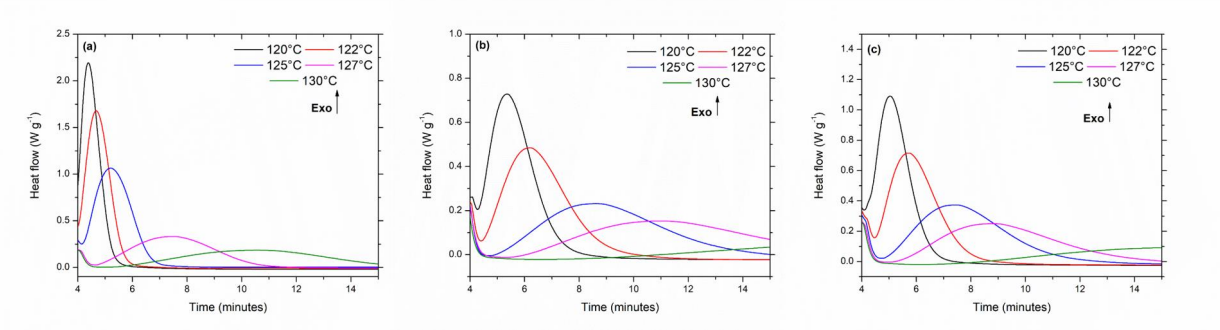


Figure C.7: Isothermal crystallization profiles for (a) PP; (b) PP/FH; and (c) PP/PH blends carried out at different crystallization temperature in the range of 120°C to 130°C.

The scans reveal that the induction time for the onset of crystallization, with the addition of the low molecular weight hydrocarbon resins is in the order, PP<PP/PH<PP/FH. The increase in induction time can be attributed to the degree of compatibility of the FH and PH

resins with PP. The FH blends are more successful in retarding the crystallization process in comparison to the PH blends, which is attributed to the better compatibility (and hence more interference with the crystallization process) [Kang et al., 2013]. In relation to MEAM, the increase in induction time can (a) improve the adhesion of the melt to the printing platform and hence minimize/eliminate warpage of the printed parts; and (b) improve interlayer adhesion when parts are built in a layer by layer manner, increasing the strength of the additively manufactured parts.

C.9 Effect of cooling rate on crystallization behavior of the blends

The effect of cooling rate on crystallization was studied with regard to the layer by layer deposition and subsequent part build up associated with the MEAM printing process. The aim of the tests is to determine a time-temperature dependence on the crystallization behavior of the blends as a function of composition. The crystallization curves related to time at two different cooling rates (10°C min^{-1} and 50°C min^{-1}) are illustrated in Figure C.8. Table C.4 summarizes the time required for crystallization for the different blends at two different cooling rates.

Table C.4: Effect of cooling rate on the time required to reach the crystallization peak for PP, PP/PH, and PP/FH blends while maintaining isothermal crystallization conditions.

Sample designation	Time required for peak crystallization (minutes)	
	10°C min^{-1} cooling rate	50°C min^{-1} cooling rate
Pure PP	9.4	5.2
PP/PH 95/05	13.5	8.0
PP/PH 90/10	14.3	9.8
PP/PH 85/15	15.8	10.9
PP/PH 80/20	17.1	13.1
PP/FH 95/05	12.9	7.9
PP/FH 90/10	16.9	11.6
PP/FH 85/15	16.9	12.7

The cooling rate experiments support the conclusion that increasing resin percentage increases the overall time for crystallization, though this difference becomes smaller as resin content is increased. This agrees with the results obtained from isothermal crystallization experiments. At the higher cooling rate, the time required for peak crystallization decreases compared to that for the lower cooling rates. At lower cooling rates, the polymer chains undergo reorganization at the molecular level as the blends are cooled to the desired crystallization temperature. Higher cooling rates induce the polymer chains to organize under non-equilibrium conditions [Martini et al., 2002].

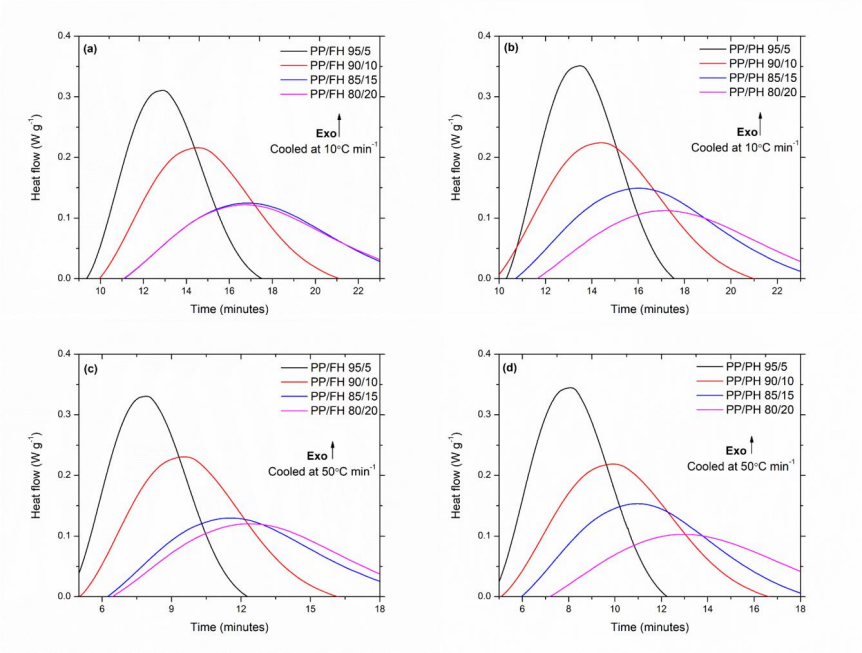


Figure C.8: Crystallization profiles during cooling from the melt for (a) PP/FH blend cooled at 10°C/min; (b) PP/PH blend cooled at 10°C/min; (c) PP/FH blend cooled at 50°C/min and (d) PP/PH blend cooled at 50°C/min.

The degree of crystallinity generally decreases at the higher cooling rate and smaller spherulites are formed while the slower cooling rate results in the formation of larger spherulites. Slower cooling also results in formation of highly pure crystals while rapid cooling results in low purity crystal formation [Piccarolo et al., 1992]. Pure crystals are desired for good mechanical properties, but since the MEAM process involves rapid cooling and the presence of hydrocarbon resins in the blends, it is expected the formed crystals will have low purity. Thus, the printed part will have inferior tensile strength and modulus than parts processed by

traditional techniques with lower cooling rates. However, higher cooling rates result in the formation of smaller crystals which can lead to better elongation in the printed parts.

C.10 Size of spherulites formed during isothermal crystallization of PP/hydrocarbon resin blends

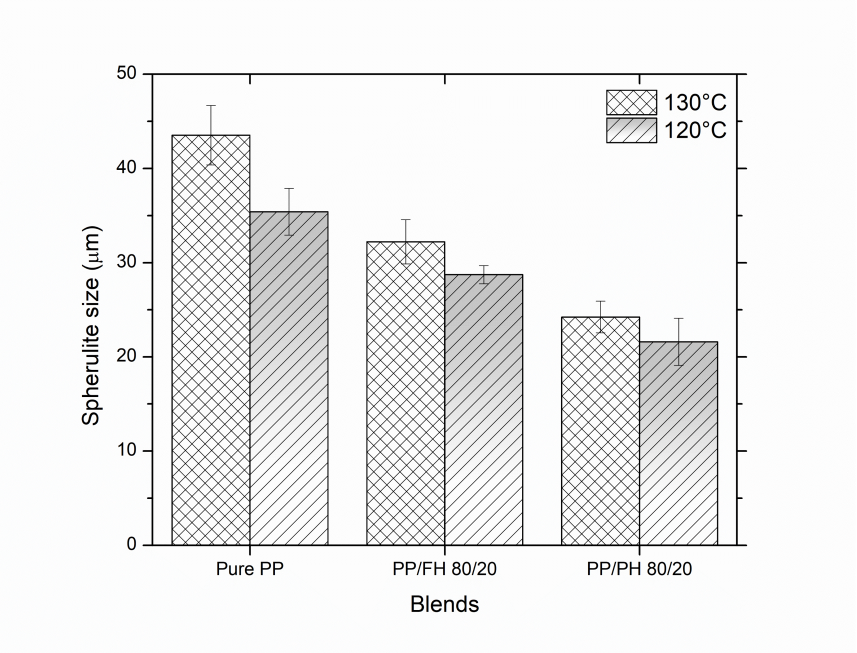


Figure C.9: Effect of crystallization temperature and resin type on the size of the spherulites formed during cooling from the melt and held isothermal at different crystallization temperatures (120° C and 130° C) for pure PP and its blends with hydrocarbon resins.

C.11 Mechanical properties of PP/FH blends printed at ±45° raster angle

In the case of PP/FH blends, as the resin content increases from 5 to 20 percent, the tensile modulus and tensile strength decreases as illustrated in Figure C.10. The tensile strength of the 80/20 PP/FH blend decreases by 43% as compared to the pure PP printed part. Similar

decreases in the tensile strength have been reported for PP/natural rubber and PP/recycled rubber blends prepared in a Brabender [Ismail and Suryadiansyah, 2002].

The maximum elongation at break of the pure PP printed part is similar to that of injection molded (IM) part but decreases significantly with the addition of resins, which can be attributed to stress concentration effects. The values decrease by 64% for the 80/20 blend of PP/FH in comparison to pure PP prints. It is interesting to note that the elongation at break for the blends are in the same range as those reported for wood-fiber/PP composites with flame retardants [Zhang et al., 2012]. Moreover, the values reported in this study are higher than that of PP/wood flour composites [Ichazo et al., 2001] as well as highly filled (>20%) PP/carbon-black and PP/carbon fiber composites [Kaynak et al., 1996].

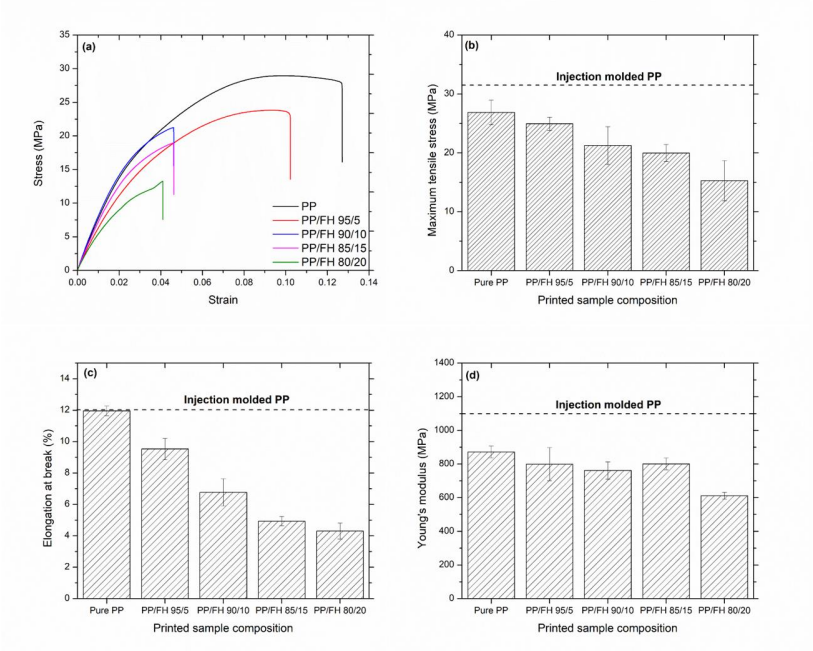


Figure C.10: (a) Stress-strain curves for the PP/FH printed parts (±45° raster angle) in compositional ratios up to 20 wt% resin; (b) effect of increasing FH resin content on the maximum tensile stress; (c) effect of increasing FH resin content on the elongation at break; and (d) effect of increasing FH resin content on the Young's modulus of the printed parts of PP/FH blends.

Finally, the tensile modulus of the 80/20 PP/FH blends decreases by 30% as compared to the pure PP printed part. The decrease in modulus can be attributed to the miscibility of the FH resin with the PP matrix, which interferes with PP crystallization and reduces the

overall crystallinity. Under high deformations, the adhesion at the interface is poor and the presence of resins in the PP matrix gives rise to defects at the interface which are responsible for the reduced values of tensile modulus in the PP/FH blends [Mohd Ishak et al., 2001]. However, it must be noted that the tensile moduli of printed PP/FH blends are still inferior (27-44% lower) to that of IM PP.

C.12 Mechanical properties of annealed PP/FH blends printed at ±45° raster angle

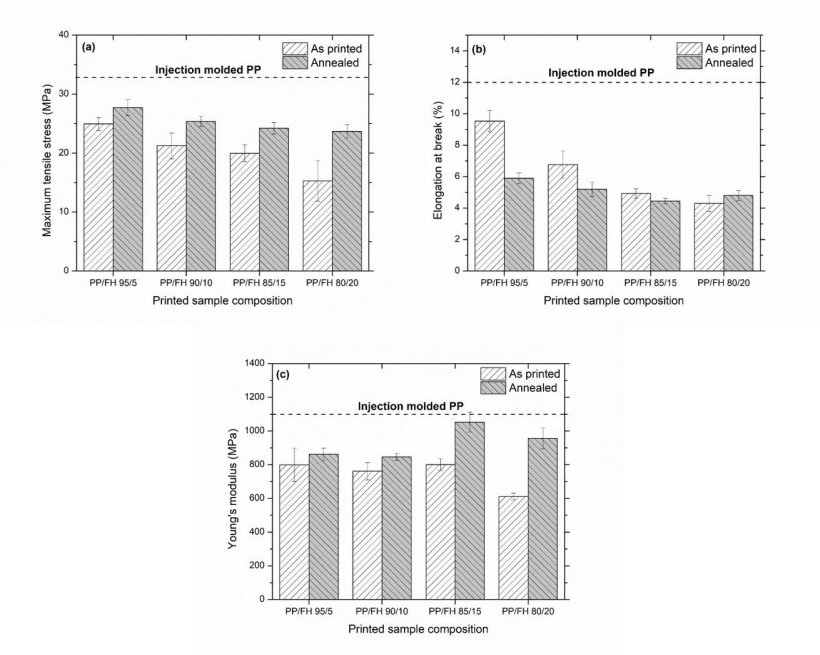


Figure C.11: Comparison of the (a) maximum tensile stress; (b) elongation at break; and (c) Young's modulus of the as printed and annealed PP/FH parts (±45° raster angle) with respect to injection molded PP.

C.13 Mechanical properties of PP/hydrocarbon resin 80/20 blends printed at 90° raster angle

The interlayer strength was analyzed by tensile testing parts printed at 90° raster angle, where the bond strength is directly assessed. As illustrated in Figure C.12, the maximum tensile strength of pure PP and 80/20 blends of PP/FH printed at 90° raster angle are comparable, indicating there is negligible change in the interlayer adhesion in the samples. However, a 20% improvement in tensile strength was observed for the 80/20 PP/PH blend printed part which suggests better interlayer diffusion and bonding strength. The soft tacky nature of the PH resins suggests more molecular mobility that is expected to enhance interlayer adhesion, resulting in improved tensile properties of the printed parts.

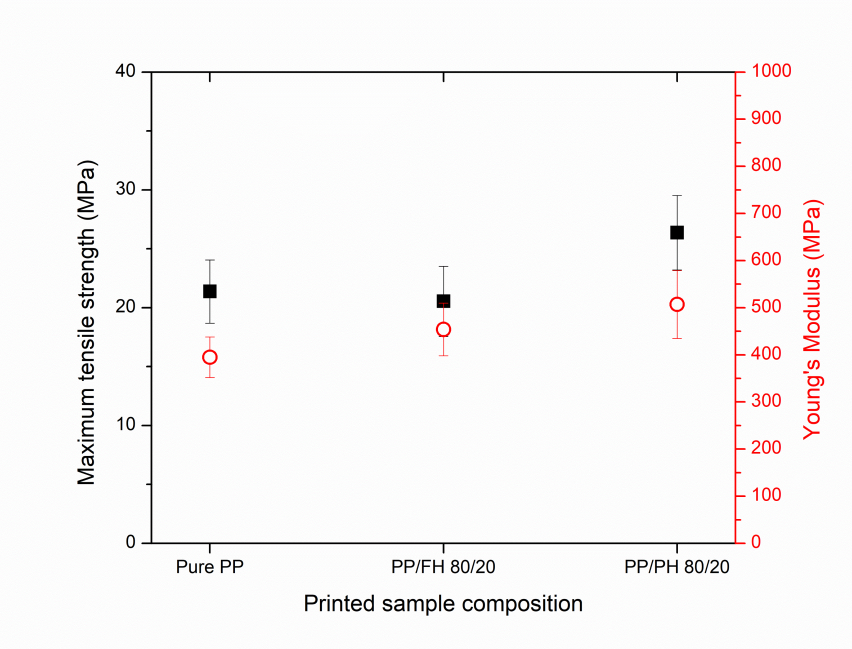


Figure C.12: Tensile strength and tensile modulus of pure PP and 80/20 blends of PP/FH and PP/PH printed under the same conditions as used in this study at 90° raster pattern. This raster pattern allows to directly measure the strength of interlayer bonding by testing the printed layer adhesion.

Moreover, the Young's modulus of 80/20 blend of PP/PH is 28% higher than that of pure PP printed under the same conditions. This provides further evidence to the improved interlayer

adhesion since the modulus is calculated from the initial portion of the stress-strain curve and any imperfections or defects at the interfacial layers can lead to reduction in the value of the Young's modulus [Mohd Ishak et al., 2001].